Semifluorinated theranostic nanoparticles:

development of stabilized colloidal drug delivery vehicles

by

Sarah E. Decato

A dissertation submitted in partial fulfillment of

the requirements for the degree of

Doctor of Philosophy

(Chemistry)

at the

UNIVERSITY OF WISCONSIN-MADISON

2015

Date of final oral examination: May 29th, 2015

The dissertation is approved by the following members of the Final Oral Committee:

Sandro Mecozzi, Associate Professor, Pharmaceutical Sciences and Chemistry
Helen E. Blackwell, Professor, Chemistry
Weiping Tang, Associate Professor, Pharmaceutical Sciences and Chemistry
Charles Lauhon, Associate Professor, Pharmaceutical Sciences
Nicholas Abbott, Professor, Chemical and Biological Engineering

Semifluorinated theranostic nanoparticles: development of stabilized colloidal drug delivery vehicles

Sarah E. Decato

Under the supervision of Professor Sandro Mecozzi

At the University of Wisconsin-Madison

ABSTRACT

A large majority of the drugs on the market and in the pipeline exhibits significant hydrophobic character, requiring careful formulation to translate therapeutic effect clinically. Multifaceted colloidal nanoparticles can encapsulate hydrophobic drugs, such as chemotherapeutics, to increase solubility, lessen side effects, and target specific tissues or pathologies. Colloidal formulations are attractive drug delivery vehicles in that the properties of the nanoparticles can be tailored for the specific desired application via facile modification of the individual molecules composing them. Despite the increasing number of technologies developed for hydrophobic drug delivery, successful implementation in clinical trials remains limited, which is in part due to the inherent instability of colloidal formulations.

In this thesis multifunctional polymers have been synthesized and formulated to leverage the unique properties of fluorinated compounds in order to enhance colloid stability for increased therapeutic efficacy. The semifluorinated polymers form stable hydrophobic drug formulations, either as fluorous emulsions for intravenous delivery of anesthetics or as small, discrete micelles for chemotherapy. The latter formulation has shown high drug loading and retention of a classical chemotherapeutic (paclitaxel) in an intermediate hydrocarbon domain, while the fluorous core

inhibits recognition by the reticuloendothelial system to afford prolonged circulation *in vitro* and *in vivo*. Additionally, the fluorous core has been specifically designed to provide particle tracking via ^{19}F-MRI in addition to nanoparticle stability. The symmetrical, perfluoro-*tert*-butyl (PFtB) fluorous moiety enables theranostic (dual therapeutic and imaging) capabilities to enhance targeted delivery (by the EPR effect, in the case of chemotherapy) via enhanced stability and to provide simultaneous ^{19}F-MR imaging. These dually functional particles can be applied to diagnosis of disease and analysis of bioavailability and pharmacokinetics, which may elucidate nanoparticle behavior *in vivo* to improve future polymer and formulation design. These studies demonstrate the benefits of the PFtB polymer structure, which can be extended to serve as a stabilizing, theranostic design feature for other nanoparticle systems.

ACKNOWLEDGMENTS

Firstly, I am grateful to Professor Sandro Mecozzi for giving me the opportunity to study in his lab. I really enjoyed having significant input in the direction of my research and the freedom to explore my own ideas. I am also indebted to all my expert collaborators for their discussions, materials, time, and patience. Specifically, I would like to acknowledge funding from the NSF-EAPSI and the JSPS Summer Program for the opportunity to work with Professor Kazunori Kataoka at the University of Tokyo. The opportunity to work with him and his esteemed colleagues was extremely helpful in the development of my research. Also, the experiences I had in Japan have become fond memories, shaped by the wonderful people I met. I would like to thank the School of Pharmacy and Department of Chemistry, and the respective staff and scientists for all their help in the various stages of my graduate career, particularly Dr. Scarlett and Dr. Hill for their support and guidance during my PA and TA. I would also like to express my appreciation to my thesis committee for their time and insight.

To the Mecozzi group members both former and current, I am very thankful for your support and friendship. I am very lucky to have had the opportunity to work and laugh with all of you. I would particularly like to thank William Tucker, my partner in crime, for being my companion over these past 5 years. I couldn't have done it without you.

At UW-Madison I was also extremely lucky to meet my soul companion, Joseph Moore. Through the good times and bad you've never ceased to brighten my days (and edit my papers). You have always seen the best in people and you inspire me to be my best self. Be ever right be ever recherché. Lastly, thank you to all my friends and family, and all the friends who have become family. You are the ones on the phone at night, bolstering my confidence, listening to my woes, telling me to reach higher, push harder, and be better. You are my foundation and I would not be here without any one of you. I love you dearly.

TABLE OF CONTENTS

LIST OF FIGURES AND TABLES

LIST OF ABBREVIATIONS

A549	human lung cancer cell
ABC	accelerated blood clearance
ACN	acetonitrile
AmP	ammonium phosphate monobasic
BTF	α,α,α-trifluorotoluene
CHCA	α-cyano-4-hydroxycinnamic acid
CMC	critical micelle concentration
CPMG	Carr-Purcell-Meiboom-Gill
CT	computed tomography
DCM	dichloromethane
DHB	2,5-Dihydroxybenzoic acid
DiI	1,1'-dioctadecyl-3,3,3',3'-tetramethylindocarbocyanine perchlorate
DiO	3,3'-dioctadecyloxacarbocyanine perchlorate
DLS	dynamic light scattering
DMF	*N,N*-dimethylformamide
DMSO	dimethylsulfoxide
DNA	deoxyribonucleic acid
DSC	differential scanning calorimetry
DSPE	1,2-distearoyl-*sn*-glycero-3-phosphoethanolamine
ED_{50}	median effective dose
ELSD	evaporative light scattering detector
EPR	enhanced permeability and retention effect
EPS	electrostatic potential energy surface

FA	formic acid
FDA	Food and Drug Administration
FRET	Förster Resonance Energy Transfer
FOV	field of view
g	gram
GC	gas chromatography
GEEC	GPI-Enriched Endocytic Compartments
h	hour
hpf	hours post fertilization
HPLC	high performance liquid chromatography
IgG	immunoglobulin G
IV	intravenous
IVRTCLSM	in vitro real time confocal laser scanning microscopy
k	kilo
LC	liquid chromatography
LD_{50}	median lethal dose
m	milli
MALDI	matrix-assisted laser desorption/ionization
MOPS	3-(*N*-morpholino)propanesulfonic acid
$mPEG_{xk}$	mono-methoxy poly(ethylene glycol) of average molecular weight x-kDa (e.g. $mPEG_{2k}$ = 2,000 g/mol)
$mPEG_{xk}$-H#-F#	H# represents the number of CH_2 units in the linear alkyl chain, F# represents the number fluorocarbons in the linear fluoroalkyl chain [e.g H10F13 = $(CH_2)_{10}$-$(CF_2)_{12}$-CF_3]

MPS	mononuclear phagocyte system
MRI	magnetic resonance imaging
Ms	methanesulfonyl
MS	mass spectrometry
MSI	mass spectrometry imaging
MWCO	molecular weight cut off
n	nano
NMR	nuclear magnetic resonance
o/w	oil-in-water
OEGMA	oligo(ethylene glycol) methyl ether methacrylate
P3P	1,3-bis-(1-pyrenyl)propane
PBS	phosphate buffered saline
PC-3	prostate cancer cell line
PCL	poly(ε-caprolactone
PEG	poly(ethylene glycol)
PEG-*b*-PCL	poly(ethylene glycol)-block-poly(ε-caprolactone)
PEG-*b*-PDLA	poly(ethylene glycol)-block-poly(D-lactide
PEG-*b*-PLLA	poly(ethylene glycol)-block-poly(L-lactide
PET	positron emission tomography
PFC	perfluorocarbon
PFOA	perfluorooctanoic acid
PFOB	perfluorooctyl bromide
PFOS	perfluorooctane sulfonate
PFPE	perfluoropolyether

PFtB	perfluoro-*tert*-butyl
PLA	poly(lactic acid)
PMB	p-methoxybenzyl
PTX	paclitaxel
PVA	poly(vinyl alcohol)
PVP	poly(*N*-vinyl pyrrolidone)
QD	quantum dot
RES	reticuloendothelial system
ROS	reactive oxygen species
SAXS	small angle X-ray scattering
SNR	signal to noise ratio
SPIO	superparamagnetic iron oxide
T_1	spin-lattice relaxation
T_2	spin-spin relaxation
T_2^*	"effective" spin-spin relaxation
T_g	glass transition temperature
TEM	transmission electron miscroscopy
THF	tetrahydrofuran
TLC	thin-layer chromatography
T_m	melting temperature
TMS	tetramethylsilane
TOF	time of flight
v/v	volume/volume
WAXS	wide angle X-ray scattering

wt.	weight
WHO	World Health Organization
µ	micro

CHAPTER 1:

Introduction

*This chapter contains content that has been published under the title "Colloid and Interface Science in Pharmaceutical Research and Development". In keeping with the author's rights as described by the publisher, less than 10% of the contributed content has been used in this manuscript. Reference: Decato, S.; Mecozzi, S. Highly Fluorinated Colloids in Drug Delivery and Imaging. In *Colloid and Interface Science in Pharmaceutical Research and Development*; Elsevier, 2014; pp 319–345.

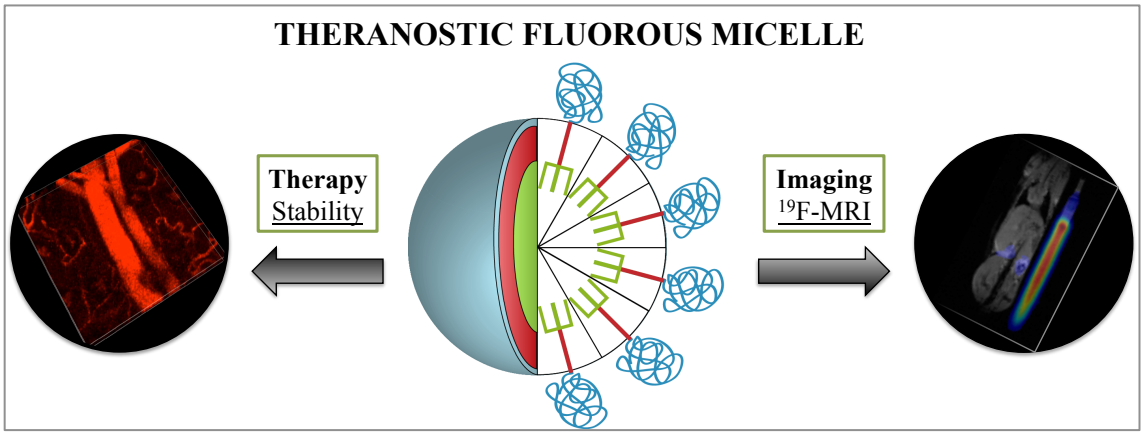

1.1 Fluorous compounds: a brief introduction to their properties and applications

1.1.1 What is the fluorous phase?

The introduction of multiple fluorine atoms into an organic molecule drastically alters the properties of the overall compound—for example those relating to thermal, mechanical, and dielectric performance[1,2,3,4]—and its subsequent formulations. The widespread utility of highly fluorinated compounds across a diverse range of research fields, is derived from such unique properties, and has allowed for the design of complex materials rapidly from cheap, simple starting materials.

The bulk or macromolecular properties of fluorinated compounds that are unmatched by their non-fluorinated counterparts, originate from the unique characteristics of the fluorine atom (**Table 1.1**). With a covalent binding energy of ~485 kJ/mol, the C—F bond is the strongest single bond in which a carbon atom can participate (in comparison, a single covalent C—H bond is ~425 kJ/mol in binding energy). The increased chemical and thermal inertness of fluorocarbons is related to this strength of the C—F bond.[5] Furthermore, fluorine is more electronegative, less polarizable, and bulkier than a hydrogen atom. Perfluorocarbon (PFC) chains, C_nF_{2n+1}, have a cross-sectional area of 30 Å^2 versus 20 Å^2 for the hydrocarbon-analog.[6] The bulkier and more

rigid PFC chains reduce conformational freedom, resulting in a preferred helical conformation, which further enhances the thermal and oxidative stability of the fluorinated compound.[7] Most importantly, PFCs experience only very weak van der Waals interactions due to the very low polarizability of the fluorine atom and of the C—F bond. This effect produces not only an increase in the hydrophobicity of the fluorinated section but also the development of lipophobic character.

	H	**F**	O	N	C	Cl	Br
Van der Waals radius (Å)	1.20	**1.47**	1.52	1.55	1.70	1.75	1.85
Pauling electronegativity	2.1	**4.0**	3.5	3.0	2.5	3.2	2.8
Length of single bond to carbon (Å)	1.09	**1.40**	1.43	1.47	1.54	1.77	1.97
Strength of bond to carbon (kcal/mol)	98	**105**	84	70	83	77	66

Table 1.1 Comparison of the properties of various elements and their bonds to carbon.
The unique attributes of the fluorine atom—specifically in comparison to hydrogen—are the origin of the unique properties of fluorinated organic molecules. Adapted from Reference 8.

The dual hydro- and lipophobicity of PFCs leads to the formation of a unique fluorous phase, which is distinct and phase-separates from both aqueous and oil-based media.[9,10] Empirically, the fluorous nature of a compound can be measured by its partition coefficient in a fluorous solvent (commonly perfluoromethylcyclohexane). Alternatively, to predict the fluorophilicity (affinity for the fluorous phase) of a compound *de novo* based on the structure is extremely difficult; however, the following general rules may be applied in most cases: A molecule consisting of ≥ 60 wt. % fluorine will most likely be fluorophilic. A compound containing significant perfluoroalkyl segments—generally > 6 perfluorocarbons or longer—will also be considered fluorous. Additionally, to improve fluorophilicity, one should minimize the potential for strong

intermolecular interactions, such as dipole-dipole, hydrogen-bonding, induction forces, etc.[11,12] These guidelines are useful for the design of simple systems but may be inadequate in predicting fluorous behavior in the variety of complicated systems to which fluorinated compounds may be applied.

1.1.2 Fluoropolymers and surfactants

The variety of desirable physicochemical properties of perfluorocarbons has been effectively manipulated in the development of fluorous polymers and surfactants to afford materials with high thermal stability, chemical resistance, mechanical properties at extreme temperatures, superb weathering resistance, oil and water repellence, and low flammability. Fluorous materials have thus become entrenched in the commodities and industrial products market, serving as fundamental components in most paints, adhesives, and other performance coatings (**Table 1.2**).[13,14,15] As reported by MarketsandMarkets (and supported by analyses from Research and Markets, Modern Plastics and Polymers, and RnR Market Research), in 2013 the global fluoropolymer market generated an estimated $6.2 billion in revenue, which is expected to reach $8.8 billion by 2019.[16]

Industries	**Functions**	**Forms**
Automotive	Mechanical property, thermal property, chemical property, and friction property.	O-rings, gaskets, valve stem seals, shaft seals, linings for fuel hoses, power steering, and transmission.
Chemical industry	Chemical resistance, mechanical property, thermal property, and weather stability.	Coatings for heat exchangers, pumps, diaphragms, impellers, tanks, reaction vessels, autoclaves, containers, flue duct expansion joints, heavy-wall solid pipe and fittings.
Electrical/electronic	Dielectric constant, flame resistance, and thermal stability.	Electrical insulation, flexible printed circuits, ultra-pure components for semiconductor manufacture.
Architectural and domestic	Weatherability, flame retardancy, friction property, thermal stability.	Water-repellent fabric, architectural fabric, non-stick coatings for cookware, and fiberglass composite for constructions.
Engineering	Mechanical property, thermal stability, chemical stability, weatherability, and surface energy.	Seats and plugs, bearings, non-stick surfaces, coatings for pipes, fittings, valve and pump parts, and gears.
Medical	Surface energy, biological stability, mechanical property, chemical resistance.	Cardiovascular grafts, ligament replacement, and heart patches.

Table 1.2 List of typical applications of fluoropolymers across a variety of industrial fields.
Chemical and thermal inertness, along with other desirable properties, enable fluoropolymers to enhance material performance in a variety of applications. Adapted from Reference 15.

Fluorous polymers and surfactants have also made a large impact in self-assembling systems. As discussed earlier, fluorous compounds provide unique properties derived from their inability to participate in significant intermolecular interactions. The resulting amphiphilic character of fluorous compounds promotes adsorption at interfaces and provides an increased driving force for self-organization in colloidal systems.[17,18] In these areas, fluoropolymers have begun to penetrate high-performance and niche markets. In particular, fluorous compounds have found unique applications in medical devices and therapies (this topic will be discussed in detail in the majority of this thesis, particularly concerning emulsion and micelle colloidal systems).

1.1.3 General applications in medical and pharmaceutical fields

The application of fluorinated compounds in the materials industry began well over 50 years ago, but over the past several years these compounds have become more prevalent in the medical and pharmaceutical fields.[19] For example, fluorine has had a significant impact in biochemical and medicinal analytics in the field of imaging with the development of ^{18}F positron emission tomography (PET)[20] and ^{19}F magnetic resonance imaging (MRI), the latter of which will be discussed further in sub-chapter 1.3.2. With mitigated success, perfluorocarbons have also been a persistent element in the development of oxygen transport and blood substitute systems.[21,22]

Most notably, in the past decade, fluorine has made a profound impact in the pharmaceutical pipeline. Selective and strategic fluorination in a new chemical entity or existing natural product provides simplified modification of its drug action and pharmaceutical profile. For example, fluorine may be installed to deter metabolism or to modulate the drug-receptor binding interaction.[23,24] These and other applications clearly demonstrate fluorine's substantial influence on molecular conformation and molecular recognition and the advantageous properties that can be derived therefrom.

1.2 Formulations in drug delivery

1.2.1 Colloidal solutions for hydrophobic drug delivery

An estimated 40% of new pharmacologically active drugs on the market and in the pipeline are characterized as significantly hydrophobic, resulting in poor water solubility[25] (**Figure 1.1**). Despite the high therapeutic efficacy of these poorly soluble drugs, their clinical translation remains limited due to a lack of sophisticated materials to enable successful formulation.

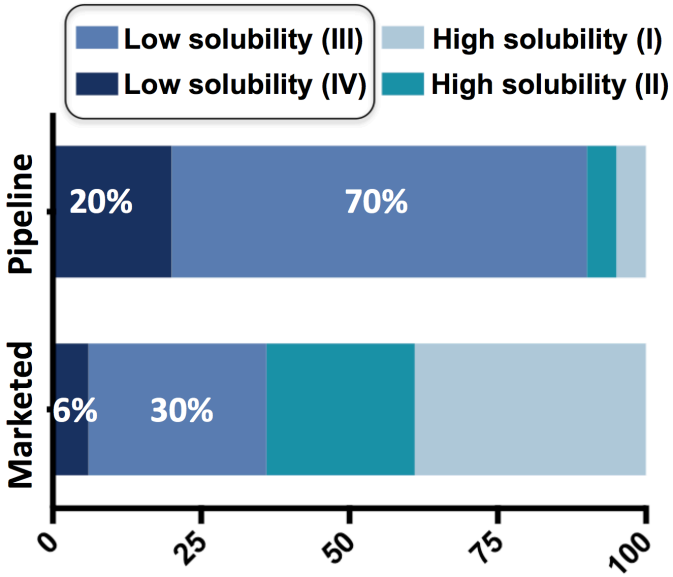

Figure 1.1 A large percentage of drugs in the pharmaceutical industry are hydrophobic.
Drug candidates and marketed drugs are categorized by class (I-IV). Class III and IV represent poorly water soluble drugs, and represent the vast majority of current and future pharmaceutical entities.

Colloidal drug formulations (consisting of small particles—typically < 1 μm—evenly dispersed in a continuous phase) are an attractive delivery platform because their characteristics are dictated by the physicochemical properties of the compounds composing them. The colloidal characteristics can be readily tuned to the specific needs of a desired application by facile modulation of the compound composition and/or structure. Modifications to colloidal particles, such as the installation of fluorinated compounds, are readily applicable to such systems, which can engage the unique properties of fluorous compounds to enhance colloidal hydrophobic drug formulations. Two hydrophobic drug formulations, emulsions and micelle self-assemblies, have

been identified in this thesis as particularly amenable to the incorporation of a fluorous component. The following sections will serve as a brief introduction to these two drug delivery platforms and will reveal why they are anticipated to particularly benefit from the properties of the fluorous phase.

1.2.2 Emulsions

Emulsions are an attractive drug delivery platform in that they are typically easy to formulate and can deliver a large payload of drug in comparison to other delivery vehicles. Emulsions are a specific subset of colloidal particles in which immiscible components are mixed and dispersed in a continuous liquid phase.[18] Emulsions are loosely categorized by their size, visible characteristics, and preparation method.[26] Of these distinguishing characteristics, the most important feature in terms of the therapeutic application is the droplet size. For safety purposes the FDA requires that a parenteral emulsion must be less than 500 nm in size to prevent embolism from obstructed capillaries.[27] This may be difficult in some cases, as the physical act of parenteral delivery itself can alter the profile (size and shape) of the emulsion formulation, leading to altered pharmaceutical and metabolic consequences from those of the initial formulation. For example, smaller droplets tend to decrease macrophage activation, which would otherwise quickly clear the formulation from circulation. Additionally, a marketable emulsion formulation should ideally be stable for several years and show little change over temperature extremes, sunlight exposure, vibrations, and humidity during shipment and storage. The strict regulations on droplet size and significant relationship between size and efficacy clearly substantiate the paramount role of stability in the emulsion design.

The ultimate size and stability of an emulsion is dependent on the component composition. The most common emulsion, oil-in-water emulsion (o/w), typically consists of a surfactant, a disperse oil phase, an aqueous medium, and in some cases an additive of limited solubility in the

aqueous medium. The surfactant serves as an emulsifier, adsorbing to the droplet interface, which decreases the interfacial tension, and increases interfacial elasticity and viscosity.[28] The components are mixed together and can be forced into smaller droplets by a high-energy input, such as a homogenizer or microfluidizer. The method of preparation must be adapted to the specific formulation and thoughtfully applied as it greatly affects the initial droplet size, which dictates the mechanism and therefore rate of droplet growth or stability.

1.2.3 Emulsion stability

All dispersions, including emulsions, are inherently thermodynamically unstable. An o/w emulsion consisting of many polydisperse droplets will break over time to return to the lower energy phase-separated system via a variety of processes, including Brownian flocculation, creaming, sedimentation flocculation, and disproportionation (or Ostwald ripening).[29] Droplet loss and ultimately phase-separation may occur by any combination of these mechanisms simultaneously (**Figure 1.2**). Creaming occurs when the emulsion forms a "cream" layer in which the concentration of the disperse phase is increased, which typically then leads to coalescence. Creaming can be deterred by decreasing the droplet size, increasing the viscosity of the emulsion, and decreasing the difference in density between the aqueous and dispersed phase.[30] Flocculation occurs due to the inherent polydispersity of the emulsion droplets. Larger droplets are moving faster and may trap or aggregate with smaller droplets. A linear movement is termed sedimentation flocculation while a random movement of the large particles is termed Brownian flocculation. Despite this classification, both typically occur simultaneously. Lastly, disproportionation (Ostwald ripening) is dictated by the rate of diffusion of the dispersed phase from small droplets to larger droplets, driven by the difference in chemical potential between small and large droplets originated by curvature effects. To deter Ostwald ripening, many times

an additive is added to the dispersed phase in order to further decrease solubility or to modify the interfacial film at the o/w interface.[31]

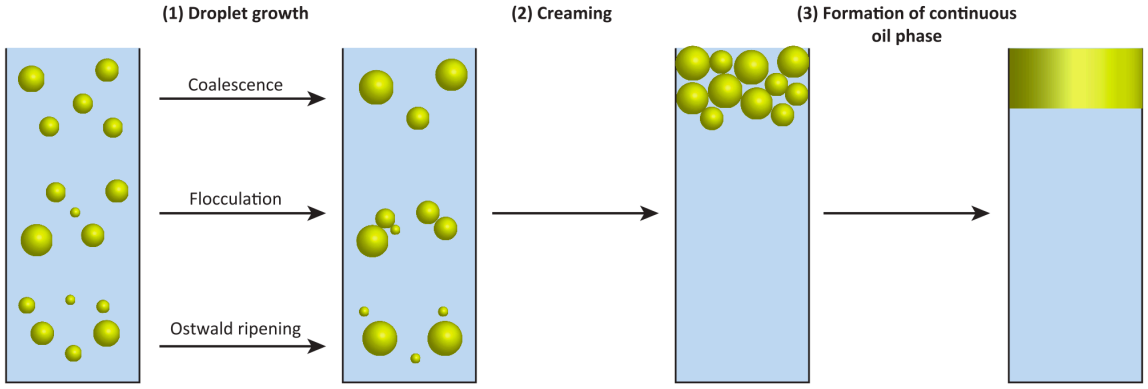

Figure 1.2 Mechanisms for emulsion destabilization.
Droplets can grow by any combination of the processes in step (**1**), depending on droplet properties, followed by creaming (**2**) and ultimately phase separation and emulsion breaking (**3**). Adapted from Reference 30.

A significant driving force for the aggregation and destabilization of emulsion droplets is van der Waals attractive interactions. Intermolecular interactions between droplets may be arrested by the increase of electrostatic or steric repulsion between droplets. In non-ionic systems large surfactant chains can be anchored or adsorbed onto the surface of the droplets to form a protective layer and increase steric repulsion. When droplets come close together in space, the surface-anchored chains interpenetrate or compress together resulting in increased osmotic repulsion (unfavorable mixing) and elastic interactions (increased entropy from volume restriction). These unfavorable interactions will mitigate the high surface energy of the droplets and deter particle size growth.[31]

Perfluorinated or semifluorinated surfactants can also serve to stabilize emulsions, especially in o/w systems, due to the decreased solubility of the fluorous-components in the aqueous continuous phase. The addition of higher-molecular-weight fluorous compounds and fluorous surfactants reduce the rate of droplet growth (decreased by approximately a factor of 8 for each CF_2). One commonly used fluorous stabilizer is perfluorooctylbromide (PFOB), which is slightly

lipophilic and therefore exhibits reduced organ retention in comparison to other high-molecular-weight fluorous compounds. Fluorous surfactants are particularly effective in stabilizing emulsions with fluorous dispersed phases. In these systems Ostwald ripening is typically the major mechanism for emulsion breaking and so the rate of increase in droplet size is a linear function of the interfacial tension and aqueous solubility of the fluorous dispersed phase over time.[32] Fluorous emulsions have found several applications that can fully exploit the properties of fluorous compounds, such as blood substitutes (which require high oxygen solubility) and ultrasound medical imaging.[1,33] Recently, the fluorous emulsions have been developed for hydrophobic drug delivery of a specific class of drugs which exhibit significant fluorophilicity.

1.2.4 Fluorous emulsions for the intravenous delivery of anesthestics

Commonly hydrophobic drugs display limited solubility in fluorous emulsions; however, several commonly used anesthetics, such as sevoflurane, isoflurane, and desflurane, are highly fluorinated and therefore have an increased affinity for fluorous emulsifiers. These volatile anesthetics are traditionally vaporized using specialized equipment and then inhaled through the lungs. Alternatively, delivery via fluorous emulsion formulation allows for intravenous delivery, which circumvents pulmonary regulation of the drug and therefore has the potential to improve induction and recovery profiles and to allow for prompt variation in the depth of anesthesia.[34] Linear diblock fluorous-copolymers, consisting of a mPEG hydrophilic section and a linear perfluorinated tail, have been developed to form o/w emulsions with high anesthetic loading for intravenous injection.[35]

Fluoropolymers developed by the Mecozzi group were able to emulsify and deliver much higher concentrations of anesthetic than current hydrocarbon-based surfactant systems due to the fluorophiliciy of the drug. The preferred clinical agent for induction and maintenance of general anesthesia is sevoflurane, which consequently has been the drug of choice in the majority of the

fluorous emulsion studies. The most promising system, consisting of 10 mM concentrations of the fluorous polymer $mPEG_{5k}$-F13 (**Figure 1.3**) and 10 % v/v of the fluorous additive PFOB (approved by the FDA for human use) was able to stably emulsify up to 30 % v/v of the fluorous anesthetic sevoflurane in normal saline. This formulation was relatively simple with only three components and showed a several-fold increase over the previously most successful reported formulation, Intralipid®: a phospholipid and soybean oil-based emulsion, which was only able to stably formulate a maximum of 3.5 v/v % of sevoflurane.[34]

The $mPEG_{5k}$-F13 fluorous emulsion was able to deliver a clinically relevant concentration of anesthetic, suitable for both induction and maintenance of general anesthesia. However, the stability of the emulsion needed to be improved by reducing the Ostwald ripening rate. Reducing the length of the mPEG in the semifluorous polymer (mPEG 5,000; n = 113, to mPEG 1,000; n = 25) reduced steric interactions between the hydrophilic head groups. Additionally, alteration of the fluorous surfactant tail structure (from linear to dibranched) was achieved from the synthesis of the dibranched, hemifluorinated $mPEG_{1k}$-diH3-F8 polymer (**Figure 1.3**), which was thought to allow for tighter packing between the surfactant molecules surrounding the sevoflurane nanodroplet. Both modifications provided a dense and more rigid outer-layer surrounding each droplet and reduced the rate of diffusion of the anesthetic out of the droplets (**Figure 1.4**). The new fluorous emulsions were stable for over one year and maintain an average droplet size under 400 nm.[35,36]

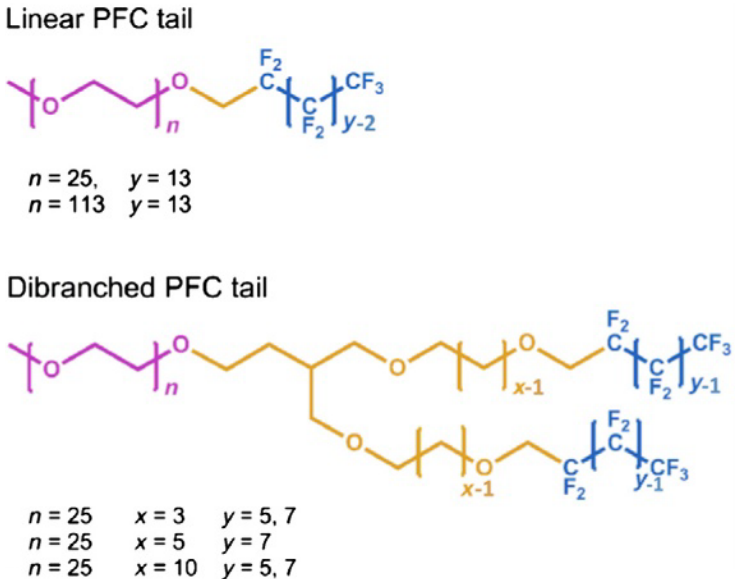

Figure 1.3 Fluorous diblock copolymers developed for IV delivery of fluorophilic anesthetics.
Original linear tail design consisting of a mPEG hydrophilic head and fluorophilic tail (**top**) was changed to a dibranched structure (**bottom**), and the size of the polar head group was reduced to allow for a more compact emulsion droplet design. Adapted from Reference 35.

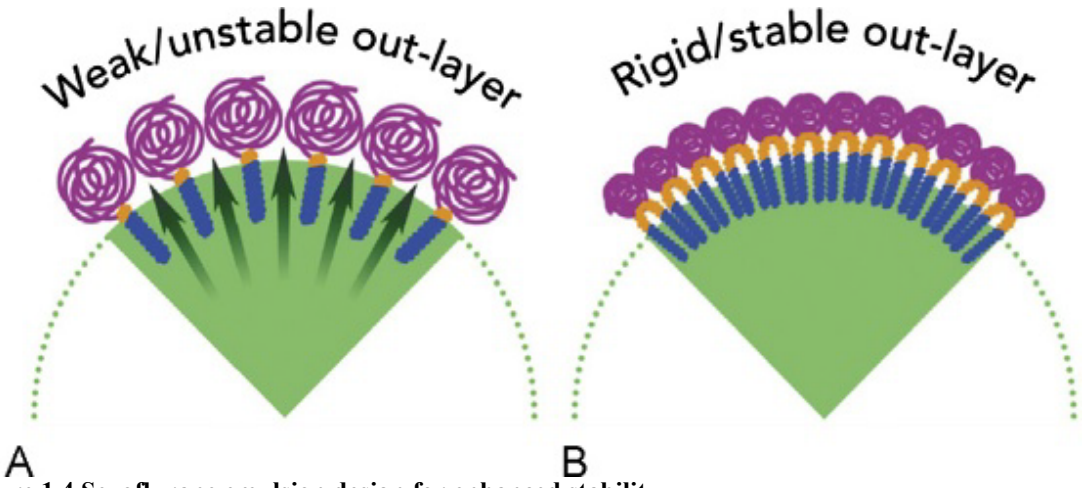

Figure 1.4 Sevoflurane emulsion design for enhanced stability.
A) Depicts facile diffusion of anesthetic molecules in solution when a large mPEG and linear fluorous tail are used. This phenomenon leads to nanoparticle growth and destabilization of the emulsion. **B**) Demonstrates the compact shell formed by the smaller mPEG and bulkier dibranched tail. This design enhances emulsion stability and reduces the rate of diffusion of the anesthetic. Adapted from Reference 36.

With the successful formulation and stabilization of the anesthetic emulsion, *in vivo* testing was performed in rats and dogs. The animal studies showed that a bolus dosing of the fluorous

emulsions allowed for smooth and rapid induction and recovery from intravenous injection of anesthetic without evidence of acute toxicity. After the bolus induction, anesthesia could also be maintained with an infusion of the anesthetic emulsion. The observed difference between the measured ED_{50} and LD_{50} of these formulations suggests that the emulsions are suitable for clinical use.[34,37] With the successful formulations in hand, a next-generation design was envisioned in which the fluorous phase could be multifunctional, serving not only as a stabilizing element for drug delivery but also as an imaging agent for *in vivo* nanoparticle tracking. This added capability could possibly allow for non-invasive pharmacokinetic or biodistribution measurements. This will be the discussed further in sub-chapter 1.3.

1.2.5 Micelle nanoparticles for drug delivery

Nanotechnology provides a platform that can be readily augmented to accommodate a variety of multifunctional features based on the desired application. Similarly to emulsion formulations, other colloidal particles have been developed that integrate recent advancements in nanotechnology for sophisticated drug-delivery applications.[38,39] Polymeric micelles are a particularly attractive drug-delivery platform as they are fairly easy to formulate and are extremely versatile. In contrast to emulsions (consisting of kinetically stabilized, large, dispersed droplets), classical micelles are thermodynamically stable self-assemblies formed by non-covalent intermolecular interactions, mainly those described by the hydrophobic effect, between individual polymer units. The size, shape, and other physicochemical properties of these polymeric micelles can thus be readily tuned via modification of the individual polymers comprising them.[40,41,42] In particular, spherical micelles have received the most attention in the field of hydrophobic drug delivery. Spherical micelles tend to form small, discrete nanoparticles, in which the hydrophilic segment of the amphiphilic polymer forms the corona, while the

hydrophobic chains form a hydrophobic core. Hydrophobic material can be encapsulated into the matrix formed by the micelle core by hydrophobic interactions or by covalent bonding with the hydrophobic polymer domain (**Figure 1.5**).[43,44]

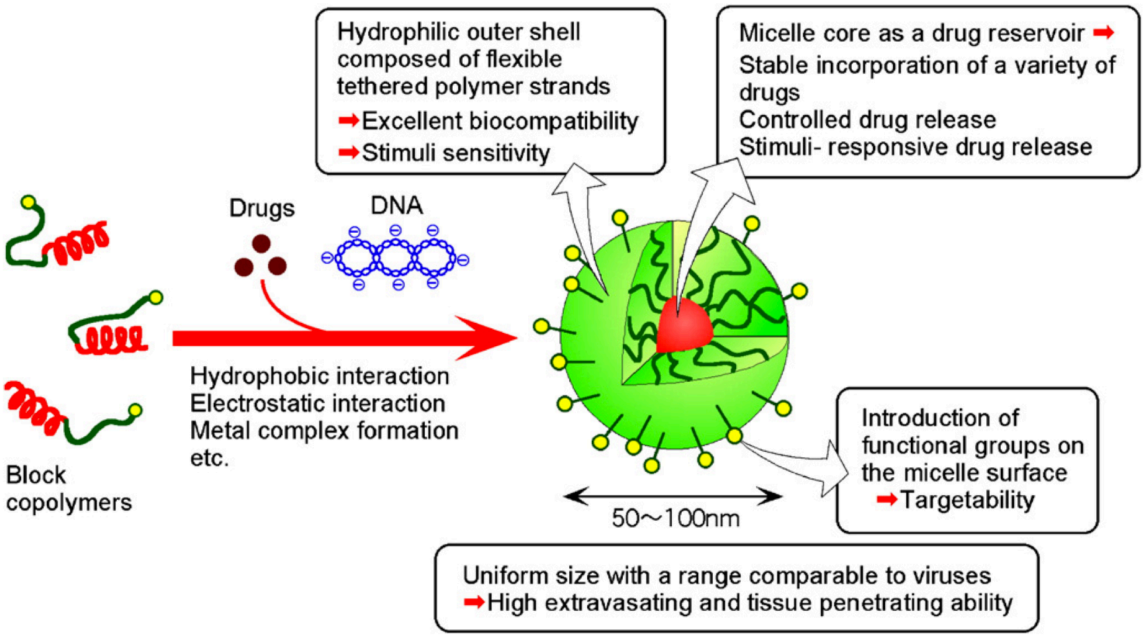

Figure 1.5 Polymeric micelles as smart and versatile delivery formulations.
The properties of the nanoparticle can be tailored for a desired application by modulation of the block copolymers that compose the micelle. Adapted from Reference 45.

Many hydrophilic blocks have been developed to serve as stable and inert micelle coronas, such as poly(ethylene glycol) (PEG), poly(*N*-vinyl pyrrolidone) (PVP), hyaluronic acid, and many others.[46,47,48] Among them, PEG is the most commonly used hydrophilic block, offering additional "stealth-like" properties and sites for further functionalization. The selection of the hydrophobic block is more specific to the demands of the chosen application, for example the structure, charge, solubility, and stability of the desired hydrophobic drug or drug cocktail. Therefore further discussion of polymeric micelles in this introduction will be addressed to the hydrophobic domain design toward the specific application of chemotherapy, which is the focus of the remainder of this work.

1.2.6 Nano-based chemotherapy: a brief introduction

The World Health Organization (WHO) reported a total of 8.2 million deaths from cancer in 2012, approximately 13% of all deaths, a figure that is increasing so rapidly that cancer is effectively the number one cause of death in the United States.[49,50,51] Cancer therapy commonly utilizes a three-pronged treatment plan combining chemotherapy, radiation, and surgery. Chemotherapy is a potent treatment method and a fundamental component of cancer therapy; however, the efficient delivery of anti-cancer drugs remains a major barrier to successful recovery. As described earlier, the majority of drugs is hydrophobic and exhibits very limited aqueous solubility, requiring proper formulation to prevent aggregation and to increase bioavailability. Chemotherapeutics are inherently toxic, and therefore their formulations must also be stable and selective in order to prevent detrimental or lethal off-target side effects.

Micelle drug delivery systems made from amphiphilic block polymers, which intrinsically self-assemble into structures with hydrophobic cores and hydrophilic exteriors, have proven to be an attractive method of delivering such poorly soluble and toxic drugs.[45] The hydrophilic head of the amphiphile provides water solubility, while the hydrophobic tail forms a core in which the drug may reside. This allows the drug to be administered intravenously and protects the encapsulated drug from metabolism or recognition by the immune system, which reduces side effects and improves bioavailability. Encapsulating the chemotherapeutic drug inside the micelle nanocarrier modulates these and other pharmacokinetic and pharmacodynamics parameters of the drug and thereby improves the therapeutic index.[52]

In addition to traditional hydrocarbon polymeric micelles, triphilic polymers have been developed that utilize the fluorous phase to initiate further phase separation within the micelle assembly.[53,54] Triphilic micelles can form exclusion zones or compartments with differing solubility and properties for the delivery of hydrophobic or reactive drugs and therapies. In such

systems hydrophobic compounds reside in the interstices of the lipid shell or at the hydrophobic-hydrophilic interfaces. The fluorous segment typically does not directly participate in the encapsulation of the hydrophobic drugs due to the lipophobic properties of the fluorocarbons but rather manipulates the packing of the hydrophobic and hydrophilic chains.[55] For example, the fluorous core may restrict or enable hydrophobic chain stretching, thereby altering the hydrophobic reservoir in which the drug can occupy.[56] As with all micelle drug delivery vehicles, their efficacy depends on several key physicochemical properties, including size, drug-loading capacity, release kinetics, and stability, which may be manipulated by adjusting the mass ratio or chemical nature of polymer blocks (e.g., side chain modification, and reversible crosslinking). These parameters will be discussed in depth in the following sub-chapters. (The fluorous nature of triphilic micelles affords additional advantageous properties, which will be discussed in sub-chapter 1.2.11.)

1.2.7 Passive-targeting via the EPR effect

Although many chemotherapeutics have been successfully formulated for improved solubility, selectivity for cancerous tissue leaves much to be desired. One approach is to tune the nanoparticle characteristics to exploit the tumor microenvironment and to distinguish tumor tissue features in order to increase bioavailability and treatment efficacy. Several hallmarks of cancerous tissue have been identified and can be leveraged to provide enhanced selectivity.[57] Specifically, the sustained angiogenesis of cancerous tissue has been exploited in the many drug-delivery designs.

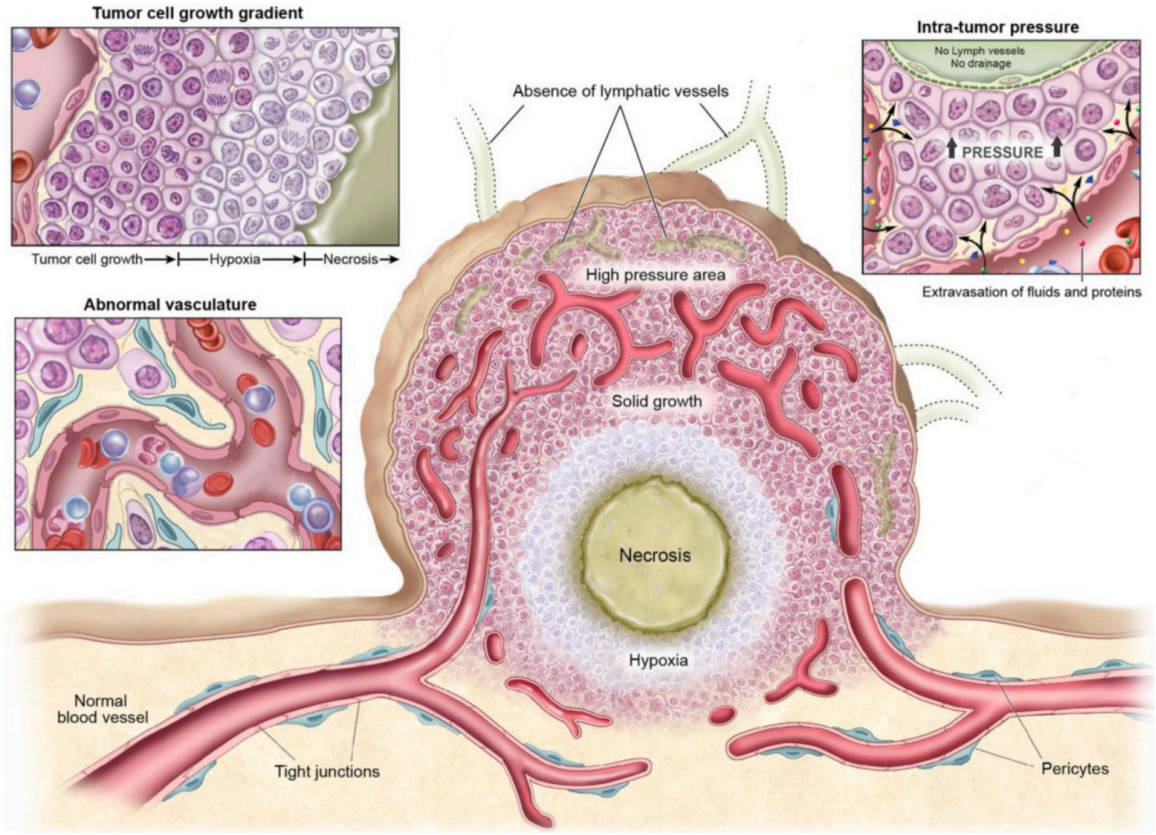

Figure 1.6 Distinct abnormalities of tumor vasculature toward enhanced chemotherapy.
Distinction between tumor tissue and healthy tissue, especially increased vascular permeability, can be manipulated for enhanced drug delivery of chemotherapeutics. Adapted from Reference 58.

Firstly, one may take advantage of the tumor vasculature abnormalities and impaired lymphatic drainage. Cancerous tissue, in an effort to gain facile access to nutrients and other resources for rapid growth, sacrifices the integrity of its tumor vascular linings, which form with poorly aligned and defective endothelial cells and absent smooth muscle cells (**Figure 1.6**).[59] The intra- and peritumoral vasculature then becomes abnormally dilated and "leaky" with wide gaps. Additionally, increased production of vascular permeability enhancing factors facilitate extravasation of small particles.[60,61] In essence these phenomena allow for passive targeting of solid tumors, termed the enhanced permeation and retention (EPR) effect (**Figure 1.7**).[58]

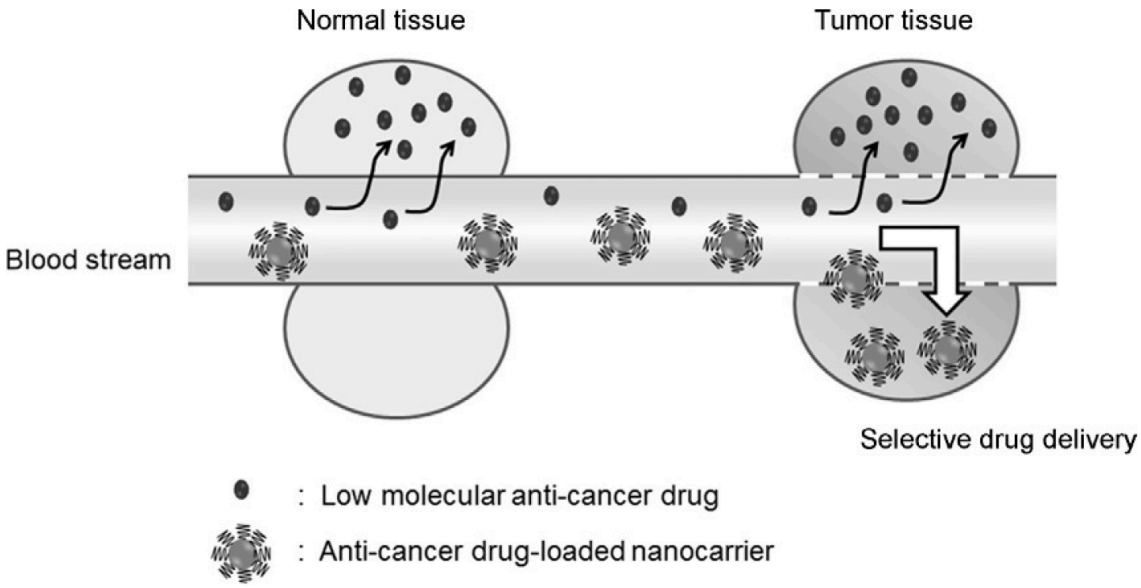

Figure 1.7 Preferential accumulation of to tumor tissue via the EPR effect.
Small nanoparticles can deliver anticancer agents preferentially to tumor tissue over healthy tissue via passive-targeting (EPR effect). Adapted from Reference 62.

Although these tumor abnormalities have been studied extensively over the past several decades, some controversy exists as to the effectiveness of the EPR effect.[63] This may, in part, be due to the tumor microenvironment, which can temper the nanoparticle's ability to accumulate around and/or within the cancer site. Cancer is one of the most complex diseases, involving extensive phenotypic and genetic variation across both the host (e.g. sex, age, hormonal status) and the tumor tissue (origin, type, developmental stage, and inter- and intratumoral heterogeneity).[57] Heterogeneity of the tumor and tumor stroma can manifest as a hypoxic gradient, increased interstitial fluid pressure, or altered extracellular matrix, and can severely impact the delivery efficacy.[50,64] It is therefore increasingly important to address such tumor heterogeneity in the drug-delivery design to maximize therapeutic efficacy and in some cases to deter drug resistance.

Besides the tumor microenvironment, the nanoparticle's structure, particularly its size, governors the extent to which it can take advantage of the EPR effect.[65,] The low-micron range is

considered the upper limit in order to prevent detrimental, and sometimes lethal, occlusion of blood capillaries. A lower size limit is typically given as 5 nm in order to escape rapid renal clearance from the blood.[59] Between these extremes, an optimum size may vary depending on the application, but generally smaller nanoparticles can preferentially extravasate from the tumor vasculature and accumulate near the tumor tissue. The cutoff sizes of the vasculature fenestrations range between 380 and 780 nm.[66] Again, it is important to keep in mind that inter- and intratumoral heterogeneity may skew the average vascular gap size (mainly towards smaller gaps) resulting in increased efficacy for smaller nanocarriers, which can penetrate deeper into the tumor.[67] Additionally, the size of the empty nanoparticle can even prompt a therapeutic effect unto itself, such as was observed in the apoptosis of breast cancer cells by exposure to 40 – 50 nm nanoparticles.[68]

Although the effect of size on nanoparticle drug delivery has been the focus of the majority of studies, the nanoparticle shape has also been investigated. Recent studies suggest that non-spherical particles can experience drag in the vasculature, thereby localizing the nanoparticles to the capillary walls to increase the potential for extravasation and accumulation at the tumor site.[69] From the evaluation of just these two parameters of shape and size, it is clear that nanoparticle design is complex and each facet may have subtle or significant impacts on therapeutic efficacy; therefore the design must be carefully scrutinized and tailored for the specific application. (The complexity and importance of various design feature supports the development of nanoparticles that can be tracked to directly image the effects of these design subtleties *in vivo*, which is the subject of sub-chapter 1.4)

1.2.8 Cellular uptake of nanoparticles

The key nanocarrier parameters of size and shape have also been evaluated in their effect on cellular uptake. Once accumulated near the tumor tissue the nanoparticle or drug must then be

internalized by the tumor cells for successful drug action. Even though understanding of the cell uptake of nanoparticles is still limited, it is generally accepted that they are transported into the cell via endocytosis—a process wherein particles are enveloped by the cell membrane.[70,71] The process is typically categorized as phagocytic or non-phagocytic. Phagocytosis is associated with the uptake of larger particles that have been opsonized and is specific to some cells, including those of the immune system, which seek to eliminate pathogens and cell debris from the plasma (this topic will be discussed in depth concerning its influence in nanoparticle blood circulation time in a later sub-chapter 1.2.10).[72]

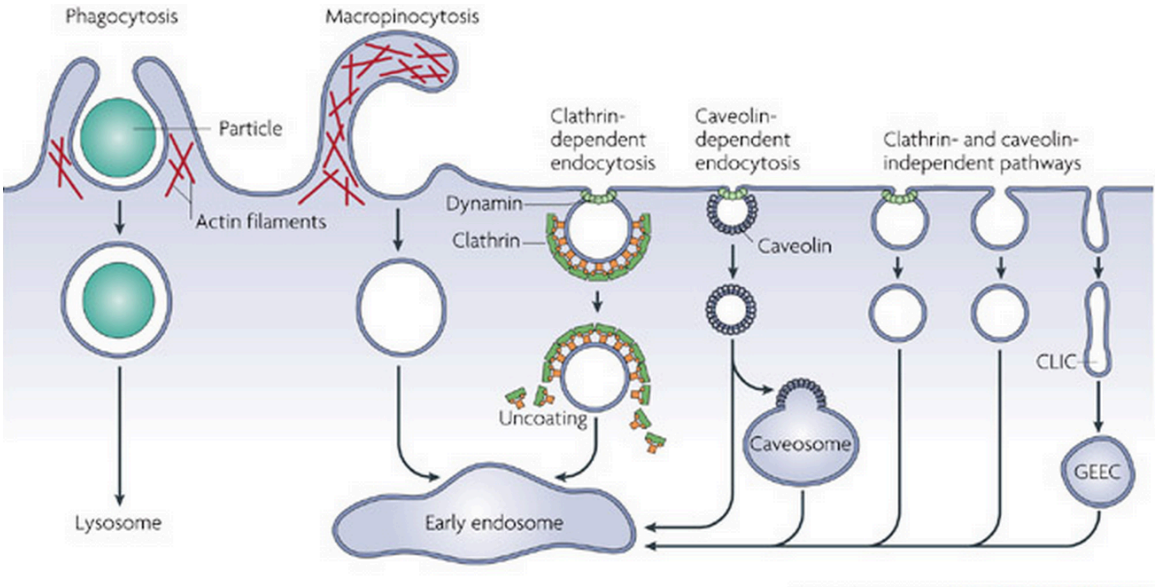

Figure 1.8 Endocytosis: entry pathways of nanoparticles in a typical cell.
Various endocytotic mechanisms for nanoparticle uptake into a general eukaryotic cell. Cell uptake depends on the particle physical properties and can influence the effectiveness of the drug delivery system. GEEC signifies GPI-Enriched Endocytic Compartments, which have not been discussed but have also been identified as major players in cell uptake in some cases. Adapted from References 73 and 74.

As for non-phagocytic endocytosis, there are several mechanisms that may take place and are mainly dictated by size and surface properties such as charge, hydrophobicity, or receptor interaction (**Figure 1.8**). clathrin-mediated endocytosis (typically in the 100 nm range), caveolae-mediated endocytosis (≤ 100 nm-sized particles), macropinocytosis (common when a large

volume of solvent is present, cell membrane extends to accommodate a maximum range of 100 nm – 5 μm).[71,73] Again, in addition to size, the shape of the nanoparticle may also affect the degree of cell uptake. Non-spherical particles have been shown in some cases to exhibit decreased internalization in comparison to spherical particles. Non-spherical particles may also invoke non-endocytotic mechanisms of entry—such as needle-like particles that may even penetrate the cell membrane—thereby complicating the delineation of the role of shape in cell uptake.[75]

It is also possible that in some instances the internalization of the nanoparticle into the cell may not be necessary. As long as the nanoparticle can accumulate for a prolonged period in the vicinity of the tumor (assisted by poor lymphatic drainage) and the drug can diffuse out without significant degradation. The free drug may then be internalized or independently diffuse through the cell membrane over time.[72,76] Whichever mechanism is used, the cell uptake of the drug, whether or not it is concomitant with the nanoparticle uptake, is a complicated process but it is clearly dependent on the concentrated and prolonged accumulation of the nanocarrier at the tumor site.

1.2.9 Active-targeting

Even with improved selectivity over healthy tissue via passive-targeting, only a very small fraction of the injected nanoparticles reach their target cells. Passive-targeting can be achieved by extravasation through intratumoral fenestrations; however, off-target accumulation is also typical in other organs with large vasculature fenestrations, specifically the liver and spleen.[50] Partly for these reasons, nanoparticle chemotherapeutics still remain poorly represented in the clinical pipeline. In 2012, roughly 1,400 nanomedicine formulations were registered for clinical trials for cancer therapy, while in the same year roughly 58,000 publications were available concerning

cancer nanoparticles.[50] Hence, there remains a stark disconnect between clinical candidates and emerging nanodelivery technologies.[77]

One effort to bridge this gap and to increase selectivity is to functionalize the nanoparticles with ligands that will bias cellular uptake (**Figure 1.9**). Termed active-targeting, this approach has quickly become an essential feature in nanovehicle engineering. Commonly, a high-affinity ligand is attached to the surface of the nanocarrier that binds selectively to a receptor on the target cell. A wide variety of ligands have been used for such purposes, including small molecules such as folic acid and carbohydrates, or macromolecules such as peptides, proteins, and antibodies.[78,79,80] In these systems delivery efficacy relies on the availability of an upregulated target receptor and the corresponding ligand, the latter of which is highly dependent upon the density and placement of the ligand on the nanoparticle surface.[81,74]

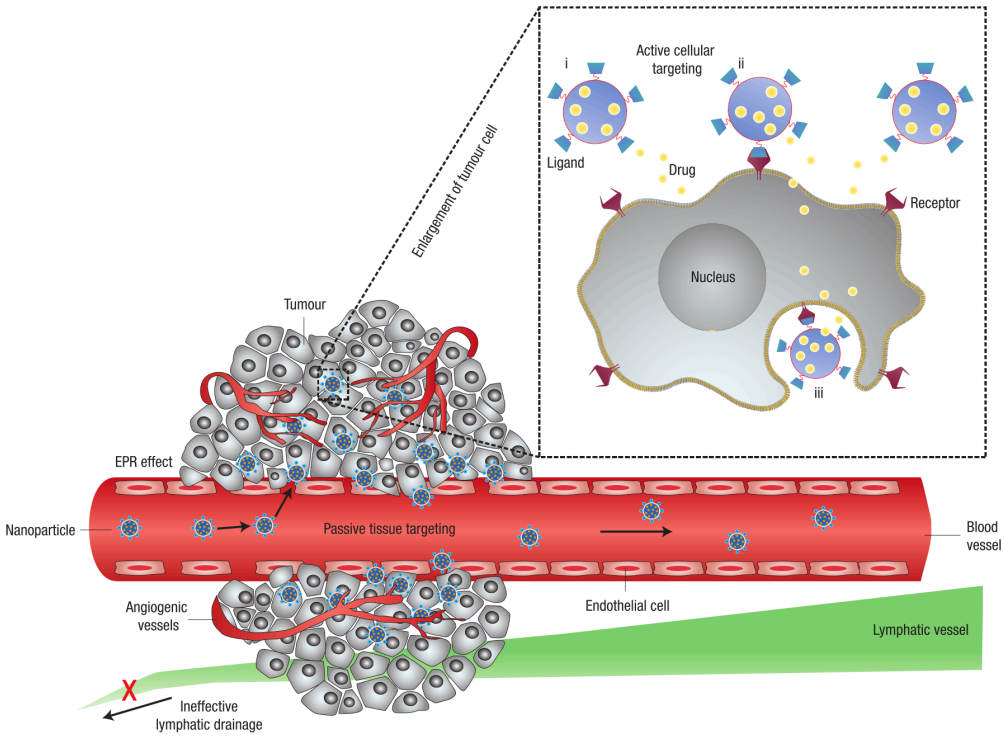

Figure 1.9 Depiction of passive- and active-targeting in chemotherapy.
Receptor-mediated active-targeting depends on prolonged circulation of nanoparticles and preferential accumulation at the tumor site (via passive-targeting). Adapted from Reference 81.

With the increasing development and success of active-targeting, it is important again to recall that active-targeting still strongly depends upon the efficacy of simultaneous passive-targeting, specifically on the nanocarrier's ability to avoid recognition by the reticuloendothelial system ((RES), which is the subject of the next sub-chapter) and subsequent premature burst release of the drug and/or clearance from blood circulation.

1.2.10 Reticuloendothelial system (RES) and its effect on nanoparticle drug delivery

Both passive- and active-targeting rely on the nanoparticle's ability to remain in circulation long enough to afford concentrated and prolonged accumulation at the tumor site. This is very difficult to achieve due to the numerous mechanisms that exist to remove foreign bodies. When delivered intravenously, the nanoparticle is immediately susceptible to adsorption by plasma proteins (opsonins such as IgG, complement factors, and fibrinogen), which then makes the nanoparticles easily recognized by the macrophages of the immune system. The main drawback to polymeric nanoparticle designs is that their structure and shape can be readily recognized, dissociated, and removed by the RES, particularly the Kupffer cells (**Figure 1.10**).[82] Premature dissociation of the delivery vehicle is extremely detrimental to the patient; not only is the bioavailability greatly diminished, but also the encapsulated drug is released as a concentrated, bolus dose to healthy cells at the site of premature release. In the case of toxic chemotherapeutic drugs, off-target bolus release can result in severe patient side effects.[81,82,83]

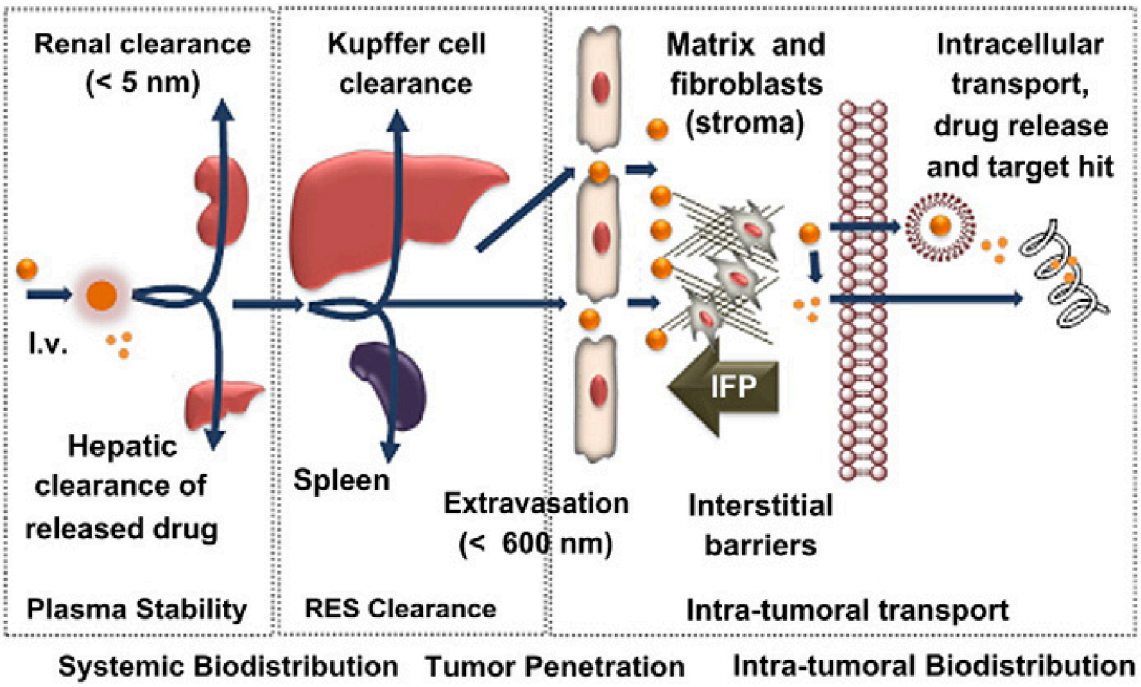

Figure 1.10. Obstacles in nanoparticle chemotherapeutic drug-delivery.
Nanoparticles injected intravenously must evade the RES and renal clearance to remain stable in plasma during systemic circulation. Evasion of the RES, resulting in prolonged blood circulation, enhances bioavailability and selectivity of the nanocarrier. Adapted from Reference 82.

Particle size and hydrophobicity are the two major determinants of the extent and method of recognition and ultimately excretion of polymeric nanoparticles. The route of elimination is mainly determined by size: particles greater than 200 nm are typically internalized by the spleen and smaller particles by the liver and bone marrow. Larger particles, 7 μm or larger, can obstruct the capillaries causing embolism and so are typically avoided for intravenous delivery applications. The phagocytic cells remove the nanoparticles by a process called opsonization where the plasma proteins are adsorbed onto the nanoparticle or individual polymer chains via hydrophobic interactions. Therefore as the hydrophobicity of the polymer increases, the potential for opsonization also increases. A sterically bulky hydrophilic block, most commonly polyethylene glycol (PEG), can be used to shield the particle against hydrophobic recognition by serum components. PEG chain length and packing density have been found to be the most

influential factors, where higher density PEGs are more effective.[84] Although PEGylated particle surfaces have been shown in some cases to induce an immune response upon repeated injection (accelerated blood clearance or ABC phenomenon)[85], surface modification with high PEG densities remains the most common method to minimize phagocytosis, as it is fairly simple and amenable to many nanoparticle platforms. However, for self-assembling systems like micelles, surface modification may not be sufficient to enhance stability in serum. The micelles are dynamic with the polymers continuously dissociating, leaving them vulnerable to sequestration by serum proteins, leading ultimately to nanoparticle instability.

1.2.11 Prolonged circulation of nanoparticles with the fluorous phase

Micelle self-assemblies are a promising chemotherapeutic drug-delivery platform that could significantly benefit from the unique properties of the fluorous phase. As described earlier, triphilic polymer micelles show interesting self-assembly behavior, organizing into unique micro-domains. However, the fluorous nature of triphilic micelles can also enhance the stability of the assemblies to prolong blood circulation and minimize phagocytosis. The lipophobic character of the fluorous phase, when installed properly into an amphiphilic polymer structure, can allow for both enhanced thermodynamic stability of the micelle self-assembly and enhanced kinetic stability of the micelle in terms of prolonged blood circulation.

A more thermodynamically stable micelle will be more robust and less prone to dissociation via dilution, opsonization, increased pressure, etc. upon or after injection. The thermodynamic stability of a polymeric micelle is described by its critical micelle concentration (CMC) (**Figure 1.11**). The CMC is the concentration at which the formation of micelles becomes favored over the individual compounds; therefore, the CMC is typically the minimum concentration used in drug formulation. Polymeric micelle CMC values are typically three orders of magnitude lower (more stable) than low-molecular-weight surfactants. Fluorous compounds are also highly surface active

and depress the CMC of self-assemblies several orders of magnitude lower than their hydrocarbon-analogs. The combination of polymeric and fluorous features stabilizes semi-fluorinated polymeric nanocarriers and reduces the required formulated dose of the surfactant.[17]

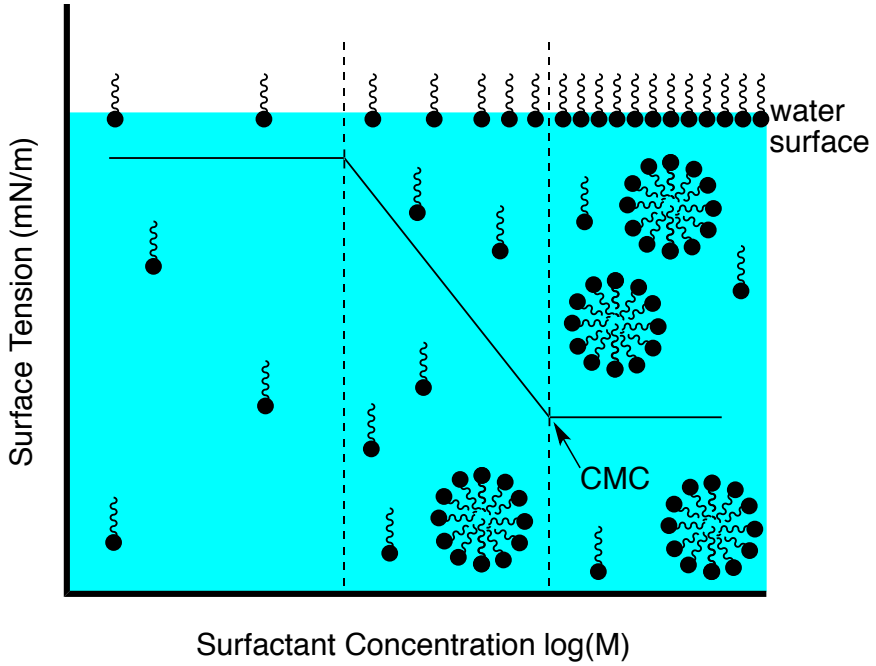

Figure 1.11 Depiction of the CMC as determined by surface tensiometry.
The CMC is an indicator of the thermodynamic stability of the micelle. Fluorous micelles exhibit significantly lower CMCs than their hydrocarbon analogs. Image created by William Tucker.

Stability gained via the installment of the fluorous phase in colloidal self-assemblies is also advantageous in reducing side effects and regulating the release of the encapsulated materials. A main concern raised in release studies of physically entrapped drugs is the sudden release, or burst, of drugs whenever or wherever the micelle begins to dissociate. A slower, sustained release of the drug from the self-assembly can result in a prolonged effect period, reduction in required dose, and even depression of toxic side effects.[86,40] The decreased aqueous solubility of the fluorinated chains decreases the exchange rate of the unimers comprising the assembly or between aggregate types of fluorous assemblies in comparison to their hydrocarbon-counterparts.

Fluorous micelles can thus modulate the rate of diffusion of the lipophilic drug out of the assembly.[43]

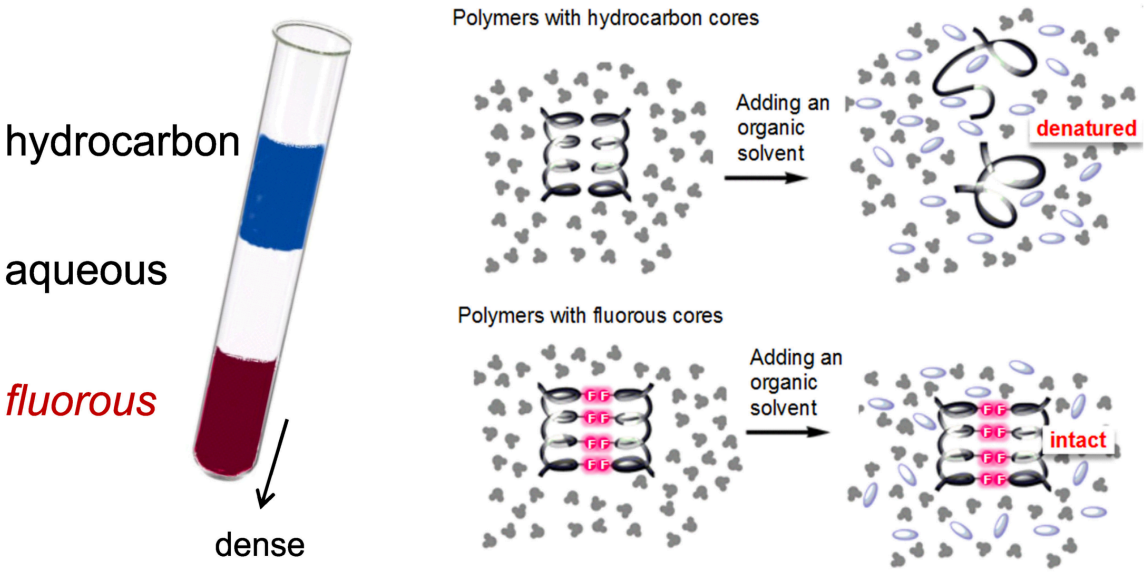

Figure 1.12 Depiction of the fluorophobic effect and its potential to stabilize nanocarriers. Perfluorinated compounds repel both hydrophobic and hydrophilic molecules and are thus immiscible with both organic and aqueous phases. Fluorous cores stabilize protein assemblies against denaturation from organic solvent (gray structures—water solvent; blue ovals—organic solvent). This enhanced stability can be extended to fluorous micelles, which would deter dissociating interactions with hydrophobic blood components to provide prolonged blood circulation. Adapted from Reference 87.

In addition to the enhanced thermodynamic stability, the fluorous nature of triphilic micelles should deter opsonization to further enhance the kinetic stability of the drug delivery vehicles *in vivo* in terms of a prolonged blood circulation time. As described earlier, the majority of designs rely on modification of the nanoparticle's surface in order to avoid dissociation and elimination by the RES. The effects of PEGylation for example have been rigorously applied and investigated and so their effects are well understood. However, less is known concerning the fluorous phase and therefore manipulations of the structure of a triphilic polymer are not readily predictable. In theory the lipophobicity or repulsion of traditional hydrophobic molecules by the fluorous phase should also extend to the hydrophobic domain of opsonins (**Figure 1.12**). The potential to inhibit serum proteins is supported by similar phenomena (fluorous repulsion of lipophilic domains),

such as the inhibition of adhesion of MIN6 cells to PFC emulsions[88] and of the reduced hydrolysis by pancreatic phospholipase A_2 of fluorinated liposomal membranes[9]. The triphilic micelles should therefore provide prolonged circulation times by deterring interactions with hydrophobic blood components, as fusion with biological membranes and blood proteins has been shown to be the main method of degradation of assemblies during parenteral delivery.[89]

1.3 Tracking drug formulations *in vivo*

The fluorous phase can be applied to enhance the properties of hydrophobic drug-delivery formulations, specifically for emulsions and micelles. The development of fluorous compounds for *in vivo* application is still in a fairly early stage, and property-to-structure relationships remain poorly understood. Even less is known concerning the behavior of fluorous formulations upon and after injection or the effects of prolonged exposure in the body or in the environment. This makes the rational design of fluorous compounds and their aggregates extremely difficult. In an attempt to rectify this knowledge gap, imaging moieties have been developed for a variety of modalities to allow for particle tracking. The following sub-chapter will describe current concerns for fluorous compounds in medical applications and the direct use of fluorous polymers as imaging handles for particle tracking.

1.3.1 Concerns for in vivo applications of nanoparticles

The most immediate concern in the development of new compounds for biological applications is acute toxicity. Surface-active molecules, which are used in a variety of drug formulations, can exhibit pronounced biological and ecological acute toxicity *in vivo*. Many surfactants can interfere and disrupt biological membranes leading to hemolytic activity.[3] Fortunately, due to their lipophobicity, the majority of fluorinated amphiphiles show little to no acute cytotoxicity or hemolytic activity. For example, perfluorinated-alkylated phosphatidylcholines and perfluorinated-alkylated telomeres have typical acute lethal doses of

several g/kg of body weight in mice. In the treatment of mouse fibroblasts and human lung epithelial cells with perfluoro-alkylated dimorpholinophosphates, it was found that the acute cytotoxicity actually decreased with increasing fluorocarbon-chain length.[90]

Despite the general lack of short-term effects from exposure to fluorous compounds, a discrete subset of fluorinated compounds must be avoided for *in vivo* applications. Long-chain perfluorinated acids (> 7 CF_2 units, particularly perfluorooctanoic acid (PFOA) and perfluorooctane sulfonate (PFOS)) have garnered much attention in the last decade for their acute toxicity and prolonged bioaccumulation and are now highly regulated.[91,92,93] Although toxic perfluorinated acids represent a small subset of fluorinated compounds, their effects are severe. Therefore, fluorous compounds must be designed to avoid decomposition to fluorotelomeres that could lead to the formation of toxic compounds such as PFOA or PFOS.[94]

Fortunately semifluorinated amphiphiles, including PEGylated fluoropolymers, experience little to no enzymatic or metabolic degradation, provided the perfluorinated moiety is installed in the polymer structure in a way that is stable under physiological conditions. Therefore ester or amide linkages should be explicitly avoided to prevent release of a fluorous alcohol that could potentially be oxidized to a toxic fluorous acid. Alternatively, fluoroether linkages are typically stable, allowing the fluorous amphiphiles to remain intact. Furthermore, it has been shown that diblocks consisting of fluorous and hydrocarbon segments tend to show similar properties to perfluorinated compounds, exhibiting low toxicity and a simpler pharmacology than their purely hydrocarbon analogs.

The major concern for semifluorinated polymers and their aggregates is the long-term effects of bioaccumulation.[95] Because fluorous chains are not typically metabolized *in vivo*, their prolonged stability lends fluorous compounds to bioaccumulate. The rate of excretion of small fluorous molecules, which is typically achieved by exhalation, depends on the length of the

fluorocarbon chain. The rate can be increased by reducing the fluorophilicity, for example, in the introduction of bromine as seen in PFOB.[96] These smaller perfluorocarbons are generally cleared by the RES after intravenous injection and evaporate through the lungs without metabolism or decomposition of the chemical structure. For larger fluorinated compounds, conjugation to soluble hydrophilic blocks, such as PEG allows for reduced bioaccumulation. PEGylated fluorous polymers are not degraded, and therefore the fluorous moiety remains attached to the highly soluble PEG. The PEGylated fluoropolymers are then eventually recognized by the RES and excreted.[97]

The semifluorinated polymers, despite their inertness, must be designed to limit the bioaccumulation of their aggregates. As with all nanoparticle, their size lends the potential for biological adverse effects since the size scale is similar to that of intracellular organelles and biomacromolecules involved in cell-signaling processes. Nanoparticles that are endocytosed and remain in lysosomes of cells for extended periods of time are typically detrimental to the cell due to the increased production of reactive oxygen species (ROS), which can lead to a variety of adverse effects (bonding with DNA, mitochondrial destabilization, or interference with cell membrane receptors)[98] (**Figure 1.13**). The toxicity of the nanoparticle will depend on its physicochemical properties: surface reactivity, particle size, surface charge, chemical composition, the presence of transition metals, and route of entry to the cell.

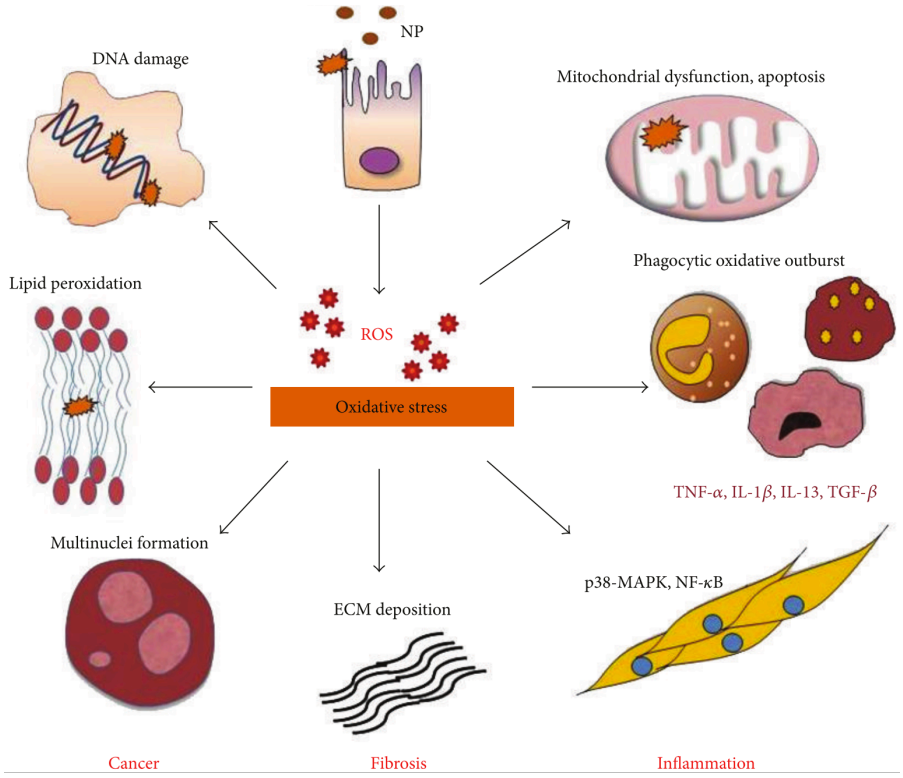

Figure 1.13 Prooxidant pathway for nanoparticle-induced toxicity.
Prolonged accumulation of solid nanoparticles can potentially generate reactive oxygen species (ROS), which lead to a variety of adverse outcomes. Adapted from Reference 98.

Micelles and emulsions, unlike solid nanoparticles or covalently linked polymeric nanoparticles, do not bioaccumulate due to the equilibrium with the unimers, which are excreted relatively quickly; therefore, their toxicity and bioaccumulation will be dictated mainly by the properties of the individual fluorous polymers. The safety of PEGylated fluoropolymers has been observed in preliminary studies in Zebrafish models, which show no adverse affects after continuous exposure to high concentrations of micelle-forming compound (preliminary MALDI-MS experiments concerning fluorous micelle exposure to Zebrafish can be reviewed in Appendix 2).

Although the majority of fluorous compounds appear safe, further studies are desirable to prognosticate the pharmacokinetics and bioaccumulation of fluorous compounds *in vivo*,

especially as fluorous compounds become more complex and integrated within high-order systems. Such studies investigating the biodistribution and excretion of fluorous compounds could be facilitated by the development of nanoparticles with the capability for *in vivo* imaging.

1.3.2 In vivo nanoparticle imaging via MRI

The past several sub-chapters have, in part, illuminated a serious demand that exists in the field of drug delivery for nanoparticle imaging. Upon and after injection of a drug delivery vehicle, the body acts as a black box, where a myriad of complex interactions involving the nanocarrier and drug take place. This behavior *in vivo* ultimately dictates the delivery efficacy; however, drug formulation design can only draw upon what is known, which is mainly the inherent physical properties of the formulation or the isolated biological behavior modeled by *in vitro* studies. Nanoparticle imaging capability could provide a way to monitor the fate of colloids *in vivo*, including behavior upon injection, mode of action, absorption, metabolism, accumulation, and excretion. Imaging could also be used to control drug release upon visualized accumulation at a target *in vivo* or identify disease markers for diagnosis.

Many standard imaging modalities exist that are suited for nanoparticle tracking, each with their own advantages and disadvantages (**Table 1.3**).[99] The modality must be carefully chosen to select the properties that best suit the desired application. Several imaging modalities, such as X-ray and PET, often rely on the use of high-energy radiation or radionuclides, which can both be detrimental to the patient. Other techniques may be limited in resolution, preventing clear imaging of certain tissues or biological events, or limited in depth, only allowing for localized or surface imaging.[100]

Technology	Means of detection	Relative advantages	Relative disadvantages
CT	Ionizing radiation (X-rays)	• High spatial resolution • High penetration depth • Clinical translation	• Limited sensitivity • Radiation
PET	Ionizing radiation (γ-rays)	• High sensitivity • High penetration depth • Clinical translation	• Limited spatial resolution • Radiation • High costs
SPECT	Ionizing radiation (γ-rays)	• High sensitivity (but lower than PET) • High penetration depth • Clinical translation	• Limited spatial resolution • Radiation
MRI	Electromagnetism	• High spatial resolution • Clinical translation	• Low throughput • High costs
US	Acoustic waves	• High spatial resolution • Low costs • Safety profile • Clinical translation	• Limited sensitivity • Operator dependency
Whole-body OI	Bioluminescent or fluorescent light	• High sensitivity • Low costs • High throughput	• Limited spatial resolution • Limited penetration depth
Two-photon OI	Fluorescent light	• High sensitivity • Novel spatiotemporal resolution	• Need to exteriorize target organ • Cannot image whole animal • Limited penetration depth

Abbreviations: CT, computed tomography; MRI, magnetic resonance imaging; OI, optical imaging; PET, positron-emission tomography; SPECT, single-photon emission computed tomography; US, ultrasound.

Table 1.3 Relative advantages and disadvantages of selected medical imaging modalities.
The imaging modality must be carefully selected with the application and desired characteristics prioritized. For nanoparticle tracking high spatial resolution and penetration depth are key parameters. Adapted from Reference 100.

MRI is an attractive technique for high resolution, full body imaging. MRI is also non-invasive and non-destructive and provides superior anatomical imaging, especially for soft tissue. The quality of anatomical imaging is crucial, as it serves as the foundation for nanoparticle tracking, providing information concerning the location of various anatomies. These images can then be superimposed or overlaid with molecular images, which give information concerning a specific site or pathology via implementation of specially designed contrast agents or imaging tracers.

Several parameters can be manipulated in order to enhance the contrast for a particular tissue or biomarker. Relaxivity mechanisms return net magnetization of the system to equilibrium, which diminishes MRI signal intensity. Longitudinal relaxation, T_1, determines the amount of time required for signal recovery between excitation pulses and therefore roughly approximates the scan time necessary for adequate signal intensity. For imaging purposes it is always best to

minimize T_1 to attain the greatest information while minimizing the amount of time the patient is in the scanner. The transverse relaxivity, T_2, relates to the signal decay over time. The longer it takes for the signal to decay, the more information, and signal, one can achieve in a given time frame. Lastly, T_2^* is considered an effective T_2 as it additionally incorporates signal loss due to instrument or environmental inhomogeneity.[101] Relaxivity mechanisms are extremely problematic in macromolecular systems, in which rotation and diffusion can be restricted, creating non-homogenous magnetic environments. However, in many cases specialized pulse sequences can be programed to minimize these effects or alternatively monopolize upon differences in relaxivity between different anatomies to enhance contrast.

Pulse sequences and contrast agents have been thoroughly exploited for the ^{1}H nucleus. Proton-MRI is best suited for anatomical imaging due to the abundance of water in the body but can also function as a molecular imaging nucleus when paramagnetic contrast sensitizers such as chelated-Gd^{III} or superparamagnetic iron oxide (SPIO) are applied. These metal-based contrast agents provide indirect imaging of affected nearby water molecules.[102] Therefore a "before" and "after" image is typically required in order to provide unambiguous localization, which unfortunately may be difficult due to patient movement during or between scanning.[103] Additionally, there has been some concern involving the potential toxicity of these compounds. Certain SPIO formulations have demonstrated altered gene expression, oxidative stress, and other biological side effects, and Gd^{III} has been shown to be particularly toxic in patients with renal deficiency.[104,105] Although the abundance of water in the body allows for superior ^{1}H signal intensity, water's ubiquity favors the implementation of heteronuclear MRI to allow for "hot-spot" molecular imaging for direct, quantifiable, and unambiguous localization and imaging.[101]

1.3.3 ^{19}F-MRI tracer agents

As suggested earlier, fluorous compounds are particularly amenable to serve as non-invasive imaging tracers. The ^{19}F nuclei can be used to provide high-resolution MR imaging of distinct tissue epitopes or biochemical processes. The ^{19}F isotope is 100% naturally abundant, and the ^{19}F resonant frequency, nuclear magnetic resonance sensitivity, and signal-to-noise ratio are high; 94%, 83%, and 89%, respectively, in comparison to ^{1}H. Endogenous fluorine in the body is typically found at concentrations far below the detection limit of MRI instruments. These collective properties of ^{19}F allow for minimal background signal and enhanced signal sensitivity in NMR applications. In addition, ^{19}F measurements can often be performed with the same MRI scanner as those used for conventional ^{1}H-MRI by simply retuning the radiofrequency coils. This eliminates the need for specialized equipment in a clinical setting and allows the ^{19}F-MR image to be superimposed onto the anatomical ^{1}H image without any ambiguity, a clear advantage over conventional optical and nuclear imaging techniques (**Figure 1.14**). Additionally, the chemical shift range of fluorine is extremely large, approximately 300 ppm, and sensitive to the chemical environment, which provides the opportunity to image multiple fluorous moieties or markers in varying biological environments simultaneously.[106,107]

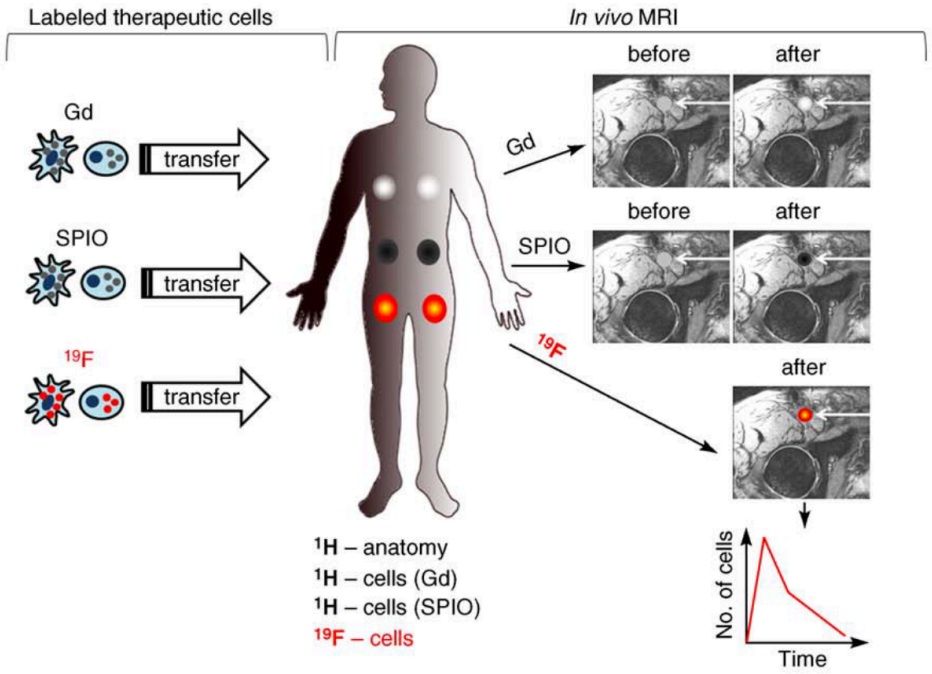

Figure 1.14 Particle tracking using MRI with contrast agents and ^{19}F tracer labels.
Gd^{III} and SPIO labeled particles typically require 'before' and 'after' images for localization (white arrows), resulting in a final hyperintense (bright) or hypointense (dark) spot signal, respectively. With a ^{19}F tracer label, imaging is longitudinal and overlaid with ^{1}H (anatomy) to give a "hot" image. Also the total ^{19}F signal can be quantitative. Adapted from Reference 101.

To achieve adequate signal intensity for an image quality similar to ^{1}H, a high fluorine density is required. It is preferred that this density arises from one MRI signal and is not divided among several peaks. Split peaks may cause artifacts, and slice displacement may occur if the bandwidth per ^{19}F image pixel is less than the chemical shift dispersion. It is also therefore important that the ^{19}F moiety experience adequate mobility to maintain an equivalent NMR environment around the fluorine atoms. Chemically selective imaging pulse sequences can be used to remove these artifacts but cannot compensate for the loss in signal, the short T_2 value, or the splitting that may occur from J-modulation.[101,96] ^{19}F-MRI pulse sequences using ultrafast imaging methods, such as keyhole techniques or echo planar imaging, can also be used to compensate for the long T_1 times of many fluorous compounds to achieve clinically relevant scan

times.[108] Keeping these parameters in mind, fluorous colloids can be designed that are capable of providing high intensity in ^{19}F-MRI.

1.3.4 Fluorous colloids as theranostic agents

Advancements in nanotechnology are currently being applied to the development of nanocarriers that combine both diagnostic and therapeutic capabilities, henceforth termed theranostic nanoparticles (**Figure 1.15**).[109,110,111,46] Traditionally, medical diagnosis and treatment are performed separately, which takes longer and may even prevent timely adjustments to treatment methods. These delays between diagnosis and treatment can be extremely detrimental in aggressive diseases like cancer. Fluorous compounds are uniquely primed to provide the benefits of both enhanced drug delivery and molecular imaging. In the previous sub-chapters the enhanced stability of fluorous emulsion and micelle formulations and the benefits of ^{19}F-MR imaging have been thoroughly described. In the remainder of the introduction, the initial work towards fluorous theranostic nanoparticles will be briefly overviewed with identification of specific areas for improvement.

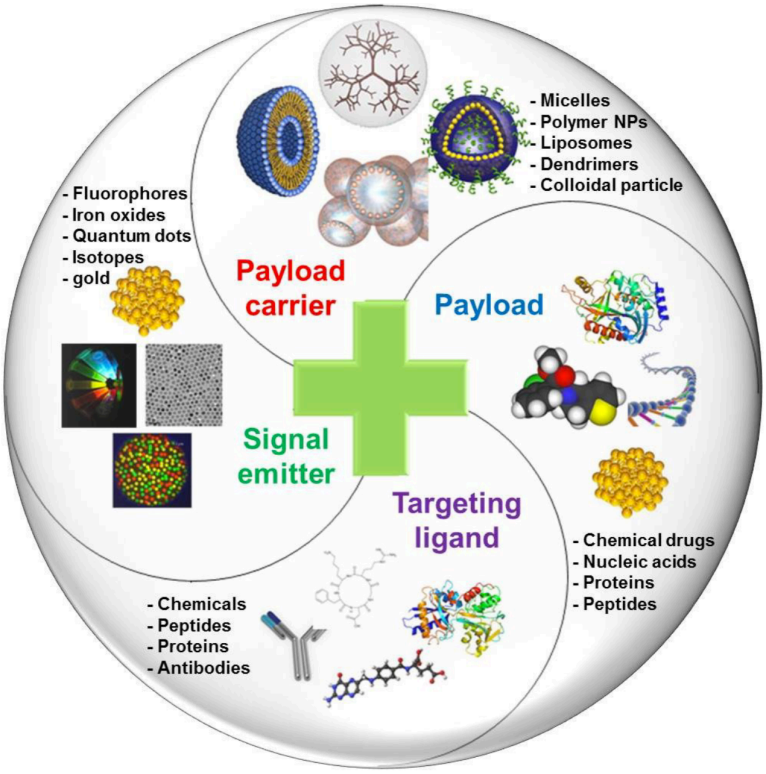

Figure 1.15 Theranostic particles: dual therapeutic and diagnostic applications.
Multifunctional, multifaceted nanoparticles with the dual and simultaneous capability for drug delivery and imaging are the new standard for modern nanocarrier design. Depicted are the four basic design components. Adapted from Reference 109.

Dual therapeutic and diagnostic particles, commonly termed theranostic particles, are a growing area of interest and have only just extended to fluorous systems. In recent ^{19}F-MR theranostic designs the ^{19}F-MR tracer was installed into the PEG corona, as it was thought that the high microviscosity and inhibited mobility of the chains comprising the core of the assembly would prevent detrimental peak broadening. Nyström *et al.* polymerized trifluoroethyl methacrylate with oligo(ethylene glycol) methyl ether methacrylate (OEGMA) to form amphiphilic theranostic nanoparticles, which demonstrated short and consistent T_1 values despite a random distribution of the trifluoroethyl ^{19}F-MR handle throughout the hydrophilic corona. However, T_2 values were significantly shortened, which they attributed to restricted movement of the perfluorinated moiety.[112] Other similar designs installed the fluorous domain on or near the

nanoparticle surface. While this has maximized fluorous imaging capabilities, it has not fully exploited the hydrophobic and lipophobic nature of the fluorous phase. In fact the location of the fluorous segments in the hydrophilic corona places them at odds with their hydrophobic character. A limited number of studies exist that evaluate ^{19}F-MRI characteristics of semi-fluorinated block copolymers with the fluorous block located within the self-assembly core. In many of these cases the random polymerization and/or interactions with hydrophobic blocks lead to non-homogeneous and shortened T_2 values, which reduce signal intensity.[113,114,115] A nanoparticle design that can simultaneously harness the stabilizing and imaging capabilities of the fluorous domain is highly desired. The following work will demonstrate the progress made thus far in this effort in two drug formulations: fluorous anesthetic emulsions and triphilic micelles for chemotherapy.

1.4 Dissertation scope

1.4.1 Rationale

The integration of fluorous compounds in hydrophobic drug delivery has the ability to enhance the stability of the drug formulations, while simultaneously providing particle tracking via ^{19}F-MR imaging. In emulsion formulations the decreased solubility of fluorous surfactants can stabilize the nanodroplets to extend shelf life and adhere to FDA droplet size regulations. Additionally, perfluorinated surfactants can stabilize fluorous anesthetics into intravenous formulations for enhanced induction, recovery, and regulation of anesthesia. For micelle nanocarriers, the extreme hydrophobicity of perfluorinated molecules can dramatically lower the CMC to enhance stability and reduce required vehicle dose. The fluorous micelles are also lipophobic and therefore have the potential to repel opsonins to increase blood circulation time. When applied to chemotherapy, the enhanced stability of the fluorous micelles serves to enhance the selectivity and bioavailability of the encapsulated drug, while reducing toxic side effects.

Lastly, the fluorous segment of such emulsion and micelle formulations can serve a dual therapeutic and diagnostic (theranostic) purpose. The ^{19}F nucleus gives high-intensity molecular images via MRI, provided an adequate localized concentration of ^{19}F probe and limited artifacts or signal broadening. The *in vivo* imaging capabilities would enable the study of nanoparticle behavior upon and after injection, to provide insight for improved drug formulation efficacy. The successful development of a ^{19}F-MRI theranostic moiety would also demonstrate the unique properties that can be achieved with fluorous systems and could serve as a multifunctional design tool for future drug delivery systems.

1.4.2 Objectives

This thesis was aimed to enhance the understanding of the relationship between PFC structure and the effects on self-assembly and imaging behavior. The objective was then to develop from that knowledge a functional fluorous moiety that could stabilize hydrophobic drug formulations and maintain high intensity for ^{19}F-MRI, specifically in fluorous emulsions and polymeric micelle formulations.

1.4.3 Research briefs and highlighted achievements

Chapter 2: Development of a multifunctional ^{19}F imaging handle for self-assemblies

The structure and fluorophilicity of the fluorous moiety was modularly investigated, with keen interest on the effect on self-assembly behavior of the polymeric micelles and on ^{19}F-MRI intensity. The ^{19}F-MRI intensity is maximized, and the image artifacts are minimized typically in systems with high symmetry and mobility (usually difficult to achieve in the core of a self-assembling and dynamic system). For delivery applications, the perfluorinated segment needed to be fluorous enough to enhance the thermodynamic stability yet adequately mobile to maintain an intense ^{19}F-MRI signal. Therefore a spherical perfluoro-*tert*-butyl (PFtB) moiety was synthesized and coupled to an $mPEG_{1k}$ or $mPEG_{2k}$ polymer; 1, 2, and 3 PFtB groups were added (termed

$PFtB_{MONO}$, $PFtB_{DI}$, and $PFtB_{TRI}$) to incrementally increase fluorophilicity. In all cases the mPEG length showed little to no effect on the amphiphile or aggregate properties. Spherical micelles and fluorous emulsions were formulated with the PFtB-polymers and characterized for their relevant physicochemical properties.

$PFtB_{DI}$ was found to be unstable under basic conditions, due to a labile adjacent hydrogen and subsequent elimination of the PFtB moiety, and therefore was not formulated for drug delivery. For fluorous sevoflurane emulsions, only $PFtB_{MONO}$ was able to form stable droplets under 500 nm; however, emulsion breaking was evident only after approximately 25 days (no significant improvement over previous linear PFC formulations). In terms of micelle formulation, only $PFtB_{TRI}$ was able to form stable, discrete micelles that were approximately 12 nm in size by DLS. The micelles exhibited low CMCs (indicative of increased thermodynamic stability) and so were then evaluated for ^{19}F-MRI capabilities via measurement of the relaxivity parameters. The $mPEG_x$-$PFtB_{TRI}$ micelles in D_2O exhibited promising NMR properties: T_1 of 0.49 s and T_2 of 0.11 s. Varying concentrations of micelles were then imaged *in vitro* via $^{19}F^-$MRI and showed a 1 mM (in terms of polymer concentration) limit of detection for the parameters used (which are clinically realistic). This preliminary work optimized the synthesis of the PFtB moiety and identified the $PFtB_{TRI}$ as a promising theranostic handle.

Chapter 3: Development of triphilic micelles for enhanced chemotherapeutic delivery

In addition to thermodynamic stability, the fluorous moiety should be properly situated within the micelle assembly to efficiently inhibit opsonization of hydrophobic blood components and thereby enhance kinetic stability, manifested as enhanced blood circulation time. The properties elucidated in the preliminary studies were thus re-evaluated in triphilic systems where a hydrocarbon segment was installed to enable hydrophobic drug delivery. A short hydrocarbon segment (consisting of ten hydrocarbon units, H10) was inserted between the mPEG hydrophilic

head and the fluorous tail (either $PFtB_{MONO}$, $PFtB_{TRI}$ and F13, which is the linear PFC equivalent of $PFtB_{TRI}$). With the addition of the hydrocarbon segment all triphilic polymers formed small discrete micelles 10–25 nm in size. However, not all micelles were able to efficiently encapsulate traditional hydrophobic drugs.

The micelles were evaluated for toxicity, drug encapsulation, release, and efficacy in a cancer cell line *in vitro*; micelles were also evaluated for stability using a common chemotherapeutic, paclitaxel, or a fluorescent probe. The efficiency of the fluorous micelles was compared directly to a traditional hydrocarbon micelle formed with $mPEG_{2k}DSPE$ polymers. The triphilic $PFtB_{MONO}$ quickly released encapsulated drug (within 9 h). The triphilic $PFtB_{TRI}$ and F13 micelles were able to encapsulate similar amounts of paclitaxel; however, only $PFtB_{TRI}$ was able to mimic $mPEG_{2k}DSPE$ to give a slow release of drug over time. The comparable drug-loading and release of $PFtB_{TRI}$ and DSPE micelles is notable in that the drug is loaded in a higher density into a thin hydrophobic shell in the case of the $PFtB_{TRI}$ (with one H10 chain), whereas the DSPE (which has two H18 chains) has a larger hydrophobic core. The most promising polymer, $PFtB_{TRI}$, was also found to be non-toxic and release drug to effectively kill cancer cells *in vitro*.

As predicted, the main advantage of the fluorous micelles was realized by the $mPEG_{2k}$-H10-$PFtB_{TRI}$ in its ability to stabilize the micelles under physiological conditions. An *in vitro* stability assay in serum showed that the triphilic $PFtB_{TRI}$ polymers were more stable than all other fluorous and $mPEG_{2k}DSPE$ micelles. This work particularly highlights how the structure of the fluorous domain (as demonstrated by $PFtB_{TRI}$'s superiority over the F13 polymer, which is analogous in fluorine content but divergent in configuration) can greatly impact the organization of the micelle self-assembly, giving rise to drastic changes in delivery performance. This work also clearly demonstrates that the fluorous phase, when properly installed, can enhance the stability of the drug formulation for the potential to increase selectivity and bioavailibility of encapsulated drug.

Chapter 4: In vivo evaluation of theranostic PFtB nanoparticles

Lastly, the *in vivo* behavior of the fluorous formulations was investigated to serve as a preliminary proof of concept for the theranostic design. $PFtB_{TRI}$ polymer micelles with a fluorescent probe encapsulated, were injected in normal mice and visualized in real-time, *in vivo* via confocal laser scanning microscopy (IVRTCLSM). It was shown that the $PFtB_{TRI}$ micelles had a prolonged circulation time (8 h), greatly increased over the free fluorescent dye (3 h). Additionally, the $PFtB_{TRI}$ micelles were not rapidly excreted by the kidney, despite their small size. A tumor model mouse was also exposed to a bolus dose of $PFtB_{MONO}$ micelles to observe biodistribution and selective tumor delivery. Full body and *ex-vivo* ^{19}F-MR imaging show a small accumulation of the polymer within the tumor; however, a significant amount of polymer was visualized within the kidneys and liver. Although polymer did not accumulate *in vivo* in adequate concentrations for high intensity ^{19}F-MR imaging outside of the kidney and liver, these data still serve as a proof of concept for the ability of the triphilic polymer micelles to serve as theranostic particles. Future modifications to the formulation design, for example the appendage of active-targeting ligands, could increase the *in vivo* accumulated concentrations of the nanocarrier to not only improve ^{19}F-MR imaging but also tumor targeting.

1.5 References

(1) Decato, S.; Mecozzi, S. Highly Fluorinated Colloids in Drug Delivery and Imaging. In *Colloid and Interface Science in Pharmaceutical Research and Development*; Elsevier, 2014; pp 319–345.

(2) Lemal, D. M. Perspective on Fluorocarbon Chemistry. *J. Org. Chem.* **2004**, *69* (1), 1–11.

(3) Krafft, M. P.; Riess, J. G. Highly Fluorinated Amphiphiles and Colloidal Systems, and Their Applications in the Biomedical Field. A Contribution. *Biochimie* **1998**, *80* (5-6), 489–514.

(4) Berger, R.; Resnati, G.; Metrangolo, P.; Weber, E.; Hulliger, J. Organic Fluorine Compounds: A Great Opportunity for Enhanced Materials Properties. *Chem. Soc. Rev.* **2011**, *40* (7), 3496–3508.

(5) Krafft, M. P. Fluorocarbons and Fluorinated Amphiphiles in Drug Delivery and Biomedical Research. *Adv. Drug Deliv. Rev.* **2001**, *47*, 209–228.

(6) Neil, E.; Marsh, G. Towards the Nonstick Egg: Designing Fluorous Proteins. *Chem. Biol.* **2000**, *7* (7), 153–157.

(7) Krafft, M. P. Controlling Phospholipid Self-Assembly and Film Properties Using Highly Fluorinated Components - Fluorinated Monolayers, Vesicles, Emulsions and Microbubbles. *Biochimie* **2012**, *94* (1), 11–25.

(8) Hunter, L. The C-F Bond as a Conformational Tool in Organic and Biological Chemistry. *Beilstein Journal of Organic Chemistry*, 2010, *6*, 1–14.

(9) Riess, J. G. Fluorinated Vesicles. *J. Drug Target.* **1994**, *2* (5), 455–468.

(10) Cametti, M.; Crousse, B.; Metrangolo, P.; Milani, R.; Resnati, G. The Fluorous Effect in Biomolecular Applications. *Chem. Soc. Rev.* **2012**, *41* (1), 31–42.

(11) Kiss, L. E.; Kövesdi, I.; Rábai, J. An Improved Design of Fluorophilic Molecules: Prediction of the Ln P Fluorous Partition Coefficient, Fluorophilicity, Using 3D QSAR Descriptors and Neural Networks. *J. Fluor. Chem.* **2001**, *108* (1), 95–109.

(12) Hu, G. X.; Zou, J. W.; Zeng, M.; Pan, S. F.; Yu, Q. Sen. 2D and 3D-QSPR Models for the Fluorophilicity of Organic Compounds in Consideration of Chirality. *QSAR Comb. Sci.* **2009**, *28* (10), 1112–1122.

(13) Gardiner, J. Fluoropolymers: Origin, Production, and Industrial and Commercial Applications. *Aust. J. Chem.* **2015**, *68* (1), 13.

(14) Landry, V.; Blanchet, P. Weathering Resistance of Opaque PVDF-Acrylic Coatings Applied on Wood Substrates. *Prog. Org. Coatings* **2012**, *75* (4), 494–501.

(15) Teng, H. Overview of the Development of the Fluoropolymer Industry. *Appl. Sci.* **2012**, *2* (2), 496–512.

(16) Fluoropolymers Market worth $8,816.4 Million by 2019 http://www.marketsandmarkets.com/PressReleases/fluoropolymers.asp (accessed Apr 22, 2015).

(17) Riess, J. G. Fluorous Micro- and Nanophases with a Biomedical Perspective. *Tetrahedron* **2002**, *58*, 4113–4131.

(18) Zarzar, L. D.; Sresht, V.; Sletten, E. M.; Kalow, J. a.; Blankschtein, D.; Swager, T. M. Dynamically Reconfigurable Complex Emulsions via Tunable Interfacial Tensions. *Nature* **2015**, *518* (7540), 520–524.

(19) Krafft, M. P.; Riess, J. G. Perfluorochemical-Based Oxygen Therapeutics, Contrast Agents, and Beyond. In *Fluorine and Health*; Elsevier, 2008; pp 447–486.

(20) Matson, J. B.; Grubbs, R. H. Synthesis of Fluorine-18 Functionalized Nanoparticles for Use as in Vivo Molecular Imaging Agents. *J. Am. Chem. Soc.* **2009**, *130*, 6731–6733.

(21) Riess, J. G. Blood Substitutes and Other Potential Biomedical Applications of Fluorinated Colloids. *J. Fluor. Chem.* **2002**, *114* (2001), 119–126.

(22) Pretula, J.; Kaluzynski, K.; Wisniewski, B.; Szymanski, R.; Loontjens, T.; Penczek, S. Formation of Poly(ethylene Phosphates) in Polycondensation of H3PO4 with Ethylene Glycol. Kinetic and Mechanistic Study. *J. Polym. Sci. Part a-Polymer Chem.* **2008**, *46* (3), 830–843.

(23) Yu, J.; Cui, W.; Zhao, D.; Mason, R. P. *Fluorine and Health*; Elsevier, 2008.

(24) Wang, J.; Sánchez-Roselló, M.; Aceña, J. L.; Del Pozo, C.; Sorochinsky, A. E.; Fustero, S.; Soloshonok, V. a.; Liu, H. Fluorine in Pharmaceutical Industry: Fluorine-Containing Drugs Introduced to the Market in the Last Decade (2001-2011). *Chem. Rev.* **2014**, *114* (4), 2432–2506.

(25) Williams, H. D.; Trevaskis, N. L.; Charman, S. a; Shanker, R. M.; Charman, W. N.; Pouton, C. W.; Porter, C. J. H. Strategies to Address Low Drug Solubility in Discovery and Development. *Pharmacol. Rev.* **2013**, *65* (1), 315–499.

(26) Anton, N.; Vandamme, T. F. Nano-Emulsions and Micro-Emulsions: Clarifications of the Critical Differences. *Pharm. Res.* **2011**, *28* (5), 978–985.

(27) Driscoll, D. F. Lipid Injectable Emulsions: Pharmacopeial and Safety Issues. *Pharm. Res.* **2006**, *23* (9), 1959–1969.

(28) Sharma, S.; Shukla, P.; Misra, A.; Mishra, P. R. Interfacial and Colloidal Properties of Emulsified Systems. In *Colloid and Interface Science in Pharmaceutical Research and Development*; 2014; pp 149–172.

(29) Urbina-Villalba, G. An Algorithm for Emulsion Stability Simulations: Account of Flocculation, Coalescence, Surfactant Adsorption and the Process of Ostwald Ripening. *Int. J. Mol. Sci.* **2009**, *10* (3), 761–804.

(30) Heeres, A. S.; Picone, C. S. F.; van der Wielen, L. a M.; Cunha, R. L.; Cuellar, M. C. Microbial Advanced Biofuels Production: Overcoming Emulsification Challenges for Large-Scale Operation. *Trends Biotechnol.* **2014**, *32* (4), 221–229.

(31) Tadros, T. Polymeric Surfactants in Disperse Systems. *Adv. Colloid Interface Sci.* **2009**, *147-148* (C), 281–299.

(32) Razgulin, A. V.; Mecozzi, S. Synthesis, Emulsification and Self-Assembly Properties of Sugar-Containing Semifluorinated Amphiphiles. *Carbohydr. Res.* **2015**, *406*, 10–18.

(33) Deshpande, N.; Needles, A.; Willmann, J. K. Molecular Ultrasound Imaging: Current Status and Future Directions. *Clin. Radiol.* **2010**, *65* (7), 567–581.

(34) Fast, J. P.; Perkins, M. G.; Pearce, R. a; Mecozzi, S. Fluoropolymer-Based Emulsions for the Intravenous Delivery of Sevoflurane. *Anesthesiology* **2008**, *109* (4), 651–656.

(35) Parlato, M. C.; Jee, J. P.; Teshite, M.; Mecozzi, S. Synthesis, Characterization, and Applications of Hemifluorinated Dibranched Amphiphiles. *J. Org. Chem.* **2011**, *76* (16), 6584–6591.

(36) Jee, J.-P.; Parlato, M. C.; Perkins, M. G.; Mecozzi, S.; Pearce, R. A. Exceptionally Stable Fluorous Emulsions for the Intravenous Delivery of Volatile General Anesthetics. *Anesthesiology*, 2012, *116*, 580–585.

(37) Taylor, M. J.; Tanna, S.; Sahota, T. In Vivo Study of a Polymeric Glucose-Sensitive Insulin Delivery System Using a Rat Model. *J. Pharm. Sci.* **2010**, *99* (10), 4215–4227.

(38) Shi, J.; Votruba, A. R.; Farokhzad, O. C.; Langer, R. Nanotechnology in Drug Delivery and Tissue Engineering: From Discovery to Applications. *Nano Lett.* **2010**, *10* (9), 3223–3230.

(39) Elsabahy, M.; Wooley, K. L. Design of Polymeric Nanoparticles for Biomedical Delivery Applications. *Chem. Soc. Rev.*, 2012, *41*, 2545–2561.

(40) Ding, J.; Chen, L.; Xiao, C.; Chen, L.; Zhuang, X.; Chen, X. Noncovalent Interaction-Assisted Polymeric Micelles for Controlled Drug Delivery. *Chem. Commun.* **2014**, *50*, 11274–11290.

(41) Rapoport, N.; Pitt, W. G.; Sun, H.; Nelson, J. L. Drug Delivery in Polymeric Micelles: From in Vitro to in Vivo. *J. Control. Release* **2003**, *91*, 85–95.

(42) Jones, M. C.; Leroux, J. C. Polymeric Micelles - A New Generation of Colloidal Drug Carriers. *Eur. J. Pharm. Biopharm.* **1999**, *48* (2), 101–111.

(43) Jee, J.-P.; McCoy, A.; Mecozzi, S. Encapsulation and Release of Amphotericin B from an ABC Triblock Fluorous Copolymer. *Pharm. Res.* **2012**, *29* (1), 69–82.

(44) Akiba, I.; Terada, N.; Hashida, S.; Sakurai, K.; Sato, T.; Shiraishi, K.; Yokoyama, M.; Masunaga, H.; Ogawa, H.; Ito, K.; Yagi, N. Encapsulation of a Hydrophobic Drug into a Polymer-Micelle Core Explored with Synchrotron SAXS. *Langmuir* **2010**, *26* (13), 7544–7551.

(45) Nishiyama, N.; Kataoka, K. Current State, Achievements, and Future Prospects of Polymeric Micelles as Nanocarriers for Drug and Gene Delivery. *Pharmacol. Ther.* **2006**, *112* (3), 630–648.

(46) Wang, Z.; Niu, G.; Chen, X. Polymeric Materials for Theranostic Applications. *Pharm. Res.* **2014**, *31* (6), 1358–1376.

(47) Han, X.; Li, Z.; Sun, J.; Luo, C.; Li, L.; Liu, Y.; Du, Y.; Qiu, S.; Ai, X.; Wu, C.; Lian, H.; He, Z. Stealth CD44-Targeted Hyaluronic Acid Supramolecular Nanoassemblies for Doxorubicin Delivery: Probing the Effect of Uncovalent Pegylation Degree on Cellular Uptake and Blood Long Circulation. *J. Control. Release* **2015**, *197*, 29–40.

(48) Ossipov, D. a. Nanostructured Hyaluronic Acid-Based Materials for Active Delivery to Cancer. *Expert Opin. Drug Deliv.* **2010**, *7*, 681–703.

(49) Siegel, R. L.; Miller, K. D.; Jemal, A. Cancer Statistics, 2015. *CA. Cancer J. Clin.* **2015**, *65* (1), 5–29.

(50) Wicki, A.; Witzigmann, D.; Balasubramanian, V.; Huwyler, J. Nanomedicine in Cancer Therapy: Challenges, Opportunities, and Clinical Applications. *J. Control. Release* **2015**, *200*, 138–157.

(51) Twombly, R. Cancer Surpasses Heart Disease as Leading Cause of Death for All but the Very Elderly. *J. Natl. Cancer Inst.* **2005**, *97* (5), 330–331.

(52) Narvekar, M.; Xue, H. Y.; Eoh, J. Y.; Wong, H. L. Nanocarrier for Poorly Water-Soluble Anticancer Drugs-Barriers of Translation and Solutions. *AAPS PharmSciTech* **2014**, *15* (4), 822–833.

(53) Amado, E.; Kressler, J. Triphilic Block Copolymers with Perfluorocarbon Moieties in Aqueous Systems and Their Biochemical Perspectives. *Soft Matter* **2011**, *7* (16), 7144–7149.

(54) Skrabania, K.; Laschewsky, A.; Berlepsch, H. V.; Böttcher, C. Synthesis and Micellar Self-Assembly of Ternary Hydrophilic- Lipophilicfluorophilic Block Copolymers with a Linear PEO Chain. *Langmuir* **2009**, *25* (29), 7594–7601.

(55) Tucker, W. B.; McCoy, A. M.; Fix, S. M.; Stagg, M. F.; Murphy, M. M.; Mecozzi, S. Synthesis, Physicochemical Characterization, and Self-Assembly of Linear, Dibranched, and Miktoarm Semifluorinated Triphilic Polymers. *J. Polym. Sci. Part A Polym. Chem.* **2014**, *52* (23), 3324–3336.

(56) Li, X.; Yang, Y.; Li, G.; Lin, S. Synthesis and Self-Assembly of a Novel Fluorinated Triphilic Block Copolymer. *Polym. Chem.* **2014**, *5*, 4553–4560.

(57) Cho, H.; Lai, T. C.; Tomoda, K.; Kwon, G. S. Polymeric Micelles for Multi-Drug Delivery in Cancer. *AAPS PharmSciTech* **2014**, *16* (1), 10–20.

(58) Kobayashi, H.; Watanabe, R.; Choyke, P. L. Improving Conventional Enhanced Permeability and Retention (EPR) Effects; What Is the Appropriate Target? *Theranostics* **2014**, *4* (1), 81–89.

(59) Fang, J.; Nakamura, H.; Maeda, H. The EPR Effect: Unique Features of Tumor Blood Vessels for Drug Delivery, Factors Involved, and Limitations and Augmentation of the Effect. *Adv. Drug Deliv. Rev.* **2011**, *63* (3), 136–151.

(60) Greish, K. Enhanced Permeability and Retention of Macromolecular Drugs in Solid Tumors: A Royal Gate for Targeted Anticancer Nanomedicines. *J. Drug Target. 15* (7-8), 457–464.

(61) Maeda, H.; Greish, K.; Fang, J. The EPR Effect and Polymeric Drugs: A Paradigm Shift for Cancer Chemotherapy in the 21st Century. *Adv. Polym. Sci.* **2006**, *193* (1), 103–121.

(62) Matsukuma, D.; Otsuka, H. *Colloid and Interface Science in Pharmaceutical Research and Development*; 2014.

(63) Nichols, J. W.; Bae, Y. H. EPR: Evidence and Fallacy. *J. Control. Release* **2014**, *190*, 451–464.

(64) Khamis, Z. I.; Sahab, Z. J.; Sang, Q.-X. A. Active Roles of Tumor Stroma in Breast Cancer Metastasis. *Int. J. Breast Cancer* **2012**, *2012*, 1–10.

(65) Tang, L.; Yang, X.; Yin, Q.; Cai, K.; Wang, H.; Chaudhury, I.; Yao, C.; Zhou, Q.; Kwon, M.; Hartman, J. a.; Dobrucki, I. T.; Dobrucki, L. W.; Borst, L. B.; Lezmi, S.; Helferich,

W. G.; Ferguson, a. L.; Fan, T. M.; Cheng, J. Investigating the Optimal Size of Anticancer Nanomedicine. *Proc. Natl. Acad. Sci.* **2014**, *111*, 15344–15349.

(66) Chen, Y. C.; Lo, C. L.; Hsiue, G. H. Multifunctional Nanomicellar Systems for Delivering Anticancer Drugs. *J. Biomed. Mater. Res. - Part A* **2013**, 2024–2038.

(67) Cabral, H.; Matsumoto, Y.; Mizuno, K.; Chen, Q.; Murakami, M.; Kimura, M.; Terada, Y.; Kano, M. R.; Miyazono, K.; Uesaka, M.; Nishiyama, N.; Kataoka, K. Accumulation of Sub-100 Nm Polymeric Micelles in Poorly Permeable Tumours Depends on Size. *Nat. Nanotechnol.* **2011**, *6* (12), 815–823.

(68) Jiang, W.; Kim, B. Y. S.; Rutka, J. T.; Chan, W. C. W. Nanoparticle-Mediated Cellular Response Is Size-Dependent. *Nat. Nanotechnol.* **2008**, *3* (3), 145–150.

(69) Ferrari, M. Beyond Drug Delivery. *Nat. Nanotechnol.* **2008**, *3* (3), 131–132.

(70) Duncan, R.; Richardson, S. C. W. Endocytosis and Intracellular Trafficking as Gateways for Nanomedicine Delivery : Opportunities and Challenges Endocytosis and Intracellular Trafficking as Gateways for Nanomedicine Delivery : Opportunities and Challenges. *Mol. Pharm.* **2012**, *9*, 2380–2402.

(71) Hansen, C. G.; Nichols, B. J. Molecular Mechanisms of Clathrin-Independent Endocytosis. *J. Cell Sci.* **2009**, *122* (11), 1713–1721.

(72) Kettler, K.; Veltman, K.; van de Meent, D.; van Wezel, A.; Hendriks, a. J. Cellular Uptake of Nanoparticles as Determined by Particle Properties, Experimental Conditions, and Cell Type. *Environ. Toxicol. Chem.* **2014**, *33* (3), 481–492.

(73) Lopez, S. How Viruses Hijack Endocytic Machinery http://www.nature.com/scitable/topicpage/how-viruses-hijack-endocytic-machinery-14364991 (accessed Apr 22, 2015).

(74) Copolovici, D. M.; Langel, K.; Eriste, E. Cell-Penetrating Peptides: Design, Synthesis, and Applications ¨. *ACS Nano* **2014**, No. 3, 1972–1994.

(75) Delgado, A. V.; López-Viota, J.; Ramos, M. M.; Arias, J. L. Particle Geometry, Charge, and Wettability. In *Colloid and Interface Science in Pharmaceutical Research and Development*; 2014; pp 443–467.

(76) Eetezadi, S.; Ekdawi, S. N.; Allen, C. The Challenges Facing Block Copolymer Micelles for Cancer Therapy: In Vivo Barriers and Clinical Translation. *Adv. Drug Deliv. Rev.* **2014**, No. 2014, 10.1016/j.addr.2014.10.001.

(77) Venditto, V. J.; Szoka, F. C. Cancer Nanomedicines: So Many Papers and so Few Drugs! *Adv. Drug Deliv. Rev.* **2013**, *65* (1), 80–88.

(78) Garanger, E.; Boturyn, D.; Dumy, P. Tumor Targeting with RGD Peptide Ligands-Design of New Molecular Conjugates for Imaging and Therapy of Cancers. *Anti-cancer agents in medicinal chemistry*, 2007, *7*, 552–558.

(79) Yameen, B.; Choi, W. Il; Vilos, C.; Swami, A.; Shi, J.; Farokhzad, O. C. Insight into Nanoparticle Cellular Uptake and Intracellular Targeting. *J. Control. Release* **2014**, *190*, 485–499.

(80) Hai-Tao, Z.; Hui-Cheng, L.; Zheng-Wu, L.; Chang-Hong, G. A Tumor-Penetrating Peptide Modification Enhances the Antitumor Activity of Endostatin in Vivo. *Anticancer. Drugs* **2011**, *22*, 409–415.

(81) Peer, D.; Karp, J. M.; Hong, S.; Farokhzad, O. C.; Margalit, R.; Langer, R. Nanocarriers as an Emerging Platform for Cancer Therapy. *Nat. Nanotechnol.* **2007**, *2* (12), 751–760.

(82) Ernsting, M. J.; Murakami, M.; Roy, A.; Li, S. D. Factors Controlling the Pharmacokinetics, Biodistribution and Intratumoral Penetration of Nanoparticles. *J. Control. Release* **2013**, *172* (3), 782–794.

(83) Alexis, F.; Pridgen, E.; Molnar, L. K.; Farokhzad, O. C. Factors Affecting the Clearance and Biodistribution of Polymeric Nanoparticles. *Mol. Pharm.* **2008**, *5* (4), 505–515.

(84) Li, S. D.; Huang, L. Pharmacokinetics and Biodistribution of Nanoparticles. *Mol. Pharm.* **2008**, *5* (4), 496–504.

(85) Verhoef, J. J. F.; Anchordoquy, T. J. Questioning the Use of PEGylation for Drug Delivery. *Drug Deliv. Transl. Res.* **2013**, *3* (6), 499–503.

(86) Park, K. Controlled Drug Delivery Systems: Past Forward and Future Back. *J. Control. Release* **2014**, *190*, 3–8.

(87) Budisa, N.; Kubyshkin, V.; Schulze-Makuch, D. Fluorine-Rich Planetary Environments as Possible Habitats for Life. *Life* **2014**, *4* (3), 374–385.

(88) Dominguez, M. S.; Maillard, E.; Krafft, M. P.; Sigrist, S.; Belcourt, A. Prevention of Adhesion and Promotion of Pseudoislets Formation from a B-Cell Line by Fluorocarbon Emulsions. *ChemBioChem* **2006**, *7* (8), 1160–1163.

(89) Chen, H.; Kim, S.; He, W.; Wang, H.; Low, P. S.; Park, K.; Cheng, J. X. Fast Release of Lipophilic Agents from Circulating PEG-PDLLA Micelles Revealed by in Vivo Förster Resonance Energy Transfer Imaging. *Langmuir* **2008**, *24* (10), 5213–5217.

(90) Courrier, H. M.; Krafft, M. P.; Butz, N.; Porté, C.; Frossard, N.; Rémy-Kristensen, a.; Mély, Y.; Pons, F.; Vandamme, T. F. Evaluation of Cytotoxicity of New Semi-Fluorinated Amphiphiles Derived from Dimorpholinophosphate. *Biomaterials* **2003**, *24* (4), 689–696.

(91) Mariussen, E. Neurotoxic Effects of Perfluoroalkylated Compounds: Mechanisms of Action and Environmental Relevance. *Arch. Toxicol.* **2012**, *86* (9), 1349–1367.

(92) Frisbee, S. J.; Brooks, a. P.; Maher, A.; Flensborg, P.; Arnold, S.; Fletcher, T.; Steenland, K.; Shankar, A.; Knox, S. S.; Pollard, C.; Halverson, J. a.; Vieira, V. M.; Jin, C.; Leyden, K. M.; Ducatman, A. M. The C8 Health Project: Design, Methods, and Participants. *Environ. Health Perspect.* **2009**, *117* (12), 1873–1882.

(93) Zushi, Y.; Hogarh, J. N.; Masunaga, S. Progress and Perspective of Perfluorinated Compound Risk Assessment and Management in Various Countries and Institutes. *Clean Technol. Environ. Policy* **2012**, *14* (1), 9–20.

(94) Dinglasan, M. J. A.; Ye, Y.; Edwards, E. A.; Mabury, S. A. Fluorotelomer Alcohol Biodegradation Yields Poly- and Perfluorinated Acids. *Environ. Sci. Technol.* **2004**, *38* (10), 2857–2864.

(95) Krafft, M. P.; Riess, J. G. Perfluorocarbons: Life Sciences and Biomedical usesDedicated to the Memory of Professor Guy Ourisson, a True RENAISSANCE Man. *J. Polym. Sci. Part A Polym. Chem.* **2007**, *45* (7), 1185–1198.

(96) Giraudeau, C.; Djemaï, B.; Ghaly, M. A.; Boumezbeur, F.; Mériaux, S.; Robert, P.; Port, M.; Robic, C.; Bihan, D. Le; Lethimonnier, F.; Valette, J. High Sensitivity 19F MRI of a Perfluorooctyl Bromide Emulsion: Application to a Dynamic Biodistribution Study and Oxygen Tension Mapping in the Mouse Liver and Spleen. *NMR Biomed.* **2012**, *25* (4), 654–660.

(97) Riess, J. G. Perfluorocarbon-Based Oxygen Delivery. *Artif. Cells. Blood Substit. Immobil. Biotechnol.* **2006**, *34* (6), 567–580.

(98) Manke, A.; Wang, L.; Rojanasakul, Y. Mechanisms of Nanoparticle-Induced Oxidative Stress and Toxicity. *Biomed Res. Int.* **2013**, *2013*, 1–15.

(99) Lucignani, G.; Ottobrini, L.; Martelli, C.; Rescigno, M.; Clerici, M. Molecular Imaging of Cell-Mediated Cancer Immunotherapy. *Trends Biotechnol.* **2006**, *24* (9), 410–418.

(100) Studwell, A. J.; Kotton, D. N. A Shift From Cell Cultures to Creatures: In Vivo Imaging of Small Animals in Experimental Regenerative Medicine. *Mol. Ther.* **2011**, *19* (11), 1933–1941.

(101) Srinivas, M.; Heerschap, A.; Ahrens, E. T.; Figdor, C. G.; de Vries, I. J. M. 19F MRI for Quantitative in Vivo Cell Tracking. *Trends Biotechnol.* **2010**, *28* (7), 363–370.

(102) Duncan, R.; Gaspar, R. Nanomedicine (S) under the Microscope. *Mol. Pharm.* **2011**, *8*, 2101–2141.

(103) Srinivas, M.; Heerschap, A.; Ahrens, E. T.; Figdor, C. G.; de Vries, I. J. M. 19F MRI for Quantitative in Vivo Cell Tracking. *Trends in Biotechnology*, 2010, *28*, 363–370.

(104) Diezi, T. A.; Bae, Y.; Kwon, G. S. Enhanced Stability of PEG-Block-poly(N-Hexyl Stearate L-Aspartamide) Micelles in the Presence of Serum Proteins. *Mol. Pharm.* **2010**, *7* (4), 1355–1360.

(105) Baligand, C.; Vauchez, K.; Fiszman, M.; Vilquin, J.-T.; Carlier, P. G. Discrepancies between the Fate of Myoblast Xenograft in Mouse Leg Muscle and NMR Label Persistency after Loading with Gd-DTPA or SPIOs. *Gene Ther.* **2009**, *16*, 734–745.

(106) Hu, L. New MRI Techniques for Nanoparticle Based Functional and Molecular Imaging. *Washingt. Univ. St. Louis - Electron Thesis* **2012**.

(107) Boehm-Sturm, P.; Mengler, L.; Wecker, S.; Hoehn, M.; Kallur, T. In Vivo Tracking of Human Neural Stem Cells with 19F Magnetic Resonance Imaging. *PLoS One* **2011**, *6* (12), e29040.

(108) Ruiz-Cabello, J.; Barnett, B. P.; Bottomley, P. a.; Bulte, J. W. M. Fluorine (19F) MRS and MRI in Biomedicine. *NMR Biomed.* **2011**, *24* (2), 114–129.

(109) Rhee, J.-K.; Park, O.; Lee, A.; Yang, D.; Park, K. Glycol Chitosan-Based Fluorescent Theranostic Nanoagents for Cancer Therapy. *Mar. Drugs* **2014**, *12* (12), 6038–6057.

(110) Knight, J. C.; Edwards, P. G.; Paisey, S. J. Fluorinated Contrast Agents for Magnetic Resonance Imaging; a Review of Recent Developments. **2011**, 1415–1425.

(111) Du, W.; Xu, Z.; Nyström, A. M.; Zhang, K.; Leonard, J. R.; Wooley, K. L. 19F- and Fluorescently Labeled Micelles as Nanoscopic Assemblies for Chemotherapeutic Delivery. *Bioconjug. Chem.* **2008**, *19*, 2492–2498.

(112) Porsch, C.; Zhang, Y.; Östlund, Å.; Damberg, P.; Ducani, C.; Malmström, E.; Nyström, A. M. In Vitro Evaluation of Non-Protein Adsorbing Breast Cancer Theranostics Based on 19F-Polymer Containing Nanoparticles. *Part. Part. Syst. Charact.* **2013**, *30*, 381–390.

(113) Peng, H.; Blakey, I.; Dargaville, B.; Rasoul, F.; Rose, S.; Whittaker, A. K. Synthesis and Evaluation of Partly Fluorinated Block Copolymers as MRI Imaging Agents. *Biomacromolecules* **2009**, *10* (2), 374–381.

(114) Ogawa, M.; Kataoka, H.; Nitahara, S.; Fujimoto, H.; Aoki, H.; Ito, S.; Narazaki, M.; Matsuda, T. Water-Soluble Fluorinated Polymer Nanoparticle as 19FMRI Contrast Agent Prepared by Living Random Copolymerization from Dendrimer Initiator. *Bull. Chem. Soc. Jpn.* **2012**, *85* (1), 79–86.

(115) Nurmi, L.; Peng, H.; Seppala, J.; Haddleton, D. M.; Blakey, I.; Whittaker, A. K. Synthesis and Evaluation of Partly Fluorinated Polyelectrolytes as Components in 19F MRI-Detectable Nanoparticles. **2010**, 1039–1047.

CHAPTER 2:

Development of a multifunctional ^{19}F imaging handle for self-assemblies

*This chapter is published, in part, under the title "Synthesis and characterization of perfluoro-*tert*-butyl semifluorinated amphiphilic polymers and their potential application in hydrophobic drug delivery"– Reference: Decato, S.; Bemis, T.; Madsen, E.; Mecozzi, S. *Polym. Chem.* **2014**, *5*, 6461.

Abstract

Semifluorinated polymer surfactants, composed of a monomethyl poly(ethylene glycol) (mPEG) hydrophilic head group and 1, 2, or 3 perfluoro-*tert*-butyl (PFtB) groups as the fluorophilic tail, were synthesized, and their aqueous forumulations were investigated as a potential design for theranostic nanoparticles. The PFtB surfactants demonstrate several similar characteristics to those of polymers with linear perfluorocarbon tails, despite differences in the tail structure. For example, $PFtB_{MONO}$ (fluorous tail with only 1 PFtB group) polymer solutions stably emulsified 20 % v/v sevoflurane with perfluorooctyl bromide (PFOB) as a stabilizer. Polymers with three PFtB groups ($PFtB_{TRI}$) solely formed stable, spherical micelles, approximately 12 nm in size. Additionally, these PFtB polymers have the potential to serve as ^{19}F-MRI tracer agents. $PFtB_{TRI}$ micelles gave one narrow ^{19}F-NMR signal in D_2O, with T_1 and T_2 parameters of approximately 500 and 100 ms, respectively. ^{19}F-MR images of PFtB polymer solutions at 1 mM gave an intense signal at 4.7 T without sensitizers or selective excitation sequences. These preliminary data demonstrate the potential of the PFtB moiety as a basic design feature that can be further modified to provide dual drug-delivery and imaging capabilities in nanocarrier systems.

2.1 Motivation and intent

Polymeric colloids have proven to be powerful tools in the delivery of hydrophobic drugs. Micelle and emulsion formulations have been identified as two drug delivery platforms of interest as they are amenable to the relatively facile installation of a fluorous segment within the amphiphilic molecules comprising them, affording unique and advantageous properties. Functionalized semifluorintaed mPEG polymers have been shown to form aggregates of tailored size and shape that exhibit enhanced thermodynamic and *in vivo* (kinetic) stability.

Previous research in the development of fluorous polymers focused on linear PFC domains for the intravenous (IV) delivery of volatile anesthetics that would provide enhanced pharmacodynamics parameters[1] and for the stabilization of micelles for controlled release of hydrophobic drug delivery[2]. With the continued development of the fluorous drug formulations there was a keen interest to be able to gain insight into the *in vivo* behavior upon and after injection. Tracking the journey and biological interactions undergone by the semifluorinated polymers and their corresponding formulations *in vivo* would provide valuable information for improved design and would investigate the impact that the fluorous domain imparts in these formulations. More specifically an understanding of the particle behavior *in vivo* could allow for non-invasive, *in vivo* pharmacokinetic or biodistribution measurements.

This chapter describes the design of a triphilic polymer intended to form theranostic nanoparticles (providing dual drug delivery and imaging capabilities simultaneously). The fluorous tail serves to stabilize the drug formulation and to enable ^{19}F-MRI particle tracking. Notably it has been shown that with this design the ^{19}F-MR capabilities are maintained even when formulated as a self-assembly, where the imaging label is restricted to a crowded and dynamic environment. This work serves as a proof of concept and demonstrates the utility of the fluorous design.

2.2 Synthesis, formulation, and calibration of linear PFC emulsions

Preliminary work was done to investigate the degree of variability in the preparation of the linear PFC sevoflurane emulsions. Due to the volatility of the fluorous anesthetic it was possible that slight variations in preparation techniques could manifest in drastic changes in formulated sevoflurane concentrations. Therefore the precision of emulsion preparation from operator to operator was evaluated. The particular linear PFC polymer of interest was the $mPEG_{1k}$-F13, which was synthesized by direct conjugation of the $mPEG_{1k}$-OMs to the commercially available F13 alcohol according to the previously published procedure.[3] The polymer was purified via flash chromatography and the isolated product was assessed by NMR, HPLC, and MALDI-MS. Emulsions of 20 % v/v of sevoflurane, 10 % v/v PFOB, and 10 mM $mPEG_{1k}$-F13 in sterilized normal saline were prepared and filtered according to the standard protocol.[1,]

Once adequate polymer stock was acquired, a calibration experiment was established in which separate operators independently prepared a series of emulsions from the same polymer batch with varying concentrations of sevoflurane ranging from 0 % to 40 % v/v. It is interesting to note the visual differences between the emulsions, especially after filtration (**Figure 2.1** and **2.2**). Phase separation was visually apparent for all emulsions above 20 % v/v of sevoflurane, which is the maximum stable dose at the 10 mM surfactant and 10% v/v additive concentrations of the standard protocol.

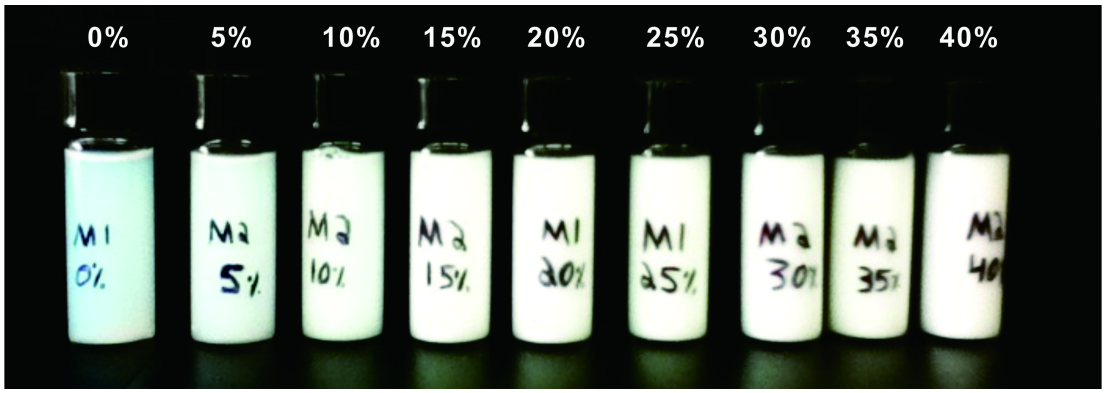

Figure 2.1 $mPEG_{1k}$-F13 sevoflurane emulsion calibration series before filtration.
Visual differences in opacity can be observed over the varying concentrations of sevoflurane.

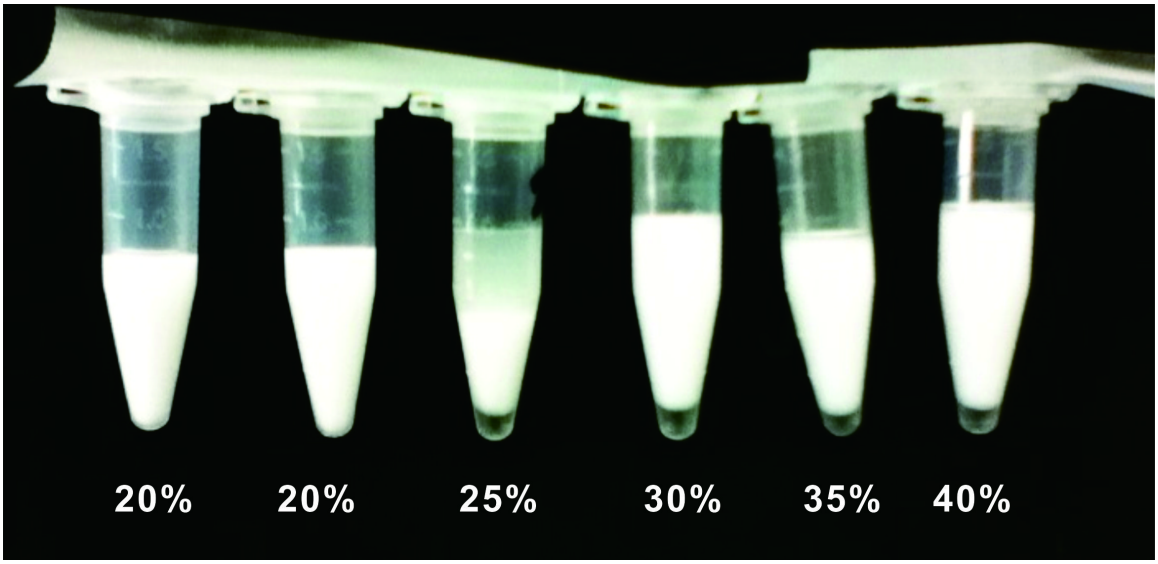

Figure 2.2 $mPEG_{1k}$-F13 sevoflurane emulsion calibration series after filtration.
Note 20% v/v is presented twice to show consistent results from both formulation operators. Visual sedimentation is apparent at 25% and phase separation is evident above 20% v/v sevoflurane.

In order to compare the effective concentration of sevoflurane in the prepared emulsions across operators, weight differences between the calibration series was measured. LC/MS, NMR, and spectroscopy methods were not feasible due to incompatibility of the sevoflurane with the available detectors and separatory columns (arising in part from the high volatility and fluorophilicity) and due to the high viscosity and opacity of the emulsion. GC/MS was also ruled out due to the difficulty in generating a reliable and concentrated volume of sevoflurane in the

headspace of the vial. Once the emulsions were prepared and filtered, an aliquot of each emulsion was isolated, sealed, and weighed. This weight was then plotted over the entire concentration range and provided a linear plot (except for emulsions above 25 % v/v as these were unstable and began to phase separate immediately after formulation), which was compared with the emulsions prepared by the alternative operator. The particle size of each emulsion was also measured, which did not indicate significant change in average droplet size with different operators. Also, the weight of emulsions prepared for previous animal studies correlated well to the desired sevoflurane content when applied to the calibration curve. Although, this method does not allow for a quantitative determination of the amount of sevoflurane in the emulsion, this effort demonstrates that the emulsions can be reliably prepared with different operators.

Emulsion preparation is extremely important and can dictate the subsequent properties throughout the formulation lifetime from marketing to clinical efficiency. However, it can be extremely difficult to correlate physical properties optimized during formulation with clinical results (or to predict clinical outcomes). The effectiveness of the emulsion formulation, as with other colloidal formulations (such as polymeric micelles), relies heavily upon its behavior during and after administration, which may be drastically altered from that pre-injection. The capability for direct nanoparticle imaging of the *in vivo* behavior of such drug-delivery systems would serve to elucidate the biological response arising from subtle modifications in formulation and thereby enhance nanoparticle design and treatment efficacy. Particle tracking would be particularly advantageous in the development of new and more sophisticated formulations, including fluorous colloids.

Typical methods of particle tracking were not amenable to our formulations, either due to high cost (e.g. radiolabeling with ^{18}F) or to detrimental alterations in polymer structure leading to interference with droplet stability or self-assembly (e.g. chelated MRI labels or conjugated

quantum dots (QDs)). Small fluorescent molecule labels are compatible—and were used in some instances—with *in vitro* cell imaging or *in vivo* imaging of subcutaneous or surface features. However, ideally a full-body, deeply penetrating imaging method was desired to following the particle from injection, to target localization, and ultimately to excretion. It was with these features in mind that a ^{19}F-MR imaging modality was chosen, in that the fluorous segment of the polymer could be expanded as a multipurpose design feature: a driving force for assembly (in terms of micelle formulations) and particle stability and an imaging handle for ^{19}F-MRI for particle tracking. The successful combination of these features into one fluorous moiety would enable theranostic capabilities: dual drug delivery and imaging.

2.3 Rationale for the perfluoro-*tert*-butyl (PFtB) tracer design

The traditional linear PFC tail of the amphiphilic polymer was redesigned to serve as a ^{19}F-MR label for molecular imaging of injected semifluorinated polymers and their aggregates *in vivo*. In order to maintain the capabilities for stable drug formulation in both emulsion and micelle systems, and the advantageous properties developed in the linear fluorous polymers, each element of the new ^{19}F-MR tracer polymers needed to be carefully considered. In order to isolate the effects from alterations of the fluorous moiety the initial polymer design consisted of only two domains: a hydrophilic block to allow for water solubility and a fluorous domain to provide amphiphilic character and ^{19}F-MR imaging capabilities.

As with previous polymer designs, PEG was chosen for the hydrophilic block for its high water solubility, low-cost, flexibility, and "stealth" surface properties discussed earlier. This last feature is especially important to deter phagocytic opsonization by the RES and increase the bioavailability of the drug formulation. For the fluorous domain, there were several parameters to consider in designing a fluorous tail that could provide ^{19}F-MR capabilities but could also maintain the molecular recognition behavior arising from significant fluorous character.

A well-executed semifluorinated polymer design has the potential to not only provide enhanced stability as a self-assembly or emulsion but also to serve as a potential label for ^{19}F-MRI. Small molecule PFCs[4], particularly perfluoropolyether (PFPE)[5,6], and perfluorooctylbromide (PFOB)[7], have been investigated for imaging purposes[8]; however, despite their success in ^{19}F-MRI particle tracking, many linear or asymmetric PFCs experience significant ^{19}F signal splitting, which decreases effective signal and image quality. Additionally multiple signals could prevent the definitive use of ^{19}F-MR spectroscopy to distinguish the aggregated or non-aggregated states of the amphiphilic polymers. Therefore for the amphiphilic fluorous polymer design an alternative approach was used to facilitate synthesis, to minimize perturbations in self-assembly, to avoid the use of long-chain PFCs (which are potentially toxic and bioaccumulative), and to maximize signal intensity and imaging capabilities. The fluorous moiety was designed so that all fluorine atoms were NMR equivalent to give rise to a single ^{19}F-NMR signal. This minimized loss in signal intensity resulting from dipolar interactions between neighboring fluorine atoms and protons, and from broadening of ^{19}F peaks due to the sensitivity of the ^{19}F chemical shift of each CF_2 unit.[9] NMR equivalent fluorine groups will also maximize signal-to-noise ratios (SNR) without application of selective excitation sequences.

After considering NMR equivalent fluorine concentration, the next major parameter to consider in tracer agent design is relaxation time. The resulting assemblies must exhibit short spin-lattice (T_1) and long spin-spin (T_2) values to maintain high signal intensity. In dynamic systems, such as micelle self-assemblies, the T_2 relaxation time is particularly prone to shortening, resulting in significant loss in signal intensity. In a study by Nyström *et al*. no ^{19}F signal could be detected from an aqueous assembly when a fluorinated segment was installed within a rigid hydrophobic core.[10] Following studies by Peng *et al.* demonstrated that self-assemblies with more fluid cores allowed for increased ^{19}F signal.[11] A recent approach to afford

sufficient tracer relaxivities was developed by Whittaker *et al*. in which charged monomer units were utilized to increase mobility of the fluorinated segment[12]; however, this may not be unilaterally advantageous as nanoparticles with charged surfaces exhibit increased recognition by the RES.[13] Collectively, these studies demonstrate the importance of careful consideration of nanoparticle design, especially in terms of tracer mobility to maintain NMR equivalency throughout the fluorous domain.

In this study, a branched fluorous architecture was installed to achieve increased mobility, or increased fluidity. Typically when tracer or contrast agents are installed in the core of the nanoparticle the signal intensity is dramatically reduced. However, branched structures experience frustrated packing and reduce interactions between non-equivalent fluorine atoms, which reduces the loss of contrast from dipolar interactions between nuclear spins[14]. The perfluoro-*tert*-butyl (PFtB) moiety was selected as it is highly branched and has demonstrated advantageous characteristics as a general ^{19}F-MRI contrast agent, ^{19}F-Imaging Tracer (^{19}FIT)[15]. The modularly symmetrical ^{19}FIT molecule is composed of a branched PEG hydrophilic head group with amide linkages and a tail consisting of three PFtB groups. Aqueous solutions of these molecules exhibited a single ^{19}F signal even as aggregates. Additionally, they showed no acute toxicity *in vivo* with a residence half-life of approximately 0.5 days in mice and no evidence of organ retention or *in vivo* degradation. These studies demonstrate the PFtB's advantageous properties for *in vivo* imaging contrast. However, the ^{19}FIT molecule was designed for general contrast and therefore is not directly amenable to serve as a theranostic particle for molecular imaging. Also the extent of the surface-active properties of PFtB polymers had not previously been rigorously investigated.

Acknowledging that the PFtB group is a radical deviation from the conventional linear perfluorocarbon chain, the physicochemical properties and the self-assembly behavior were

characterized to provide insight into the relationship between shape and subsequent properties of the polymers and their corresponding nanoparticles. In preliminary studies the physicochemical properties of semifluorinated polymers in aqueous solution arising from the introduction of one or multiple PFtB moieties were measured. Additionally, the potential application as molecular ^{19}F-MR imaging tracer agents was evaluated for those polymers capable of forming stable assemblies. The basic amphiphilic polymer design is composed of a fluorous tail, which is modularly increased in fluorophilicity to include 1, 2, and 3 PFtB groups ($PFtB_{MONO}$, $PFtB_{DI}$, and $PFtB_{TRI}$, respectively, **Figure 2.3**) and a hydrophilic monomethyl poly(ethylene glycol) (mPEG) head group. The mPEG length is relatively small (1,000 and 2,000 g/mol average molecular weight) in order to provide aqueous solubility and prolonged evasion from blood clearance by the mononuclear phagocyte system (MPS) while maximizing the percent fluorine per molecule, which is directly proportional to ^{19}F signal intensity.

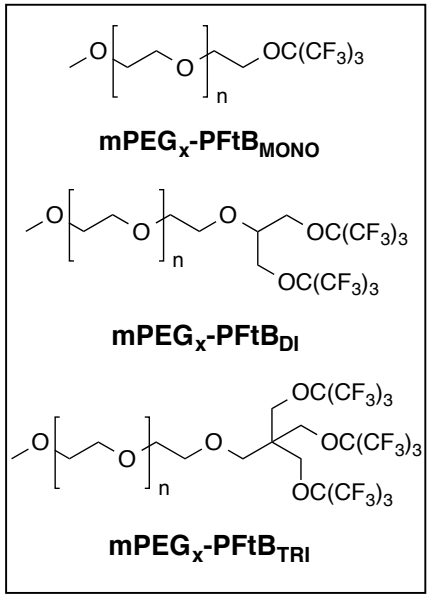

Figure 2.3. Fluorous $mPEG_x$-$PFtB_y$ polymers designed as ^{19}F-MRI tracers.
Polymers were synthesized to investigate the effects on self-assembly and imaging behavior with modular increase in fluorophilicity ($PFtB_{MONO}$ → $PFtB_{TRI}$).

The PFtB group, when properly installed in an amphiphilic polymer, can drive the self-assembly of small, stable micelles in aqueous media and provide significant signal intensity for ^{19}F-MR imaging. The proposed polymers serve as a foundation for a multifunctional polymer design that can be modulated to include other intermediate blocks for hydrophobic drug or dye encapsulation. The surface can also be readily decorated with fluorophores, positron emission tomography (PET) radioisotopes, or other contrast labels for multi-modality imaging. Additionally, site-specific targeting ligands may also be conjugated to the nanoparticle surface to increase bioaccumulation and cell uptake of drug-containing nanocarriers to specific tissue[16]. The versatile multifunctional amphiphile design described herein demonstrates the potential for PFtB-based polymers to serve as effective theranostic particles[17], capable of monitoring the behavior of colloidal drug systems *in vivo* including pharmacokinetics and biodistribution[18].

2.4 Results and discussion

2.4.1 Synthetic scheme and rationale

Synthesis of the $PFtB_{MONO}$-terminated polymers was carried out by direct substitution of the mPEG-OMs by the potassium salt of the PFtB alcohol according to the procedure described by Rábai, *et al.*[19] (**Figure 2.4** and **Figure 2.5**). These reactions were straightforward and high yielding, with relatively short reaction times. The resulting compounds were very soluble in water and therefore amenable to forming aqueous nano-assemblies.

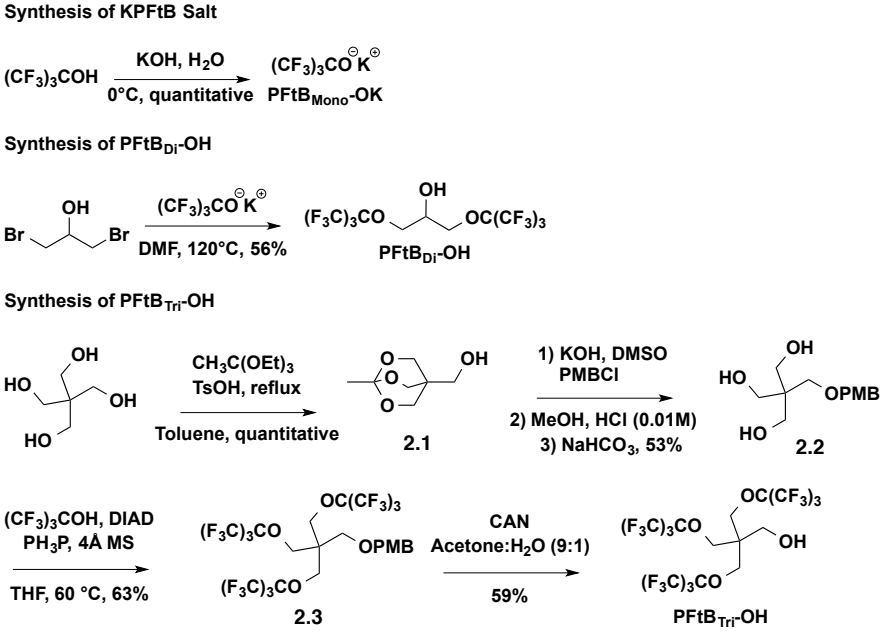

Figure 2.4 Synthesis of three fluorous alcohols: $PFtB_{MONO}$, $PFtB_{DI}$, and $PFtB_{TRI}$.
The synthesis of $PFtB_{MONO}$-OK and $PFtB_{DI}$-OH, are achieved according to previous literature procedures[19,20]. The $PFtB_{TRI}$-OH is achieved by modification a previous literature procedure[21,22] for small-scale reaction conditions.

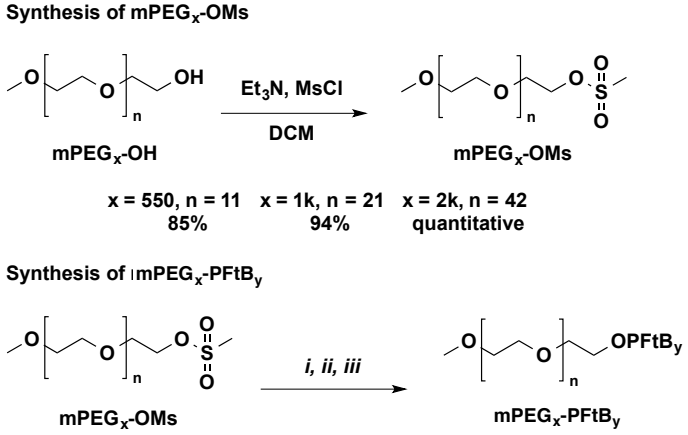

Figure 2.5. Synthetic scheme for all three $mPEG_x$-$PFtB_y$ polymers.
$mPEG_x$-$PFtB_{MONO}$, $mPEG_x$-$PFtB_{DI}$, and $mPEG_x$-$PFtB_{TRI}$ were synthesized via substitution of $mPEG_x$-OMs by the corresponding PFtB alcohol. N/A signifies that the desired product could not be purely resolved from a reaction side-product, $mPEG_x$-$PFtB_{MONO}$.

The $PFtB_{DI}$ polymer series presented several difficulties but provided keen insight into bioorthogonal fluoropolymer design. The $PFtB_{DI}$ alcohol was synthesized in refluxing DMF and purified by vacuum distillation according to the synthesis described by Nemes *et al.*[20] The volatility and limited solubility of the resulting alcohol made it difficult to separate from the DMF solvent without significant loss of the product under vacuum. The alcohol was also difficult to visualize by TLC despite the hydroxyl functionality. Most importantly, the $PFtB_{DI}$ alcohol is prone to decomposition under subsequent basic reaction conditions, which had been similarly demonstrated in the synthesis of a PFtB containing peptide[23].

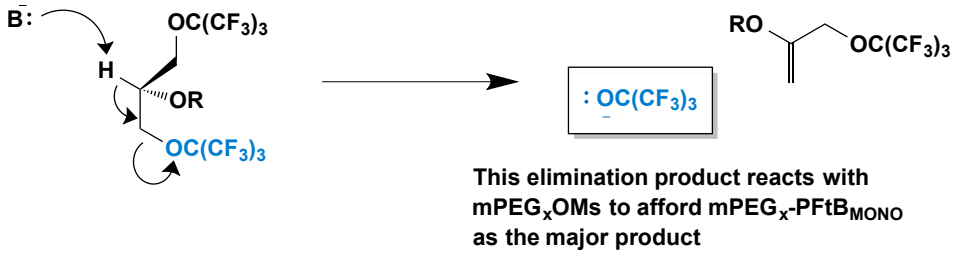

Figure 2.6 β-hydride elimination of $PFtB_{DI}$ moiety.
The $PFtB_{DI}$ alcohol (R = H) is readily eliminated under basic conditions necessary for the polymer functionalization (coupling of the fluorous alcohol to the $mPEG_x$-OMs). This susceptibility to basic elimination most likely also extends to the $mPEG_x$-$PFtB_{DI}$ polymer.

Elimination of the β-hydrogen resulted in the release of the PFtB oxide, which readily reacted via substitution with the mPEG mesylate to form the $mPEG_x$-$PFtB_{MONO}$ polymer rather than the desired $mPEG_x$-$PFtB_{DI}$ polymer (**Figure 2.6**). A mixture of the $mPEG_x$-$PFtB_{MONO}$ and $mPEG_x$-$PFtB_{DI}$ polymers was evident by MALDI-MS and by NMR, which approximated the compounds to be present in a 9:1 ratio, respectively. These two polymers can be isolated up to approximately 95% purity via flash chromatography without significant loss in yield. However, the significant decomposition of the $PFtB_{DI}$ alcohol indicates that the $mPEG_x$-$PFtB_{DI}$ may also be prone to

degradation. Therefore, a biocompatible fluoropolymer design should avoid β-hydrogens adjacent to the PFtB oxide, which would be detrimental if eliminated *in vivo*.

The $mPEG_x$-$PFtB_{TRI}$ polymer series was more challenging to synthesize. Nevertheless, it provides the largest percent fluorine possible from a single fluorous tail, while maintaining a robust design that can avoid decomposition. The synthesis of the $PFtB_{TRI}$ alcohol was modified from the synthesis by Yu *et al*.[21,22] for small-scale reaction conditions. The steric hindrance and electron withdrawing character of the PFtB groups necessitated vigorous Mitsunobu reaction conditions to afford the desired tri-substituted pentaerythritol. Adjustments to heat and reaction time had little effect compared to the concentration of the reaction mixture. A p-methoxybenzyl (PMB) protecting group was used in lieu of more resilient groups, such as the benzyl functionality due to difficulty in deprotection. It should also be noted that the resulting $PFtB_{TRI}$ alcohol, once deprotected, sublimed under vacuum at room temperature and was difficult to visualize by standard TLC stains. Purification was therefore achieved using a Combi-Flash system equipped with an evaporative light scattering detector (ELSD) while minimizing exposure to vacuum. However, as suggested in a similar synthesis from Yu *et al*.[21,22,15], purification from large-scale synthesis may be achieved by simple phase separation. The resulting $mPEG_{1k}$-$PFtB_{TRI}$ and $mPEG_{2k}$-$PFtB_{TRI}$ polymers were sparingly soluble in water. Solutions exceeding 5 mM were extremely viscous, approaching gelification. Since the desired application of the polymers was to form aqueous self-assemblies, the $mPEG_{550}$-$PFtB_{TRI}$ was not synthesized, as this decrease in the hydrophilic block would further decrease the aqueous solubility of the polymer.

2.4.2 Physicochemical characterization: CMC and DLS

Once synthesized, each polymer CMC was measured by surface tension using the Wilhemy method. A reference compound, which has been thoroughly characterized in the literature, $mPEG_{2k}$-DSPE 1,2-distearoyl-sn-glycero-3-phosphoethanolamine-N-[methoxy(polyethylene

glycol)-2000][24], was purchased and analyzed to provide comparison to these distinct triphilic polymer surfactants. The corresponding CMC value for each polymer was then used as the lower limit for all future assembly studies. Of the synthesized PFtB polymers, the $mPEG_x$-$PFtB_{TRI}$ polymers solely demonstrated typical micelle behavior with a clear sigmoidal curve and a CMC value below log(M) = -3 (or 1 mM, **Table 2.1**). The $PFtB_{MONO}$ polymer was not adequately fluorophilic to drive self-assembly of the unimers into regular, stable aggregates.

Table 2.1 CMC and DLS particle size measurements of aqueous polymer solutions.
CMC values determined by surface tensiometry using the Wilhelmy method. [a]Particle sizes of semifluorinated polymers measured by DLS as determined by volume with spherical fits. Data is given with the standard deviation. Each measurement was performed above the measured CMC and was repeated three times (n = 3). (%) signifies the percent of total particles of that particular size by volume. [b]N/A signifies that no CMC value could be determined since no constant minimum surface tension could be achieved. $mPEG_{2k}$-DSPE is presented as a reference compound.

Polymer	pCMC (-log(M))	Particle Size by DLS (nm)[a]
$mPEG_{550}$-$PFtB_{MONO}$	N/A[b]	4.4 ± 1.2 (99.9 %)
$mPEG_{1k}$-$PFtB_{MONO}$	N/A[b]	68.9 ± 35.8 (100 %)
$mPEG_{2k}$-$PFtB_{MONO}$	N/A[b]	32.7 ± 7.8 (38.1 %), 153.8 ± 82.7 (61.9 %)
$mPEG_{1k}$-$PFtB_{TRI}$	5.02 ± 0.05	11.1 ± 2.8 (99.7 %)
$mPEG_{2k}$-$PFtB_{TRI}$	5.32 ± 0.06	11.8 ± 3.6 (99.8 %)
$mPEG_{1k}$-F13[25]	6.08 ± 0.13	11.9 ± 1.3 (99.9 %)
$mPEG_{2k}$-DSPE[25]	4.90 ± 0.17	13.9 ± 1.6 (100 %)

The DLS further indicated that the $mPEG_x$-$PFtB_{MONO}$ polymers did not form micelles in aqueous solution, as the particles sizes were atypically large and had wide size distributions. The only exception was the $mPEG_{550}$-$PFtB_{MONO}$; however, the extremely small size and high concentration necessary to observe these aggregates prevent them from being applicable for drug delivery formulation, if they are in fact micelles. Aggregate shape could not be confirmed; however, the DLS measurements suggested that the particles are irregular and most likely transient as the particle size distribution changed throughout the measurement. In contrast, the

DLS measurements of the $mPEG_x$-$PFtB_{TRI}$ polymers indicated the formation of stable micelles, approximately 12 nm in size, which was not significantly affected by mPEG length. (It is important to reemphasize that this size is within range to utilize the EPR effect to increase accumulation at cancerous tissue.) This behavior and size was very similar to its linear counterpart, $mPEG_{1k}$-F13, where F13 corresponds to a linear PFC consisting of 13 PFC units, which had previously been synthesized for sevoflurane emulsion formulations.

2.4.3 Transmission electron microscopy (TEM)

Due to the PFtB's considerable deviation from a typical linear tail structure it was important to confirm the shape of the $mPEG_x$-$PFtB_{TRI}$ polymer assemblies. Other polymer series, $mPEG_x$-$PFtB_{MONO}$ was not analyzed due to random aggregation and $mPEG_x$-$PFtB_{DI}$ was analyzed although prior to identification of impurities. Therefore these images are not discussed further except to reveal that the cryo-TEM images of aqueous polymer aggregates appeared highly solvated (due to the relatively large mPEG corona). The high solvation, along with the small size of the fluorinated core, provided little to no contrast between the vitrified water and the hydrated particles[26]. The sample preparation provides several other possible origins for the poor visualization of nanoparticles in the cryo-TEM measurements. The solution viscosity and hyperhydrophobicity of the fluorous polymer tails may have prevented good adhesion of the micelles during blotting. This would have significantly reduced the number of particles before vitrification. To limit variables in sample preparation and image contrast a negative staining method was used with uranyl acetate. Negative staining again provided mitigated success mainly due to impurities of the $mPEG_x$-$PFtB_{DI}$ and from particle-particle aggregation that occurred during staining and drying process. Once the impurity of the $mPEG_x$-$PFtB_{DI}$ polymers was realized and the $mPEG_x$-$PFtB_{TRI}$ polymers had been successfully synthesized an alternative approach was used to try to completely minimize preparation effects. An aqueous solution of

$mPEG_{1k}$-$PFtB_{TRI}$ polymer was blotted onto a grid and quickly dried. With this preparation the particles exhibited reduced aggregation and imaged using the higher resolution cryo-TEM instrument. Although the dried assemblies may deviate in size from those present in aqueous conditions, the dried TEM image (**Figure 2.7**) showed that the stable assemblies were spherical in shape, which corroborates the DLS data. Although these initial TEM experiments were not very successful, further TEM experiments could be informative as long as significant time is spent to elucidate the proper sample preparation parameters necessary to adhere the fluorous micelles to the grid and minimize particle-particle aggregation, most importantly those concerning blotting and concentration.

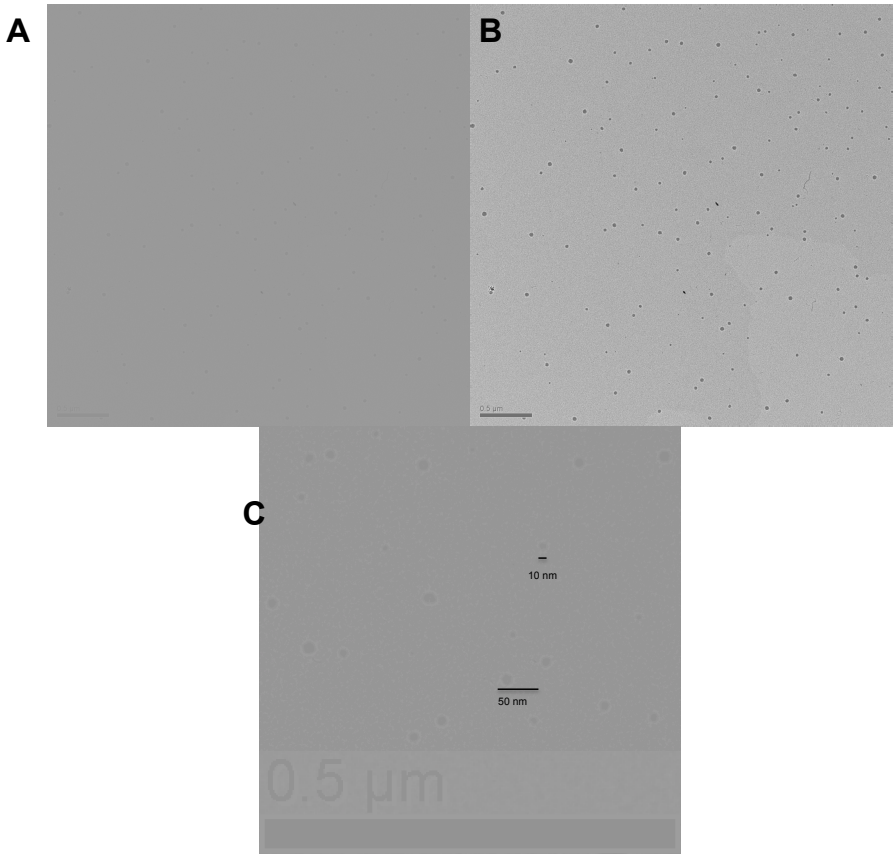

Figure 2.7 TEM of $mPEG_{1k}$-$PFtB_{TRI}$.
An aqueous $mPEG_{1k}$-$OPFtB_{TRI}$ 1 mM micelle solution was dried and visualized via TEM. **A**: Image without alterations, **B**: Image with post-processing contrast enhancement, and **C**: Original contrast image with post-processing magnification. Poor contrast is mainly due to the significant hydration of the mPEG.

Despite difficulties in direct visualization of the nanoparticles via TEM, the collective physicochemical data suggests that despite the deviation in tail structure, these polymers can form stable, spherical micelles. This behavior indicates that these PFtB amphiphiles are effective surfactants, which could serve as emulsifiers or could form stable micelle drug-delivery vehicles if an intermediate hydrocarbon segment were installed in the polymer design.

2.4.4 Fluorous tail structure: EPS computation, core microviscosity, and hemolysis

To further investigate the distinct structure and subsequent physicochemical properties of the PFtB group, a calculation of the electrostatic potential energy surface (EPS) of both the PFtB-OH and the F13-OH was performed using the SPARTAN'10 program package (**Figure 2.8**). These calculations showed the difference in electrostatic properties and molecular shape between the $PFtB_{TRI}$ and the linear F13 groups. The surface of the $PFtB_{TRI}$ alcohol appeared to be disk-shaped in contrast to the rod-shaped F13 alcohol. This disk orientation may allow for a more compact and viscous core, despite the relatively large steric bulk, leading to smaller micelles than one may have anticipated.

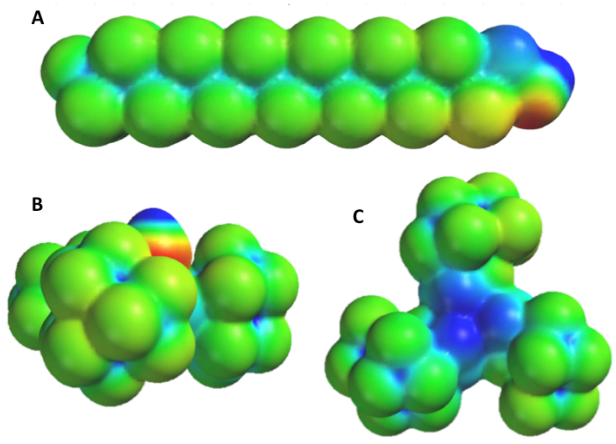

Figure 2.8 EPS calculated for linear and PFtB fluorous tails.
6-31G** electrostatic potential surfaces calculated with SPARTAN'10 software of **A**: Side-on view of linear F13 alcohol, **B**: PFtB-OH side-on view, and **C**: back-face view of PFtB-OH opposite the hydroxyl group. Values range from +150 kcal/mol to -150 kcal/mol, with red and blue signifying a value greater than or equal to the maximum in negative potential and positive potential, respectively.

The differences in fluorous tail packing suggested by EPS calculations were investigated via measurements of the microviscosity of the micelle core for both the $mPEG_{1k}$-$PFtB_{TRI}$ and the $mPEG_{1k}$-F13 by analyzing the fluorescence of an encapsulated P3P dye (**Table 2.2**). Other polymer series were not measured, as they did not form discrete and stable micelle assemblies. The microviscosity assay measures the ratio of the fluorescence intensity of the monomer and the eximer of an encapsulated dye. Higher microviscosity, or higher intensities of the monomer to eximer, results from a reduced mobility of the encapsulated probe and therefore indicates a more crystalline environment.

Table 2.2 Microviscosity of semifluorinated polymers.
Microviscosity of the polymer micelles was determined by fluorescence measurements of encapsulated P3P dye with error reported as STD. Higher values indicate higher microviscosity of the micelle core. $mPEG_{2k}$-DSPE is present as a reference compound.

Polymer	Microvisocsity
$mPEG_{1k}$-$PFtB_{TRI}$	5.2 ± 0.4
$mPEG_{1k}$-F13[25]	3.4 ± 0.2
$mPEG_{2k}$-DSPE[25]	5.6 ± 0.2

Again $mPEG_{2k}$-DSPE was analyzed as a reference compound. In comparison to the linear $mPEG_{1k}$-F13 polymer, the $PFtB_{TRI}$ polymer had a significantly higher microviscosity (**Table 2.2**). The bulky $PFtB_{TRI}$ disks may provide increased entanglement of the polymer chains to increase microviscosity in comparison to the linear tail of the $mPEG_{1k}$-F13.

Since these polymers were ultimately designed for *in vivo* drug delivery applications it was prudent to quickly and roughly assess the acute toxicity of these PFtB polymers. The PFtB polymers have proven efficient surfactants via CMC measurements and although the fluorous nature of the PFtB polymers should deter hemolytic behavior in comparison to hydrocarbon analogs it was still practical to assess the preliminary biocompatibility of the PFtB polymers. A hemolysis assay against rabbit red blood cells was performed with two representative polymers, $mPEG_{1k}$-$PFtB_{MONO}$ and $mPEG_{1k}$-$PFtB_{TRI}$ were exposed at 0.1, 1, and 10 mM over 3 h. The

polymers demonstrated less than 5 % lysis in comparison to the positive control of Milli-Q water. This demonstrates that these polymers are hemolytically safe and therefore are not restricted from further *in vitro* or *in vivo* applications.

2.4.5 Emulsions of sevoflurane anesthetic

The installation of the PFtB fluorous tail, when equipped with adequate fluorophilicity allowed for the formation of small, discrete micelle self-assemblies. Previous work with the linear PFC analogs of the PFtB polymers, mainly $mPEG_{1k}$-F13[1], demonstrated a unique ability of semifluorinated polymers to emulsify volatile fluorinated anesthetics. Stable emulsions of these anesthetics can be administered intravenously and have the potential to increase safety and reduce cost of anesthesia. Although the ability to form stable self-assemblies is not a requisite for suitable surfactant behavior as an emulsion, the similarities in micelle behavior between $mPEG_{1k}$-F13 and the $mPEG_x$-$PFtB_{TRI}$ polymers indicated substantial fluorophilicity of the PFtB tail, which could similarly be leveraged to stabilize fluorous emulsions. A 20 % v/v sevoflurane emulsion with 10 % v/v PFOB was prepared in the same manner as with previous $mPEG_{1k}$-F13 emulsions. The droplet size was measured over time and the Ostwald ripening rate monitored.

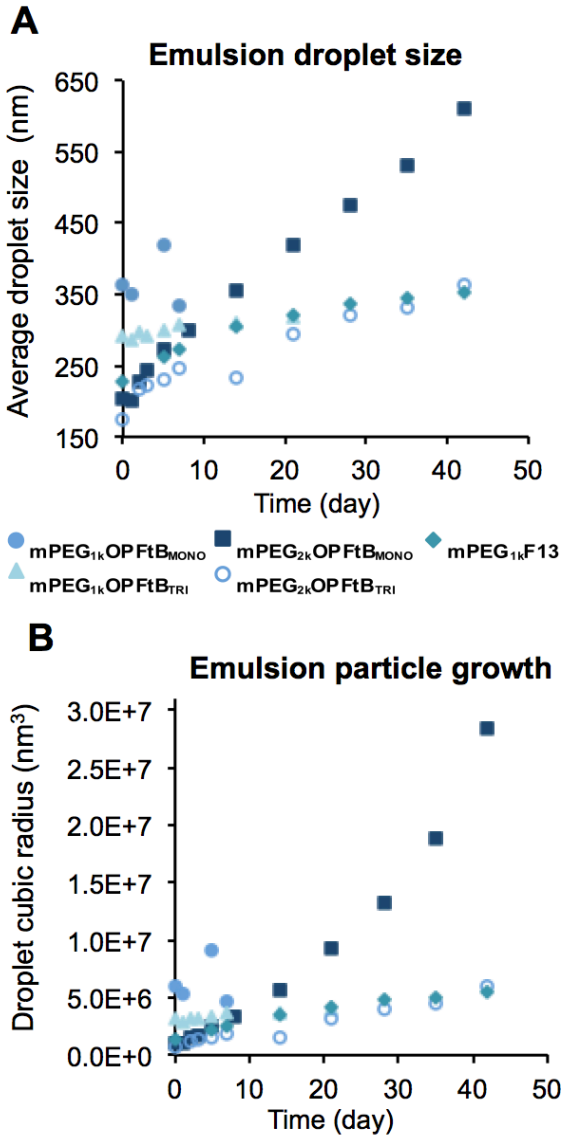

Figure 2.9 Fluorous sevoflurane emulsions' droplet size and growth rate.
A: Plot of emulsion average droplet size over time as measured by DLS. **B**: Plot of emulsion droplet size growth over time as measured by DLS. Linear growth of the cubic radius of the droplet over time indicates the droplets are undergoing Ostwald ripening. Note that not all polymers were measured over 50 days due to premature phase separation. In both graphs error bars are omitted for clarity.

Both $PFtB_{MONO}$ and $PFtB_{TRI}$ were able to form emulsions with high concentrations of fluorous anesthetics, yet only the latter was able to stabilize the particles over time (**Figure 2.9**). $PFtB_{MONO}$-polymer stabilized emulsion particles grew rapidly and led to phase separation within 3 - 42 days, depending on the mPEG length ($mPEG_{550}PFtB_{MONO}$ is not included in the plot as the

emulsion immediately began to phase separate, with droplet sizes well exceeding 1 micron). For the most successful $PFtB_{MONO}$ polymer, the average droplet size of the $mPEG_{2k}$-$PFtB_{MONO}$ emulsion began to grow rapidly after seven days post-formulation in a non-linear relation to the cubic-radius over time, possibly indicating a significant destabilization mechanism operating in conjunction with Ostwald ripening. Alternatively the $PFtB_{TRI}$ polymers maintained small droplet sizes and were more stable than their $PFtB_{MONO}$ counterparts by at least 2 weeks. There was also dependence on the mPEG length of the polymer, where $mPEG_{2k}$-PFtB polymers had smaller initial droplet sizes and were more resistant to phase separation. This is a crucial factor for intravenous delivery applications and for practical product shelf life.

The successful emulsification of sevoflurane by $PFtB_{TRI}$ polymers again demonstrates that despite the large structural differences between the linear F13 tail and the $PFtB_{TRI}$ tail, both the branched and linear fluorous polymers exhibit sufficient surfactant behavior to stabilize both micelle and emulsion formulations. However, the divergent effects must be noted from the mPEG length in the emulsion stability—$mPEG_{1k}$-F13 was the most stable F13 emulsion, while $mPEG_{2k}$-$PFtB_{TRI}$ was the most stable $PFtB_{TRI}$ emulsion—and the drastic difference in CMC between $mPEG_{1k}$-F13 and $mPEG_{1k}$-$PFtB_{TRI}$ (nearly an order of magnitude difference). These select instances of discrepancy, which arise despite the equivalency in number of fluorine atoms, suggests that an altered configuration of the fluorous tail may have significant impacts on the packing of the surfactants within the formulations (as suggested also by EPS calculations) and may be intensified with the installment of additional hydrophobic chains.

2.4.6 ^{19}F-MR imaging characterization

With the surfactant and drug formulation capabilities of the $mPEG_x$-$PFtB_{TRI}$ well established, the function of the fluorous tail as a ^{19}F-MRI tracer agent was investigated. For optimal signal intensity, the $mPEG_x$-$PFtB_{TRI}$ polymer was solely chosen for analysis, as these compounds had

the highest percent fluorine per molecule of the series and exhibited the best physicochemical nanoparticle characteristics. Preliminary relaxivity measurements in D_2O at 9.4 T showed that these polymers have one single, narrow ^{19}F resonance at approximately -70 ppm, and a half-width of approximately 15-25 Hz, arising from 27 equivalent ^{19}F atoms per molecule. These polymers also exhibited short T_1 values that provide quick recovery, increased scan efficiency for spin-density weighted images and show relatively long T_2 values that predict minimal decay in signal intensity over that scan time (**Table 2.3**). The characteristics of the $mPEG_x$-$PFtB_{TRI}$ polymers is in stark contrast with the $mPEG_{1k}$-F13 polymer, which as an aqueous assembly exhibits six ^{19}F signals that are extremely broadened to the point of almost complete signal nullification. In total, these results indicated that the $mPEG_x$-$PFtB_{TRI}$ polymers could feasibly serve as effective ^{19}F-MRI contrast agents due to their short T_1 times and single ^{19}F resonance, removing the need for spectroscopic imaging techniques.

Table 2.3 ^{19}F relaxivity measurements of $PFtB_{TRI}$ polymer in aqueous solution.
^{19}F relaxivity measurements in D_2O at 9.4 T above CMC concentration. $PFtB_{TRI}$ polymers exhibit ^{19}F-NMR characteristics amenable to ^{19}F-MR imaging: a single ^{19}F resonance, short T_1 values and relatively long T_2 values.

Polymer	T_1 (s)	T_2 (s)
$mPEG_{1k}$-$PFtB_{TRI}$	0.53 ± 0.01	0.11 ± 0.01
$mPEG_{2k}$-$PFtB_{TRI}$	0.49 ± 0.01	0.11 ± 0.01

The mPEG length had little effect on the T_2 values, indicating that both polymer tails had similar degrees of mobility. This enhanced mobility in comparison to linear fluorous tails in aqueous self-assemblies suggested that the non-linear structure of the PFtB group allows for enhanced mobility of the fluorous tail[27]. High mobility of the PFtB group in the assembled micelle is not in conflict with the microviscosity measurements discussed previously. The increased microviscosity of the $mPEG_{1k}$-$PFtB_{TRI}$ micelle core in comparison to the linear $mPEG_{1k}$-F13 micelle core was hypothesized to derive from restricted dynamics of the entire

unimer rather than the fluorous tail itself. Mobility of the PFtB group has been shown to be maintained even in crowded environments such as lipid-membrane bound states[23]. In the self-assembly these bulky fluorous tails exhibit adequate mobility, which is characteristic of a fluorous domain due to limited van der Waals interactions, and therefore maintain high signal intensity for NMR applications.

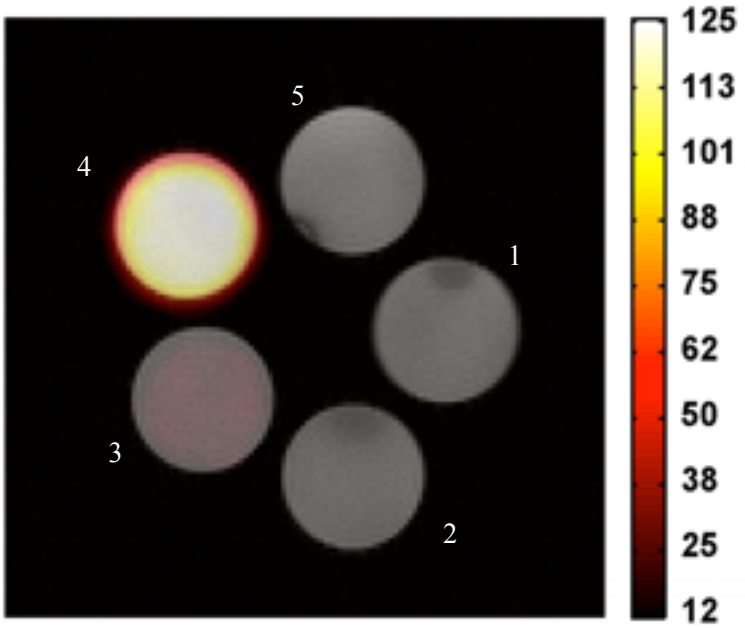

Figure 2.10 Fluorous PFtB polymer ^{19}F-MR imaging phantoms.
^{19}F-MR phantom images superimposed upon ^{1}H-MR images of $mPEG_{1k}$-$PFtB_{TRI}$ polymer solutions in Milipore water, with 25 min scan time, at 4.7 T and scaled according to SNR. From top center moving clock-wise: **5**) Blank (0 mM), **1**) 0.01 mM, **2**) 0.1 mM, **3**) 1 mM, and **4**) 5 mM. The 5 mM phantom shows strong signal while 1 mM demonstrates the current limit of detectability with the minimal imaging parameters used.

After these successful preliminary relaxivity measurements, the $mPEG_{1k}$-$PFtB_{TRI}$ phantoms, ranging in concentration from 0.01 mM to 5 mM, were imaged at 4.7 T (**Figure 2.10**). These polymer solution images show molecular ^{19}F images overlaid upon anatomical ^{1}H images. SNR was sufficient even at a molecular concentration of 1 mM, corresponding to a ^{19}F concentration of 27 mM, a high yet feasible concentration for *in vivo* accumulation of the labeled polymer

considering the low field strength and lack of sensitizers or signal enhancing sequences. Therefore the detection limit could be significantly lowered and the SNR could potentially be augmented with more efficient pulse sequences or higher field strengths[28]. Additionally, when all the echoes and slices are summed for the 5mM and 1mM phantoms, the relative intensity ratio between the two was calculated between 5.23:1 and 5.49:1. Since the images were performed as a spin-density weighted image (where TR>>T1 and TE < T2) then the theoretical intensity ratio should be 5:1. These results suggest that the quantification of polymer concentration from the ^{19}F-MRI is accurate to within 10 % of the actual concentration.

2.5 Conclusions

Semifluorinated surfactants with bulky PFtB tails have been prepared and shown to self-assemble into small, discrete, spherical micelles in aqueous solution. The $PFtB_{TRI}$ polymers and their linear counterpart, $mPEG_{1k}$-F13, both assemble into spherical micelles approximately 12 nm in size. However, the $PFtB_{TRI}$ polymer has a microviscosity that is approximately 1.5 times that of the linear $mPEG_{1k}$-F13. Although both polymers have the same mPEG length and the same number of fluorine atoms in their tail, the disk shape of the $PFtB_{TRI}$ tail appears to allow for an alternative packing of unimers in the micelle, resulting in a highly viscous core. The $mPEG_x$-$PFtB_{TRI}$ polymers were also able to stably emulsify 20 % v/v sevoflurane with 10 % v/v PFOB as an additive. This further demonstrates that despite the distinct tail structure, these polymers are effective surfactants.

PFtB fluorous tails not only engender stable self-assembly but may also serve as a ^{19}F-MRI contrast agents. $PFtB_{TRI}$ polymer micelles gave rise to a single, narrow ^{19}F-NMR signal in D_2O. These assemblies exhibit short T_1 and long T_2 values demonstrating their potential towards ^{19}F-MR imaging. Polymer phantoms show effective contrast as low as 1 mM molecular concentration, corresponding to 27 mM fluorine concentration. This preliminary data

demonstrates the multifunctional utility of the PFtB fluorous tail as both a stabilizing force in colloidal formulations and as a ^{19}F-MRI label, and therefore the potential for theranostic therapy.

2.6 Experimental

2.6.1 General materials and methods

1H,1H-perfluorotetradecanol was purchased from SynQuest Laboratories Inc. (Alachua, FL). Perfluoro-*tert*-butanol was purchased from Matrix Scientific (Columbia, SC). Rabbit red blood cells (10%, 15 mL) were purchased from Lampire Biological Laboratories Inc. (Pipersville, PA). All other reagents and solvents were purchased from Sigma Aldrich Co. (Milwaukee, WI) and used as received, unless otherwise specified. Small molecule and polymer chromatographic separations were performed using Silicycle 60 Å SiO_2 or using a Combi-flash Rf 200 (Teledyne ISCO, Lincoln, NE) equipped with ELSD for compound visualization using REDI-Sep Rf Gold high performance silica cartridges.

^{1}H, ^{19}F, and ^{13}C NMR spectra were obtained on Varian Unity-Inova 400 or Unity-Inova 500 spectrometers using $CDCl_3$ as the solvent with trimethylsilane (TMS) as an internal reference at 25 °C unless otherwise specified. Polymer purity was analyzed by HPLC with a Gilson 321 Pump (Middleton, WI) equipped with a Jordi Gel DVB 500 Å column (Bellingham, MA) and a Gilson Prep-ELSD and by MALDI-MS on a Bruker Ultraflex III MALDI TOF/TOF using α-cyano-4-hydroxycinnamic acid (CHCA) matrix unless otherwise specified.

2.6.2 Sevoflurane emulsion protocol

Polymer solutions were prepared by direct dilution of lyophilized solid in sterile, normal saline solution to a total volume of 11.9 mL. The solutions were sonicated until completely dissolved. A 3.4 mL volume of Sevoflurane from Abbott Labs (N. Chicago, IL) and 1.7 mL of perfluorooctyl bromide from SynQuest Laboratories, Inc. (Alachua, FL) were added to the polymer solution via a 1 mL Eppendorf pipet for a total volume of 17 mL. The high-speed

homogenizer (Power Gen 500) from Fisher Scientific (Hampton, NH) and the microfluidizer (model 110 S) from Microfluidics Corp. (Newton, MA) were first cleaned with 70 % and 100 % ethanol, followed by 70 % and 100 % methanol, and finally with three rinses of Millipore water. Once prepared the mixture was then homogenized with the high-speed homogenizer for 1 min at 21,000 rpm at room temperature. The crude emulsion was then microfluidized for 1 min at 5,000 psi with the cooling bath kept at 10 °C. The final emulsion was then filtered with a 30 mm dia., 0.45 μm nylon filter and stored in 45 mL plastic centrifuge tubes from Corning Inc. (Corning, NY) at 4 °C. After preparation and filtration of the emulsions, the emulsion droplet sizes were measured by dynamic light scattering using the Malvern Zetasizer Nanoseries Nano-ZS from Malvern (Westborough, MA). An aliquot of the emulsion, approximately 25 μL, was diluted in 3 mL of Milipore water to achieve an intensity factor range of 300-350. Each measurement was run for 5 minutes at room temperature and repeated in triplicate. The data was analyzed using Gaussian analysis and reported as a volume-weighted average diameter. The emulsion errors for all polymers were taken as an average of the standard deviations of each individual measurement. The standard deviation of the average error for the reported polymers was 14.73 nm (minimum error: 21.16 and maximum error: 71.68) with the exception of $mPEG_{2k}$-$PFtB_{MONO}$ (minimum error: 19.73 and maximum error: 246.64). The average particle size standard deviation was then used to determine the uncertainty in the Ostwald ripening rate data as follows:

$$OstwaldRipeningRate = \frac{dr^3}{dt}$$

$$F(r) = r^3$$

So if:

$$\sigma_{F(r)}^2 = \left(\frac{dF}{dr}\right)^2 \sigma_r^2 = \left(3r^2\right)^2 \sigma_r^2$$

Then:

$$\sigma_{F(r)} = 3r^2 \sigma_r$$

2.6.3 $mPEG_{1k}$-F13 emulsion calibration

Emulsion Preparation: The polymer solution was made by diluting 2.138 g of $mPEG_{1k}$-F13 in 120 mL of normal saline. This was heated and sonicated until completely dissolved. Once cooled to room temperature the solution was divided into 10 centrifuge tubes in 11.9 mL amounts. To this was added the appropriate amount of sevoflurane as listed above via 1 mL pipet. The homogenizer and microfluidizer were rinsed with 70% EtOH and then with a gradient of water and MeOH between each sample. The tubes were then each homogenized for 1 min. at 22,500 rpm and following, prepared in the microfluidizer at 5,000 psi for 1 min. From each emulsion 4 mL were transferred via 1 mL pipet to a pre-weighed vial and measured. This was repeated in triplicate for each percentage. The calibration curve is depicted below.

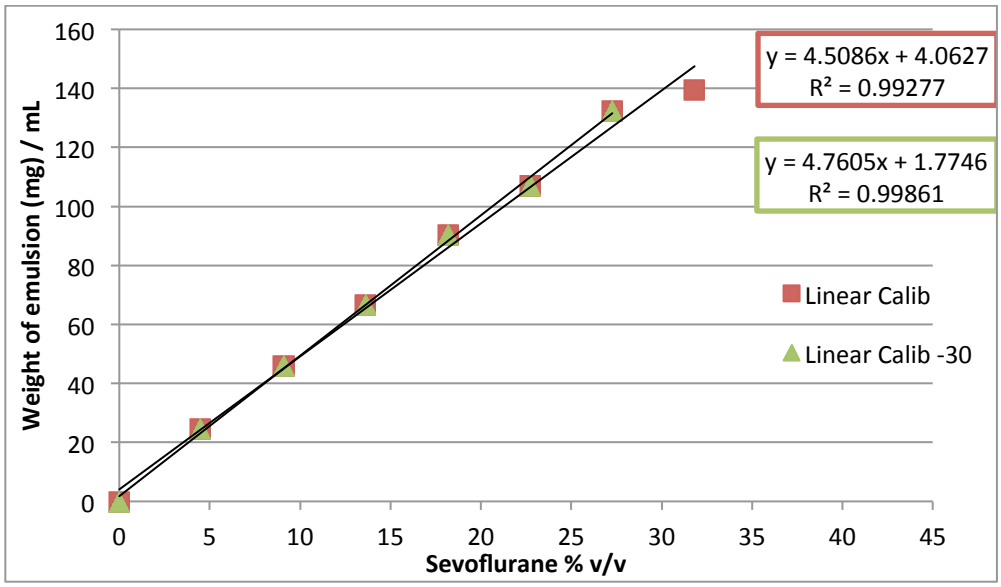

Emulsion weight per volume was plotted against theoretical sevoflurane concentration. Red squares indicate linear fit for sevoflurane concentration 0-30 % v/v. Green triangles indicate linear fit for sevoflurane concentration 0-25 % v/v (This showed a better fit due to phase separation that occurred with the 30 % v/v sample; "- 30"). This curve serves as a calibration

curve to compare the desired sevoflurane content to the calculated content by weight to evaluate variability between operators.

Comparison between operators gave an average standard deviation over all concentrations between 0-20 % v/v sevoflurane of 5.3 mg/mL. A 20 % v/v emulsion used in a previous *in vivo* assay weighed 97.86 mg/mL, which correlates to 20.2 % v/v sevoflurane as calculated from the calibration curve using data from 0-30 % v/v sevoflurane. (Points from 35-40% sevoflurane do not give a linear relationship as they had mostly likely begun to phase separate when the aliquot was taken (and so were not homogeneous). Additionally, when each emulsion formulation was measured via DLS there was no significant change in particle size depending on the operator (as plotted for 20 % v/v sevoflurane).

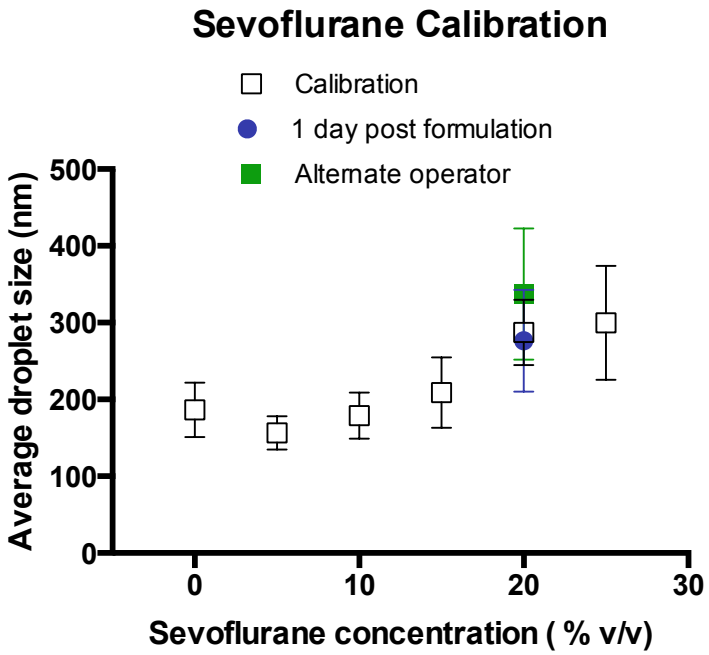

2.6.4 Synthesis of mPEG$_x$-PFtB$_y$ polymers

"mPEG$_x$-OMs" monomethyl-polyethyleneoxide mesylate. In a typical reaction, to a solution of mPEG$_x$-OH (2.5 mmol) in DCM (anhydrous, 30 mL) under argon was syringed triethylamine (0.87 mL, 6.25 mmol), followed by MsCl (0.39 mL, 5 mmol). The solution was stirred as it

warmed to room temperature and was allowed to stir overnight. After this time, the reaction mixture was washed with NH_4Cl_{aq} (2 x 50 ml), brine (50 ml), dried over $MgSO_4$, filtered, and the solvent reduced to 10 mL *in vacuo*. The product was precipitated with diethyl ether at 0 °C (~250 mL) and collected by filtration. The precipitate was redissolved in DCM (50 mL) and the volume was reduced to ~10 mL *in vacuo*. Benzene was added to the solution (~10 mL), which was then frozen in an acetone/dry ice bath and dried overnight *in vacuo*. Note one must keep the polymer cold and work quickly with smaller mPEG polymers, which have low melting points. ***mPEG$_{550}$-OMs****:* Yield 85%. ^{1}H NMR ($CDCl_3$, 400 MHz): δ 4.39-4.37 (m, 2H), 3.83-3.81 (m, 1H), 3.78-3.76 (m, 2H), 3.64 (m, 47H), 3.56-3.54 (m, 2H), 3.47 (m, 1H), 3.38 (s, 3H), 3.09 (s, 3H). ***mPEG$_{1k}$-OMs****:* Yield 94%. ^{1}H NMR ($CDCl_3$, 400 MHz): δ 4.39-4.37 (m, 2H), 3.83-3.81 (m, 1H), 3.78-3.75 (m, 2H), 3.64 (m, 89H), 3.56-3.54 (m, 2H), 3.48-3.45 (m, 1H), 3.38 (s, 3H), 3.09 (s, 3H). ***mPEG$_{2k}$-OMs****:* Yield quantitative. ^{1}H NMR ($CDCl_3$, 400 MHz): δ 4.39-4.37 (m, 2H), 3.83-3.81 (m, 2H), 3.78-3.76 (m, 4H), 3.64 (m, 160H), 3.56-3.54 (m, 2H), 3.48-3.45 (m, 2H), 3.38 (s, 3H), 3.08 (s, 3H).

"KOPFtB" Potassium perfluoro-*tert*-butoxide. According to procedure by Rábai *et al*.,[19] KOH was diluted in 25 mL of deionized water (6.542 g, 0.12 mol) and to this solution was added (25.01 g, 0.11 mol) perfluoro-*tert*-butyl alcohol with stirring at 0°C. The reaction was allowed to stir for 3 h, after which the reaction mixture stirred for an additional 30 min at room temperature. The pH of the clear reaction mixture was confirmed to be < 8 and then concentrated *in vacuo*. The white solid was allowed to dry in a desiccator over drierite for two days with a quantitative yield (note that residual KOH may still be present). $^{13}C\{^1H\}$ NMR ($CDCl_3$, 101 MHz): δ 123.1 (q, J = 294.8 Hz, (CF_3), 79.8 (decet, J = 29.9Hz ($C(CF_3)_3$), 68.8 (CH_2), 68.5 (CH). ^{19}F NMR (376 MHz, $CDCl_3$): δ -75.28 (s).

"$PFtB_{MONO}$" series synthesis: $mPEG_x$-$PFtB_{MONO}$. In a typical reaction, to a solution of $mPEG_x$-OMs (0.48 mmol) in dioxane (2.5 mL), KPFtB (0.72 mmol) was added. The reaction mixture was stirred under Ar at 90 °C for 2 h. The reaction was monitored by HPLC and once complete the reaction was cooled to room temperature. The reaction mixture was taken up in DCM, quenched and washed with sat. NH_4Cl_{aq}, dried over $MgSO_4$, and the solvent was reduced *in vacuo*. The product was then precipitated from the organic phase with ether at 0°C and isolated by filtration. The solid was dissolved in 5 mL of DCM and 5 mL of benzene was added, which was then frozen in a dry-ice/acetone bath and dried overnight *in vacuo*. **$mPEG_{550}$-$PFtB_{Mono}$**: Yield 81 %. ^{1}H NMR ($CDCl_3$, 400 MHz): δ 4.15 (t, *J* = 4.8Hz, 2H), 3.83-3.82 (m, 1H), 3.73 (t, J = 5.2Hz, 2H), 3.64 (m, 58H), 3.59 (s, 1H), 3.55-3.54 (m, 2H), 3.47-3.45 (m, 1H), 3.38 (s, 3H). ^{19}F NMR (376 MHz, $CDCl_3$): δ -70.78 (s). MALDI MS Performed on a Fourier Transform Mass Spectrometer (Varion-902 MS) equipped with MALDI. $[M+Na]^+$ calcd. for $C_{35}H_{63}F_9O_{16}Na^+$ = 933.39; found: 933.37. **$mPEG_{1k}$-$PFtB_{Mono}$**: Yield 71 %. ^{1}H NMR ($CDCl_3$, 400 MHz): δ 4.15 (t, *J* = 4.8Hz, 2H), 3.83-3.81 (m, 1H), 3.74-3.72 (m, 2H), 3.64 (m, 90H), 3.55 (m, 2H), 3.48-3.45 (m, 1H), 3.38 (s, 3H). ^{19}F NMR (376 MHz, $CDCl_3$): δ -70.78 (s). MALDI MS: $[M+Na]^+$ calcd. for $C_{49}H_{91}F_9O_{23}Na^+$ = 1241.57; found: 1241.5. **$mPEG_{2k}$-$PFtB_{Mono}$**: Yield 70 %. ^{1}H NMR ($CDCl_3$, 400 MHz): δ 4.15 (t, *J* = 4.8Hz, 2H), 3.83-3.81 (m, 1H), 3.74-3.72 (m, 3H), 3.64 (m, 160H), 3.56-3.54 (m, 2H), 3.48-3.45 (m, 1H), 3.38 (s, 3H). ^{19}F NMR (376 MHz, $CDCl_3$): δ -70.78 (s). MALDI MS: $[M+Na]^+$ calcd. for $C_{95}H_{183}F_9O_{46}Na^+$ = 2254.17; found: 2255.9.

^{1}H-NMR ($CDCl_3$, 400 MHz)

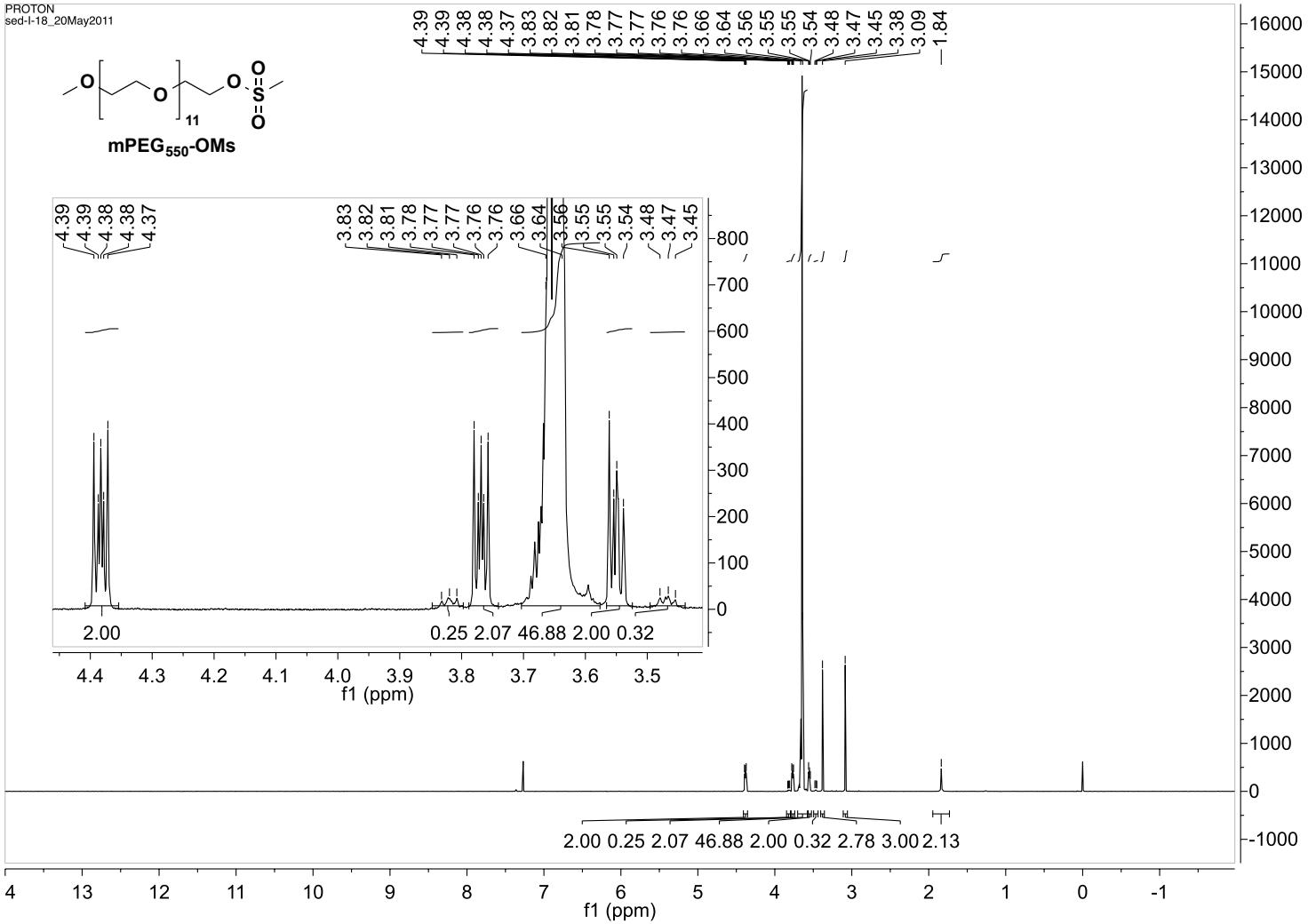

^{1}H-NMR ($CDCl_3$, 400 MHz)

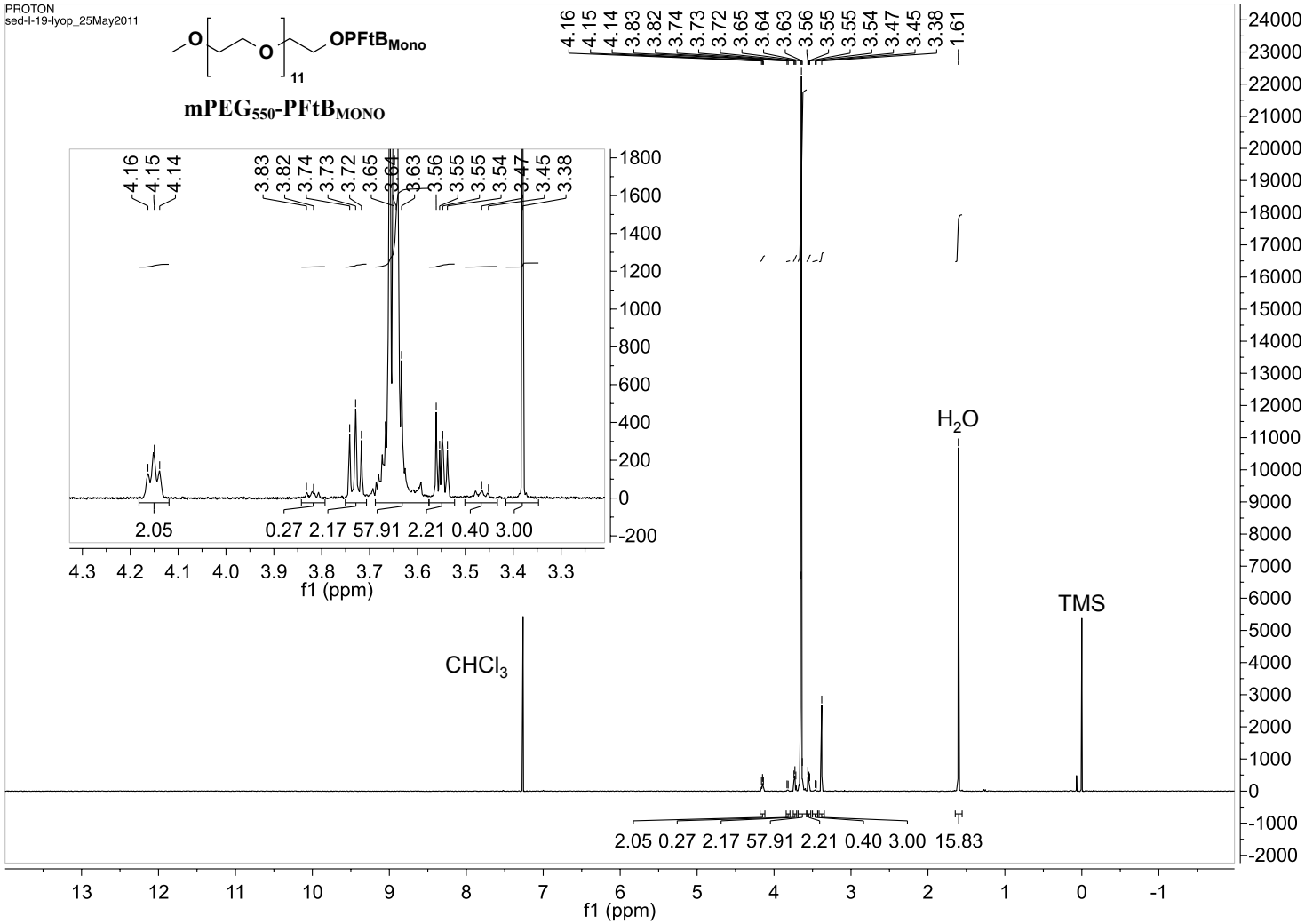

^{19}F-NMR ($CDCl_3$, 376 MHz)

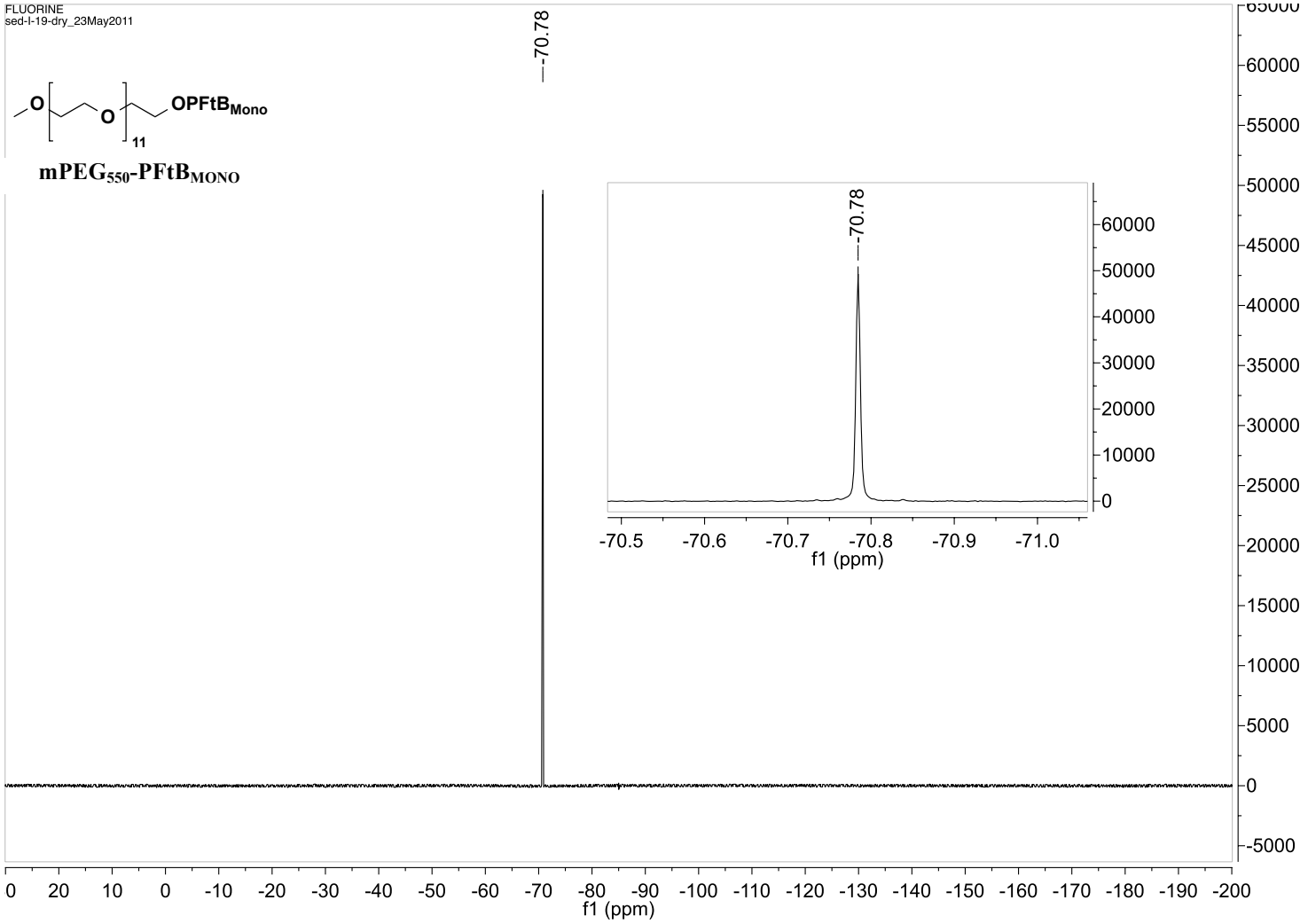

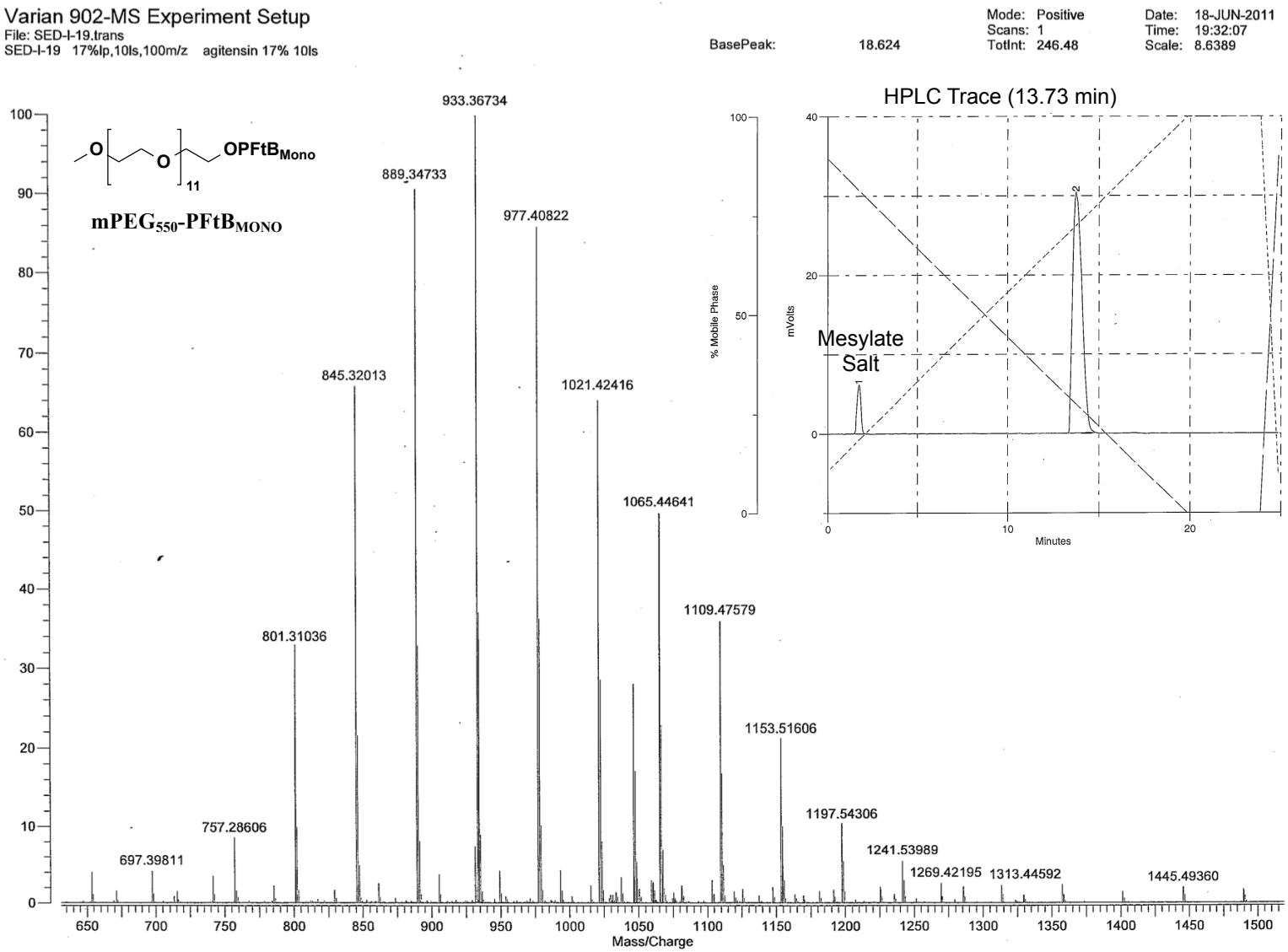
Varian 902-MS Experiment Setup
File: SED-I-19.trans
SED-I-19 17%Ip,10Is,100m/z agitensin 17% 10Is
BasePeak: 18.624
Mode: Positive
Scans: 1
TotInt: 246.48
Date: 18-JUN-2011
Time: 19:32:07
Scale: 8.6389
O
O
OPFtB$_{Mono}$
11
mPEG$_{550}$-PFtB$_{MONO}$
933.36734
889.34733
977.40822
845.32013
1021.42416
1065.44641
1109.47579
801.31036
1153.51606
757.28606
1197.54306
697.39811
1241.53989
1269.42195
1313.44592
1445.49360
Mass/Charge
% Mobile Phase
HPLC Trace (13.73 min)
mVolts
Mesylate
Salt
Minutes

^{1}H-NMR ($CDCl_3$, 400 MHz)

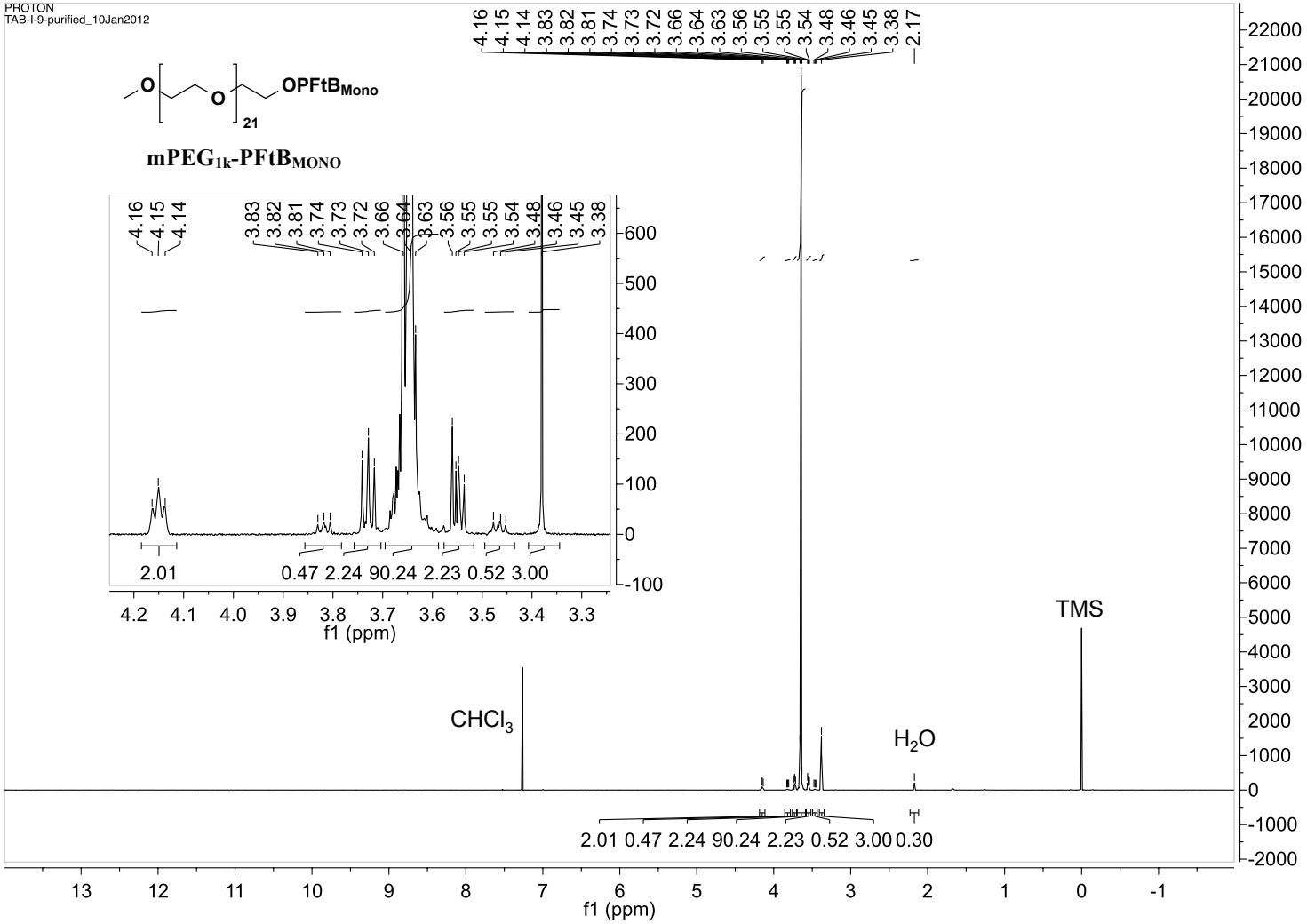

^{19}F-NMR ($CDCl_3$, 376 MHz)

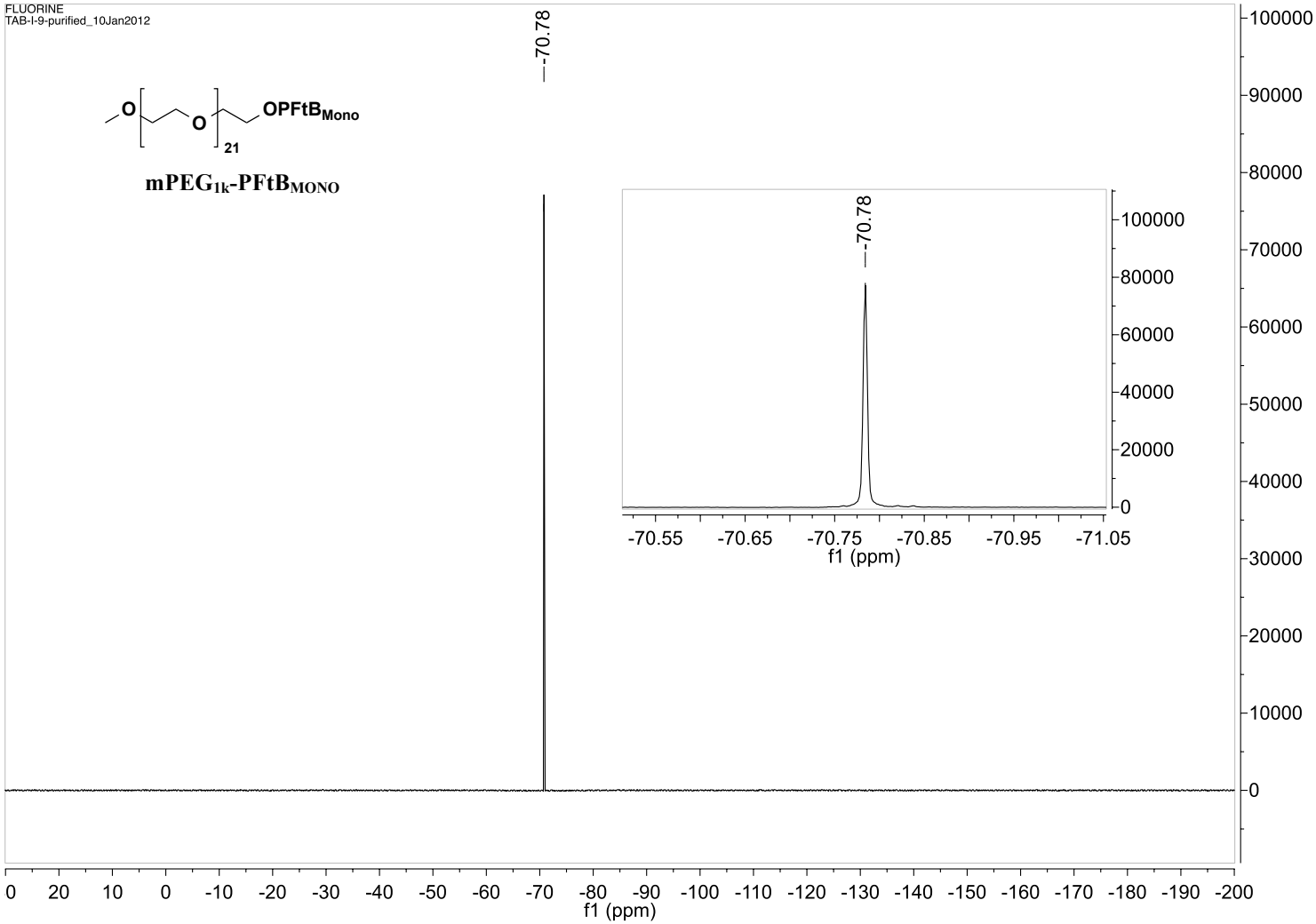

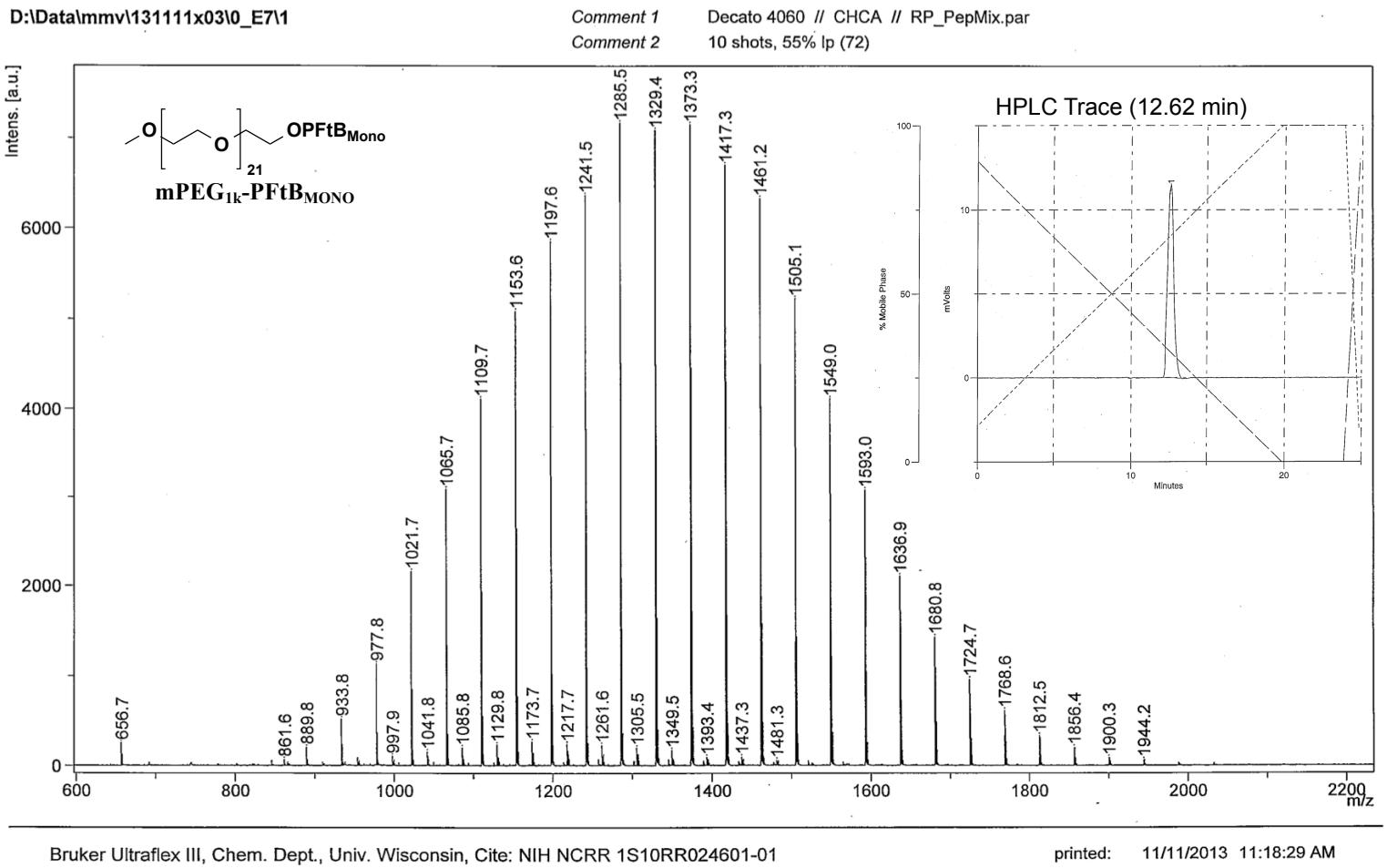
D:\Data\mmv\131111x03\0_E7\1
Comment 1 Decato 4060 // CHCA // RP_PepMix.par
Comment 2 10 shots, 55% lp (72)
Intens. [a.u.]
OPFtB Mono
21
mPEG1k-PFtBMONO
HPLC Trace (12.62 min)
% Mobile Phase
mVolts
Minutes
656.7
861.6
889.8
933.8
977.8
997.9
1021.7
1041.8
1065.7
1085.8
1109.7
1129.8
1153.6
1173.7
1197.6
1217.7
1241.5
1261.6
1285.5
1305.5
1329.4
1349.5
1373.3
1393.4
1417.3
1437.3
1461.2
1481.3
1505.1
1549.0
1593.0
1636.9
1680.8
1724.7
1768.6
1812.5
1856.4
1900.3
1944.2
m/z
Bruker Ultraflex III, Chem. Dept., Univ. Wisconsin, Cite: NIH NCRR 1S10RR024601-01
printed: 11/11/2013 11:18:29 AM

^{1}H-NMR ($CDCl_3$, 400 MHz)

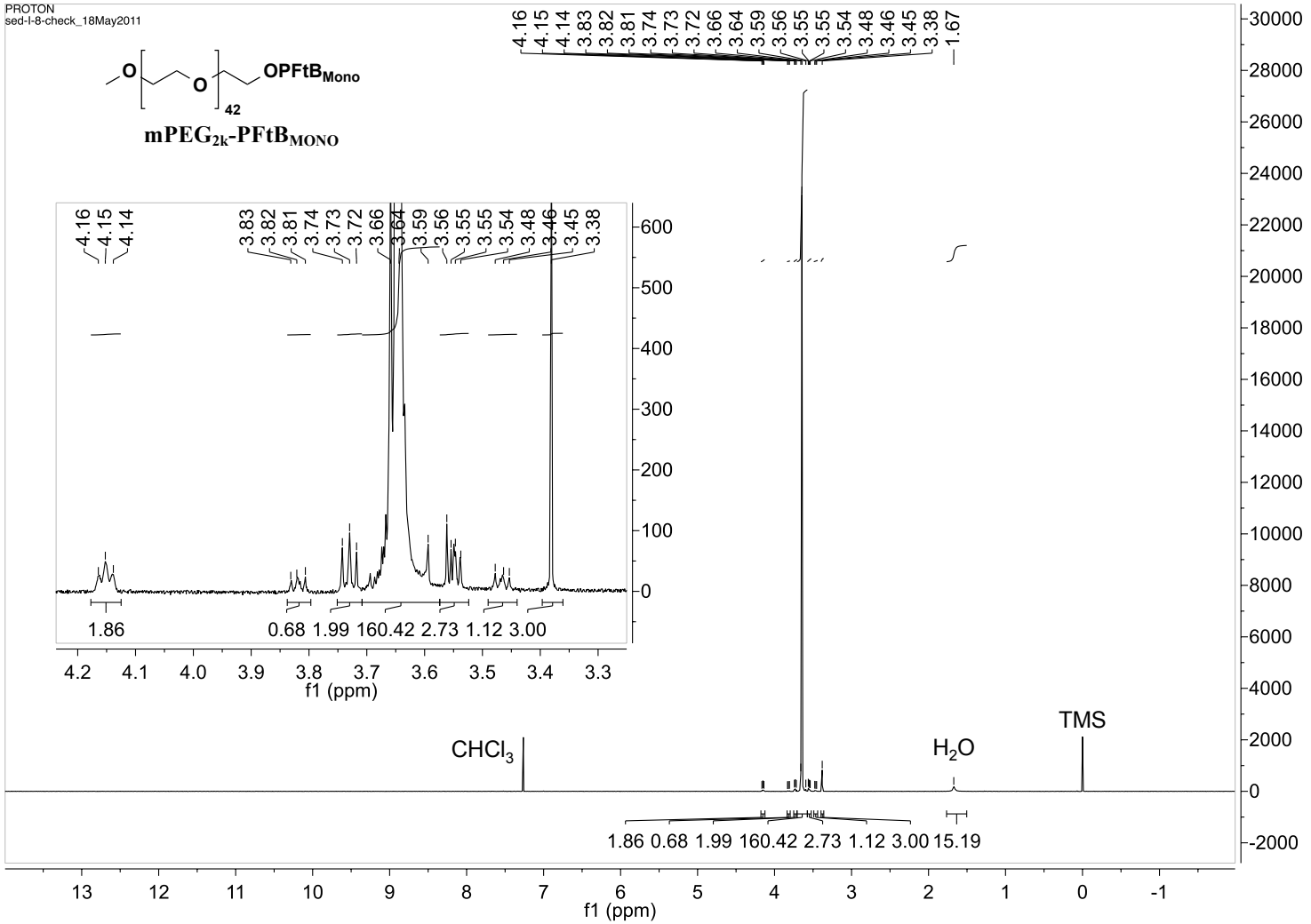

^{19}F-NMR ($CDCl_3$, 376 MHz)

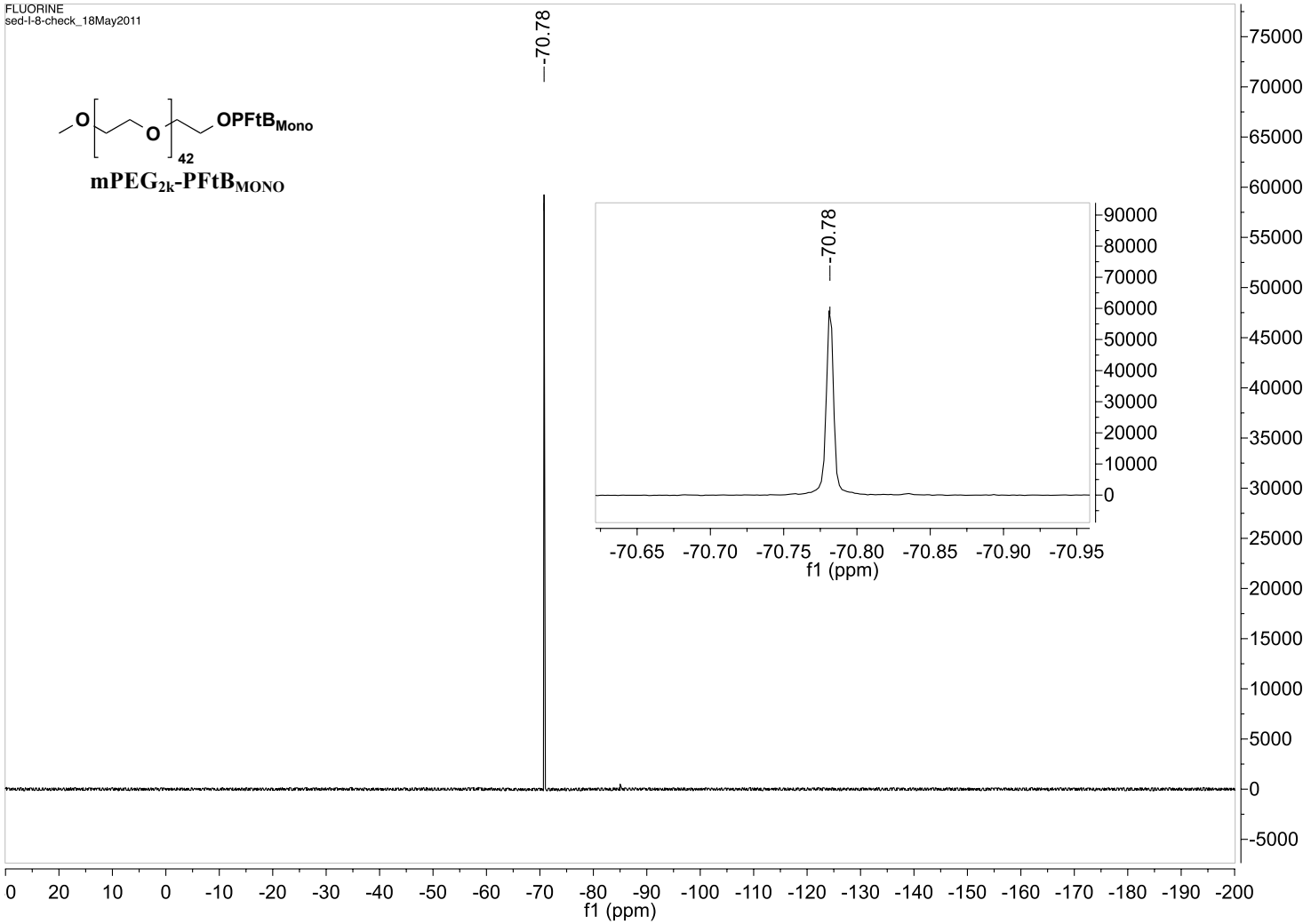

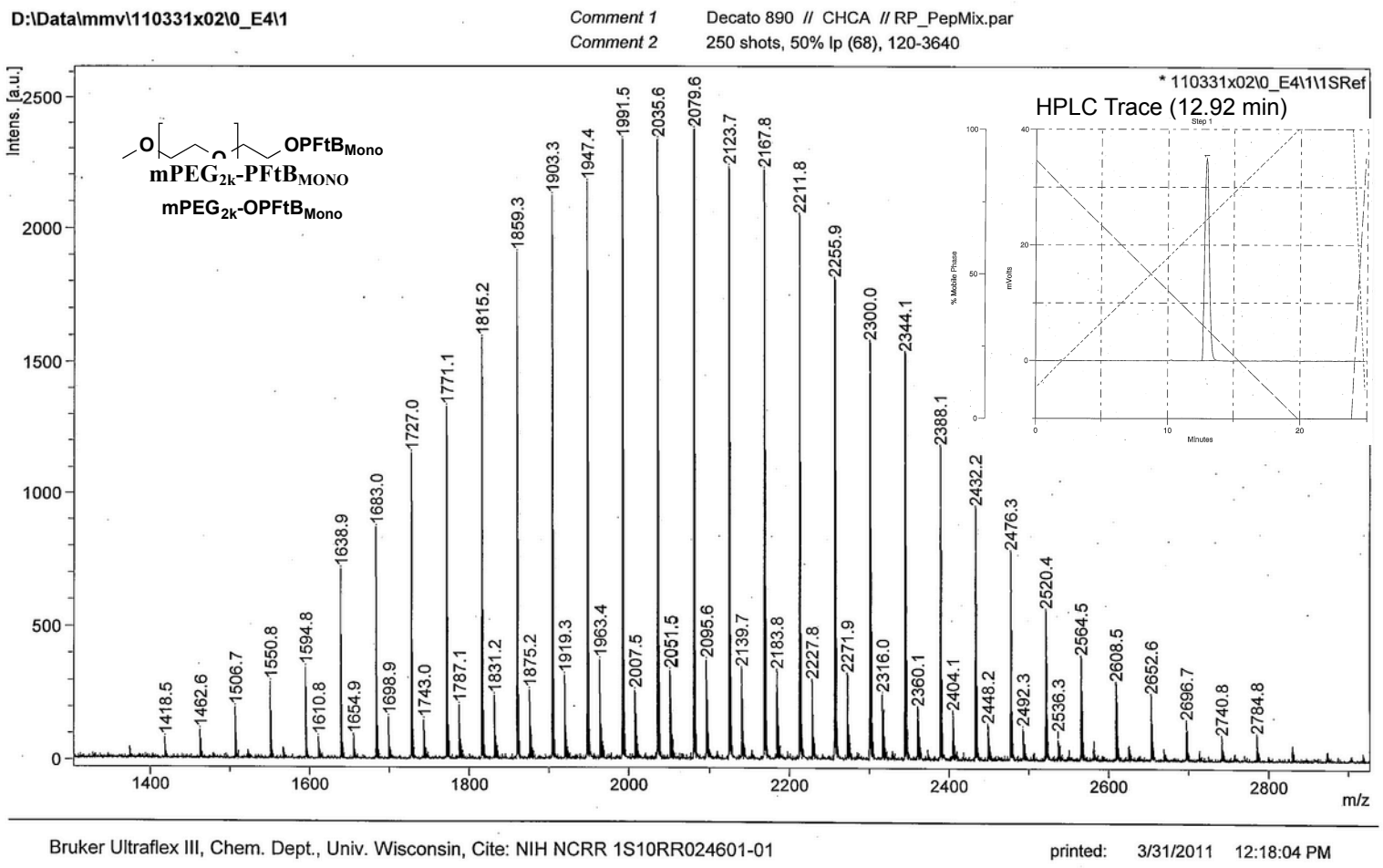
D:\Data\mmv\110331x02\0_E4\1
Comment 1 Decato 890 // CHCA // RP_PepMix.par
Comment 2 250 shots, 50% Ip (68), 120-3640
* 110331x02\0_E4\1\1SRef
HPLC Trace (12.92 min)
mPEG2k-PFtBMONO
mPEG2k-OPFtBMono
OPFtBMono
Intens. [a.u.]
m/z
Minutes
% Mobile Phase
mVolts
Bruker Ultraflex III, Chem. Dept., Univ. Wisconsin, Cite: NIH NCRR 1S10RR024601-01
printed: 3/31/2011 12:18:04 PM

"$PFtB_{DI}$-OH"1,3-bis(1,1,1,3,3,3-hexafluoro-2-(trifluoromethyl)propan-2-yloxy)propan-2-ol. According to Nemes *et al*.[20], a stirred mixture of 1,3- dribromopropan-2-ol (0.39 mL, 3.95 mmol) and potassium perfluoro-*tert*-butoxide (2.64 g, 9.64 mmol) in dry DMF (10 mL) was heated to 120 °C under argon for 20 h. Water (20 mL) and ether (10 mL) were added, and the aqueous phase was separated and extracted with ether. The organic layers were then combined, washed with water, dried over $MgSO_4$, and filtered. The solvent was removed *in vacuo* and the residue was distilled to afford the product as a colorless, viscous oil (bp 74-79 °C/2.67kPa) with a yield 56 %. ^{1}H NMR ($CDCl_3$, 400 MHz): δ 4.13 - 4.06 (m, 5H), 2.50 (bs, 1H, OH). $^{13}C\{^1H\}$ NMR (CDCl3, 101 MHz): δ 120.3 (q, J = 294.8 Hz, (CF_3), 79.8 (decet, J = 29.9Hz ($C(CF_3)_3$), 68.8 (CH_2), 68.5 (CH). ^{19}F NMR ($CDCl_3$, 376 MHz): δ -71.40 (s).

"$PFtB_{DI}$" series synthesis. $mPEG_x$-$PFtB_{DI}$: In a typical reaction, at 0 °C was added NaH (3.78 mmol) to a suspension of $PFtB_{DI}$-OH (1.9 mmol) in 15 mL of dry THF under argon. This was allowed to stir for 30 min at 0 °C. After this time, $mPEG_x$-OMs (1.26 mmol) was added at 0 °C. The reaction mixture was allowed to stir as the mixture warmed slowly to room temperature. The reaction mixture was then refluxed until determined to be complete by HPLC. The reaction mixture was then diluted with DCM, quenched and washed with sat. NH_4Cl_{aq}, dried over $MgSO_4$, and concentrated to 10 mL *in vacuo*. The crude product was then precipitated from the organic phase with ether in a dry-ice/acetone bath. The solid was isolated by filtration and then dissolved in 5 mL of DCM. Benzene (5 mL) was added, which was then frozen in dry-ice/acetone bath and dried overnight *in vacuo.* The crude product was purified using the Combi-flash purification system with a C-18 reverse phase Silica column using a water/MeOH (0.1% FA) to DCM/MeOH gradient. The reaction mixtures containing $mPEG_x$-$PFtB_{DI}$ and $mPEG_x$-$PFtB_{MONO}$ could not be purely resolved.

Separation of the two major products from $mPEG_{1k}$-$PFtB_{DI}$ synthesis: After extraction and precipitation from ether the $mPEG_{1k}$-$PFtB_{DI}$ crude product was dissolved in DCM and loaded onto a pre-packed celite cartridge. The compounds were eluted using the Combi-Flash system equipped with a C-18 gold column with a 0.1% Water/MeOH to DCM/MeOH gradient.

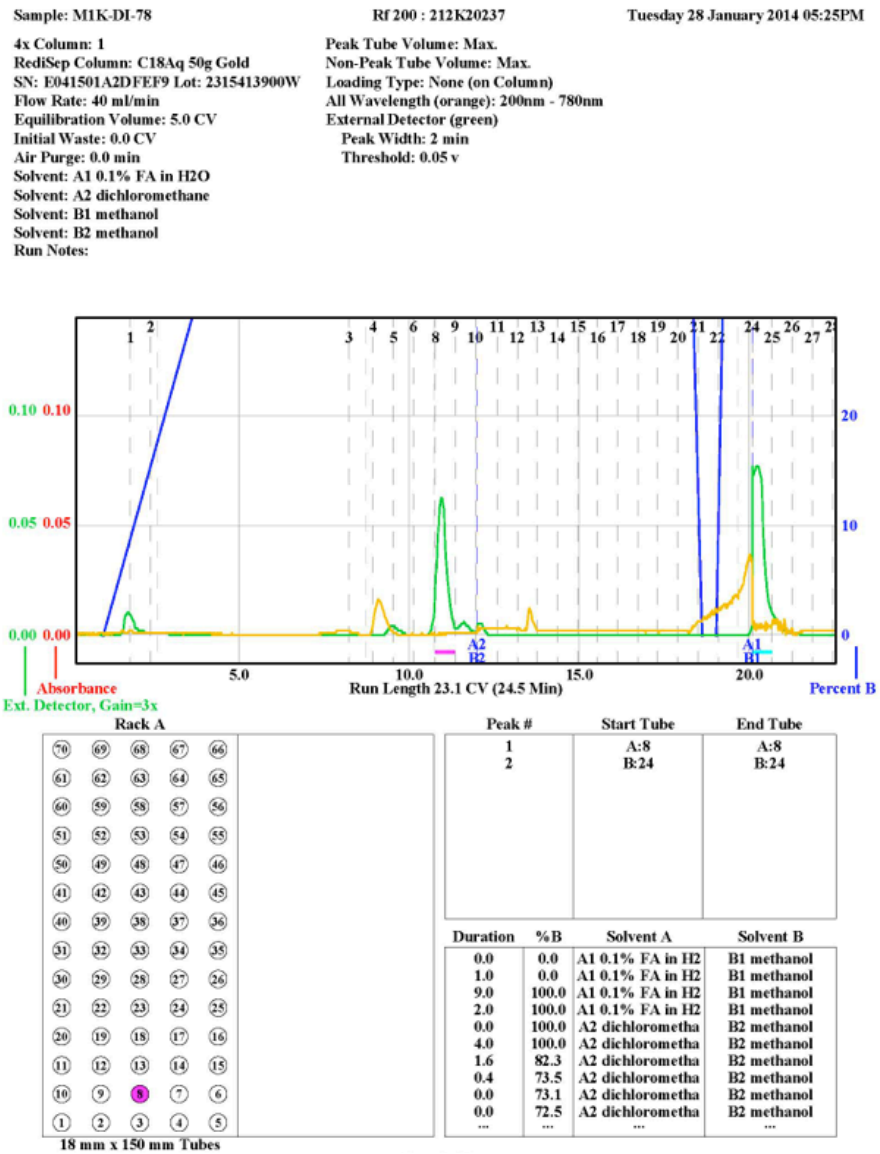

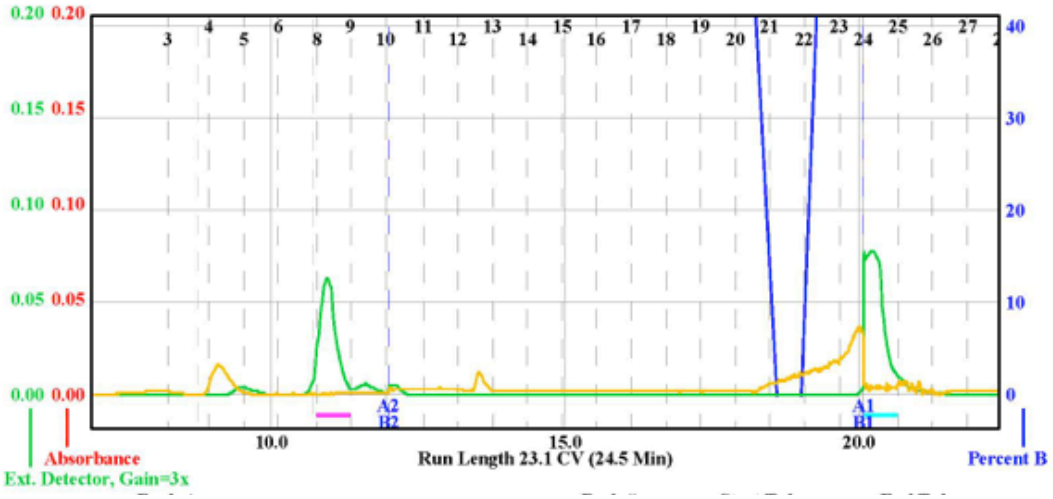

Column fraction 4+5, 8, 9, 10, and 23+24 were collected separately, reduced under vacuum, and analyzed by NMR. Fraction 4-5 contained unreacted $mPEG_{1k}$-OMs. Only fractions 8 and 9 showed PEGylated, fluorous compounds. Fraction 8 and 9 were extremely similar by ^{1}H-NMR except for the slight shift in the triplet around 4 ppm. However, the ^{19}F-NMR showed a clear shift between the two compounds and also revealed that the two compounds had not been completely separated during flash chromatography. To determine the identity of each fraction, the compounds were analyzed via MALDI-MS, which revealed that the major product (fraction 8) was actually $mPEG_{1k}$-$PFtB_{MONO}$ and the minor product (fraction 9) was the desired product $mPEG_{1k}$-$PFtB_{DI}$. From the ^{19}F-NMR the ratio of MONO:DI is approximately 9:1.

^{1}H-NMR: (top – "combi_2", fraction 8 (Combi-flash), mPEG$_{1k}$-PFtB$_{MONO}$, middle – "check", Precipitated mixture pre-Combi-flash, bottom – "combi_3", fraction 9 (Combi-flash), mPEG$_{1k}$-PFtB$_{DI}$)

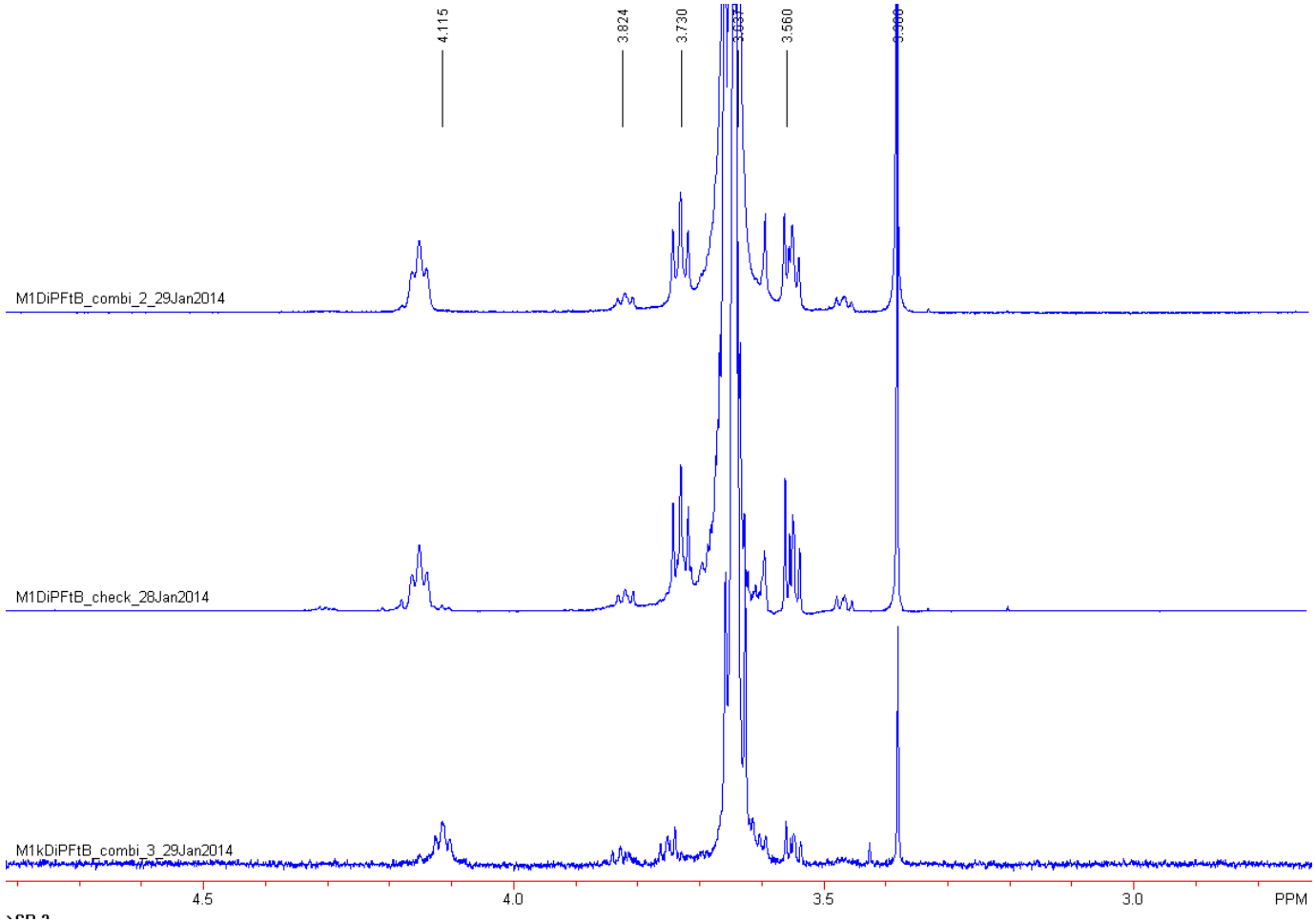

^{19}F-NMR: (top – fraction 8 ($mPEG_{1k}$-$PFtB_{MONO}$), middle – mixture, bottom – fraction 9 ($mPEG_{1k}$-$PFtB_{DI}$))

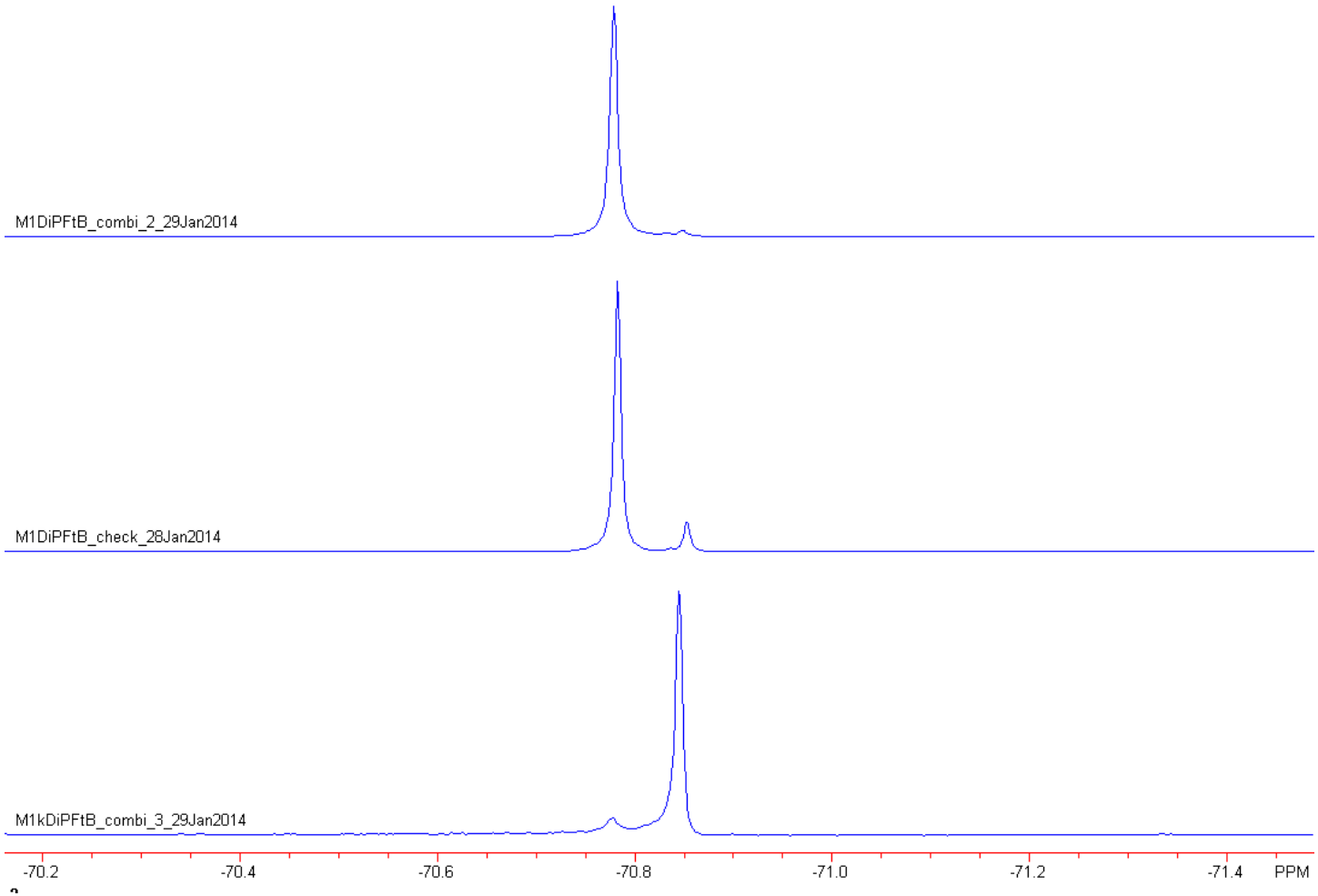

MALDI-MS: fraction 8 ($mPEG_{1k}$-$PFtB_{MONO}$)

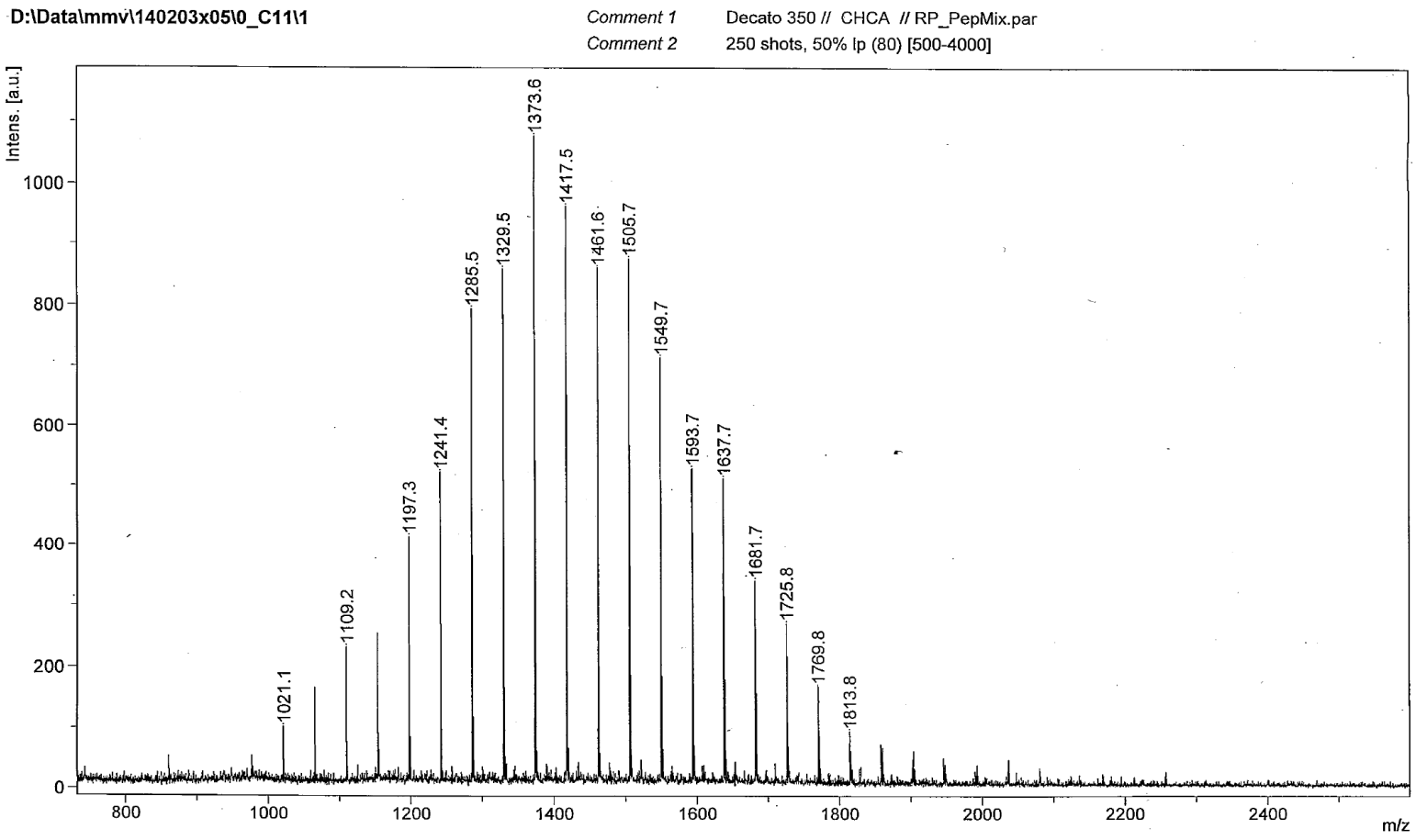

MALDI-MS: fraction 9 ($mPEG_{1k}$-$PFtB_{DI}$)

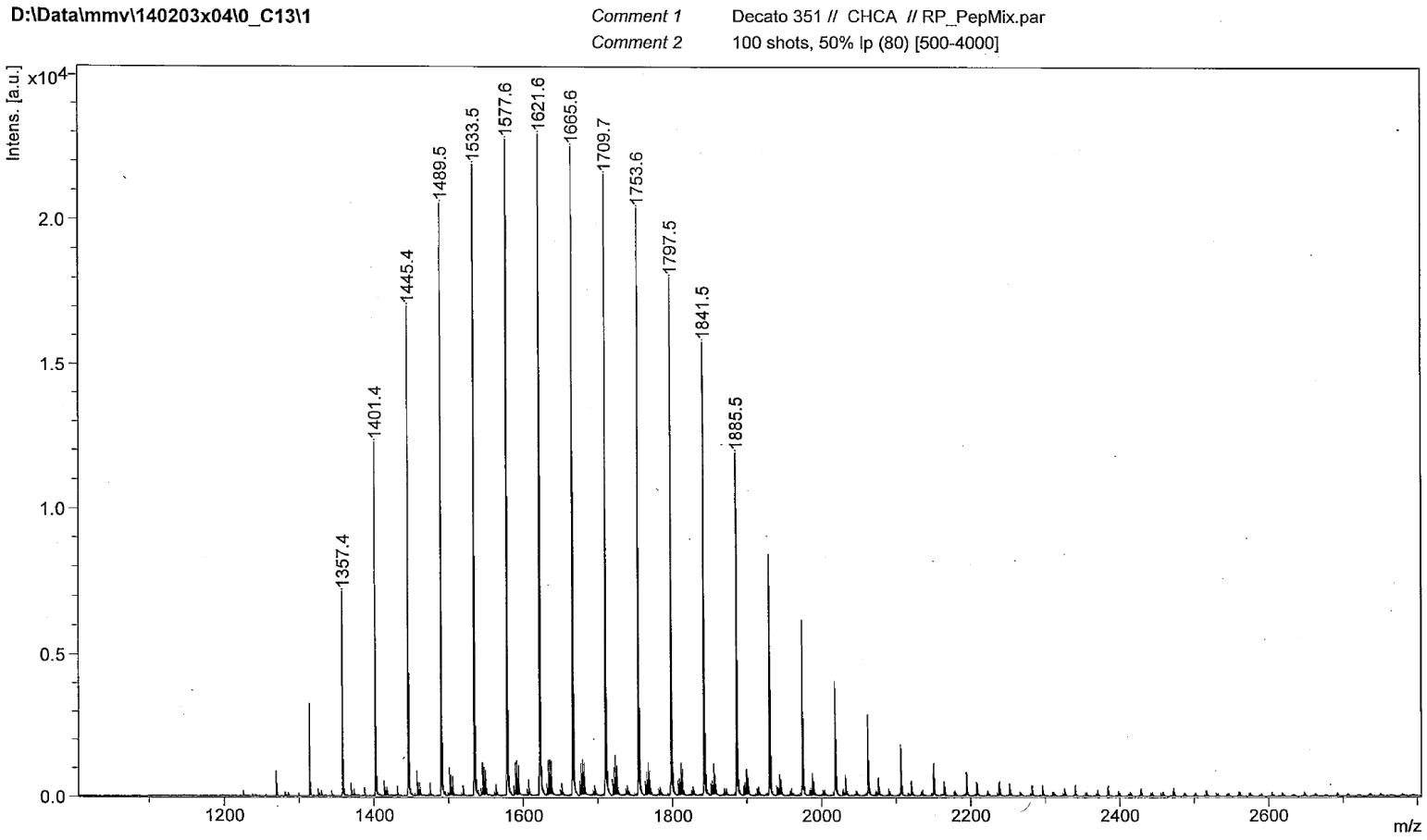

(1-methyl-2,6,7-trioxa-bicyclo[2.2.2]octan-4-yl)methanol (2.1). Synthesis was performed according to the procedure from Yu *et al.*[15] with minor modifications as described by Grubbs *et al.*[29] In a typical reaction, pentaerythritol (1.98 g, 14.5 mmol) and *p*-toluenesulfonic acid (28 mg, 0.15 mmol) were combined and suspended in 25 mL of dry toluene and heated to reflux (~125 °C) with a dean stark trap and condenser under Ar. To the refluxing reaction mixture was added triethylorthoacetate (2.7 mL, 14.7 mmol). The reaction mixture was allowed to reflux for approximately 24 h until the solution became clear with no visible solid particles. Once complete, 8 drops of triethylamine were added and the reaction mixture was filtered while hot. The solution was then concentrated *in vacuo* with a quantitative yield. ^{1}H NMR ($CDCl_3$, 400 MHz): δ 4.00 (s, 6H, CH_2), 3.44 (d, J = 4.8Hz, 2H, CH_2), 1.73 (t, J = 4.8Hz, 1H, OH), 1.44 (s, 3H, CH_3). ^{13}C{^{1}H} NMR ($CDCl_3$, 101 MHz): δ 108.9, 69.4, 61.4, 35.6, 23.3.

2-(hydroxymethyl)-2-(((4-methoxybenzyl)oxy)methyl)propane-1,3-diol (2.2). In a typical reaction, KOH pellets were crushed to a powder (2.929 g, 51.45 mmol) and added to stirring dry DMSO (20 mL) at room temperature. The suspension was allowed to stir for 5 min. Then **1** was added (1.648 g, 10.29 mmol) followed quickly by *p*-methoxybenzyl chloride (2.06 mL, 15.22 mmol). The reaction mixture was allowed to stir for 2.5 h. The reaction mixture was then diluted with water (100 mL) and extracted with diethyl ether, washed with brine and water, dried over $MgSO_4$, and concentrated to a white solid *in vacuo*. The residue was dissolved in methanol (40 mL) and treated with 0.01 M HCl (26 mL) at room temperature and was allowed to stir for 1 h. To this was then added 0.967 g of $NaHCO_3$ and was stirred for an additional 1 h. The reaction mixture was then concentrated *in vacuo*. To the residue was added 5 mL of MeOH and filtered. The oil was collected and concentrated *in vacuo*. The residue was purified by flash chromatography on silica gel with 10:6:1 EtOAc:Cyclohexane:MeOH to yield 53 %. ^{1}H NMR ($CDCl_3$, 400 MHz): δ 7.23 (d, J = 8.8 Hz, 2H), 6.89 (d, J = 8.8 Hz, 2H), 4.44 (s, 2H), 3.81 (s,

3H), 3.71 (s, 6H), 3.48 (s, 2H), 2.52 (bs, 3H, OH). $^{13}C\{^{1}H\}$ NMR ($CDCl_3$, 101 MHz): δ 159.5, 130.0, 129.5, 114.1, 73.6, 72.2, 64.2, 55.5, 45.3.

^{1}H-NMR ($CDCl_3$, 400 MHz)

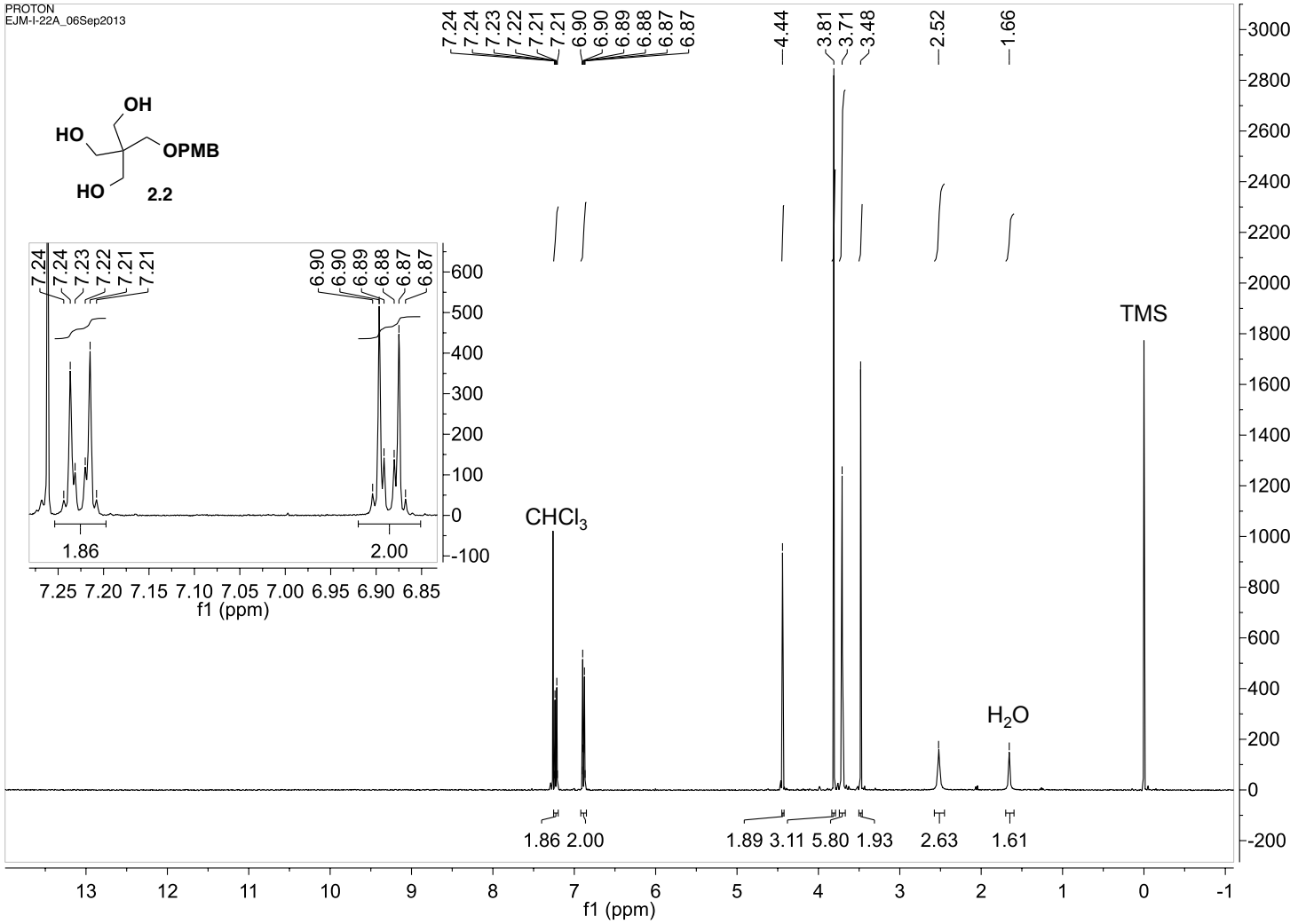

$^{13}C\{^{1}H\}$-NMR ($CDCl_3$, 101 MHz)

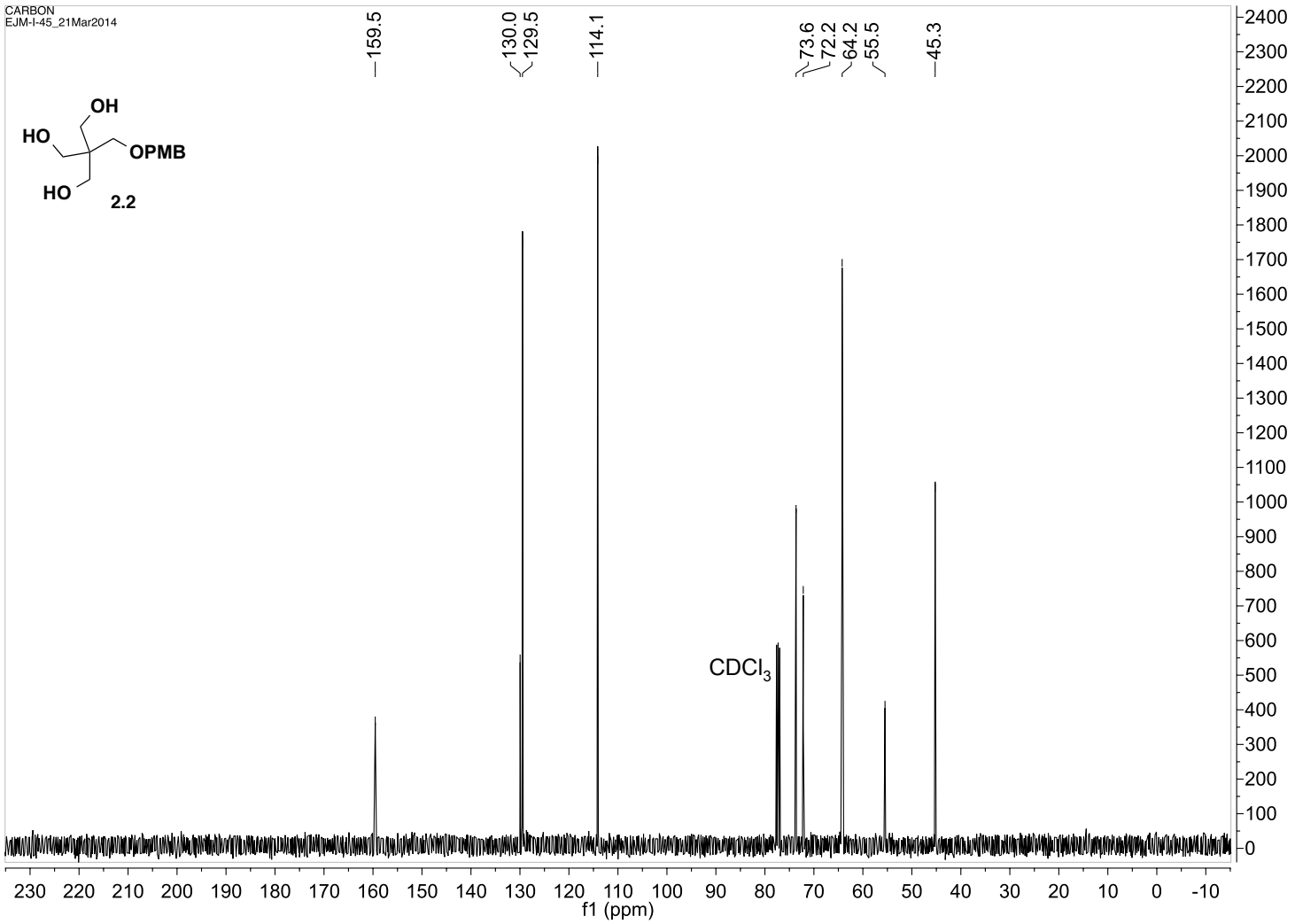

"PFtB$_{TRI}$-PMB" (2.3). In the optimized reaction, **2** (2.5 g, 9.7 mmol) was added to a (60 mL) pressure round bottom flask with 25 mL of dry THF. To this was added triphenylphosphine (11.52 g, 43.92 mmol), followed by 4 Å MS (2.5 g, powdered and previously activated at 280 °C *in vacuo*) and cooled to 0°C under argon with stirring. Once cooled, (8.88 g, 43.92 mmol) DIAD was added with a glass syringe dropwise. After the addition, the mixture was allowed to stir for approximately 30 min as it warmed to room temperature. After this time, (10.37 g, 43.92 mmol) of perfluoro-*tert*-butanol was added with a glass syringe in one portion and the vessel was quickly sealed. The reaction mixture was allowed to stir at 60°C with the Teflon cap screwed onto the sealed vessel for 3 days. After this time, 20 mL of water was added and allowed to stir for 10 min. The reaction mixture was allowed to cool to room temperature and the solvent was removed *in vacuo*. The residue was redissolved in ether and filtered through packed Celite. The filtrate was washed with brine, dried over $MgSO_4$, filtered, and concentrated *in vacuo*. The residue was then purified with the Combi-flash purification system with a normal-phase silica Gold column using a 0-10% EtOAc/Hexanes gradient to yield 63 %. ^{1}H NMR ($CDCl_3$, 400 MHz): δ 7.18 (d, J = 8.8 Hz, 2H), 6.88 (d, J = 8.8 Hz, 2H), 4.38 (s, 2H), 4.04 (s, 6H), 3.81 (s, 3H), 3.40 (s, 2H). ^{13}C{^{1}H} NMR ($CDCl_3$, 101 MHz): δ 159.7, 129.6, 120.3 (q, J = 278.6 Hz, (CF_3), 113.9, 79.9 (decet, J = 30.1 Hz ($C(CF_3)_3$), 73.6, 65.6, 65.2, 55.3 46.4. ^{19}F NMR (376 MHz, CDCl3): δ -71.84 (s).

^{1}H-NMR ($CDCl_3$, 400 MHz)

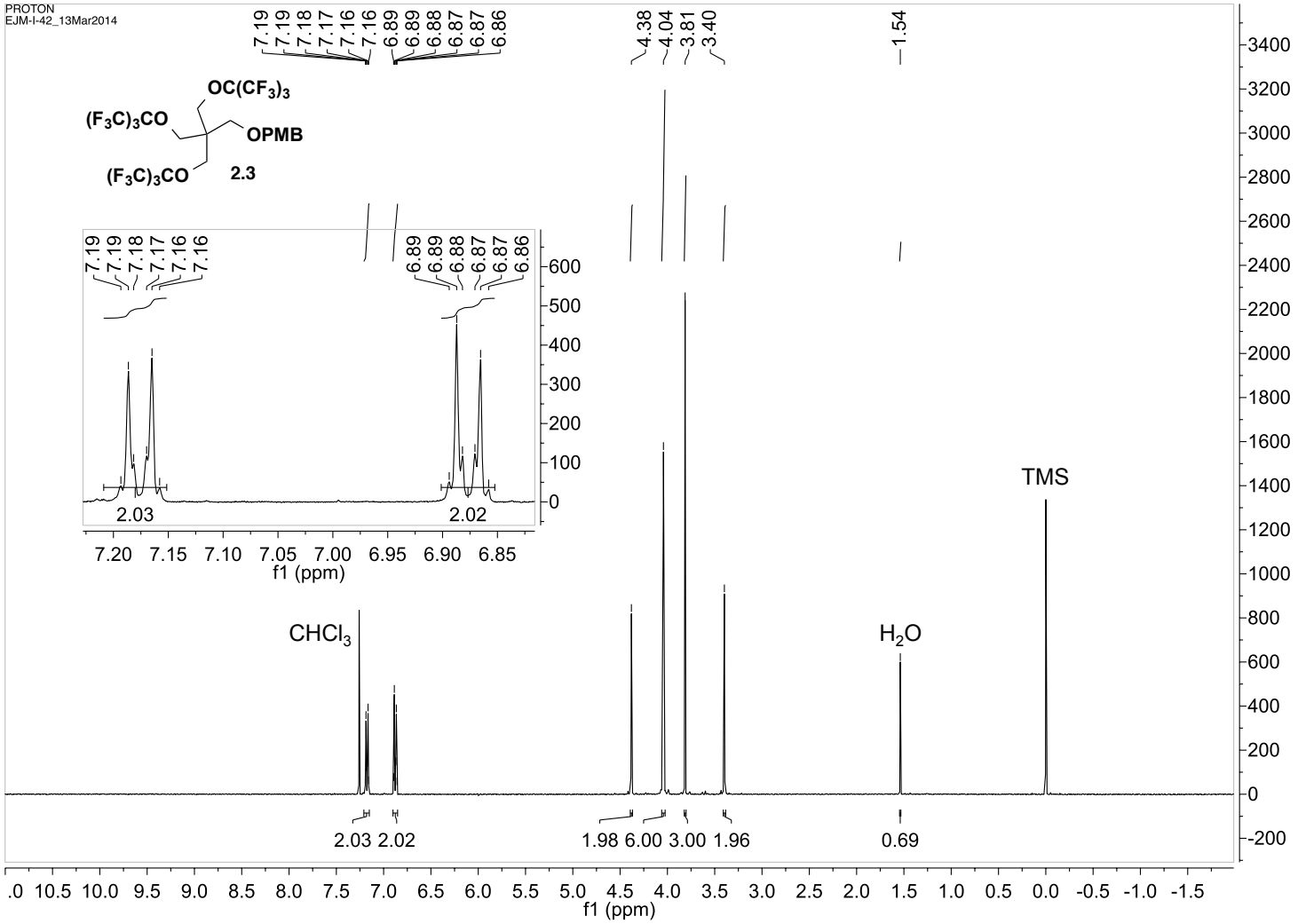

$^{13}C\{^{1}H\}$-NMR ($CDCl_3$, 101 MHz)

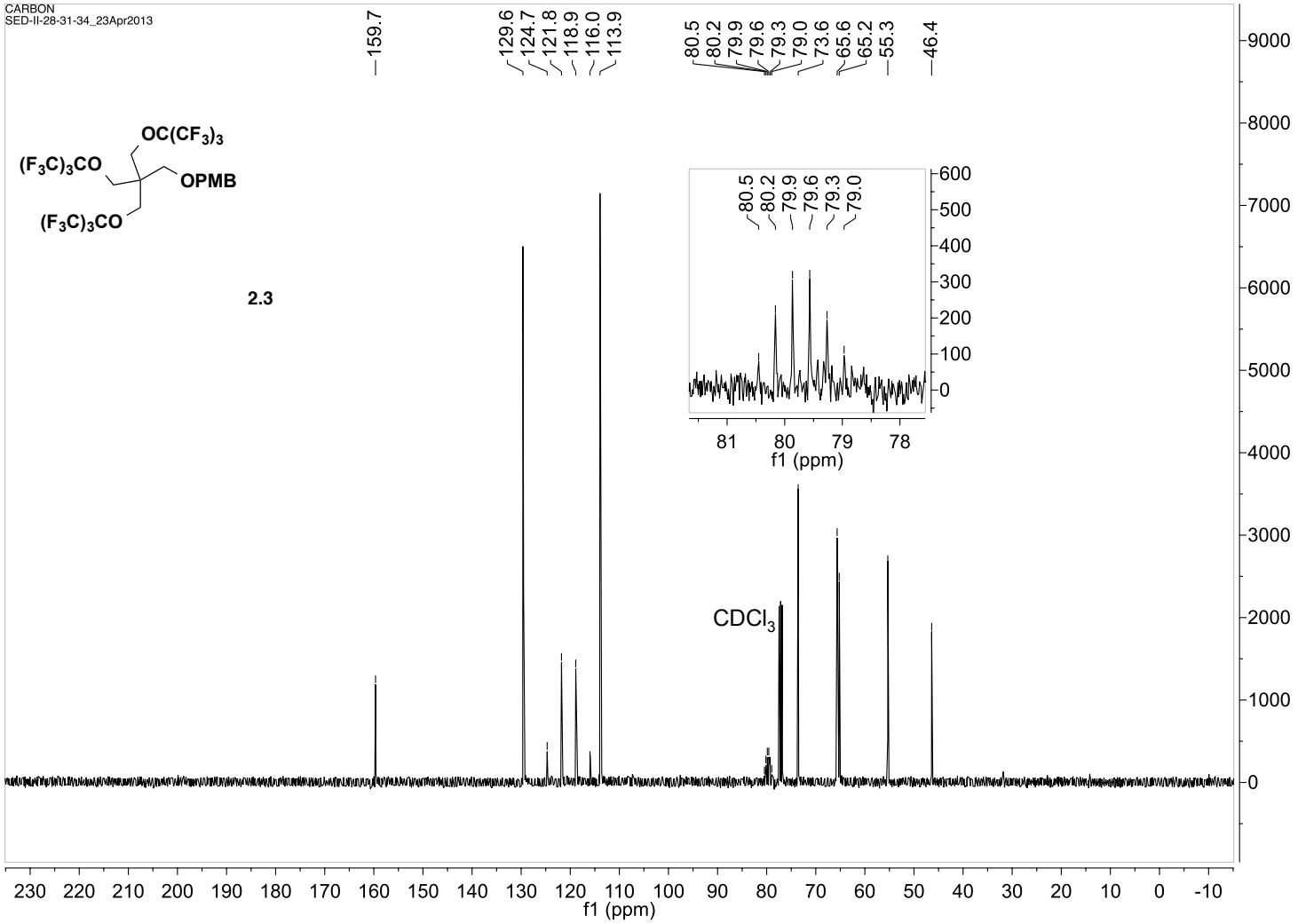

^{19}F-NMR ($CDCl_3$, 376 MHz)

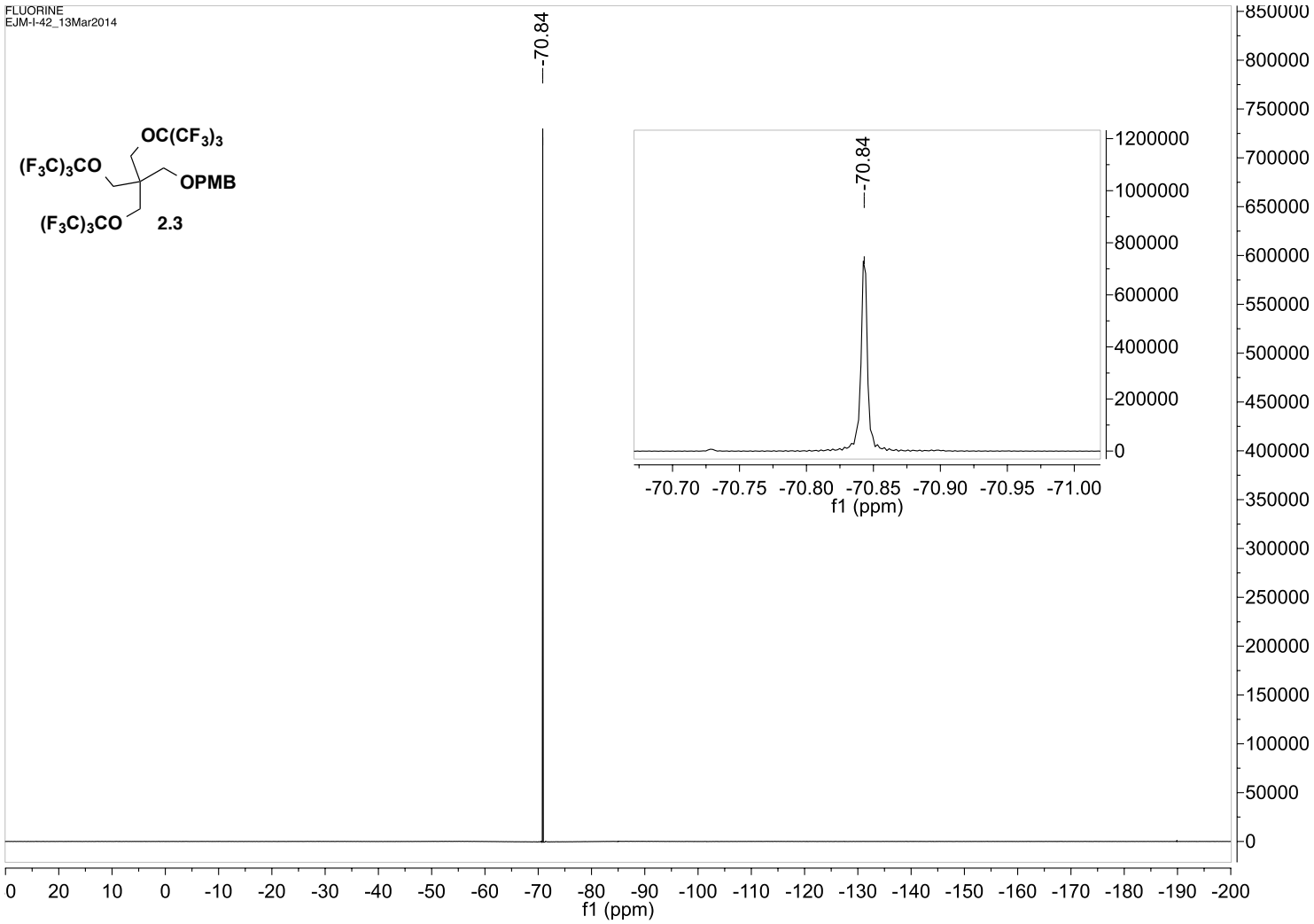

"$PFtB_{TRI}$-OH". To a stirring mixture of **3** (2.0 g, 2.23 mmol) in 12 mL of THF/H_2O (9:1, v:v) was added ceric ammonium nitrate (CAN) (4.94 g, 8.93 mmol) under argon at room temperature. The mixture was then refluxed with vigorous stirring. The reaction was monitored by TLC and was found to be complete after 1 h and 15 min. After this time the reaction mixture was diluted with sat. $NaHCO_3$, extracted with ether, and dried over $MgSO_4$, and concentrated under vacuum for only 1 min. The final compound should only have minimal exposure to vacuum since the product was found to sublime under high vacuum. The crude residue was then purified with the Combi-flash purification system with a normal-phase silica Gold column using a 0-10 % EtOAc/Hexanes gradient to give 59 % yield. ^{1}H NMR (CD_3COCD_3, 400 MHz): δ 4.50 (t, J = 1.6 Hz, 1H, OH), 4.25 (s, 6H), 3.71 (d, J = 1.6 Hz, 2H). $^{13}C\{^1H\}$ NMR (CD_3COCD_3, 101 MHz): δ 120.4 (q, J = 300.0 Hz, (CF_3), 79.7 (decet, J = 28.6Hz ($C(CF_3)_3$), 66.4, 57.5, 46.9. ^{19}F NMR (376 MHz, CD_3COCD_3): δ -71.51 (s).

"$PFtB_{TRI}$" series synthesis: $mPEG_x$-$PFtB_{TRI}$. In a typical reaction at 0 °C was added NaH (1.26 mmol) to a suspension of $PFtB_{TRI}$-OH (0.63 mmol) in 10 mL of dry THF under argon. This was allowed to stir for 30 min at 0 °C. After this time, $mPEG_x$-OMs (0.32 mmol) was added at 0 °C. The reaction mixture was allowed to stir as the mixture warmed slowly to room temperature. The mixture was then refluxed and monitored by HPLC. When determined to be complete the reaction mixture was then diluted with DCM, quenched and washed with sat. NH_4Cl_{aq}, dried over $MgSO_4$, and concentrated to 10 mL *in vacuo*. The crude product was then precipitated from the organic phase with ether in a dry-ice/acetone bath. The solid was isolated by filtration and then dissolved in 5 mL of DCM and 5 mL of benzene, which was then frozen in dry-ice/acetone bath and dried overnight *in vacuo*. The crude product was purified with the Combi-flash purification system with a C-18 reverse phase Silica column using a water/MeOH (0.1% FA) to DCM/MeOH gradient. **$mPEG_{1k}$-$PFtB_{TRI}$**: Yield 56%. ^{1}H NMR ($CDCl_3$, 400 MHz): δ 4.05 (s, 6H), 3.83-3.81

(m, 1H), 3.66-3.54 (m, 96 H), 3.48-3.47 (m, 1H), 3.45 (s, 2H), 3.38 (s, 3H). ^{19}F NMR ($CDCl_3$, 376 MHz): δ -70.82 (s). MALDI MS: $[M+Na]^+$ calcd. for $C_{66}H_{107}F_{27}O_{28}Na^+$ = 1883.64; found: 1883.5. **$mPEG_{2k}$-$PFtB_{TRI}$**: Yield 59%. ^{1}H NMR ($CDCl_3$, 400 MHz): δ 4.05 (s, 6H), 3.83-3.81 (m, 1H), 3.66-3.54 (m, 167H), 3.47-3.45 (m, 1H), 3.45 (s, 2H), 3.38 (s, 3H). ^{19}F NMR ($CDCl_3$, 376 MHz): δ -70.84 (s). MALDI MS: $[M+Na]^+$ calcd. for $C_{102}H_{179}F_{27}O_{46}Na^+$ = 2676.11; found: 2675.6.

^{1}H-NMR ($CDCl_3$, 400 MHz)

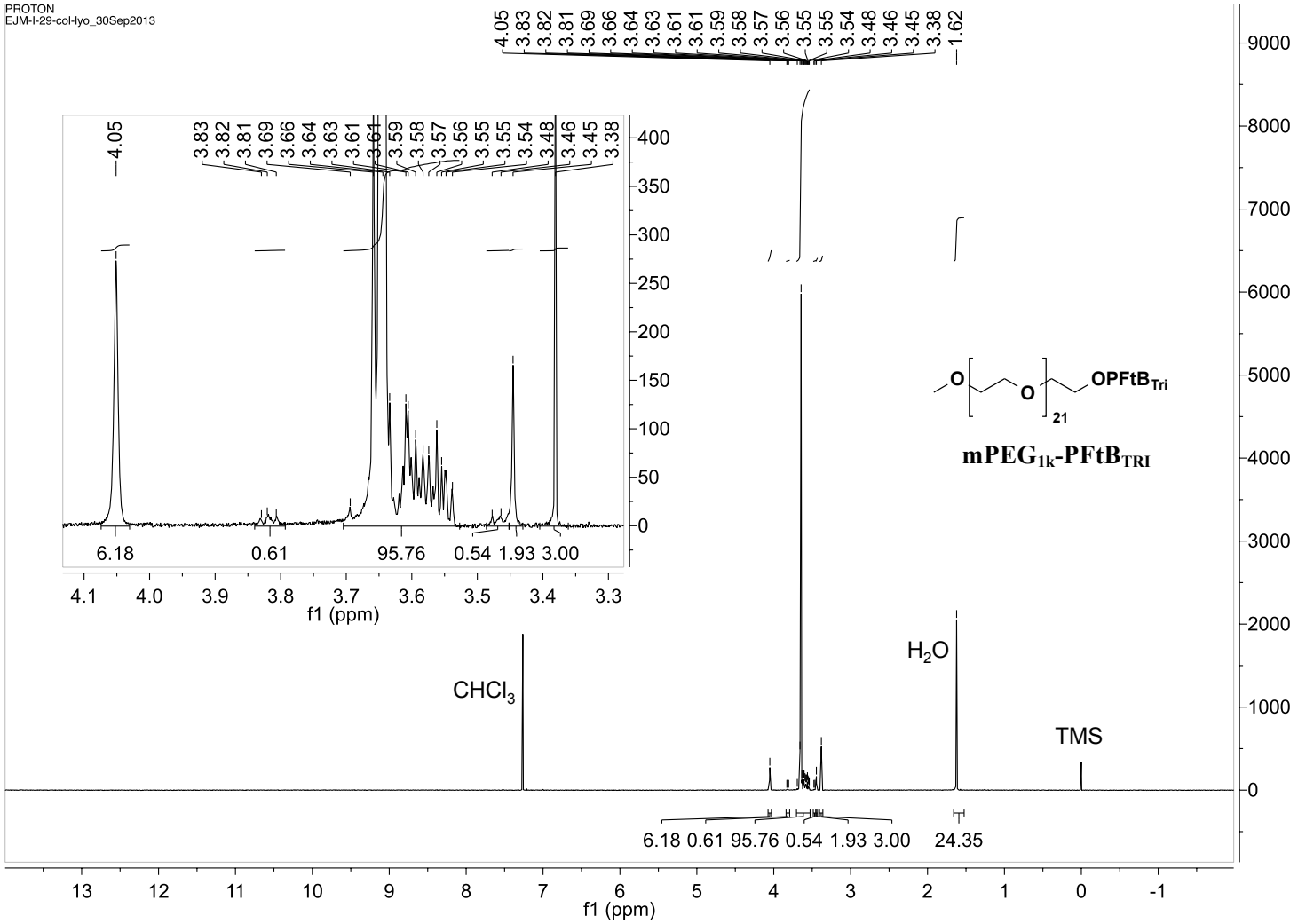

^{19}F-NMR ($CDCl_3$, 376 MHz)

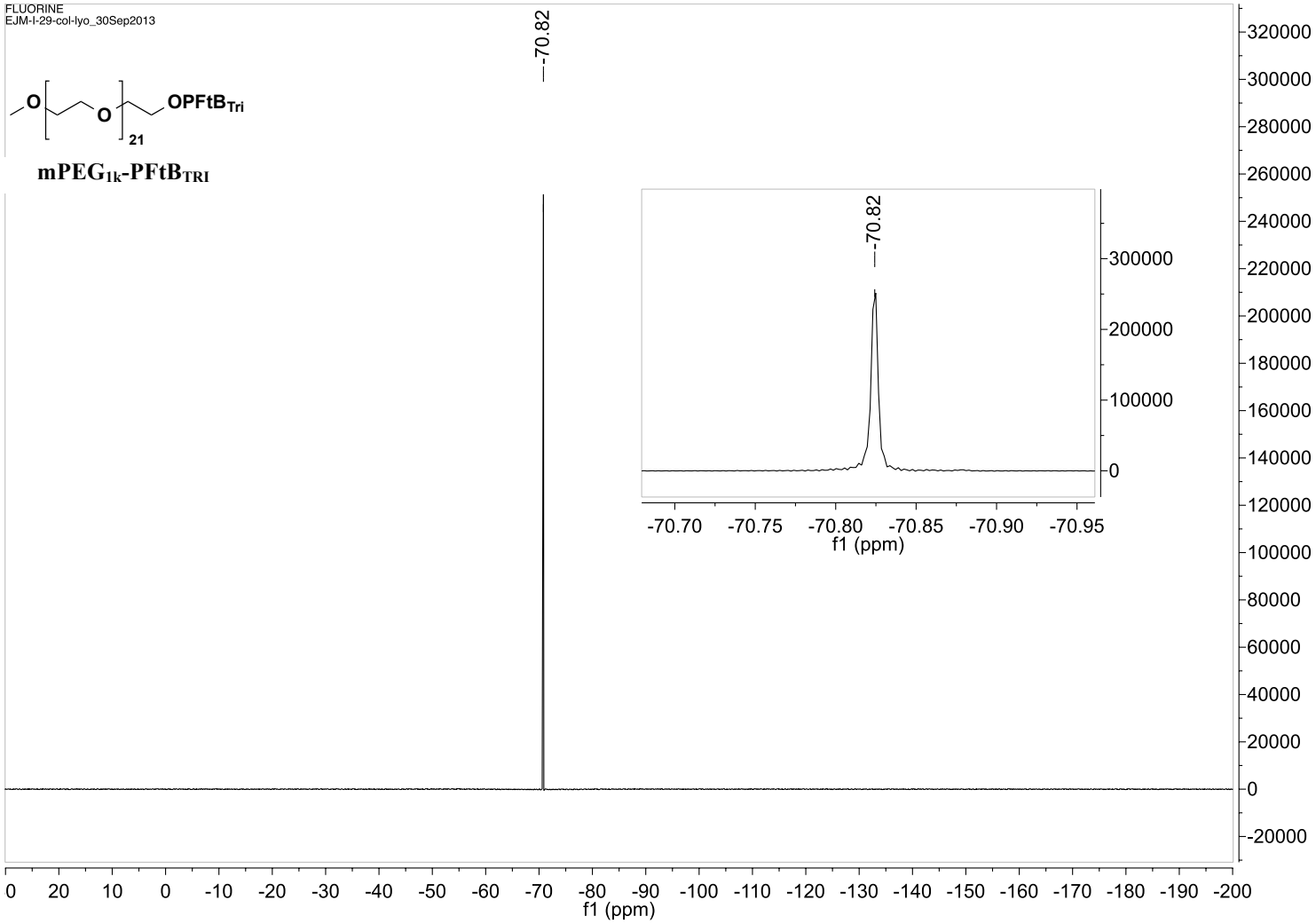

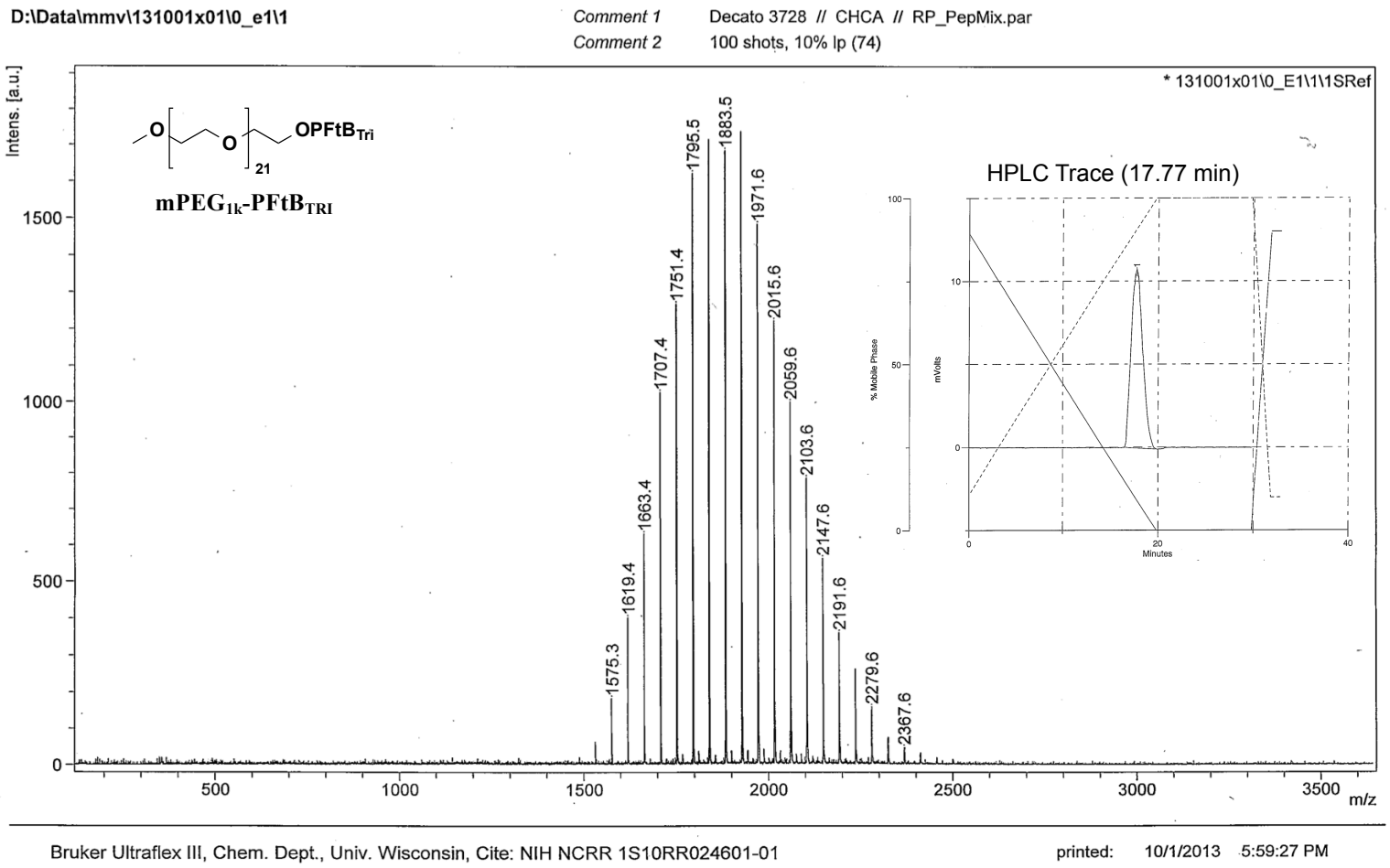
D:\Data\mmv\131001x01\0_e1\1
Comment 1 Decato 3728 // CHCA // RP_PepMix.par
Comment 2 100 shots, 10% lp (74)
* 131001x01\0_E1\1\1SRef
Intens. [a.u.]
mPEG1k-PFtBTRI
HPLC Trace (17.77 min)
% Mobile Phase
mVolts
Minutes
1575.3
1619.4
1663.4
1707.4
1751.4
1795.5
1883.5
1971.6
2015.6
2059.6
2103.6
2147.6
2191.6
2279.6
2367.6
m/z
Bruker Ultraflex III, Chem. Dept., Univ. Wisconsin, Cite: NIH NCRR 1S10RR024601-01
printed: 10/1/2013 5:59:27 PM

^{1}H-NMR ($CDCl_3$, 400 MHz)

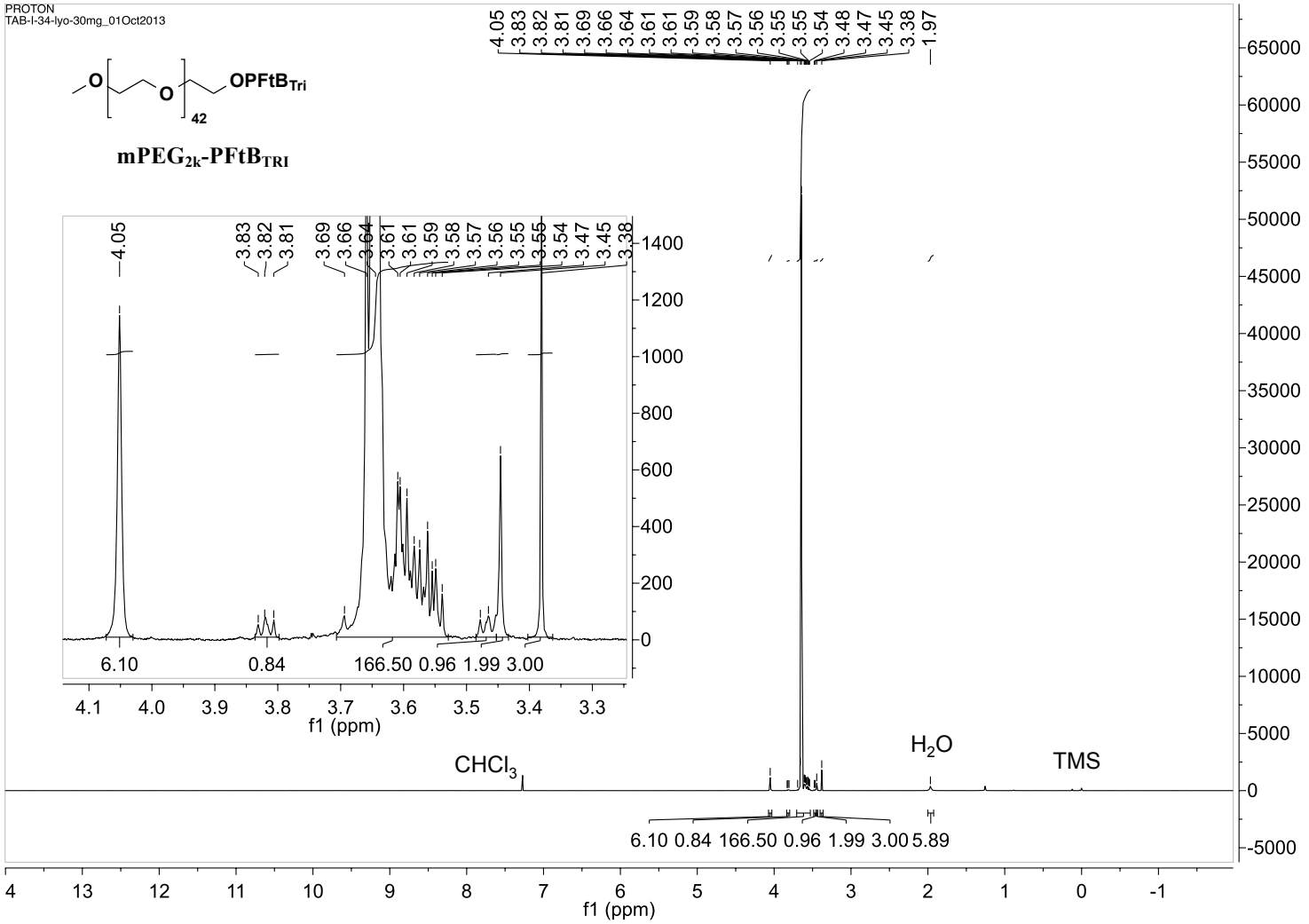

^{19}F-NMR ($CDCl_3$, 376 MHz)

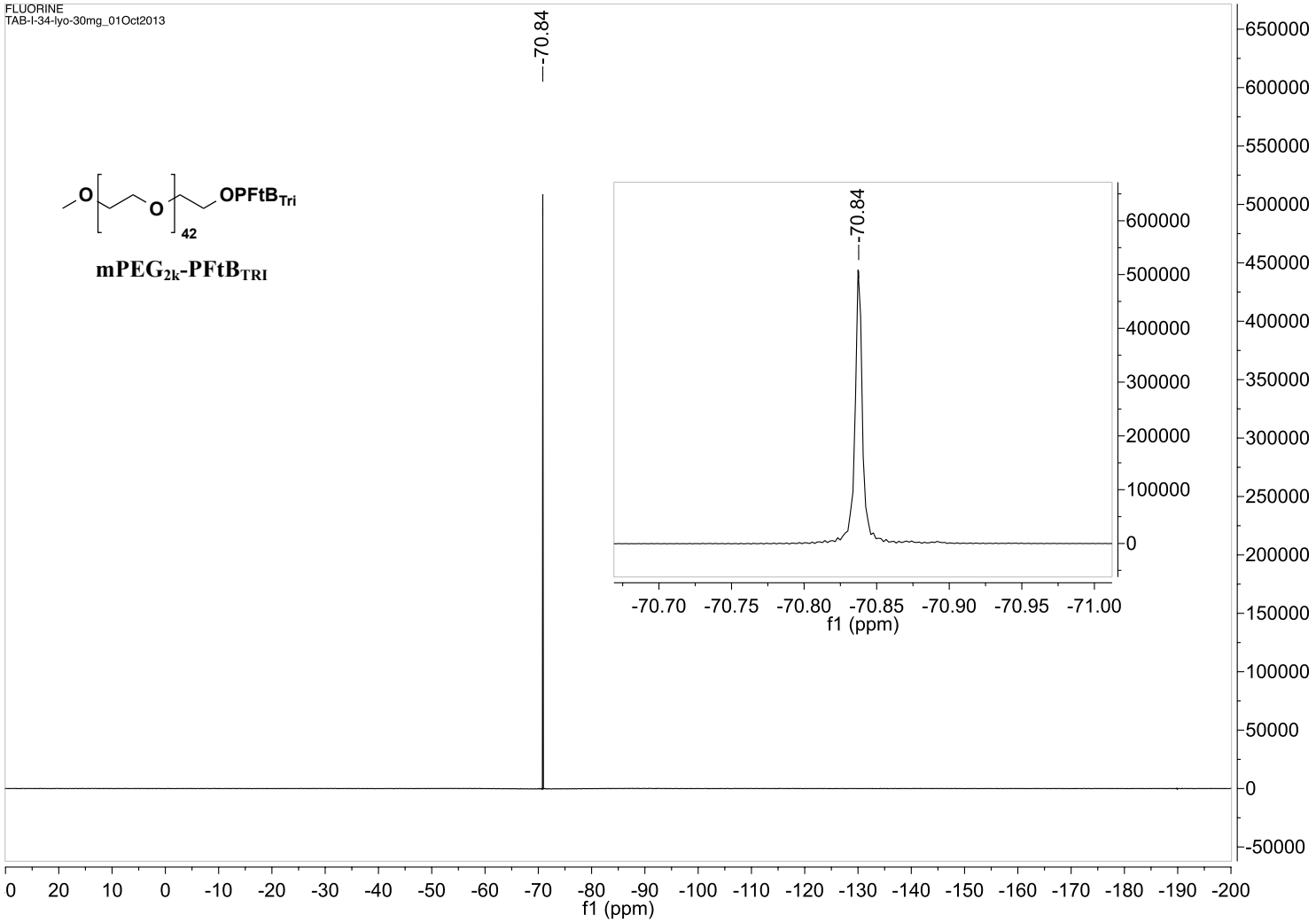

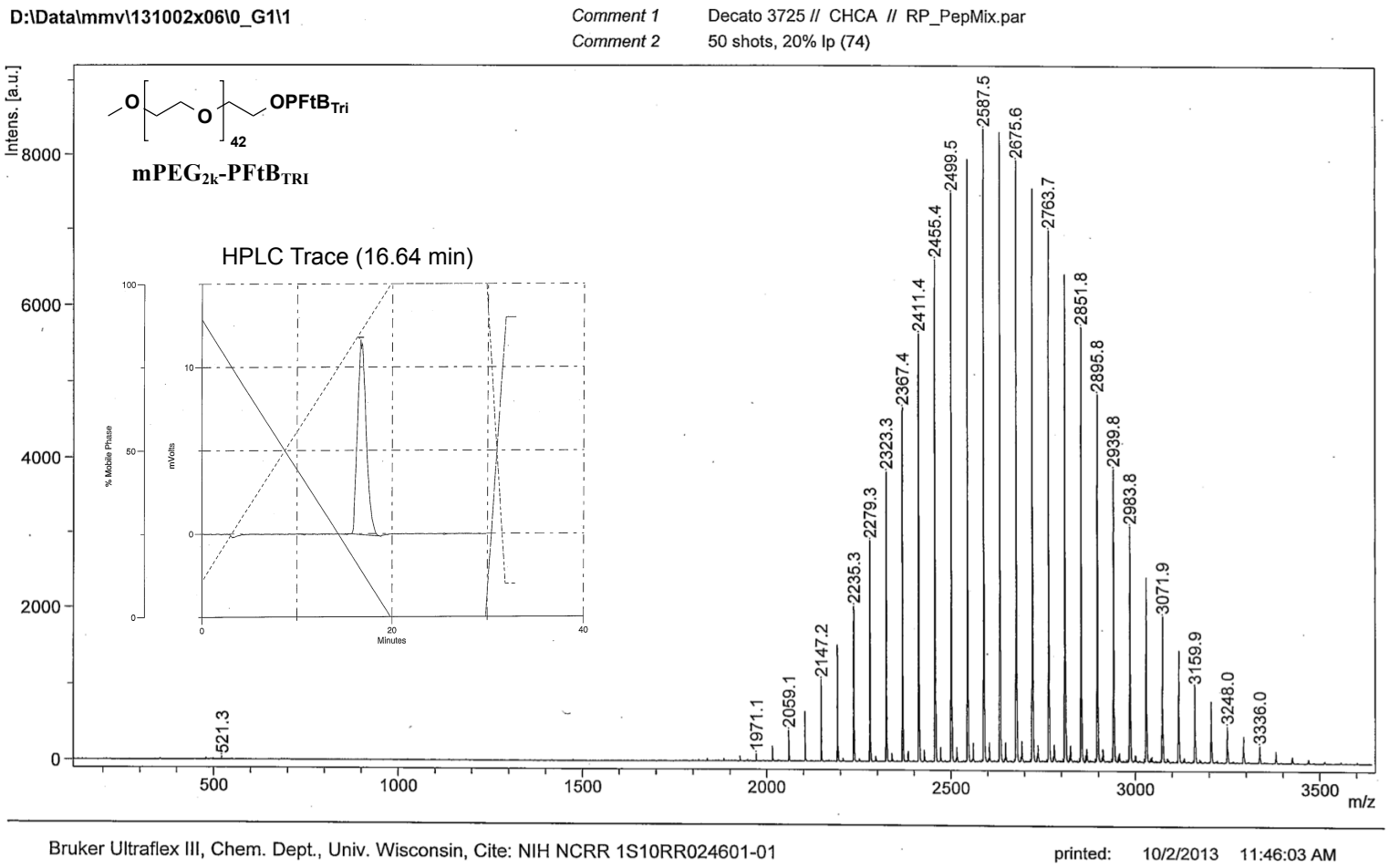
D:\Data\mmv\131002x06\0_G1\1
Comment 1 Decato 3725 // CHCA // RP_PepMix.par
Comment 2 50 shots, 20% Ip (74)
Intens. [a.u.]
OPFtB$_{Tri}$
42
mPEG$_{2k}$-PFtB$_{TRI}$
HPLC Trace (16.64 min)
% Mobile Phase
mVolts
Minutes
521.3
1971.1
2059.1
2147.2
2235.3
2279.3
2323.3
2367.4
2411.4
2455.4
2499.5
2587.5
2675.6
2763.7
2851.8
2895.8
2939.8
2983.8
3071.9
3159.9
3248.0
3336.0
m/z
Bruker Ultraflex III, Chem. Dept., Univ. Wisconsin, Cite: NIH NCRR 1S10RR024601-01
printed: 10/2/2013 11:46:03 AM

2.6.5 Critical micelle concentration (CMC)

The appropriate polymer was dissolved in Milipore Milli-Q water (equipped with a 0.22 μm filter) in a 20 mL disposable scintillation vial to the desired maximum concentration (dependent upon the solubility of the polymer in water and upon the available quantity of polymer). The solution was then shaken, sonicated for 20 min, and allowed to equilibrate for 24 hours. (If bubbles were still present after this time, the solution was allowed to continue to equilibrate until all bubbles had dissipated.) Serial dilutions were then prepared from this stock solution to achieve the desired concentrations, again allowing for each dilution to equilibrate before subsequent dilution. After all dilutions were prepared, they were allowed to equilibrate for an additional 24 hours. A custom round platinum rod, with a diameter of 1.034 mm with a wetted length of 3.248 mm from KSV Instruments, (Helsinki, Finland) was cleaned with ethanol and dried in a Bunsen burner flame. The surface tension of Millipore water was measured first and the value confirmed to be within ± 2 mN/m of the literature value (72.8 mN/m). The surface tension of each vial was then measured using the Wilhelmy method, beginning with the least concentrated, at room temperature on a KSV sigma 701 tensiometer from KSV Instruments (Helsinki, Finland) equipped with a Schott Titronic Universal dispenser for automatic CMC measurements and a Julabo F12-MC circulator for constant temperature control. Each sample was measured in quadruplicate and the average recorded. The CMC value was determined from the intersection of the slope at the crossover point and the slope at high concentrations. The error in the CMC measurement was calculated by applying a weighted least squares analysis to the linear sections of interest. The individual uncertainties of the two slopes and intercepts produced by the weighted least squares analysis were then propagated through as follows:

$$x_{Log(M)} = \frac{b_2 - b_1}{m_1 - m_2}$$

$$\sigma_{x_{Log(M)}} = \sqrt{x^2_{Log(M)}\left[\left(\frac{\sigma_{b_2-b_1}}{b_2 - b_1}\right)^2 + \left(\frac{\sigma_{m_1-m_2}}{m_1 - m_2}\right)^2\right]}$$

Where:

$$\sigma_{m_1-m_2} = \sqrt{\sigma^2_{m_1} + \sigma^2_{m_2}} \qquad \sigma_{b_2-b_1} = \sqrt{\sigma^2_{b_2} + \sigma^2_{b_1}}$$

The weighted least squares analysis was chosen because the uncertainty of each individual data point was known, yielding insight into the precision of the CMC calculation.

Note: The $mPEG_{550}PFtB_{MONO}$ was analysed and a "CMC" value was calculated. However, this value was not reported in the discussion due to the fact that the "CMC" was only achieved with highly concentrated solutions (~ -2 log(M)) and that the surface tension above the "CMC" did not plateau and so the accuracy of this value is questionable. Also the extremely small size (~ 4 nm) of the particles measured by DLS also makes definitive identification of these particles difficult.

$mPEG_{550}$-$PFtB_{MONO}$		
log(M)	**Avg. SurfaceTension (mN/m)**	**Std. Dev.**
-0.470	29.283	0.825
-1.169	28.324	0.373
-1.868	23.334	0.674
-2.567	29.591	0.329
-3.266	35.668	0.284
-3.965	43.668	0.361
-4.664	54.411	0.938
-5.363	60.979	0.259
-6.062	65.381	0.303
-6.761	71.116	0.124
-7.460	71.175	0.192
-8.159	72.425	0.366
-0.470	29.283	0.825
-1.169	28.324	0.373
"CMC" value as shown below: -2.06 ± 0.12 log(M)		

$mPEG_{550}$-$PFtB_{MONO}$

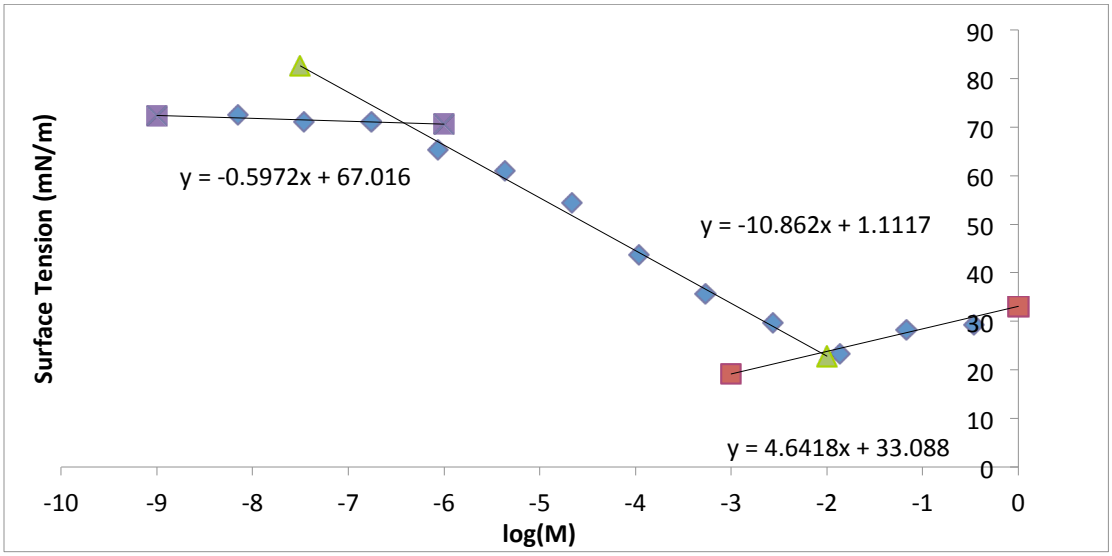

Again this "CMC" value was not reported, see note above.

$mPEG_{1k}$-$PFtB_{MONO}$		
log(M)	**Avg. Surface Tension (mN/m)**	**Std. Dev.**
-1.998925022	29.9125	0.130569266
-2.697895026	37.262	0.2501293
-3.396865031	47.5815	0.125417968
-4.095835035	55.25125	0.11176277
-4.794805039	58.42875	0.191597451
-5.493775044	61.00975	0.136289826
-6.192745048	64.3165	0.141530915
-6.891715052	71.598	0.143061758
-7.590685057	71.86525	0.157086759
-8.289655061	71.87775	0.063421211
-8.988625065	71.88075	0.092442324
-9.68759507	71.62425	0.228903728
-10.38656507	71.84425	0.193548228
-1.998925022	29.9125	0.130569266

$mPEG_{1k}$-$PFtB_{MONO}$

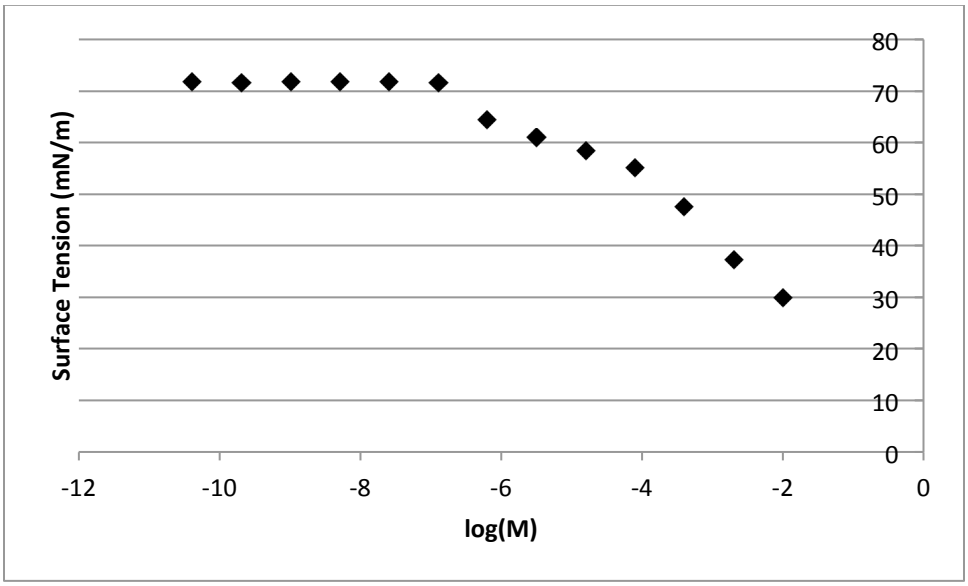

$mPEG_{2k}$-$PFtB_{MONO}$		
log(M)	**Avg. Surface Tension (mN/m)**	**Std. Dev.**
-2.01	37.60	0.15
-3.05	42.63	0.31
-4.09	50.00	0.11
-5.13	58.37	0.09
-6.17	61.67	0.12
-7.21	68.42	0.30
-8.25	71.67	0.15
-9.29	71.88	0.14
-10.34	71.87	0.34

$mPEG_{2k}$-$PFtB_{MONO}$

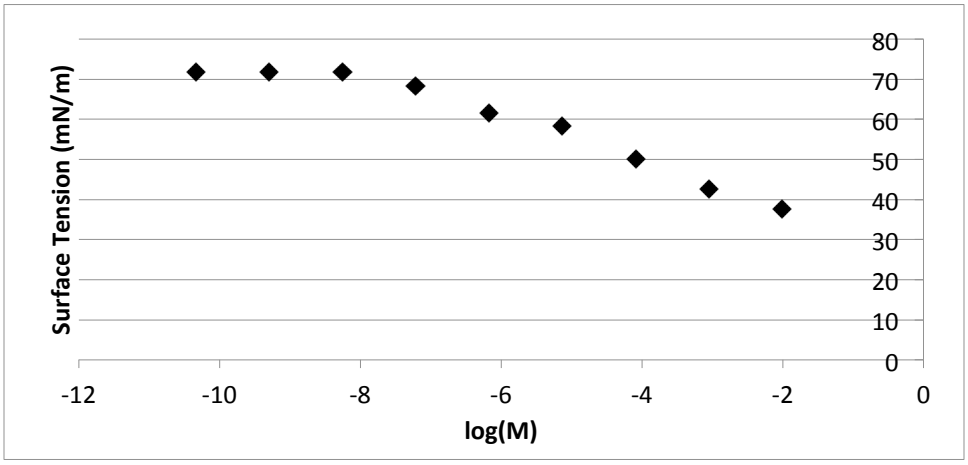

$mPEG_{1k}$-$PFtB_{TRI}$		
log(M)	**Avg. Surface Tension (mN/m)**	**Std. Dev.**
-2.11	19.58	0.12
-2.71	19.63	0.09
-3.32	19.70	0.15
-3.92	19.94	0.15
-4.52	20.30	0.05
-5.12	22.19	0.79
-5.72	48.79	0.14
-6.33	72.68	0.07
-6.93	72.96	0.03
-7.53	72.99	0.08
-8.13	73.03	0.07
-8.73	72.93	0.09
-9.34	72.87	0.09
-9.94	72.90	0.06

$mPEG_{1k}$-$PFtB_{TRI}$

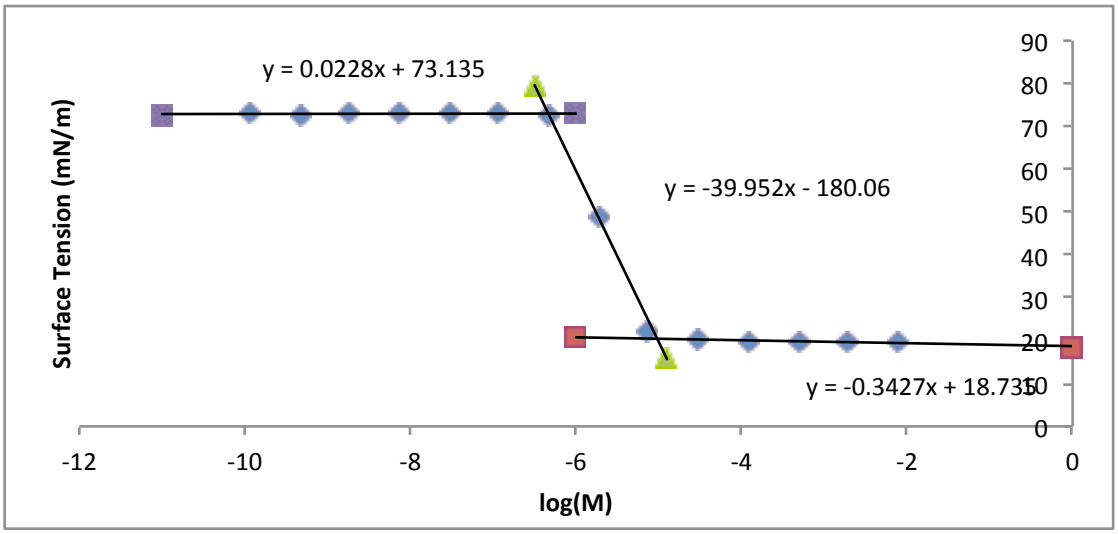

$mPEG_{2k}$-$PFtB_{TRI}$		
log(M)	**Avg. Surface Tension (mN/m)**	**Std. Dev.**
-2.32	26.75	0.11
-2.92	26.95	0.04
-3.52	27.16	0.16
-4.12	27.61	0.05
-4.73	27.83	0.10
-5.33	29.71	0.23
-5.93	48.90	0.14
-6.53	72.20	0.19
-7.13	73.28	0.11
-7.74	73.18	0.07
-8.34	73.36	0.09
-8.94	73.46	0.11
-9.54	73.12	0.04
-10.14	73.01	0.13

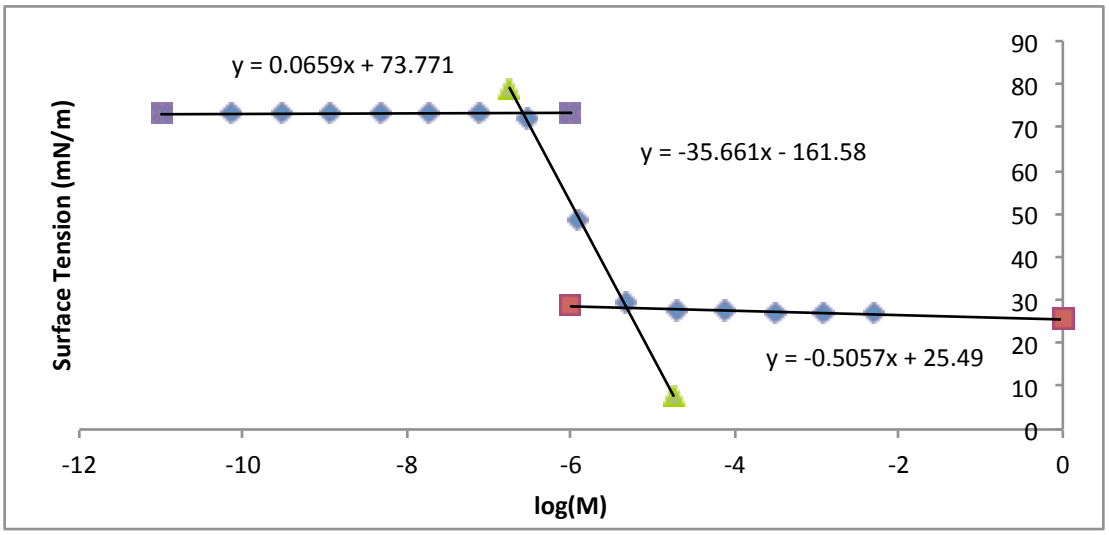

2.6.6 Dynamic light scattering (DLS)

Samples were prepared by direct dilution of the polymer in Milli-Q water to the desired concentration (above the CMC, typically 10 mM). Particle sizes of polymer solutions were analyzed by dynamic light scattering using a NICOMP 380ZLS from Particle Sizing Systems (Santa Barbara, CA) without further dilution in Plastibrand 1.5 mL PS semi-micro disposable

cuvettes from Sigma Aldrich Co. (Milwaukee, WI). Each sample was measured before and after filtration with a 4 mm dia., 0.45 μm or 0.22 μm nylon syringe filter from Thermo Fisher Scientific Inc. (Fitchburg, WI). Each particle size analysis was performed at room temperature and repeated in triplicate with the number of scans of each run determined automatically by the instrument according to the concentration of the solution. The data was analyzed using NICOMP analysis and reported as volume weighted average diameters. Error was reported as the standard deviation of the particle diameter as reported by the NICOMP software.

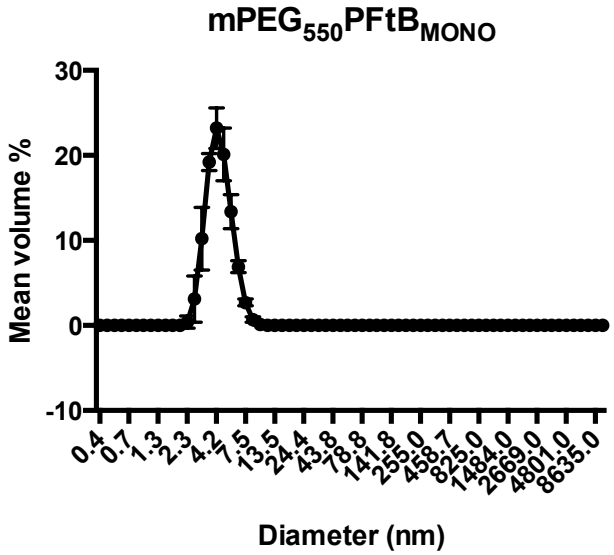

$mPEG_{550}$-$PFtB_{MONO}$ analyzed at CMC concentration 2 (-1.169 log(M)) and filtered with 0.22 μm filter. Results were highly variable from sample to sample indicating that these aggregates may not be very stable.

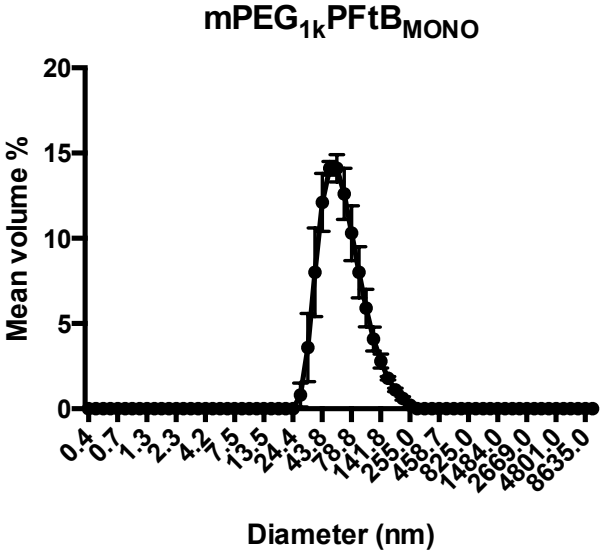

$mPEG_{1k}$-$PFtB_{MONO}$ analyzed as a thin-film at 10 mM and filtered with 0.22 μm filter. Results were highly variable from sample to sample and during measurement indicating that these aggregates may not be very stable.

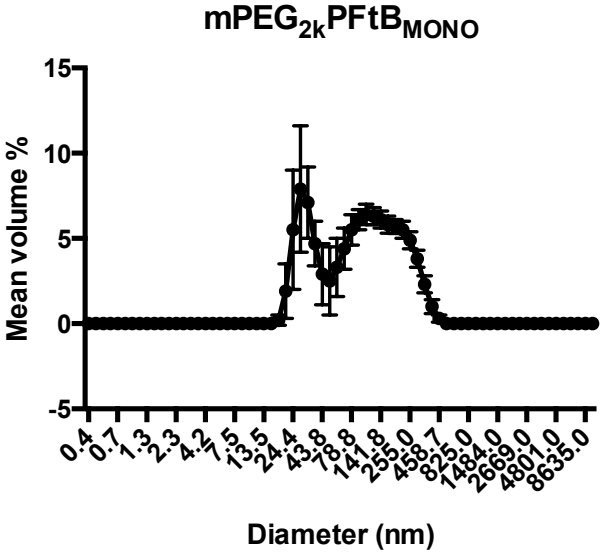

$mPEG_{2k}$-$PFtB_{MONO}$ analyzed at 5 mM and filtered with 0.22 μm filter. Results were highly variable from sample to sample and during measurement indicating that these aggregates may not be very stable.

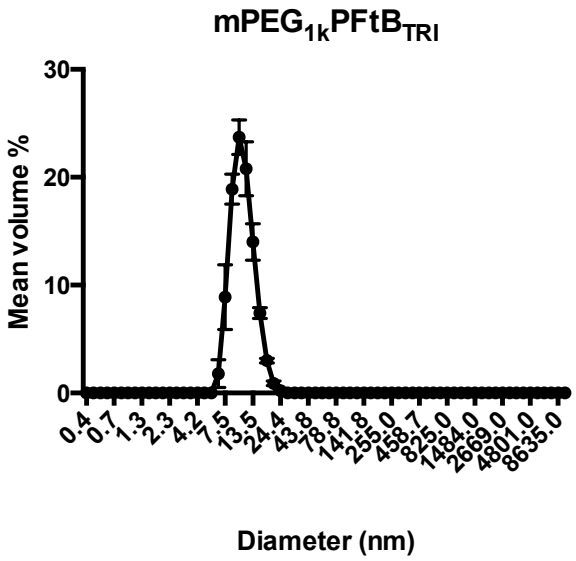

$mPEG_{1k}$-$PFtB_{TRI}$ analyzed at CMC concentration 2 (-2.71 log(M)) and filtered with 0.45 μm filter. Results were consistent from sample to sample indicating that these aggregates are stable.

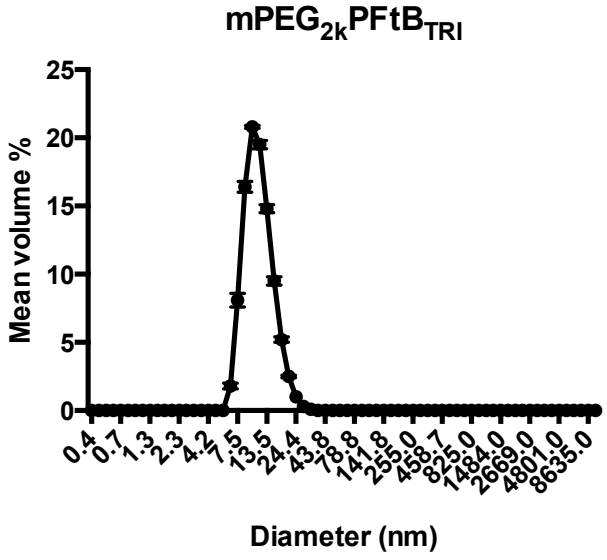

$mPEG_{2k}$-$PFtB_{TRI}$ analyzed at CMC concentration 2 (-2.92 log(M)) and filtered with 0.45 μm filter. Results were consistent from sample to sample indicating that these aggregates are stable.

2.6.7 Transmission electron microscopy (TEM)

Solvent Evaporation method (Film preparation): Polymer is dissolved in an organic solvent (either MeOH, ACN, or acetone) to a desired concentration. The polymer solution is added to a 25 mL round bottom flask and rotated for 5 minutes at 60 °C on a rotary evaporator. Then the solvent is removed *in vacuo* with rotation for 15 minutes. The remaining film rests at room temperature for 5 min, then after this time is dispersed with an aqueous solvent at 60 °C. After equilibrating for 15 min the solution is filtered.

Cryo-TEM: Polymer micelle solutions were prepared using the solvent evaporation method above with MeOH as the organic solvent and 60 °C Mili-Q water as the aqueous dispersing solvent at a concentration 60 mg/0.5mL (~96 mM). This extremely high concentration was used as no particles could be visualized at lower concentrations (0.1 wt. % or 10 mM). These samples were filtered with a 0.2 μm nylon filter (previous examination of filter effects showed no difference between nylon and recycled cellulose filtered samples). A 1 μL drop of the polymer solution was pipetted onto a lacey carbon grid in a controlled humidity environment (Vitrobot). The sample was blotted with filter paper at a setting of 0 and then plunged into liquid ethane and cooled and stored in liquid nitrogen. DLS was taken directly after TEM imaging, which confirmed the formation of aggregates.

These sample preparation conditions formed fairly thick ice for this sample, which can be seen by “stacking” of aggregates. Two main types of aggregates were seen: spheroid type aggregates between 10-20 nm and larger spheroid type aggregates between 100-150 nm. Note that these larger particles seem to have a darker ring inside the spheroid. All these particles are; however, irregular and seem to aggregate together randomly.

To simplify the sample preparation in order to reduce variables, which may have limited nanoparticle visualization, the negative staining method was used using 2 wt. % uranyl acetate

solution (pH 4.2 to 4.5). Although this would involve drying the sample, and would therefore not necessarily truly represent the dynamic self-assembling aggregates present in aqueous solution, it would at least allow us a foundation to build upon in terms of sample preparation. Unfortunately it was discovered after this imaging that the sample $mPEG_{1k}$-$PFtB_{DI}$ was actually a mixture of mostly $mPEG_{1k}$-$PFtB_{MONO}$ and $mPEG_{1k}$-$PFtB_{DI}$. Since $mPEG_{1k}$-$PFtB_{MONO}$ did not form stable micelles this may have been the reason that random aggregates were observed.

TEM images of the $mPEG_{1k}$-$PFtB_{DI}$ polymer

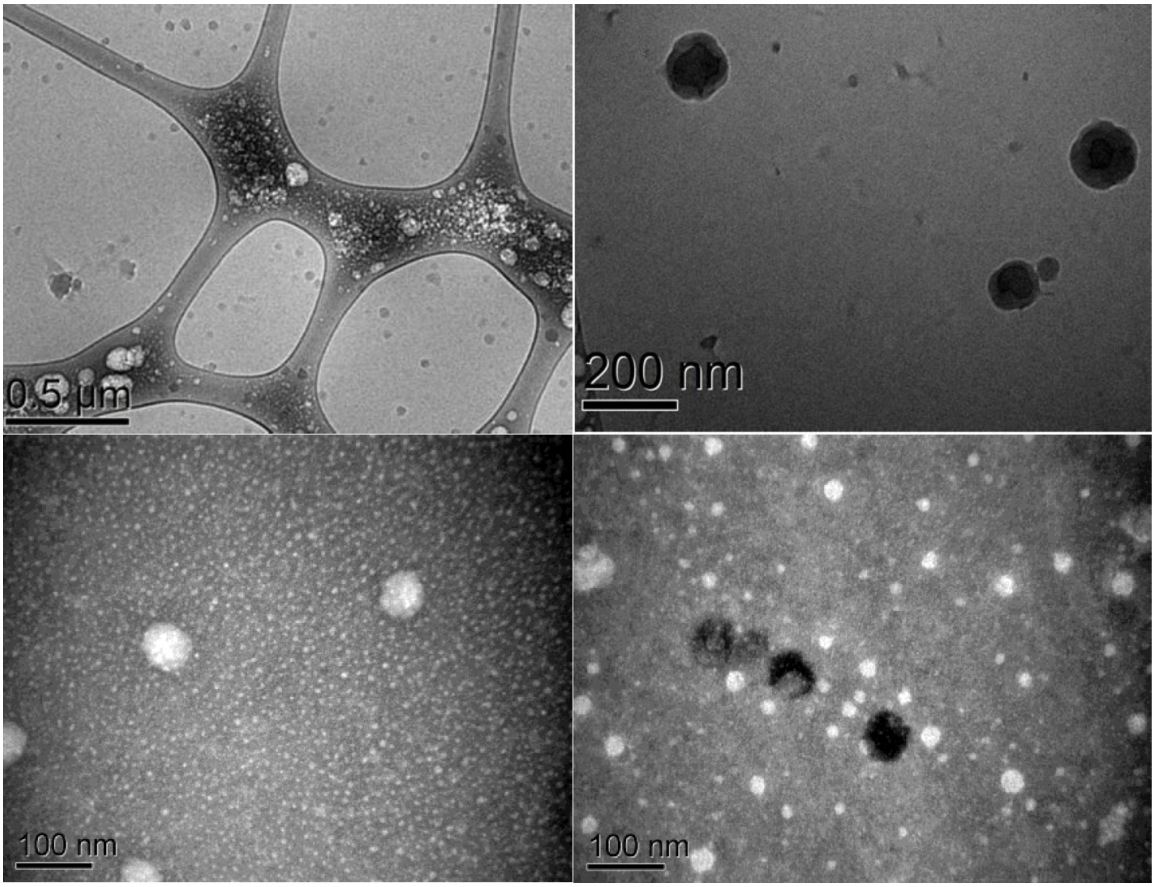

Top: Cryo-TEM image taken at 60 mg/mL filtered with a 0.22 µm recycled cellulose filter at two magnifications (left and right). **Bottom**: Negatively-stained TEM images at 1.5 mg/mL with 2 wt. % uranyl acetate, left is filtered with 0.45 µm nylon filter and right with a 0.2 µm recycled cellulose filter.

Despite the impurity of the $mPEG_{1k}$-$PFtB_{DI}$ polymer, the sample preparation still needed to be optimized since images of pure polymers such as $mPEG_{5k}$-F10-DSPE, which was confirmed by DLS to form discrete micelles, did not show an reasonable population of particles via Cryo-TEM as would be expected by the concentration of the polymer solution (26 mg/mL or 4.6 mM). Actually in this case a very thin ice was formed and easily damaged by the laser. The totality of the variability experienced throughout these preliminary TEM studies supports the systematic assessment of the sample preparation parameters in the future, especially concerning concentration, grid coating, blotting (force and paper), and vitrification.

TEM image of the $mPEG_{5k}$-F10-DSPE polymer

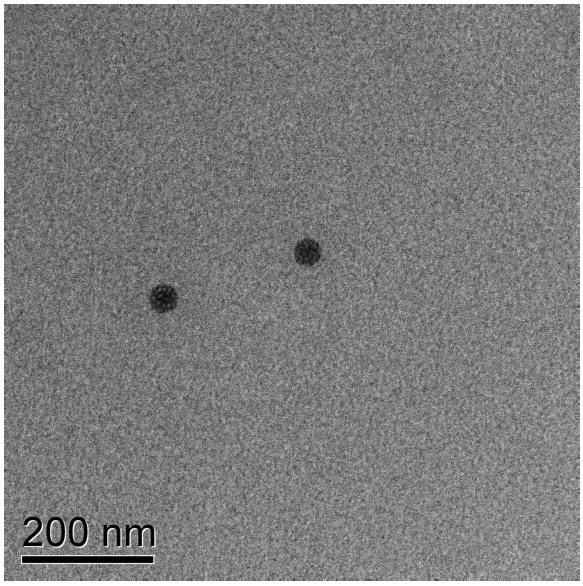

Cryo-TEM image taken at 26 mg/mL or 4.6 mM and filtered with a 0.45 μm nylon filter.

For the images provided in the results and discussion section of this chapter the polymer solution was prepared by direct dilution in Milli-Q water. Due to poor contrast in aqueous samples, 4 μL of a 1 mM polymer solution was pipetted onto the lacey carbon grid from Electron Microscopy Sciences (Hatfield, PA) and dried for 10 s under a heat lamp. The grids were imaged

using the Technai T-12 Cryo TEM operating at 120 kV. Images were taken with a Gatan Ultrascan CCD camera with resolution of 2048 x 2048 pixels.

2.6.8 Electrostatic potential surface (EPS) calculations

Calculations were performed using Spartan'10 from Wavefunction Inc. (Irvine, CA). The surfaces were generated by mapping 6-31G** electrostatic potentials onto surfaces of molecular electron density (0.002 electron/Å) and color-coding. In all surfaces, the potential energy values range from +150 kcal/mol to -150 kcal/mol, with red signifying a value greater than or equal to the maximum in negative potential and blue signifying a value greater than or equal to the maximum in positive potential (credit to Professor Sandro Mecozzi).

2.6.9 Microviscosity

Polymer solutions of 0.2 $mmolL^{-1}$ in acetonitrile and 1,3-bis-(1-pyrenyl)propane (P3P) solution of 2.7 $ngmL^{-1}$ in chloroform were prepared. Micelle solutions were then prepared via the solvent evaporation method: 1 mL of polymer solution and 67 µL of the P3P solution were added to a 25 mL round-bottom flask covered in foil. The samples were heated to 60 °C and rotated on the rotary evaporator without vacuum for 5 min. The samples were then condensed under reduced pressure for 15 min while rotating, allowed to cool for 5 min, and then dispersed with 1 mL of 60 °C phosphate buffered saline (PBS). The samples were shaken vigorously and then filtered with a 4 mm dia., 0.45 µm nylon filter and stored in amber vials. The fluorescence analysis was carried out on an AMINCO-Bowman Series 2 spectrometer from Thermo Fisher Scientific (Fitchburg, WI) with excitation at 333 nm, emission at 378 nm, and a spectral window of 350 – 500 nm. Error was reported as the standard deviation from triplicate measurements.

$mPEG_{1k}$-$PFtB_{TRI}$

***376* nm**	***480* nm**	***Im/Ie Ratio***	
1.60	0.29	5.53	
1.61	0.31	5.22	
1.55	0.32	4.84	
		5.19	**Ave**
		0.35	**Std. Dev.**

2.6.10 Hemolysis

Polymer solutions ($mPEG_{1k}$-$PFtB_{MONO}$ and $mPEG_{1k}$-$PFtB_{TRI}$) were made by direct dilution in sterile PBS. Suspended rabbit red blood cells (10 %, 15 mL) were centrifuged (2,000 rpm, 2 min, 25 °C, 450g), the supernatant was removed, and the cells were resuspended in 15 mL of sterile PBS. To each well of a clear 96-well plate was added varying amounts of rabbit red blood cells and (100 – x) µL of sterile PBS buffer, where x represents the amount of rabbit red blood cells (10, 20, 50, and 100 µL) that was added to the respective well. Each experimental condition was repeated in triplicate. Finally, 100 µL of the appropriate polymer solution was added to each well. The plates were incubated statically at 37°C for 3 h. The plates were then centrifuged to pellet the cells (4 min, 25 °C, 450g). A 100 µL portion of supernatant from each well of culture was transferred to a fresh, clear 96-well plate. Absorbance at 420 nm and 540 nm was measured for each well using a plate reader and percent hemolysis was determined, with complete (100%) hemolysis achieved in the positive control by treating red blood cells with 100 µL of Milli-Q water in place of polymer solution.

2.6.11 Emulsions of sevoflurane

For emulsion preparation protocol see section 2.6.1

$mPEG_{550}PFtB_{MONO}$ sevoflurane emulsions were prepared using the standard protocol; however, they began to phase separate immediately after formulation. Despite this the droplet size was measured by DLS and the average size was found to be very large (well over 1 micron) with a large polydispersity. In order to try to form stabilized emulsions with droplets under 500 nm, the polymer concentration was increased up to approximately 25 mM. Unfortunately even with increasing polymer concentration the emulsions still immediately phase-separated.

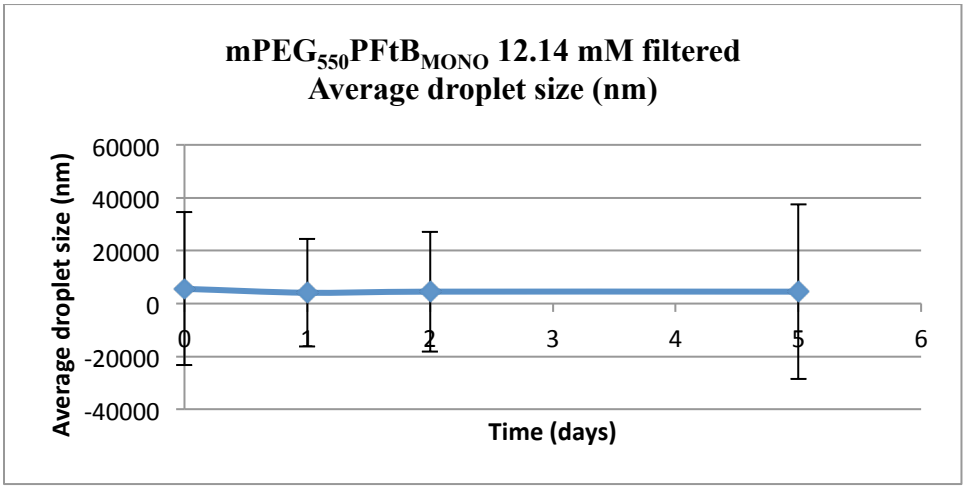

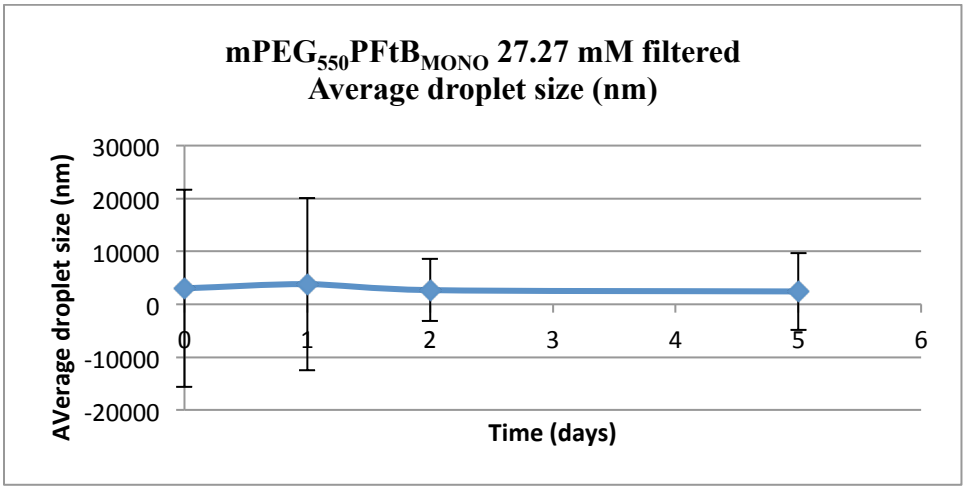

2.6.12 ^{19}F-NMR relaxivity and in vitro ^{19}F-MRI

Samples were prepared by direct dilution to achieve a 10 mM concentration in D_2O with TMS as an internal standard and the temperature maintained at 25°C. Micelle formation was confirmed by DLS. The ^{19}F relaxation parameters, T_1 and T_2 measurements of the micelles, were conducted on a Varian Unity-Inova 400 MHz spectrometer. The T_1 was determined using an inversion recovery experiment acquired with 12 independent, quadratically spaced variable (tau) values covering a range up to 5 times the estimated T_1, 0.4 s. The T_2 was determined using a Carr-Purcell-Meiboom-Gill, CPMG, pulse sequence experiment acquired with 12 independent, quadratically spaced variable (tau) values covering a range up to 5 times the estimated T_2, 0.4 s. For T_1 and T_2 measurements: 90° pulse = 13.4 μs, nt = 4, spectral window (T_1) = 21575.0 Hz and spectral window (T_2) = 15763.5 Hz

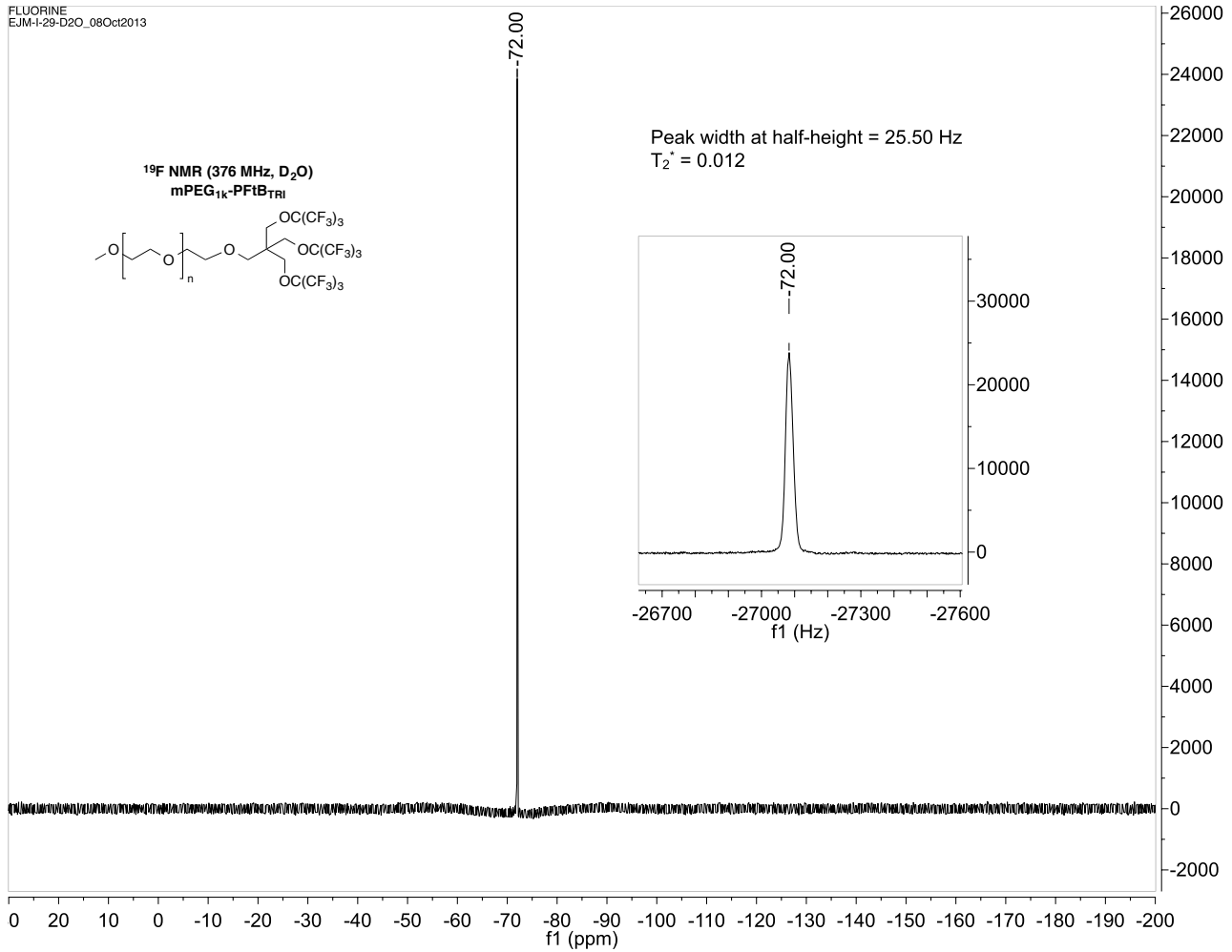
FLUORINE
EJM-I-29-D2O_08Oct2013
-72.00
^{19}F NMR (376 MHz, D_2O)
$mPEG_{1k}$-$PFtB_{TRI}$
$OC(CF_3)_3$
$OC(CF_3)_3$
$OC(CF_3)_3$
O
O
O
n
Peak width at half-height = 25.50 Hz
T_2^* = 0.012
-72.00
30000
20000
10000
0
-26700
-27000
-27300
-27600
f1 (Hz)
26000
24000
22000
20000
18000
16000
14000
12000
10000
8000
6000
4000
2000
0
-2000
0 20 10 0 -10 -20 -30 -40 -50 -60 -70 -80 -90 -100 -110 -120 -130 -140 -150 -160 -170 -180 -190 -200
f1 (ppm)

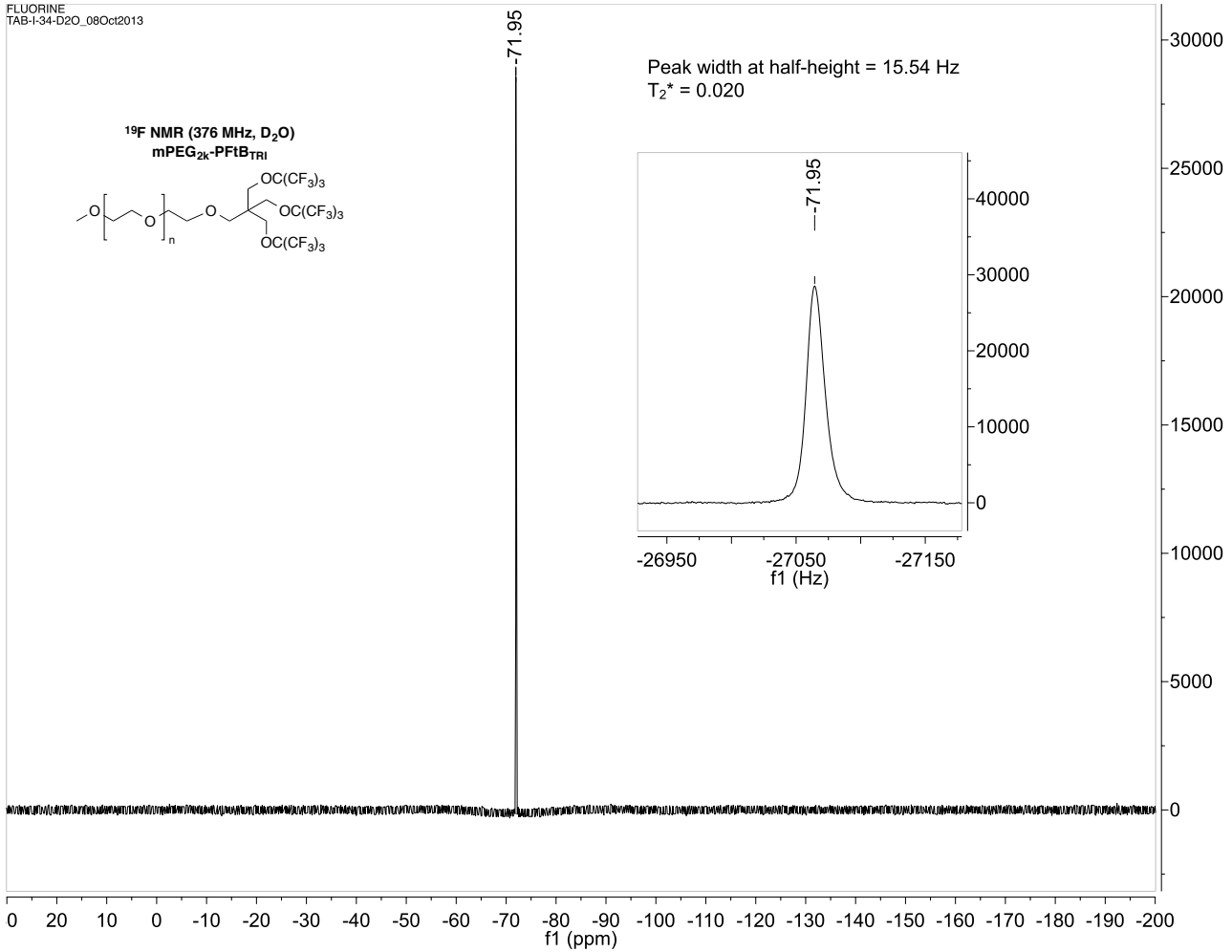
FLUORINE
TAB-I-34-D2O_08Oct2013
-71.95
Peak width at half-height = 15.54 Hz
T2* = 0.020
19F NMR (376 MHz, D2O)
mPEG2k-PFtBTRI
OC(CF3)3
OC(CF3)3
OC(CF3)3
O
O
n
O
-71.95
-26950
-27050
-27150
f1 (Hz)
f1 (ppm)

T_1: $mPEG_{1k}$-$PFtB_{TRI}$

Time (s)	Intensity (obs.)
0.01389	-57.2
0.05556	-44.3
0.125	-34.5
0.2222	-17.3
0.3472	-2.88
0.5	13.8
0.6806	29.5
0.8889	44.3
1.125	56.2
1.389	65.3
1.681	75.8
2	81

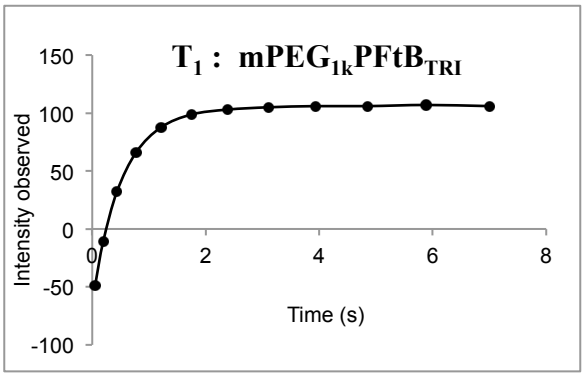

T_2: $mPEG_{1k}$-$PFtB_{TRI}$

Time (s)	Intensity (obs.)
0.016	162
0.064	102
0.16	47.6
0.272	18.1
0.432	5.38
0.624	1.78
0.848	0.8
1.104	0.91
1.408	0.66
1.744	0.67
2.096	-0.81
2.496	0.5

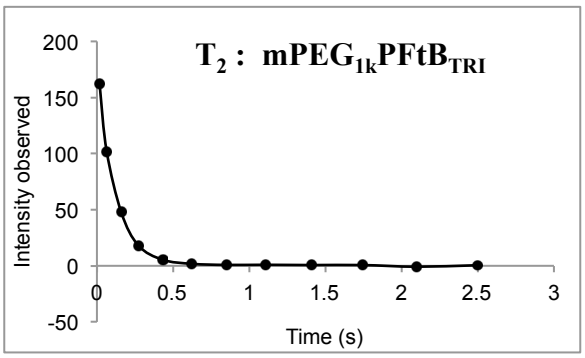

T_1: $mPEG_{2k}$-$PFtB_{TRI}$	
Time (s)	**Intensity (obs.)**
0.03472	-56.4
0.1389	-25.1
0.3125	14.1
0.5556	49.6
0.8681	75.1
1.25	91.3
1.701	99.6
2.222	103
2.812	105
3.472	105
4.201	106
5	106

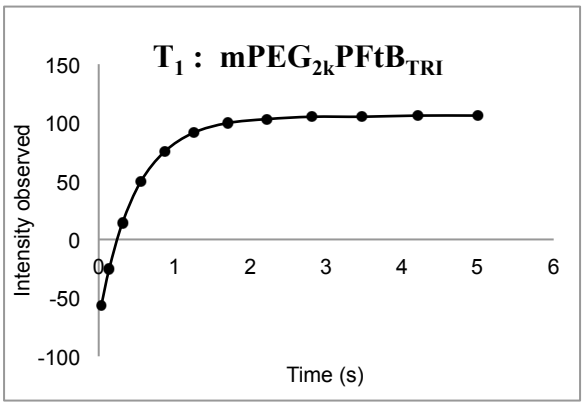

T_2: $mPEG_{2k}$-$PFtB_{TRI}$	
Time (s)	**Intensity (obs.)**
0	279
0.016	230
0.048	173
0.08	130
0.128	84
0.192	48.3
0.256	26.9
0.336	14.2
0.416	6.89
0.528	3.04
0.624	1.6
0.752	0.97

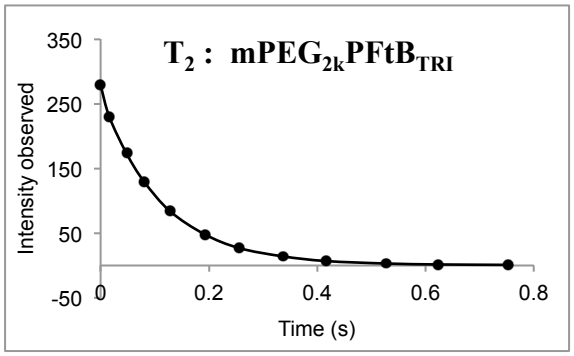

MRI images were acquired using a Varian 4.7 T small animal scanner using a home-built ^{19}F quadrature volume coil with a 1.5 ’’ diameter and 3 ’’ in length. The temperature was maintained at 26 °C. A polymer stock solution of $mPEG_{1k}$-$PFtB_{TRI}$ was prepared by direct dilution of lyophilized solid polymer sample to the highest phantom concentration in Milli- Q water. Lower phantom concentrations were made as serial dilutions from the stock solution in Milli-Q water. Micelle formation was confirmed by DLS. Phantom polymer solutions; 5 mM, 1 mM, 0.1 mM,

0.01 mM, and 0 mM, were transferred to Teflon-free glass vials and ^{1}H images of the phantoms were acquired using a gradient echo pulse sequence with 0.3 × 0.3 × 2.0 mm^3 spatial resolution, 32 × 32 mm^2 field-of-view (FOV), 0.1 s TR, 2.12 ms TE, 20° flip angle, 350 Hz/pixel bandwidth, 8 averages and 1 min 17 sec imaging time. ^{19}F images of the phantoms were acquired using a spin echo pulse sequence with a 1.0 × 1.0 × 2.0 mm^3 spatial resolution, 32 × 32 mm^2 FOV, 2 s TR, 6 ms TE, 32 echoes, 1050 Hz/pixel bandwidth, 24 averages, and 25 min 36 sec imaging time. Images were summed along the echo dimension to increase SNR efficiency by taking advantage of the long T_2.

2.7 Acknowledgements

The research described in this article was partially supported by the National Institutes of Health (grant # GM079375 to SM) and by the University of Wisconsin-Madison School of Pharmacy. Sincere thanks Dr. Jeremy Gordon and the Small Animal Imaging Facility for help with ^{19}F imaging and to the NSF-funded University of Wisconsin Materials Research Science and Engineering Center (DMR-1121288) and the Small Molecule Screening and Synthesis Facility for the use of their facilities and instrumentation. Also thanks to Professor Jamey Weichert, Professor Glen Kwon, and William Tucker for helpful discussions.

2.8 References

(1) Fast, J. P.; Perkins, M. G.; Pearce, R. a; Mecozzi, S. Fluoropolymer-Based Emulsions for the Intravenous Delivery of Sevoflurane. *Anesthesiology* **2008**, *109* (4), 651–656.

(2) Jee, J.-P.; McCoy, A.; Mecozzi, S. Encapsulation and Release of Amphotericin B from an ABC Triblock Fluorous Copolymer. *Pharm. Res.* **2012**, *29* (1), 69–82.

(3) Parlato, M. C.; Jee, J. P.; Teshite, M.; Mecozzi, S. Synthesis, Characterization, and Applications of Hemifluorinated Dibranched Amphiphiles. *J. Org. Chem.* **2011**, *76* (16), 6584–6591.

(4) Lanza, G. M.; Winter, P. M.; Neubauer, A. M.; Caruthers, S. D.; Hockett, F. D.; Wickline, S. a. 1H/19F Magnetic Resonance Molecular Imaging with Perfluorocarbon Nanoparticles. *Curr. Top. Dev. Biol.* **2005**, *70* (05), 57–76.

(5) Janjic, J. M.; Srinivas, M.; Kadayakkara, D. K. K.; Ahrens, E. T. Self-Delivering Nanoemulsions for Dual Fluorine-19 MRI and Fluorescence Detection. *J. Am. Chem. Soc.* **2008**, *130* (9), 2832–2841.

(6) Patrick, M. J.; Janjic, J. M.; Teng, H.; O'Hear, M. R.; Brown, C. W.; Stokum, J. a.; Schmidt, B. F.; Ahrens, E. T.; Waggoner, A. S. Intracellular pH Measurements Using Perfluorocarbon Nanoemulsions. *J. Am. Chem. Soc.* **2013**, *135* (49), 18445–18457.

(7) Soman, N. R.; Lanza, G. M.; Heuser, J. M.; Schlesinger, P. H.; Wickline, S. a. Synthesis and Characterization of Stable Fluorocarbon Nanostructures as Drug Delivery Vehicles for Cytolytic Peptides. *Nano Lett.* **2008**, *8* (4), 1131–1136.

(8) Díaz-López, R.; Tsapis, N.; Fattal, E. Liquid Perfluorocarbons as Contrast Agents for Ultrasonography and 19F-MRI. *Pharm. Res.* **2010**, *27* (1), 1–16.

(9) Yu, J.; Kodibagkar, V. D.; Cui, W.; Mason, R. P. 19F: A Versatile Reporter for Non-Invasive Physiology and Pharmacology Using Magnetic Resonance. *Curr. Med. Chem.* **2005**, *12* (7), 819–848.

(10) Nyström, A. M.; Bartels, J. W.; Du, W.; Wooley, K. L. Perfluorocarbon-Loaded Shell Crosslinked Knedel-like Nanoparticles: Lessons Regarding Polymer Mobility and Self Assembly. *J. Polym. Sci. A. Polym. Chem.* **2009**, *47* (4), 1023–1037.

(11) Peng, H.; Blakey, I.; Dargaville, B.; Rasoul, F.; Rose, S.; Whittaker, A. K. Synthesis and Evaluation of Partly Fluorinated Block Copolymers as MRI Imaging Agents. *Biomacromolecules* **2009**, *10* (2), 374–381.

(12) Nurmi, L.; Peng, H.; Seppala, J.; Haddleton, D. M.; Blakey, I.; Whittaker, A. K. Synthesis and Evaluation of Partly Fluorinated Polyelectrolytes as Components in 19F MRI-Detectable Nanoparticles. **2010**, 1039–1047.

(13) Li, S. D.; Huang, L. Pharmacokinetics and Biodistribution of Nanoparticles. *Mol. Pharm.* **2008**, *5* (4), 496–504.

(14) Du, W.; Nystrom, a M.; Zhang, L.; Powell, K. T.; Li, Y.; Cheng, C.; Wickline, S. a; Wooley, K. L. Amphiphilic Hyperbranched Fluoropolymers as Nanoscopic F Magnetic Resonance Imaging Agent Assemblies. *Biomacromolecules* **2008**, *9*, 2826–2833.

(15) Jiang, Z. X.; Liu, X.; Jeong, E. K.; Yu, Y. B. Symmetry-Guided Design and Fluorous Synthesis of a Stable and Rapidly Excreted Imaging Tracer for19F MRI. *Angew. Chemie - Int. Ed.* **2009**, *48* (26), 4755–4758.

(16) Torchilin, V. P. Targeted Pharmaceutical Nanocarriers for Cancer Therapy and Imaging. *AAPS J.* **2007**, *9* (2), E128–E147.

(17) Porsch, C.; Zhang, Y.; Östlund, Å.; Damberg, P.; Ducani, C.; Malmström, E.; Nyström, A. M. In Vitro Evaluation of Non-Protein Adsorbing Breast Cancer Theranostics Based on 19F-Polymer Containing Nanoparticles. *Part. Part. Syst. Charact.* **2013**, *30*, 381–390.

(18) Richardson, J. C.; Bowtell, R. W.; Mäder, K.; Melia, C. D. Pharmaceutical Applications of Magnetic Resonance Imaging (MRI). *Adv. Drug Deliv. Rev.* **2005**, *57* (8), 1191–1209.

(19) Szabó, D.; Mohl, J.; Bálint, A. M.; Bodor, A.; Rábai, J. Novel Generation Ponytails in Fluorous Chemistry: Syntheses of Primary, Secondary, and Tertiary (nonafluoro-Tert-Butyloxy)ethyl Amines. *J. Fluor. Chem.* **2006**, *127* (11), 1496–1504.

(20) Nemes, A.; Tölgyesi, L.; Bodor, A.; Rábai, J.; Szabó, D. Greener Fluorous Chemistry: Convenient Preparation of New Types of "CF 3-Rich" Secondary Alkyl Mesylates and Their Use for the Synthesis of Azides, Amines, Imidazoles and Imidazolium Salts. *J. Fluor. Chem.* **2010**, *131* (12), 1368–1376.

(21) Jiang, Z. X.; Yu, Y. B. The Design and Synthesis of Highly Branched and Spherically Symmetric Fluorinated Macrocyclic Chelators. *Synthesis (Stuttg).* **2008**, No. 2, 215–220.

(22) Jiang, Z. X.; Yu, Y. B. The Design and Synthesis of Highly Branched and Spherically Symmetric Fluorinated Oils and Amphiles. *Tetrahedron* **2007**, *63* (19), 3982–3988.

(23) Buer, B. C.; Levin, B. J.; Marsh, E. N. G. Perfluoro-Tert-Butyl-Homoserine as a Sensitive 19F NMR Reporter for Peptide-Membrane Interactions in Solution. *J. Pept. Sci.* **2013**, *19* (February), 308–314.

(24) Weissig, V.; Whiteman, K. R.; Torchilin, V. P. Accumulation of Protein-Loaded Long-Circulating Micelles and Liposomes in Subcutaneous Lewis Lung Carcinoma in Mice. *Pharm. Res.* **1998**, *15* (10), 1552–1556.

(25) Tucker, W. B.; McCoy, A. M.; Fix, S. M.; Stagg, M. F.; Murphy, M. M.; Mecozzi, S. Synthesis, Physicochemical Characterization, and Self-Assembly of Linear, Dibranched, and Miktoarm Semifluorinated Triphilic Polymers. *J. Polym. Sci. Part A Polym. Chem.* **2014**, *52* (23), 3324–3336.

(26) Johansson, E.; Lundquist, A.; Zuo, S.; Edwards, K. Nanosized Bilayer Disks: Attractive Model Membranes for Drug Partition Studies. *Biochim. Biophys. Acta - Biomembr.* **2007**, *1768* (6), 1518–1525.

(27) Du, W.; Nyström, A. M.; Zhang, L.; Powell, K. T.; Li, Y.; Cheng, C.; Wickline, S. a.; Wooley, K. L. Amphiphilic Hyperbranched Fluoropolymers as Nanoscopic 19F Magnetic Resonance Imaging Agent Assemblies. *Biomacromolecules* **2008**, *9* (10), 2826–2833.

(28) Ruiz-Cabello, J.; Barnett, B. P.; Bottomley, P. a.; Bulte, J. W. M. Fluorine (19F) MRS and MRI in Biomedicine. *NMR Biomed.* **2011**, *24* (2), 114–129.

(29) Gorodetskaya, I. a.; Choi, T. L.; Grubbs, R. H. Hyperbranched Macromolecules via Olefin Metathesis. *J. Am. Chem. Soc.* **2007**, *129* (42), 12672–12673.

CHAPTER 3:

Development of triphilic micelles for enhanced chemotherapeutic delivery

*This chapter will be published, in part as "Long-circulating drug nanocarriers: branched semi-fluorous cores enhance stability of triphilic polymer self-assemblies" by Sarah E. Decato, William B. Tucker, Eric J. Madsen, Yutaka Miura, Kazunori Kataoka and Sandro Mecozzi.

Abstract.

The development of polymeric micelle drug delivery vehicles has been a major research effort over the last decade. The utility of micelle therapeutics in the field of chemotherapy is promising; however, successful translation into the clinic has been difficult due in part to the low bioavailability of the encapsulated drugs arising from the instability of the micelle nanoparticles. A branched triphilic, semifluorinated polymer was synthesized and characterized, that forms small micelle self-assemblies approximately 14 nm in size. The micelles form an intermediate hydrophobic shell, capable of loading and retaining significant hydrophobic drug payload, and a perfluoro-*tert*-butyl (PFtB) fluorous core, which imparts enhanced thermodynamic and *in vivo* stability to the micelle assemblies. The fluorophilicity and structure of the PFtB moiety were both found to be essential to afford this enhanced stability, which can be leveraged as a design element to improve micelle based drug-delivery efficacy.

3.1 Motivation and intent

Nanotechnology provides an advantageous platform to address the major challenges of cancer therapy, specifically in chemotherapeutic drug delivery. Although chemotherapy is an essential component of cancer treatment, the inherent toxicity and low blood-solubility of the drugs often result in poor treatment efficacy and severe patient side effects.[1,2] Through a collective research effort across a variety of fields, various nano-sized drug carriers have been developed that may address several of the limitations in current chemotherapy practices.[3] A promising subset of these nanocarriers are self-assembling polymeric aggregates. Specially designed amphiphilic polymers self-organize in water to form larger, more complex structures that can be readily modified in size and shape according to the needs of the specific application.[4] Chemotherapeutics are then encapsulated inside these aggregate structures, providing enhanced solubility. Typically, the unimers composing the self-assemblies are chosen to be of a size that can be easily excreted by renal filtration to reduce bioaccumulation. With further careful design and surface modification of the aggregate, imaging and tumor targeting ligands can be incorporated into the nanocarrier to increase bioavailability and reduce side effects of the encapsulated drug.[5,6]

Polymeric micelle self-assemblies are uniquely poised to serve as efficient chemotherapeutic delivery vehicles.[7,8] They are small in size—typically 10–100 nm—and are therefore able to exploit the enhanced permeation and retention (EPR) effect to increase preferential delivery of the drug to cancerous cells over healthy cells.[9,10] The vasculature surrounding cancerous tissue is typically malformed with small gaps. The EPR effect is the exploitation of this phenomenon to direct and accumulate small nanocarriers[11] within tumor tissue, facilitated by impaired lymphatic drainage at the tumor site.[12,13] Tumor heterogeneity and varying tumor microenvironments can alter the impact of the EPR effect[14], therefore sub-50 nm particles are preferred to enhance penetration in hypovascular or hypopermeable tumors, such as intractable pancreatic tumors.[15]

The accumulated drug-carrier can then utilize any appended targeting ligands to further increase cell uptake and penetration. Much research has been focused on this last aspect of tumor targeting: active-targeting ligands. However, the efficacy of the targeting ligand strongly relies upon the nanocarrier's ability to remain in circulation in the blood long enough to accumulate at the tumor site.

Prolonged blood circulation can be difficult to achieve, mainly due to the numerous mechanisms by which a foreign body can be recognized, removed from circulation, and ultimately excreted.[16] Although increasing the size of a nanoparticle generally leads to increased circulation time, small particles are still preferred not only to take advantage of the EPR effect, but also to reduce blood clearance and serum protein absorption.[17] Typically, the amphiphilic polymers contain a hydrophobic block that is used to encapsulate and solubilize drug. Unfortunately, this block can also be recognized by hydrophobic blood components, such as serum proteins, that dissociate the aggregate and result in a burst release of the toxic drug. Although the hydrophobic block is essential to the nanocarrier design, prolonged circulation can still be achieved by enhancing the stability of the aggregate.[18,19]. The insertion of fluorous domains into the structure of an amphiphilic polymer provides an attractive way to enhance stability of the nanocarrier.

3.2 Triphilic polymer design

The hyper-hydrophobicity and lipophobicity of a fluorous segment increases both the *in vivo* (kinetic) and the inherent thermodynamic stability of the micelle aggregate.[20,21] For this end, a specially designed perfluoro-*tert*-butyl (PFtB) amphiphilic polymer has been synthesized and characterized that forms small, discrete micelles. The triphilic nature of the micelles induces internal segregation[22], self-assembling to form a small hydrophobic shell that can encapsulate hydrophobic drugs with high loading efficiency and retention, and a fluorous core, which

enhances both the kinetic and thermodynamic stability of the micelle, allowing for prolonged stability both *in vitro* and *in vivo*.

The semifluorinated polymers are a second-generation design based upon an mPEG-fluorocarbon polymer series as described previously (Chapter 2).[21] The *tris*-perfluoro-*tert*-butyl ($PFtB_{TRI}$) moiety was chosen to provide 27 symmetrical fluorine atoms that would give rise to a single, intense ^{19}F-NMR signal. This design served as a proof of concept, demonstrating that an amphiphile containing this fluorous PFtB tail can form small, discrete micelles that can be visualized via ^{19}F magnetic resonance imaging (MRI). In the second-generation design the original semifluorinated polymer was expanded to include a short hydrocarbon chain between the mPEG and fluorocarbon segments to allow for hydrophobic drug loading capabilities. Although the imaging capabilities of these next-generation polymers are not discussed here, the $PFtB_{TRI}$ group still allows for their potential application as theranostic (dual delivery and imaging) agents (see Chapter 4).

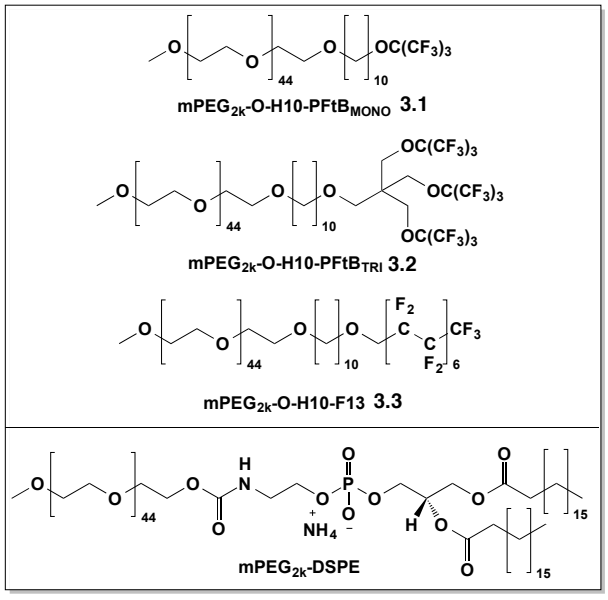

Figure 3.1 Triphilic PFtB fluorous polymer design.
Top: Triphilic PFtB polymers designed to elucidate the effects of fluorophilicity and tail structure. **Bottom**: Classical phospholipid amphiphile used in traditional micelle drug delivery, provided for comparison.

Three novel semifluorinated polymers, **3.1**, **3.2**, and **3.3 (Figure 3.1)**, are presented, which maintain equal mPEG and hydrocarbon length and arrangement but vary in fluorine content (**3.1** vs **3.2**, **3.3**) and fluorocarbon configuration (**3.2** vs **3.3**). The 1,2-distearoyl-*sn*-glycero-3-phosphoethanolamine-*N*-[methoxy(polyethylene glycol)-2000 (mPEG$_{2k}$-DSPE), a classical, extensively characterized, mPEG-phospholipid polymer[23,24], was chosen to compare the properties of the new semifluorinated polymers to those of traditional polymeric amphiphiles used in drug delivery applications. mPEG$_{2k}$-DSPE forms micelle self-assemblies of a comparable size to those formed by polymer **3.1**-**3.3**. Differences observed between the semifluorinated and the classical micelles will demonstrate how the installation of a fluorous core can serve as a tool to enhance the stability, and therefore delivery, of encapsulated hydrophobic cargo.

3.3 Results and discussion

3.3.1 Synthetic scheme and rationale

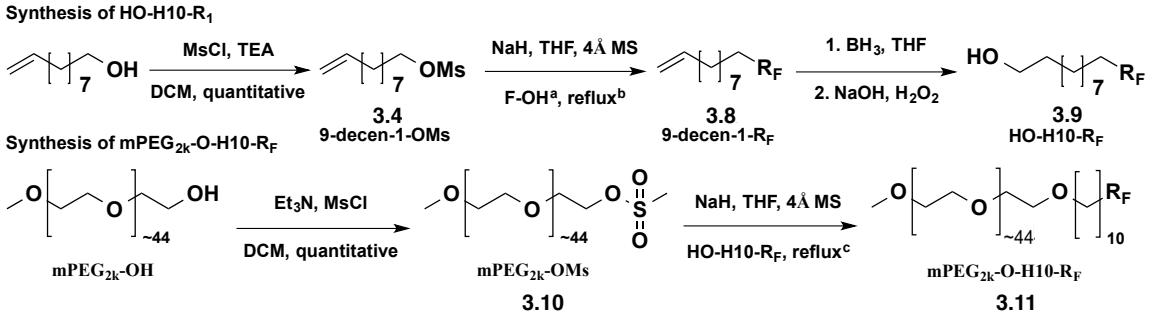

R_1	[a]Fluorous alcohol (F-OH)	[b,c]Reflux time (days)	Percent Yield		
			9-decen-1-R_F	HO-H10-R_F	mPEG$_{2k}$-O-H10-R_F
$PFtB_{MONO}$	(3.5) $K^{\oplus}\,^{\ominus}OC(CF_3)_3$	[b]1, [c]2	99%	59%	(**1**) 79%
$PFtB_{TRI}$	(3.6) HO, $OC(CF_3)_3$ ×3	[b]3, [c]7	67%	93%	(**2**) 63%
F13	(3.7) HO, $C(F_2)_6CF_3$	[b]4, [c]7	31%	75%	(**3**) 38%

Figure 3.2 Synthesis of the triphilic fluorous polymers.

The semifluorous polymers were synthesized via a substitution reaction between the respective hydrocarbon-fluorocarbon alcohol (HO-H10-R_F) and $mPEG_{2k}$-OMs (**Figure 3.2**). The desired hydrocarbon–fluorocarbon alcohol was prepared by mesylation of commercially available 9-decen-1-ol, followed by substitution with the corresponding fluorous alcohol (F-OH) that was either purchased (F13-OH) or synthesized as described previously (Chapter 2).[25] The synthesis of the fluorous polymers was fairly straightforward and relatively high yielding despite the long-reaction times. Significant improvements were made in the $mPEG_{2k}$-OMs coupling to the F-OH by adding 4 Å MS. This was particularly true in the case of $PFtB_{TRI}$-OH as this compound was difficult to dry due to volatility. The F13-polymer exhibited the lowest yields, which is most likely due to the increased surface-activity seen with these compounds as evident by the extreme amount of foam produced during all steps of the reaction and purification in comparison to the other fluorous polymers.

3.3.2 Physicochemical characterization: CMC, DLS, and microviscosity

The addition of the ten-unit hydrocarbon (H10) segment did not disturb the polymer's ability to form small, discrete micelles in aqueous solution at sub-mM critical micelle concentrations (CMCs). It is important to note that the semifluorinated micelles remained below 30 nm and maintained a narrow size distribution (**Table 3.1**).

Table 3.1 Phyiscochemical characteristics of the amphiphilic polymers.
Physicochemical characterization of $mPEG_{2k}$-O-H10-R_F polymers and their aqueous micelle assemblies [a]Critical micelle concentration (CMC) was determined by surface tensiometry. [b]Size of micelles reported by percent volume (%) as hydrodynamic diameter, determined by dynamic light scattering (DLS) using spherical fits. [c]Microviscosity measured via encapsulated 1,3-bis-(1-pyrenyl)propane (P3P) fluorescence.

Compound	pCMC (-log(M)[a]	DLS nm[b]	Microviscosity[c]
$mPEG_{2k}$-O-H10-$PFtB_{MONO}$	4.82 ± 0.05	10.6 ± 1.8 (99.8%)	3.81 ± 0.16
$mPEG_{2k}$-O-H10-$PFtB_{TRI}$	3.98 ± 0.14	13.3 ± 2.0 (100%)	6.58 ± 0.14
$mPEG_{2k}$-O-H10-F13	4.49 ± 0.18	21.5 ± 6.7 (98.7%)	6.44 ± 0.10
$mPEG_{2k}$-DSPE[20]	4.90 ± 0.17	13.9 ± 1.6 (100%)	5.60 ± 0.22

The size of the nanoparticle will determine the rate of extravasation and uptake of the drug-carrier from the vasculature into the tumor cells.[26] These small semifluorinated micelles are therefore well equipped to maximize accumulation of the encapsulated drug despite the heterogeneity present in various cancer types and patient populations. After this initial characterization to confirm that micelles could indeed be formed, it was then crucial to identify which polymer(s) could maximize encapsulation and retention of hydrophobic drugs. A rough indication of drug-loading capability can be ascertained by microviscosity via fluorescence measurements of an encapsulated dye. An increased microviscosity inside the micelle assembly indicates restricted movement of the polymer chains, which typically correlates to higher encapsulation of hydrophobic material.[27,28] Compounds **3.2** and **3.3** demonstrated a microviscosity nearly twice that of compound **3.1** (**Table 3.1**) and therefore should also show enhanced encapsulation capability.

3.3.3 Encapsulation of paclitaxel (PTX)

To further elucidate the relationship between polymer structure and encapsulation efficiency, a classical, hydrophobic chemotherapeutic, paclitaxel (PTX)[29] was then encapsulated within the

semifluorinated micelles via the solvent evaporation method. The amount of encapsulated drug was quantified by HPLC both upon formulation and after 24 hours (**Figure 3.3**).

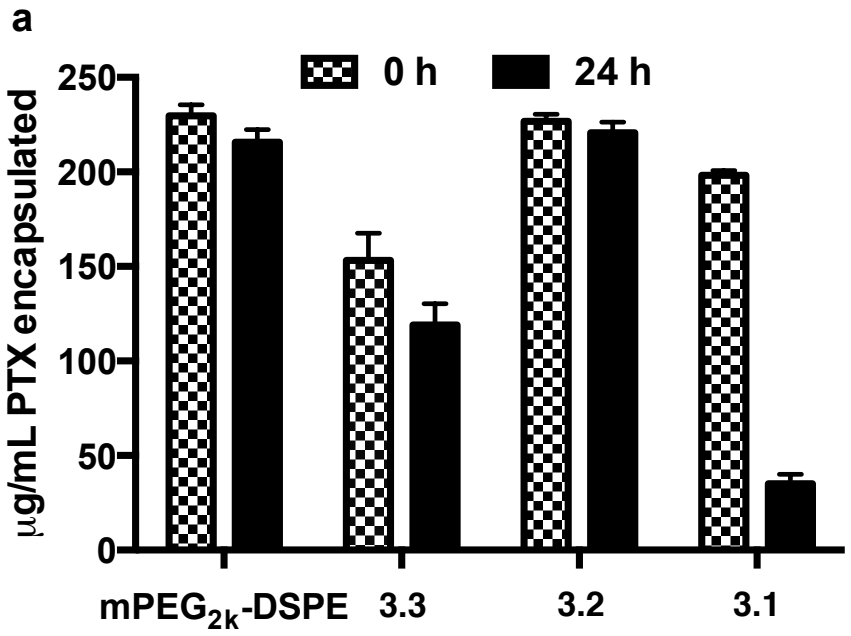

Figure 3.3 Amphiphilic polymer encapsulation of paclitaxel (PTX).
Encapsulation of PTX at 0 and 24 h, quantified by HPLC. Fluorous polymer **3.1** and **3.2** show comparable initial loading (0 h) to the classical $mPEG_{2k}$-DSPE micelles; however, only **3.2** also shows comparable retention after 24 h.

Polymers **3.1** and **3.2** showed comparable initial encapsulation rates; however, after 24 hours only polymer **3.2** and $mPEG_{2k}$-DSPE showed high retention of PTX. In terms of the drug-loading capacity, the percent-weight encapsulation of PTX after 24 h into **3.2** and $mPEG_{2k}$-DSPE micelles was comparable (3.22 ± 0.08 and 3.21 ± 0.10 wt.%, respectively). The fluorous core micelles formed by polymer **3.2** appear to encapsulate and retain a larger density of the hydrophobic drug inside a small intermediate hydrophobic shell in comparison to a traditional hydrophobic core formed by two octadecyl hydrocarbon (H18) chains ($mPEG_{2k}$-DSPE). This significant result demonstrates that a small intermediate shell in the micelle can encapsulate comparable amounts of hydrophobic drug to that bound within the large hydrophobic core of a traditional micelle. It is

also important to highlight that the identity of the fluorous domain greatly affects the drug loading efficiency. Firstly, the rapid release of drug from polymer **3.1** micelles ($PFtB_{MONO}$) demonstrates the need for significant tail perfluorination to generate adequate fluorophilicity to provide micelle stability. In addition to fluorophilicity, the tail structure is also crucial to achieving desired nanocarrier properties. Compounds **3.2** and **3.3** have the same number of fluorine atoms in the polymer tail but differ in configuration: branched and linear, respectively. Encapsulation data demonstrate that the non-linear arrangement of the fluorine-bearing carbon atoms in polymer **3.2** enhances the micelle behavior. The fluorous core formed from linear-fluorocarbon tail polymer **3.3** was only able to encapsulate 1.77 ± 0.17 wt.% after 24 h., 55% less than its branched counterpart, **3.2.**

3.3.4 Cell culture: Hemolysis and A549 human lung cancer cell toxicity

Compound **3.2** was selected for further investigation, as it demonstrated the desirable drug loading qualities of a classical micelle drug-delivery vehicle. Due to the surfactant properties of **3.2**, the acute toxicity was evaluated at clinically relevant concentrations,[30] showing less than 5% hemolytic activity against rabbit red blood cells relative to a positive control after 3 h of exposure. Next, a cell viability assay was performed against the A549 human lung cancer cell line (**Figure 3.4**).

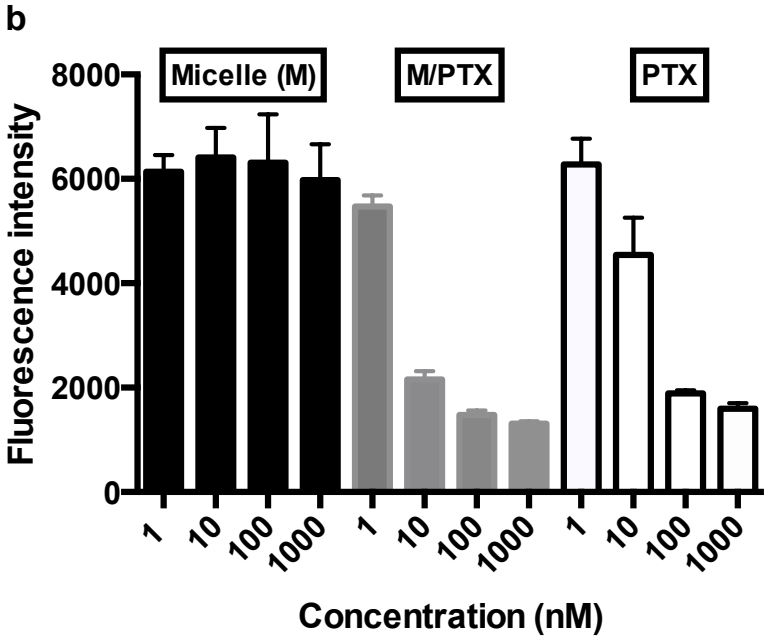

Figure 3.4 Cell toxicity of PTX-loaded mPEG$_{2k}$-O-H10-PFtB$_{TRI}$ micelles.
Cell viability assay of A549 human lung cancer cells against empty (M) and PTX-loaded mPEG$_{2k}$-O-H10-PFtB$_{TRI}$ (**3.2**) micelles (M/PTX) and free PTX in a 0.05% DMSO solution (PTX).

The empty micelles of compound **3.2** again showed no acute toxicity to the cells, while the cell death profile after exposure to PTX-loaded micelles closely resembled that of the cells treated with equivalent concentrations of PTX in a 0.05% DMSO solution. This assay further demonstrated that the drug is encapsulated within the micelles and can be successfully released to treat cancer cells *in vitro*. It has been demonstrated that **3.2** efficiently encapsulates hydrophobic material in the confined hydrophobic domain between the mPEG corona and the fluorous core. Also, drug encapsulation, retention, and potency have not been deterred, despite the drug's potentially increased exposure to the hydrophilic interface by residing in a thin intermediate shell rather than a traditional hydrophobic core. In essence, polymer **3.2** has been shown to be on par with traditional micelle delivery systems. The following results serve to differentiate the potential

of this triphilic polymer design from a classical micelle vehicle by demonstrating its ability to enhance the encapsulated drug's bioavailability via increased blood-circulation time.

3.3.5 In vitro time-release profile

Previous preliminary studies[20] demonstrated that introducing a fluorous core in a micelle decreases the solubility of the polymer unimers, thereby imparting enhanced thermodynamic stability. Additionally, the micelle's kinetic or *in vivo* stability should also dramatically increase since fluorocarbons repel classical hydrophobic molecules. Installing a large $PFtB_{TRI}$ group at the polymer terminus can leverage this lipophobic character to inhibit destabilizing interactions with hydrophobic blood components to prolong the circulation of the micelles in blood. The extent of this enhanced kinetic stabilization was tested *in vitro* (and *in vivo*, see Chapter 4). Initially, an *in vitro* time-release study was performed where all three semifluorinated polymers were tested, as no correlation between encapsulation capability and stability can be assumed. PTX was encapsulated within each micelle and dialyzed under sink conditions in buffer for one week. Aliquots of the micelle solutions were obtained at various time points, and the amount of PTX remaining within the micelle vehicles was quantified by HPLC. The time-release profiles were plotted for each compound (**Figure 3.5**).

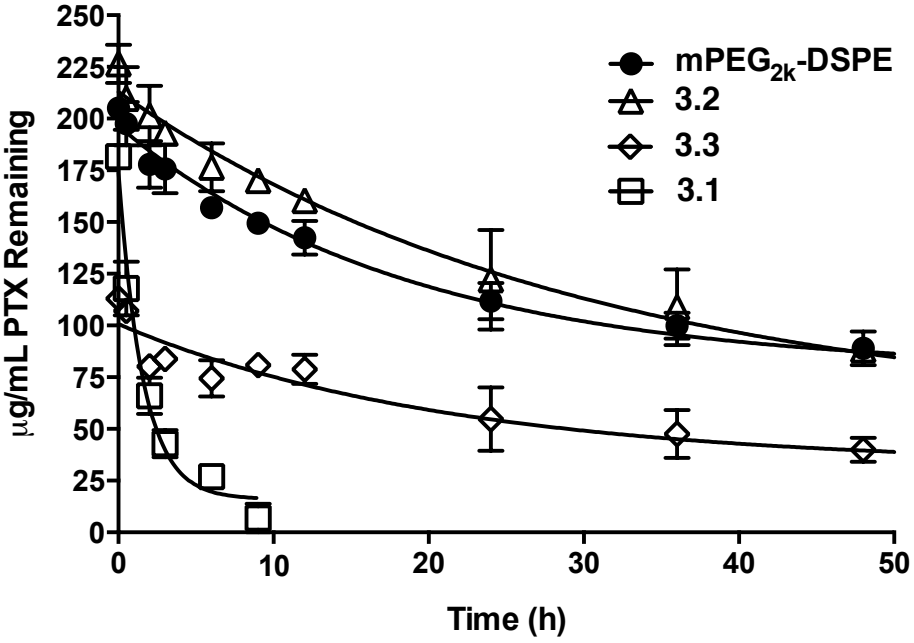

Figure 3.5 *In vitro* time-release of PTX from amphiphilic micelles.
Time-release profiles of the semifluorinated polymers and classical $mPEG_{2k}$-DSPE PTX-loaded micelles. Micelles were dialyzed under sink conditions up to 1 week (the first 50 h are plotted). The remaining PTX encapsulated in the micelles was quantified by HPLC.

Compound **3.1** showed complete release by approximately 9 h and compound **3.3** was unable to fully encapsulate and retain the entirety of drug loaded in this assay. Compound **3.2** showed the slowest release profile of all the semifluorinated polymers and showed comparable release to the classical micelle. This routine *in vitro* assay again identified **3.2** as the lead polymer and encouraged further investigation of this polymer design in a more complex system where the influence of hydrophobic blood components could be realized.

3.3.6 In vitro serum stability: FRET assay

To provide an initial assessment of stability under physiological conditions, an *in vitro* study was performed in which a FRET dye pair was encapsulated within the semifluorinated and $mPEG_{2k}$-DSPE micelles. The FRET ratio was measured over time after dilution in human serum

(**Figure 3.6**).[31] An initial decrease in the FRET ratio within the first 25 min is typical as loosely bound fluorescent dye releases from the micelle corona or hydrophobic-hydrophilic interface. Also the FRET dyes are charged species and therefore the maximum dye loading for each polymer is variable. The stability of the micelles is indicated by a consistent FRET ratio over time. Micelles which are dissociated by the serum proteins will show a continue decrease in FRET ratio over time until reaching 0.4, the basal FRET ratio. Compound **3.2** maintained a fairly constant FRET ratio, showing the least change over several hours (see supplemental information). $mPEG_{2k}$-DSPE micelles showed a 14% decrease in the FRET ratio, while polymer **3.2** micelles showed < 1 % decrease over 2 h.

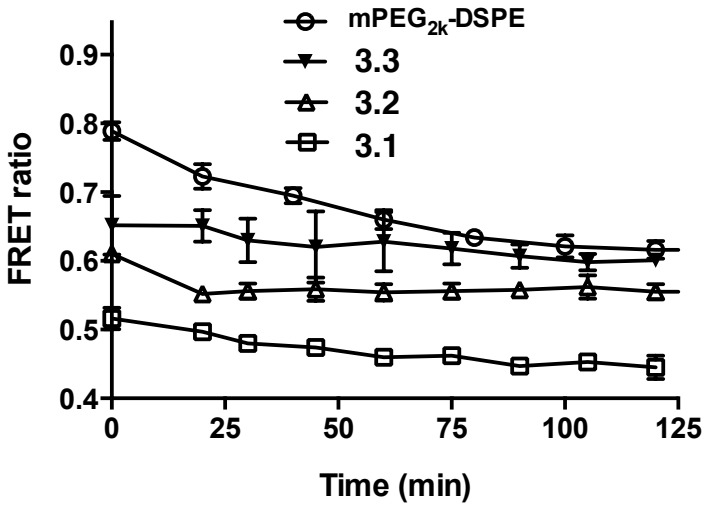

Figure 3.6 *In vitro* serum stability of amphiphilic micelles.
DiI and DiO FRET dye pair were encapsulated within the amphiphilic micelles. The micelles were diluted in human serum with gentle agitation and the FRET ratio was measured over time. Decreasing values indicate micelle instability and dissociation.

This experiment further demonstrated that **3.2** formed the most stable micelles relative to both of the other semifluorinated polymers and the traditional $mPEG_{2k}$-DSPE polymer. Collectively, these data demonstrate the advantages of using semifluorinated polymeric micelles

in drug delivery. These polymers should allow for long circulation times related to both enhanced thermodynamic and kinetic stability of the self-assembly.

3.4 Conclusion

Installation of a branched, fluorous tail at the terminus of a PEGylated amphiphile allows for the formation of small, discrete micelles that can encapsulate and retain hydrophobic compounds in a small intermediate hydrophobic shell. Furthermore, the perfluoro-*tert*-butyl (PFtB) tail deters destabilizing interactions with hydrophobic blood components, which prolongs the circulation time of the micelles and encapsulated cargo. Furthermore, the original design intent of the PFtB tail to provide 27 chemically equivalent fluorine atoms suitable for ^{19}F-MR imaging, remains as an additional advantageous feature of the polymer structure.[25] This triphilic nanocarrier design provides inherent stability for increased bioavailability and reduced toxic-side effects, highlighting how careful manipulation of the fluorous phase can afford properties unparalleled by non-fluorinated compounds.

3.5 Experimental

3.5.1 General materials and methods

1H,1H-perfluorotetradecanol was purchased from SynQuest Laboratories Inc. (Alachua, FL). Perfluoro-*tert*-butanol was purchased from Matrix Scientific (Columbia, SC). 1,2-distearoyl-*sn*-glycero-3-phosphoethanolamine-*N*-[methoxy(polyethylene glycol)-2000] (mPEG$_{2k}$-DSPE) was purchased from Avanti Polar Lipids (Alabaster, AL). Paclitaxel (PTX) was purchased from LC Laboratories (Woburn, MA). 1,3-*Bis*-(1-pyrenyl)propane (P3P) was purchased from Life Technologies (Carlsbad, CA). Pooled normal human serum was purchased from Innovative Research (Novi, MI). Rabbit red blood cells (10%, 15 mL) were purchased from Lampire Biological Laboratories Inc. (Pipersville, PA). A549 human lung cancer cells were purchased from American Type Culture Collection (ATCC, Manassas, VA). (All solvents were of ACS

grade or higher and were purchased from Sigma-Aldrich (St. Louis, MO). Mili-Q water was acquired from Milipore Mili-Q system equipped with a 0.22 μm filter. All other reagents and solvents were purchased from Sigma Aldrich Co. (Milwaukee, WI) and used as received, unless otherwise specified. Small molecule and polymer chromatographic separations were performed using Silicycle 60 Å SiO_2 or using a Combi-flash Rf 200 (Teledyne ISCO, Lincoln, NE) equipped with ELSD for compound visualization using REDI-Sep Rf Gold high performance silica cartridges.

^{1}H, ^{19}F, and ^{13}C NMR spectra were obtained on Varian Unity-Inova 400 or Unity-Inova 500 spectrometers using $CDCl_3$ as the solvent with tetramethylsilane (TMS) as an internal reference at 25 °C unless otherwise specified. Polymer purity was analyzed by MALDI-MS on a Bruker Ultraflex III MALDI TOF/TOF using α-cyano-4-hydroxycinnamic acid (CHCA) matrix unless otherwise specified.

3.5.2 Synthesis and chemical characterization

9-decen-1-OMs (3.4): To a dry roundbottom flask, in an ice-water bath under argon, was added 50 mL of dry dichloromethane (DCM), 9-decen-1-ol (1.3 mL, 17 mmol) and triethylamine (TEA, 4.3 mL, 31 mmol). This stirred for 30 min before methanesulfonyl chloride (MsCl, 1.3 mL, 17 mmol) was added drop-wise. After running overnight, the reaction was diluted with 100 mL of DCM and then washed with 3 x 50 mL aliquots of saturated ammonium chloride (NH_4Cl) solution. The organic layers were dried over $MgSO_4$ and condensed under reduced pressure to give 3.2 g (quantitative yield) of yellow oil. ^{1}H NMR (400 MHz, $CDCl_3$): δ 5.81 (ddt, J = 17.3, 10.3, 6.7 Hz, 1 H), 4.99 (ddt, J = 17.3, 1.7, 1.2 Hz, 1 H), 4.93 (ddt, J = 10.3, 1.7, 1.2 Hz, 1 H), 4.22 (t, J = 6.7 Hz, 2 H), 3.00 (s, 3 H), 2.04 (qt, J = 5.6, 1.4 Hz, 2 H), 1.75 (q, J = 7.0 Hz, 2 H), 1.44–1.29 (m, 12 H). ^{13}C NMR (101 MHz, $CDCl_3$): δ 139.3, 114.4, 110.0, 70.4, 37.5, 33.9, 29.4, 29.3, 29.2, 29.0, 25.6.

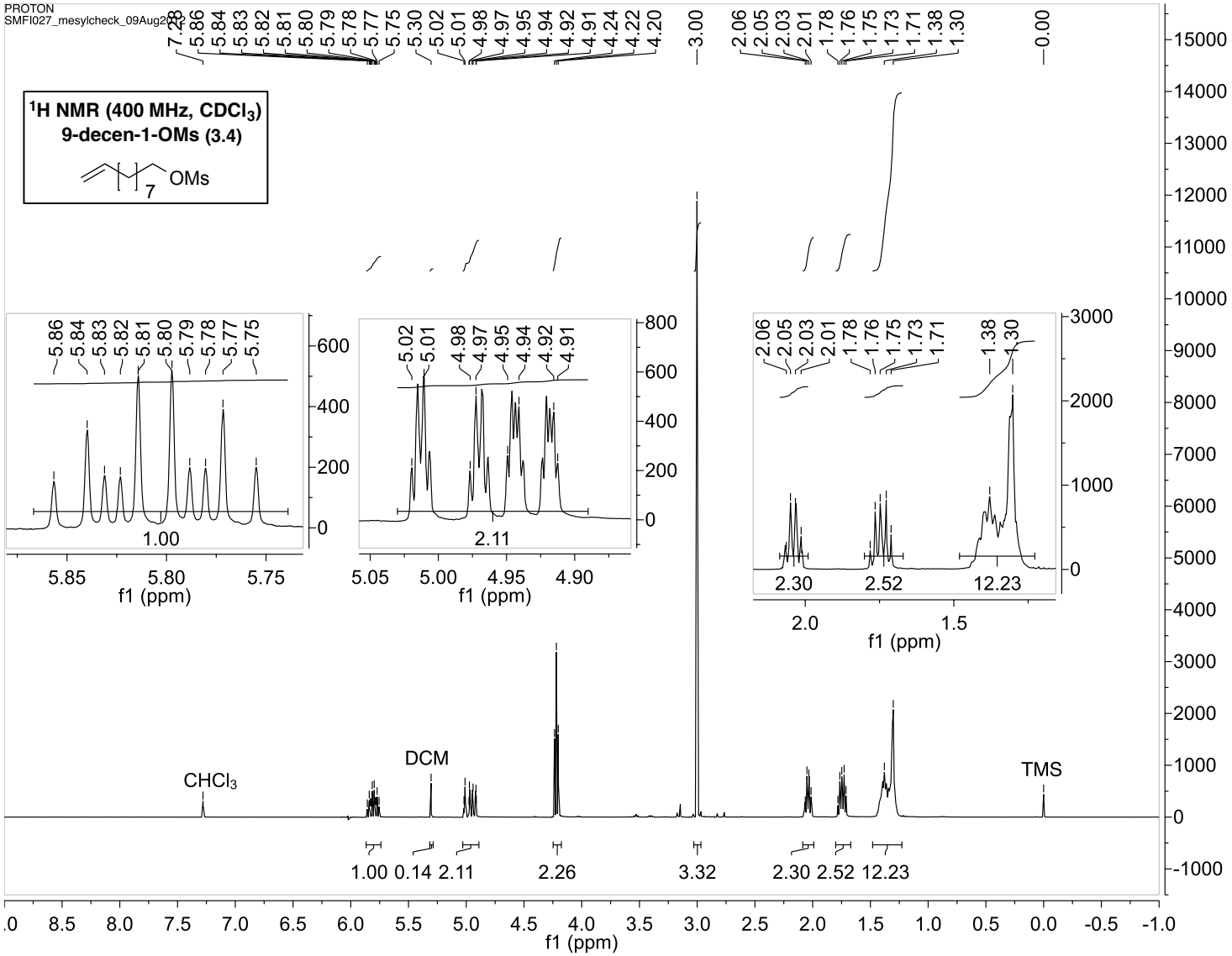
PROTON
SMFI027_mesylcheck_09Aug2012
^{1}H NMR (400 MHz, $CDCl_3$)
9-decen-1-OMs (3.4)
OMs
7
CHCl3
DCM
TMS
1.00 0.14 2.11 2.26 3.32 2.30 2.52 12.23
f1 (ppm)

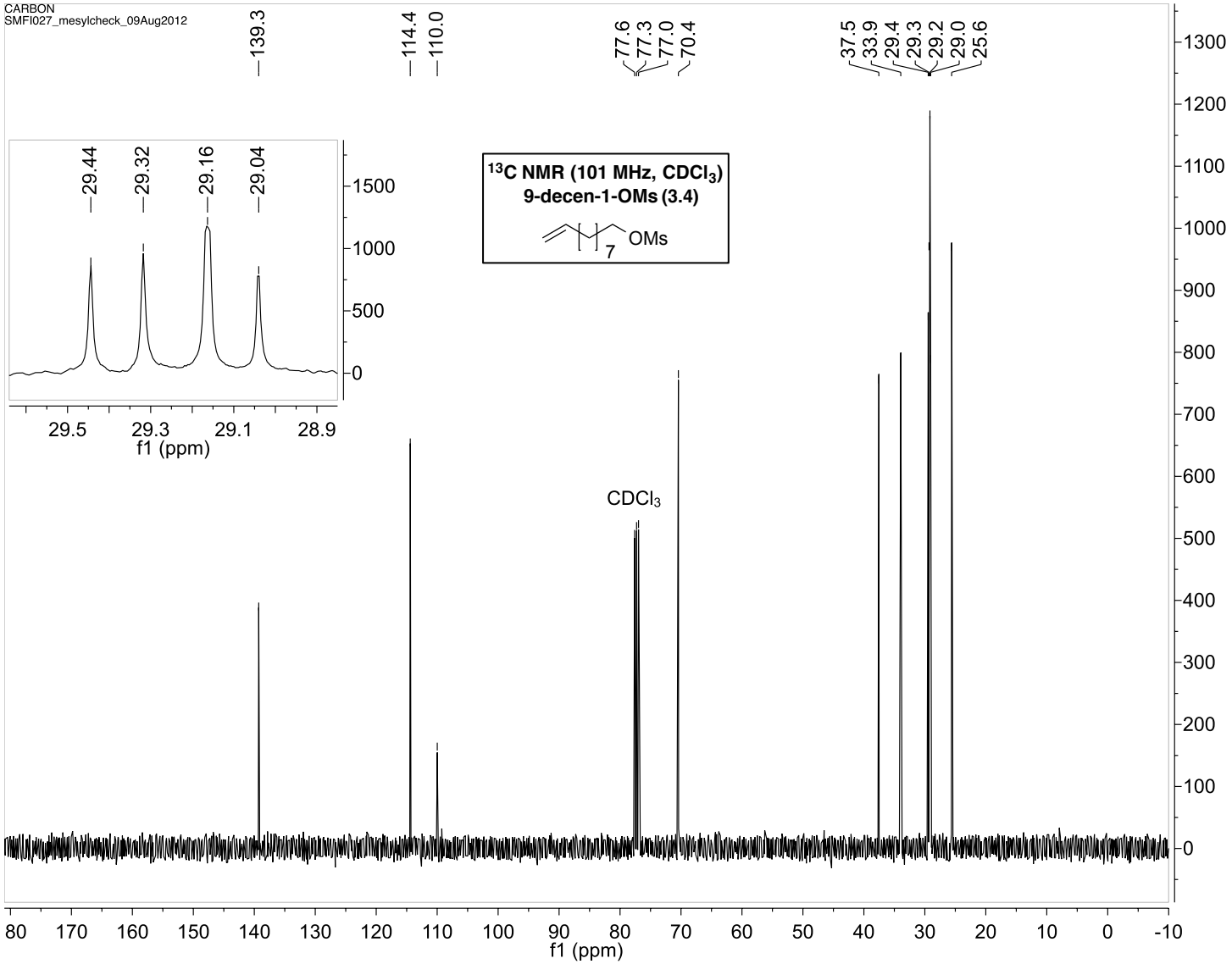
CARBON
SMFI027_mesylcheck_09Aug2012
139.3
114.4
110.0
77.6
77.3
77.0
70.4
37.5
33.9
29.4
29.3
29.2
29.0
25.6
29.44
29.32
29.16
29.04
29.5
29.3
29.1
28.9
f1 (ppm)
13C NMR (101 MHz, CDCl3)
9-decen-1-OMs (3.4)
OMs
7
CDCl3
f1 (ppm)

9-decen-1-R_F (3.8):

R_F = $PFtB_{MONO}$: To an oven-dried roundbottom flask under argon, was added 9-decen-1-OMs (**3.4**, 4.0 g, 17.1 mmol). The solid was dissolved in 30 mL of dioxane, followed by the addition of potassium perfluoro-*tert*-butoxide[25] (7.0 g, 26 mmol). The mixture was heated to reflux and allowed to stir overnight. After this time the reaction was cooled to room temperature and diluted with 100 mL of DCM. The organic phase was washed with 3 x 50 mL aliquots of saturated NH_4Cl solution, dried over $MgSO_4$ and condensed under reduced pressure to give an opaque, yellow liquid. The product was then purified by automated flash chromatography using the Combi-flash purification system using a RediSep normal-phase Gold silica column (24 g) with a 0-5% EtOAc/hexanes gradient to give 6.33 g of product (99% yield). ^{1}H NMR (400 MHz, $CDCl_3$): δ 5.83 (ddt, J = 17.3, 10.3, 6.7 Hz, 1 H), 5.02 (ddt, J = 17.3, 1.7, 1.2 Hz, 1 H), 4.96 (ddt, J = 10.3, 1.7, 1.2 Hz, 1 H), 4.04 (t, J = 6.4 Hz, 2 H), 2.11 (qt, J = 6.8, 1.4 Hz, 2 H), 1.71 (q, J = 6.5 Hz, 2 H), 1.44–1.33 (m, 10 H). ^{13}C NMR (101 MHz, $CDCl_3$): δ 139.2, 120.7 (q, J = 292.8 Hz, $C(C^*F_3)_3$), 114.3, 79.9 (decet, J = 29.1 Hz $C^*(CF_3)_3$), 70.0, 34.0, 29.91, 29.88, 29.5, 29.3, 29.2, 29.1, 25.4. ^{19}F NMR (376 MHz, $CDCl_3$) δ -71.42 (s, 9 F).

R_F = $PFtB_{TRI}$: In a typical reaction, to an oven-dried roundbottom flask under argon, was added 15 mL of anhydrous tetrahydrofuran (THF), 4 Å powdered molecular sieves (2.9 g), and $PFtB_{TRI}$-OH[25] (2.9 g, 3.7 mmol). The suspension was cooled in an ice-water bath before powdered NaH (445 mg, 18.5 mmol) was then added. This mixture was allowed to stir in the ice bath for 30 min. After this time the 9-decen-1-OMs was added (**3.4**, 433 mg, 1.8 mmol) as a solution in 5 mL of anhydrous THF. The reaction mixture was then warmed slowly to reflux and monitored by HPLC. After 1 and 2 days additional NaH (50 mg) was added to facilitate the reaction. After 3 days the reaction was determined to be complete and was allowed to cool to room temperature. The reaction was then diluted with 50 mL of DCM, quenched with 1 mL of MeOH, followed by 1

mL of water, and then filtered over Celite. The Celite was then extracted with 2 x 25 mL aliquots of ether. The organic filtrates were combined and concentrated under reduced pressure to ~10 mL. This was then washed with 3 x 50 mL aliquots of saturated NH_4Cl solution, dried over $MgSO_4$ and condensed under reduced pressure to give a crude oil. The oil was then adsorbed onto Celite with ether and the product was then purified by automated flash chromatography using the Combi-flash purification system using a RediSep normal-phase Gold silica column (40 g) with a 0-5% EtOAc/hexanes gradient to give 1.15 g of product (67% yield). ^{1}H NMR (400 MHz, $CDCl_3$): δ 5.81 (ddt, J = 17.3, 10.3, 6.7 Hz, 1 H), 4.98 (ddt, J = 17.3, 1.7, 1.2 Hz, 1 H), 4.92 (ddt, J = 10.3, 1.7, 1.2 Hz, 1 H), 4.06 (s, 6 H), 3.36 (t, J = 6.7 Hz, 2 H), 3.36 (s, 2 H), 2.04 (qt, J = 6.8, 1.4 Hz, 2 H), 1.54-1.51 (m, 2 H), 1.40–1.28 (m, 10 H). ^{13}C NMR (101 MHz, $CDCl_3$): δ 139.3, 120.4 (q, J = 292.6 Hz, $C(C^*F_3)_3$), 114.1, 79.7 (decet, J = 30.1 Hz $C^*(CF_3)_3$), 71.8, 65.8, 65.7, 46.4, 33.9, 29.52, 29.51, 29.49, 29.2, 29.1, 26.1 ^{19}F NMR (376 MHz, $CDCl_3$) δ -71.19 (s, 27 F).

R_F = F13: In a typical reaction, to an oven-dried roundbottom flask under argon, was added 150 mL of anhydrous tetrahydrofuran (THF) and 1H,1H-perfluorotetradecanol (F13-OH, 5.0 g, 7.2 mmol), followed by 4 Å powdered molecular sieves (5.0 g). The suspension was cooled in an ice-water bath before powdered NaH (1.25 g, 52.1 mmol) was then added. This mixture was allowed to stir in the ice bath for 30 min. After this time the 9-decen-1-OMs was added (**3.4**, 5.0 g, 17.2 mmol) as a solution in 5 mL of anhydrous THF. The reaction mixture was then warmed slowly to reflux and monitored by HPLC. After 1, 2, and 3 days additional NaH (50 mg) was added to facilitate the reaction. After 4 days the reaction was determined to be complete and was allowed to cool to room temperature. The reaction was then diluted with 50 mL of DCM, quenched with 1 mL of MeOH, followed by 1 mL of water, and then filtered over Celite. The Celite was then extracted with 2 x 150 mL aliquots of ether. The organic filtrates were combined and

concentrated under a stream of air over several hours. Unreacted F13-OH was then removed from the organic residue by flash chromatography on normal phase silica using a 0-5% EtOAc/hexanes gradient to give 1.89 g of a crude product (31% yield). This was carried onto the next reaction with minor impurities in that the subsequent hydrocarbon-fluorocarbon alcohol product and side-products. Having greater polarity differences allowed for easier separation in the next step (therefore due to minor impurities no NMR is provided).

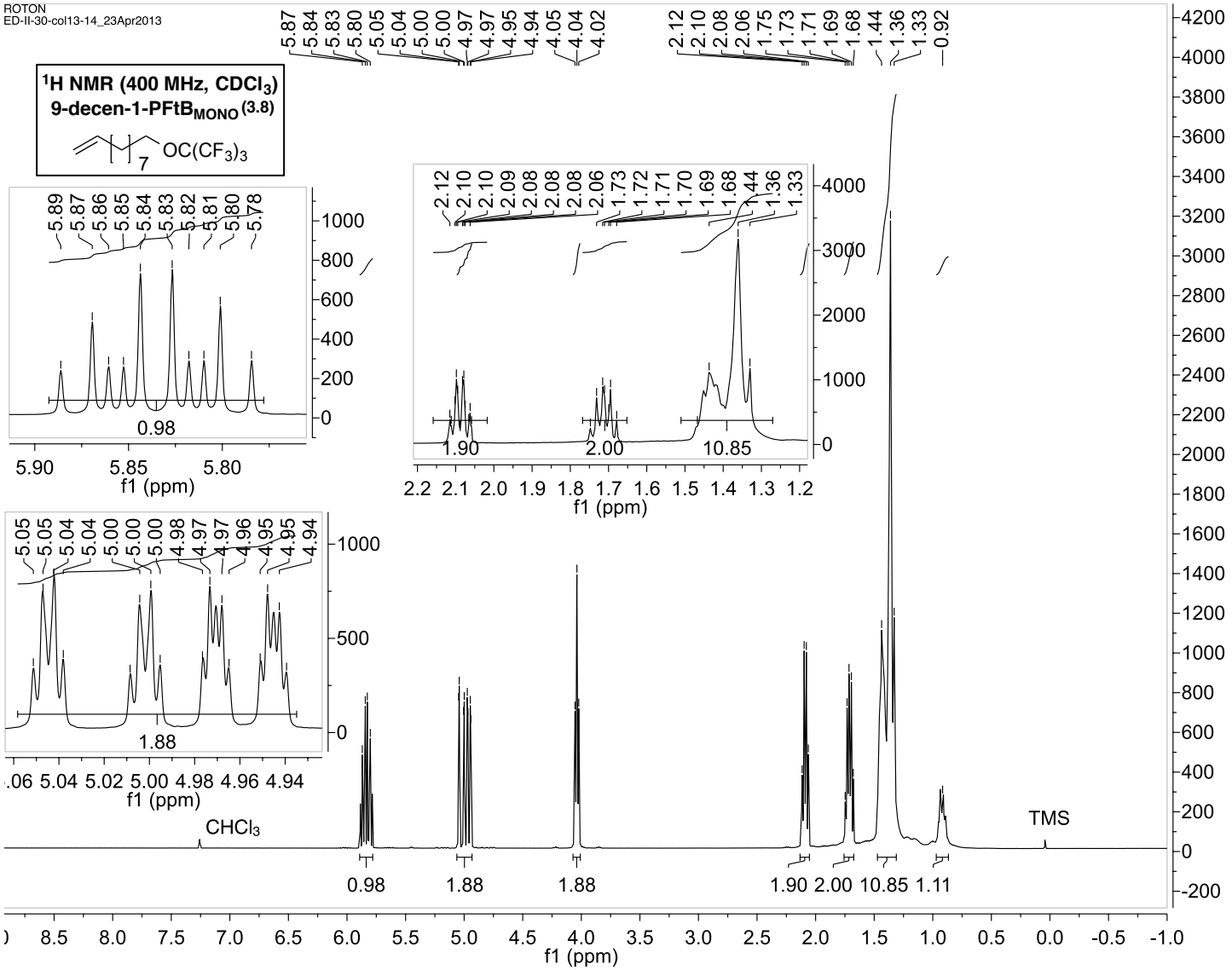
ROTON
ED-II-30-col13-14_23Apr2013
^{1}H NMR (400 MHz, $CDCl_3$)
9-decen-1-PFtB$_{MONO}$ (3.8)
$OC(CF_3)_3$
7
CHCl$_3$
TMS
f1 (ppm)
0.98
1.88
1.88
1.90
2.00
10.85
1.11

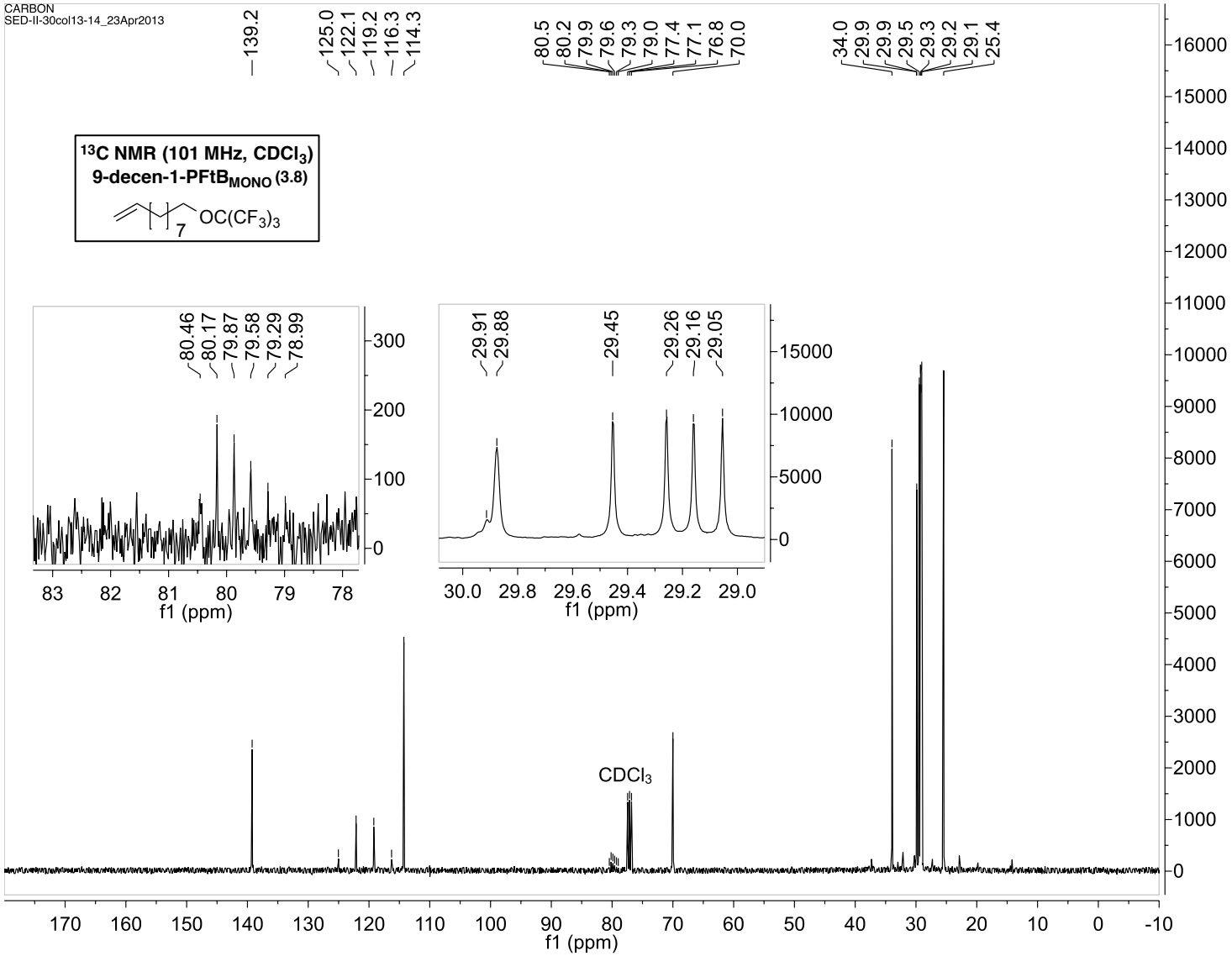
CARBON
SED-II-30col13-14_23Apr2013
139.2
125.0
122.1
119.2
116.3
114.3
80.5
80.2
79.9
79.6
79.3
79.0
77.4
77.1
76.8
70.0
34.0
29.9
29.9
29.5
29.3
29.2
29.1
25.4
13C NMR (101 MHz, CDCl3)
9-decen-1-PFtBMONO (3.8)
OC(CF3)3
7
80.46
80.17
79.87
79.58
79.29
78.99
29.91
29.88
29.45
29.26
29.16
29.05
CDCl3
f1 (ppm)

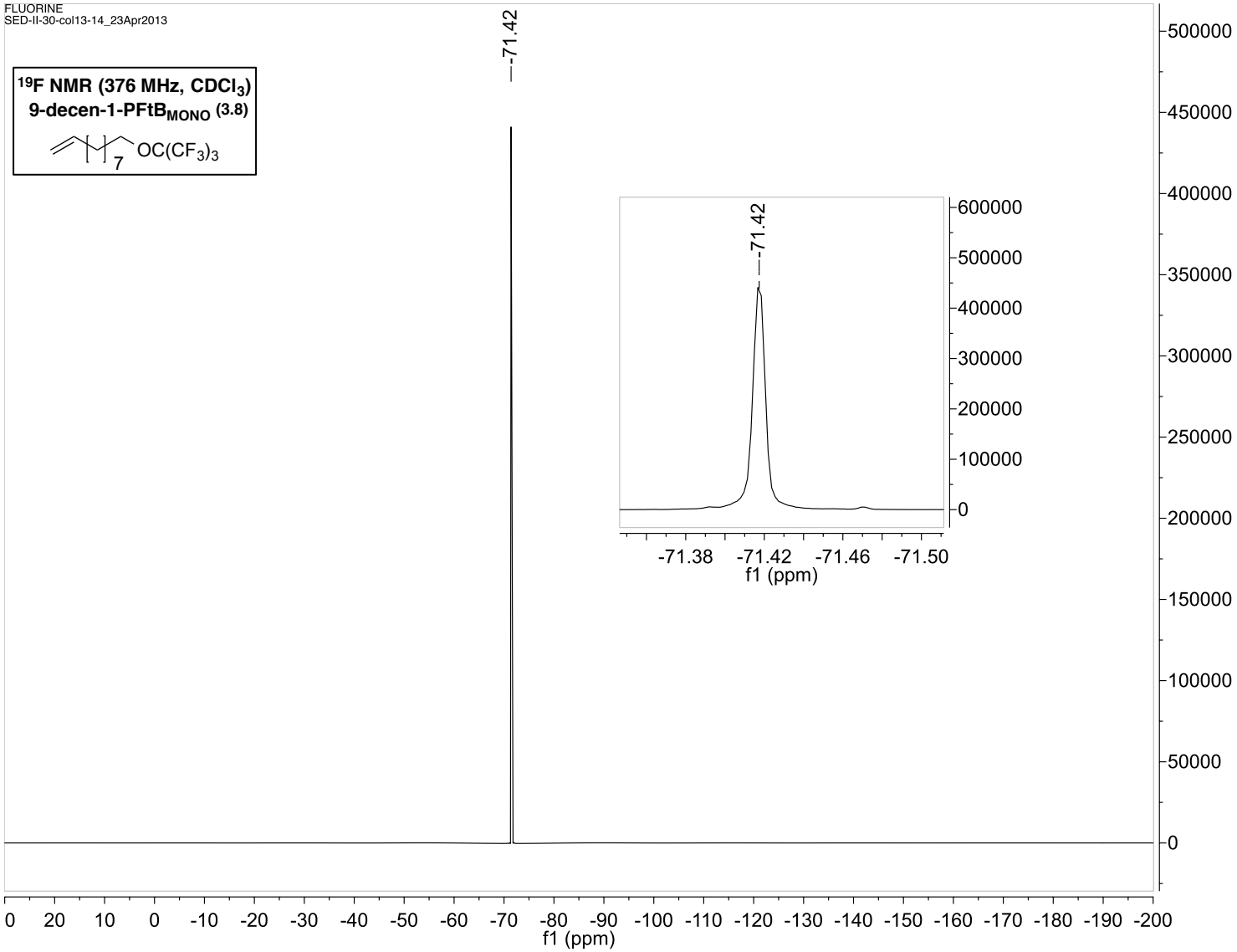
FLUORINE
SED-II-30-col13-14_23Apr2013
19F NMR (376 MHz, CDCl3)
9-decen-1-PFtBMONO (3.8)
7
OC(CF3)3
-71.42
-71.42
-71.38
-71.42
-71.46
-71.50
f1 (ppm)
f1 (ppm)

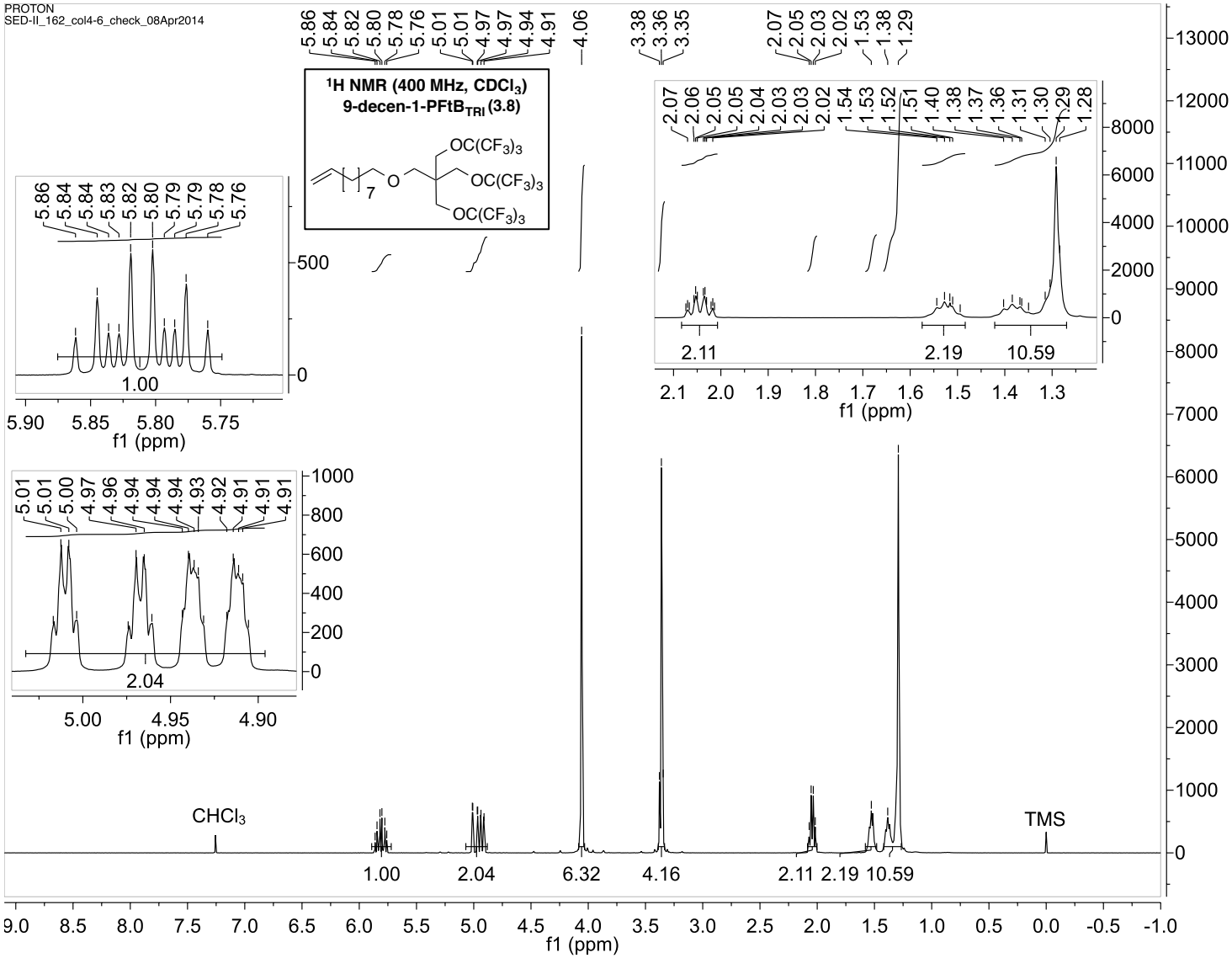
PROTON
SED-II_162_col4-6_check_08Apr2014
^{1}H NMR (400 MHz, $CDCl_3$)
9-decen-1-PFtB$_{TRI}$ (3.8)
$OC(CF_3)_3$
$OC(CF_3)_3$
$OC(CF_3)_3$
7
O
5.86 5.84 5.82 5.80 5.78 5.76 5.01 5.01 4.97 4.97 4.94 4.91 4.06 3.38 3.36 3.35 2.07 2.05 2.03 2.02 1.53 1.38 1.29
5.86 5.84 5.84 5.83 5.82 5.80 5.79 5.79 5.78 5.76
1.00
5.01 5.01 5.00 4.97 4.96 4.94 4.94 4.94 4.93 4.92 4.91 4.91 4.91
2.04
2.07 2.06 2.05 2.05 2.04 2.03 2.03 2.02 1.54 1.53 1.52 1.51 1.40 1.38 1.37 1.36 1.31 1.30 1.29 1.28
2.11 2.19 10.59
$CHCl_3$
TMS
1.00 2.04 6.32 4.16 2.11 2.19 10.59
f1 (ppm)

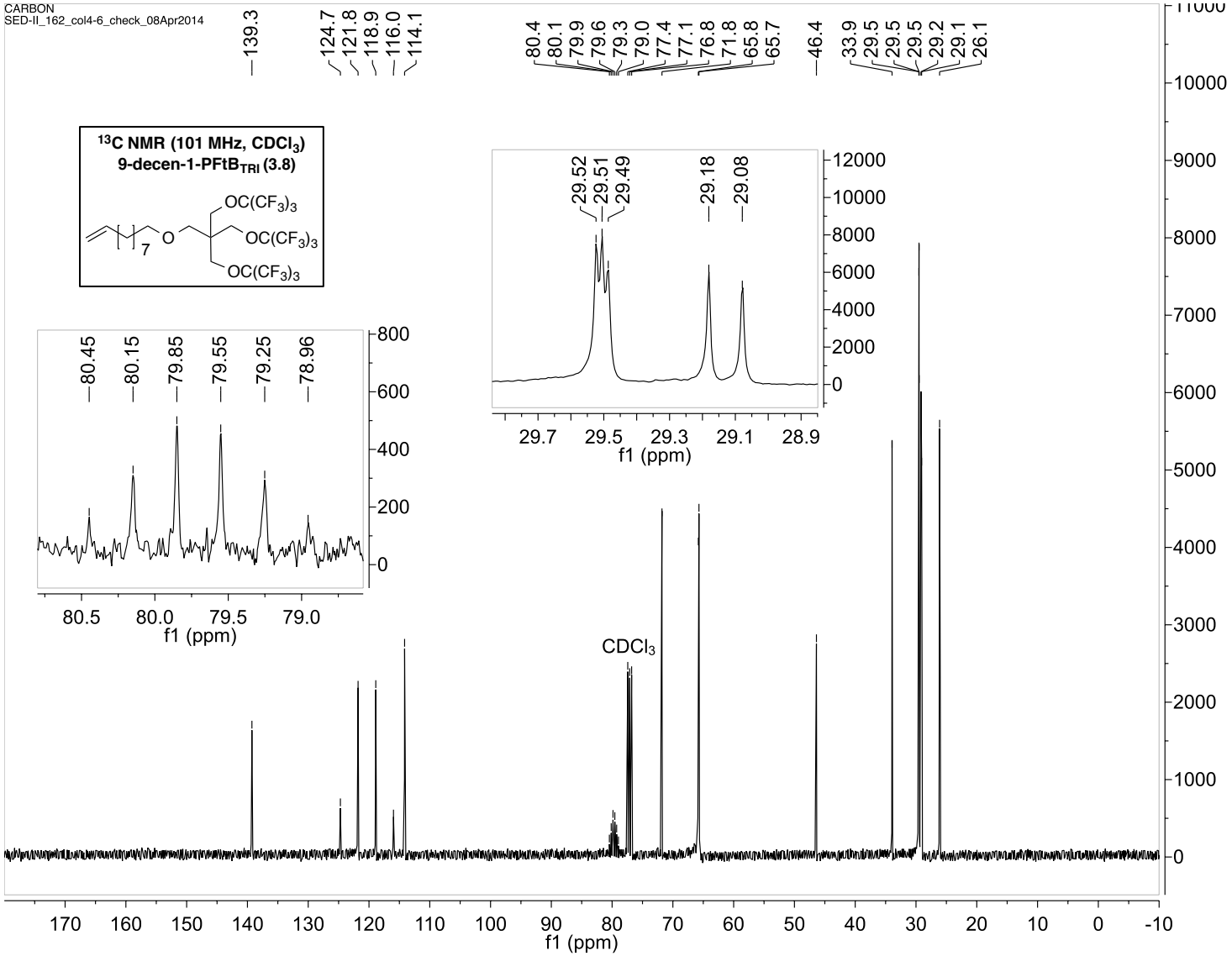
CARBON
SED-II_162_col4-6_check_08Apr2014
139.3
124.7
121.8
118.9
116.0
114.1
80.4
80.1
79.9
79.6
79.3
79.0
77.4
77.1
76.8
71.8
65.8
65.7
46.4
33.9
29.5
29.5
29.5
29.2
29.1
26.1
13C NMR (101 MHz, CDCl3)
9-decen-1-PFtBTRI (3.8)
OC(CF3)3
OC(CF3)3
OC(CF3)3
O
7
29.52
29.51
29.49
29.18
29.08
f1 (ppm)
80.45
80.15
79.85
79.55
79.25
78.96
f1 (ppm)
CDCl3
f1 (ppm)

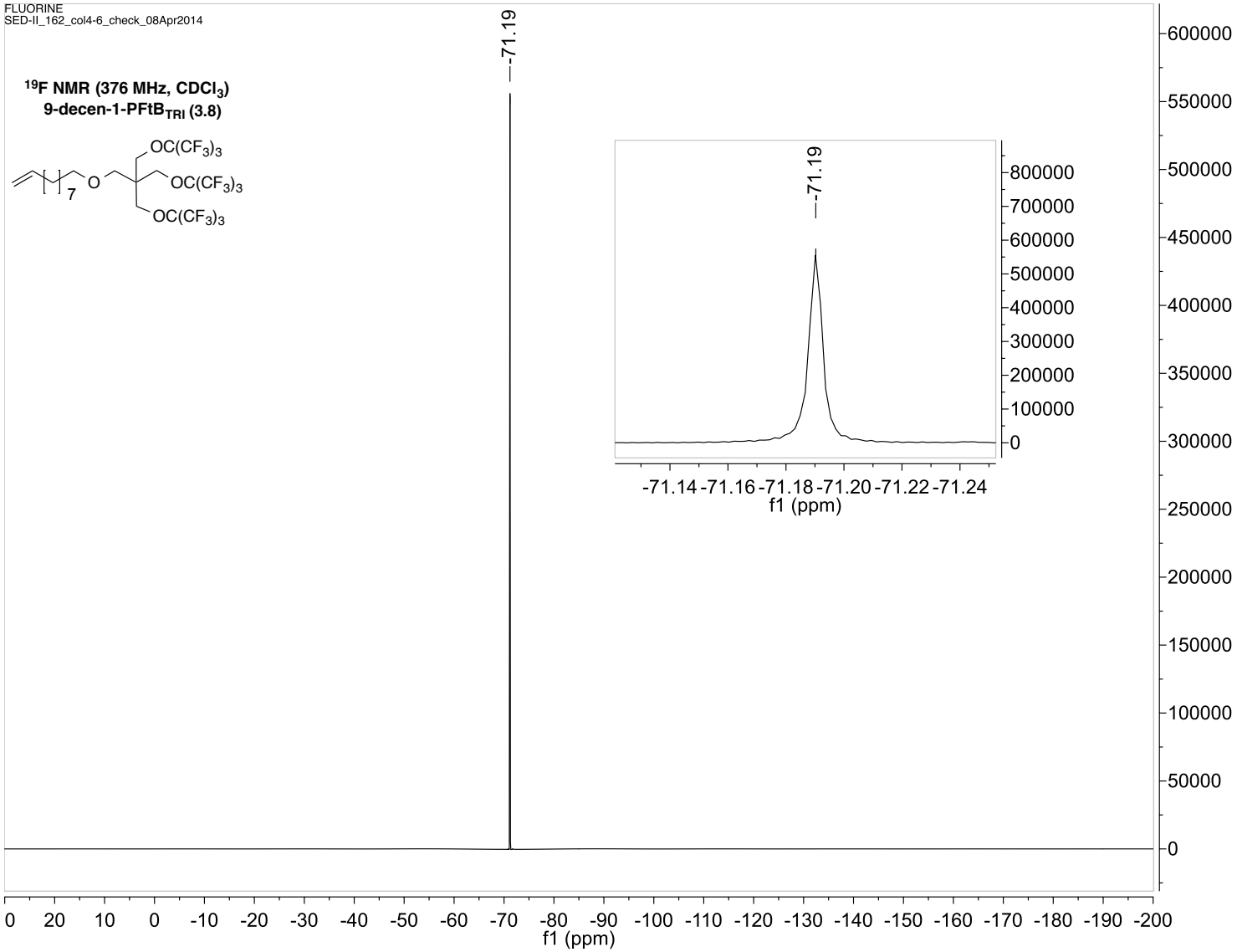
FLUORINE
SED-II_162_col4-6_check_08Apr2014
19F NMR (376 MHz, CDCl3)
9-decen-1-PFtBTRI (3.8)
OC(CF3)3
OC(CF3)3
OC(CF3)3
O
7
-71.19
-71.19
-71.14 -71.16 -71.18 -71.20 -71.22 -71.24
f1 (ppm)
0 20 10 0 -10 -20 -30 -40 -50 -60 -70 -80 -90 -100 -110 -120 -130 -140 -150 -160 -170 -180 -190 -200
f1 (ppm)

HO-H10-R_F (3.9):

R_F = $PFtB_{MONO}$ In a typical reaction, to an oven-dried roundbottom flask under argon, was added 8 mL of anhydrous tetrahydrofuran (THF) and 9-decen-1-$PFtB_{MONO}$ (**3.8, R_F = $PFtB_{MONO}$**, 3.5 g, 9.3 mmol). The mixture was cooled in an ice-water bath before BH_3·THF (14 mL of 1 M solution, 14 mmol) was added drop-wise. This mixture was allowed to stir as it warmed to room temperature overnight. After this time the reaction mixture was cooled to 10 °C in an ice-water bath and NaOH solution (15 mL of a 3 M solution in Mili-Q water, 37.2 mmol) and H_2O_2 (4.6 mL of a 9.79 M or 30 % (v/v) in water, 37.2 mmol) were sequentially added drop-wise. The reaction mixture was then heated to 50 ºC for 12 h. After this time the reaction mixture was cooled to room temperature and diluted with 100 mL of water and extracted with 3 x 50 mL aliquots of ether. The organic phases were then dried over $MgSO_4$ and concentrated under reduced pressure. The crude oil was purified on by flash chromatography on silica with 5 % EtOAc/hexanes to give 2.64 g of product (59 % yield). ^{1}H NMR (400 MHz, $CDCl_3$): δ 4.00 (t, J = 6.4 Hz, 2 H), 3.61 (t, J = 6.7 Hz, 2 H), 2.65 (bs, 1 H), 1.71-1.64 (m, 2 H), 1.60–1.53 (m, 2 H), 1.40-1.31 (m, 12 H). ^{13}C NMR (101 MHz, $CDCl_3$): δ 120.47 (q, J = 293.3 Hz, $C(C^*F_3)_3$), 80.0 (decet, J = 29.3 Hz $C^*(CF_3)_3$), 69.9, 62.8, 32.8, 29.8, 29.6, 29.53, 29.49, 29.2, 25.9, 25.4 ^{19}F NMR (376 MHz, $CDCl_3$) δ -71.24 (s, 9 F).

R_F = $PFtB_{TRI}$ In a typical reaction, to an oven-dried roundbottom flask under argon was added 1 mL of anhydrous tetrahydrofuran (THF) and BH_3·THF (14 mL of 1 M solution, 14 mmol). The mixture was cooled in an ice-water bath and 9-decen-1-$PFtB_{TRI}$ (**3.8, R_F = $PFtB_{TRI}$**, 408 mg, 0.44 mmol) in 2 mL of THF was added drop-wise. This mixture was allowed to stir as it warmed to room temperature overnight. After this time the reaction mixture was cooled to 10 °C in an ice-water bath and NaOH solution (2.2 mL of a 3 M solution in Mili-Q water, 2.2 mmol) and H_2O_2 (0.2 mL of a 9.79 M or 30 % (v/v) in water, 2.2 mmol) were sequentially added drop-wise. The

reaction mixture was then heated to 50 ºC for 3.5 h. After this time the reaction mixture was cooled to room temperature and diluted with 1 mL of water and extracted with 3 x 10 mL aliquots of ether. The organic phases were then dried over $MgSO_4$ and concentrated under reduced pressure. The crude oil was purified on by automated flash chromatography using the Combi-flash purification system using a RediSep normal-phase Gold silica column (4 g) with a 0-5% EtOAc/hexanes gradient to give 385 mg of product (93 % yield). ^{1}H NMR (400 MHz, $CDCl_3$): δ 4.05 (s, 6 H), 3.64 (t, J = 6.6 Hz, 2 H), 3.36 (t, J = 6.7 Hz, 2 H) 3.36 (s, 2 H), 1.61-1.51 (m, 4 H), 1.46 (bs, 1 H), 1.39-1.26 (m, 12 H). ^{13}C NMR (101 MHz, $CDCl_3$): δ 120.4 (q, J = 293.1 Hz, $C(C^*F_3)_3$), 79.7 (decet, J = 30.0 Hz $C^*(CF_3)_3$), 71.8, 65.8, 65.7, 63.2, 46.4, 33.0, 29.7, 29.63, 29.58, 29.55, 29.5, 26.1, 25.9 ^{19}F NMR (376 MHz, $CDCl_3$) δ -71.13 (s, 27 F).

R_F = F13: In a typical reaction, to an oven-dried roundbottom flask under argon, was added 20 mL of anhydrous tetrahydrofuran (THF) and 9-decen-1-F13 (**3.8, R_F = F13**, 650 mg, 0.8 mmol). The mixture was cooled in an ice-water bath before BH_3·THF (2 mL of 1 M solution, 1.9 mmol) was added drop-wise. This mixture was allowed to stir as it warmed to room temperature overnight. After this time the reaction mixture was cooled to 10 °C in an ice-water bath and NaOH solution (1.2 mL of a 3 M solution in Mili-Q water, 3.9 mmol) and H_2O_2 (0.4 mL of a 9.79 M or 30 % (v/v) in water, 3.9 mmol) were sequentially added drop-wise. The reaction mixture was then heated to 50 ºC for 12 h. After this time the reaction mixture was cooled to room temperature and diluted with 100 mL of water and extracted with 3 x 50 mL aliquots of ether. The organic phases were then dried over $MgSO_4$ and concentrated under reduced pressure to give 540 mg of product (75 % yield). Note: The solvent is the major peak due to limited solubility of the compound in non-fluorous solvents. (Solvent suppression techniques were not attempted and therefore this could not be avoided.) ^{1}H NMR (400 MHz, $CDCl_3$): δ 3.92 (t, J = 13.9 Hz, 2 H), 3.64 (t, J = 6.6 Hz, 2 H), 3.59 (t, J = 6.6 Hz, 2 H), 1.63-1.54 (m, 4 H), 1.40-1.26 (m, 12 H). ^{13}C

NMR (101 MHz, $CDCl_3$): δ 73.3, 67.8 (t, J = 26.2 Hz, C*H_2CF_2), 63.1, 32.8, 29.51, 29.45, 29.4, 29.3, 25.7. ^{19}F NMR (376 MHz, $CDCl_3$) δ -81.12 (3 F), -119.96 (2 F), -122.04-122.37 (16 F), -123.05 (2 F), -123.78 (2 F), -126.46 (2 F).

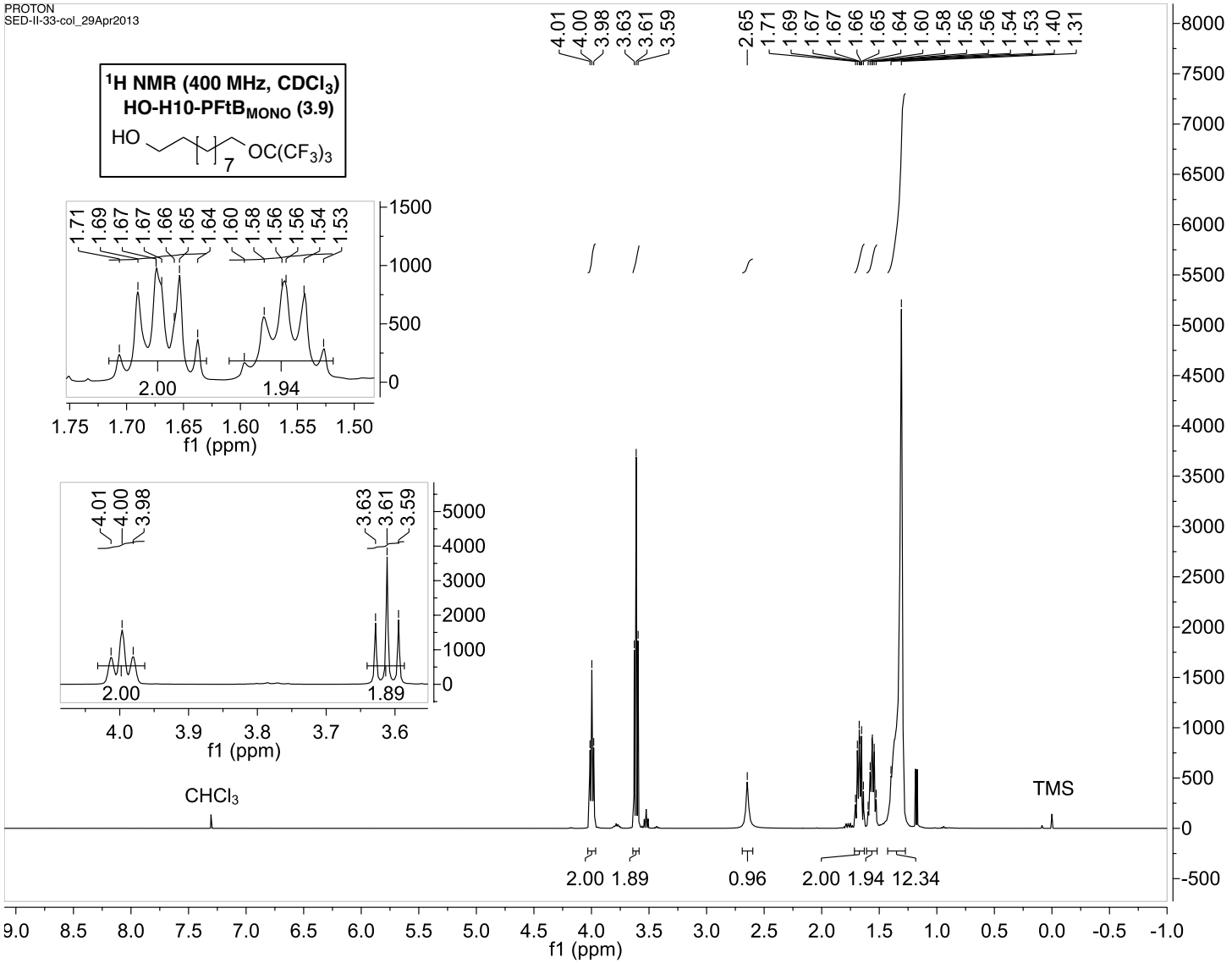
PROTON
SED-II-33-col_29Apr2013
^{1}H NMR (400 MHz, $CDCl_3$)
HO-H10-PFtB$_{MONO}$ (3.9)
HO
7
$OC(CF_3)_3$
4.01 4.00 3.98 3.63 3.61 3.59
2.65 1.71 1.69 1.67 1.67 1.66 1.65 1.64 1.60 1.58 1.56 1.56 1.54 1.53 1.40 1.31
1.71 1.69 1.67 1.67 1.66 1.65 1.64 1.60 1.58 1.56 1.56 1.54 1.53
2.00 1.94
f1 (ppm)
4.01 4.00 3.98 3.63 3.61 3.59
2.00 1.89
f1 (ppm)
$CHCl_3$
TMS
2.00 1.89 0.96 2.00 1.94 12.34
f1 (ppm)

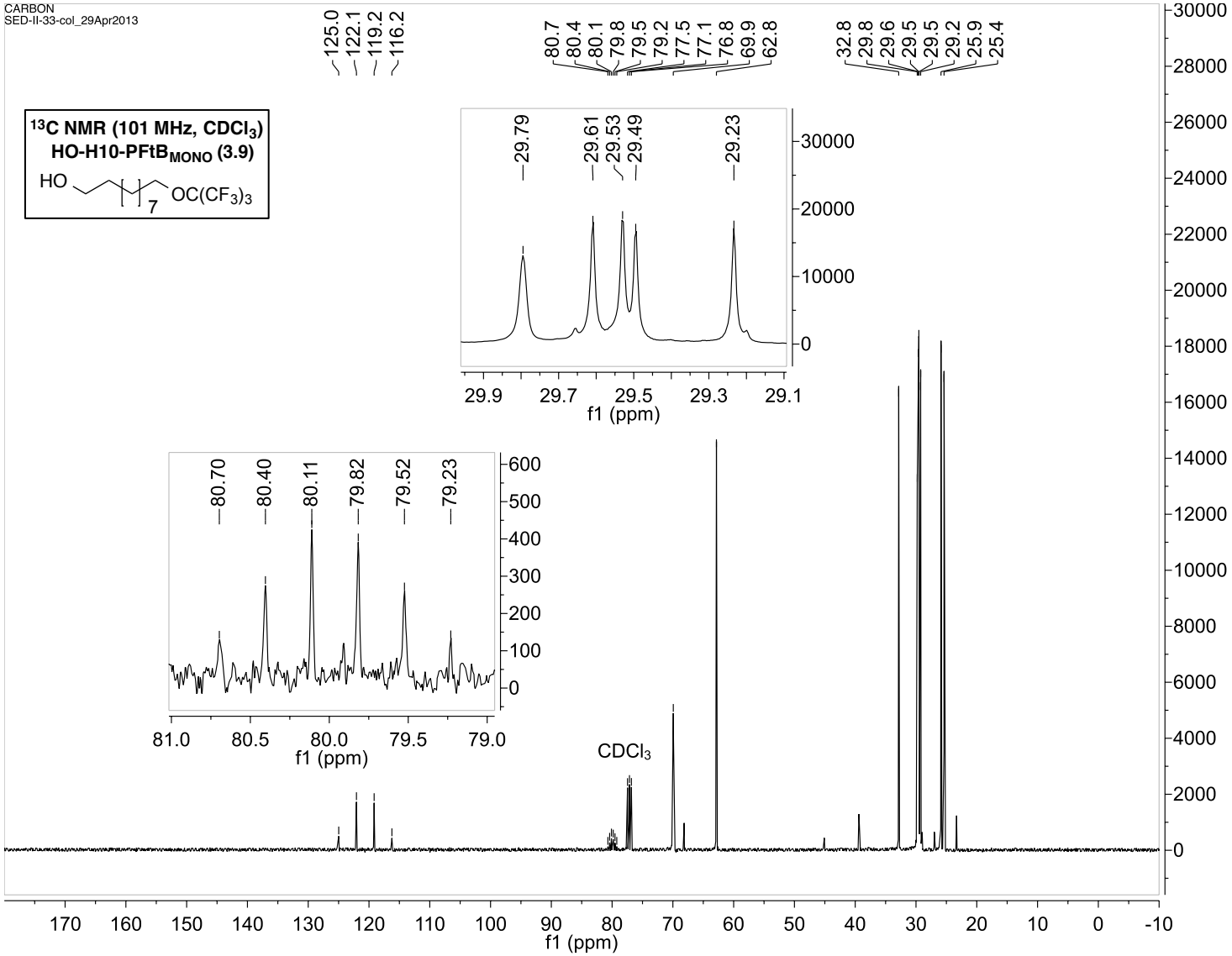
CARBON
SED-II-33-col_29Apr2013
125.0
122.1
119.2
116.2
80.7
80.4
80.1
79.8
79.5
79.2
77.5
77.1
76.8
69.9
62.8
32.8
29.8
29.6
29.5
29.5
29.2
25.9
25.4
13C NMR (101 MHz, CDCl3)
HO-H10-PFtBMONO (3.9)
HO
7
OC(CF3)3
29.79
29.61
29.53
29.49
29.23
f1 (ppm)
80.70
80.40
80.11
79.82
79.52
79.23
f1 (ppm)
CDCl3
f1 (ppm)

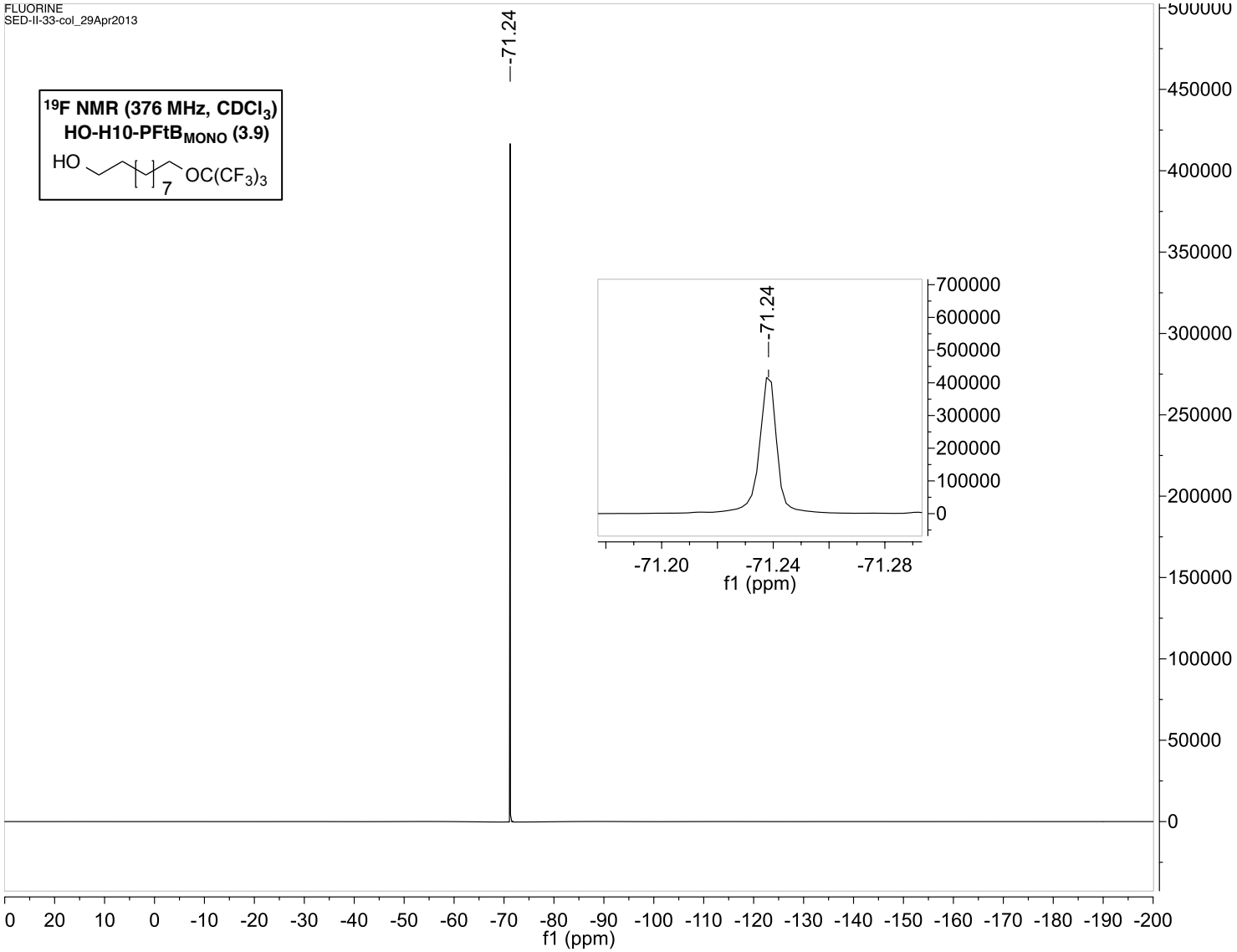
FLUORINE
SED-II-33-col_29Apr2013
-71.24
19F NMR (376 MHz, CDCl3)
HO-H10-PFtBMONO (3.9)
HO
7
OC(CF3)3
-71.24
-71.20
-71.24
-71.28
f1 (ppm)
f1 (ppm)

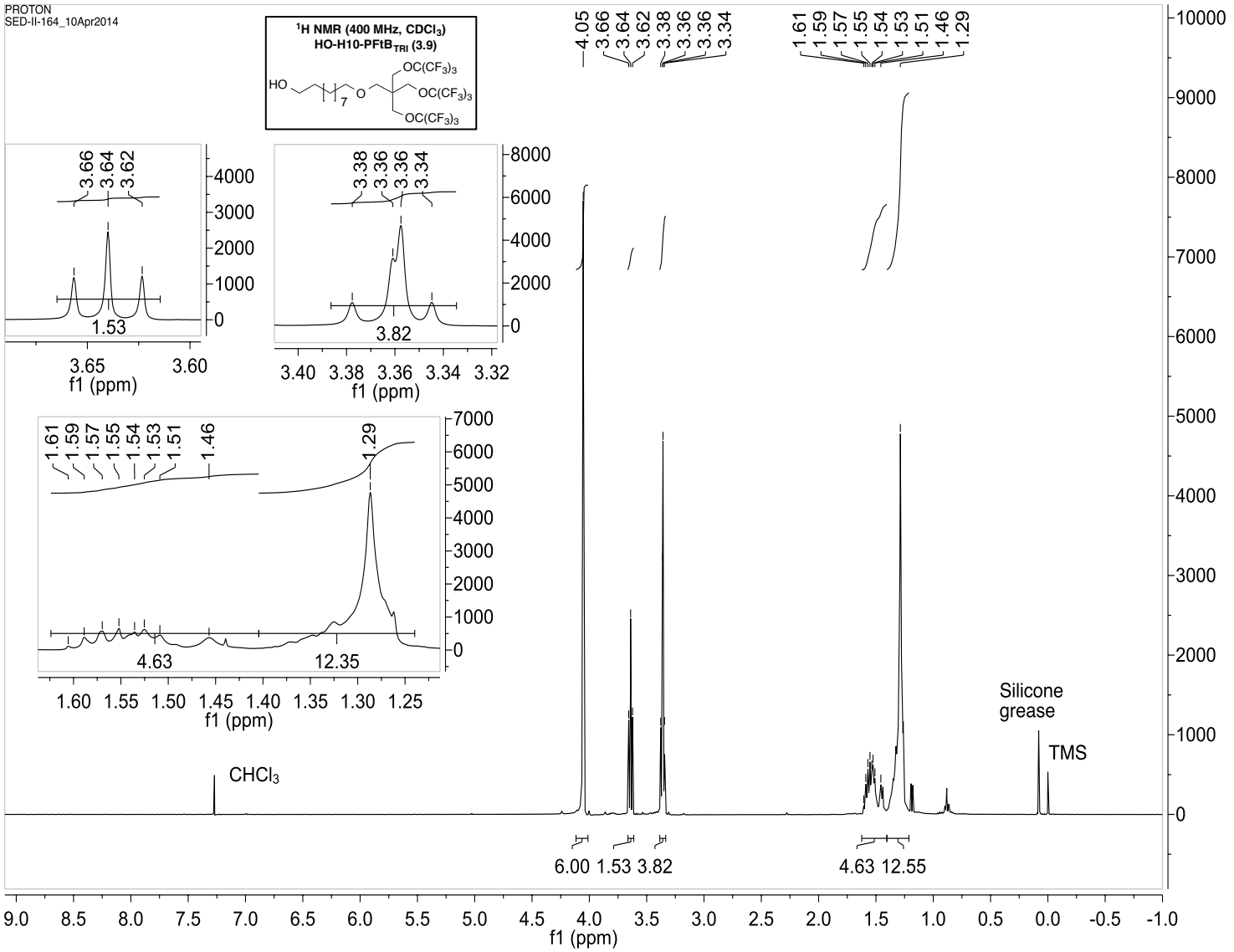
PROTON
SED-II-164_10Apr2014
^{1}H NMR (400 MHz, CDCl$_3$)
HO-H10-PFtB$_{TRI}$ (3.9)
HO
7
O
OC(CF$_3$)$_3$
OC(CF$_3$)$_3$
OC(CF$_3$)$_3$
4.05
3.66
3.64
3.62
3.38
3.36
3.36
3.34
1.61
1.59
1.57
1.55
1.54
1.53
1.51
1.46
1.29
1.53
3.82
4.63
12.35
f1 (ppm)
CHCl$_3$
Silicone grease
TMS
6.00 1.53 3.82
4.63 12.55

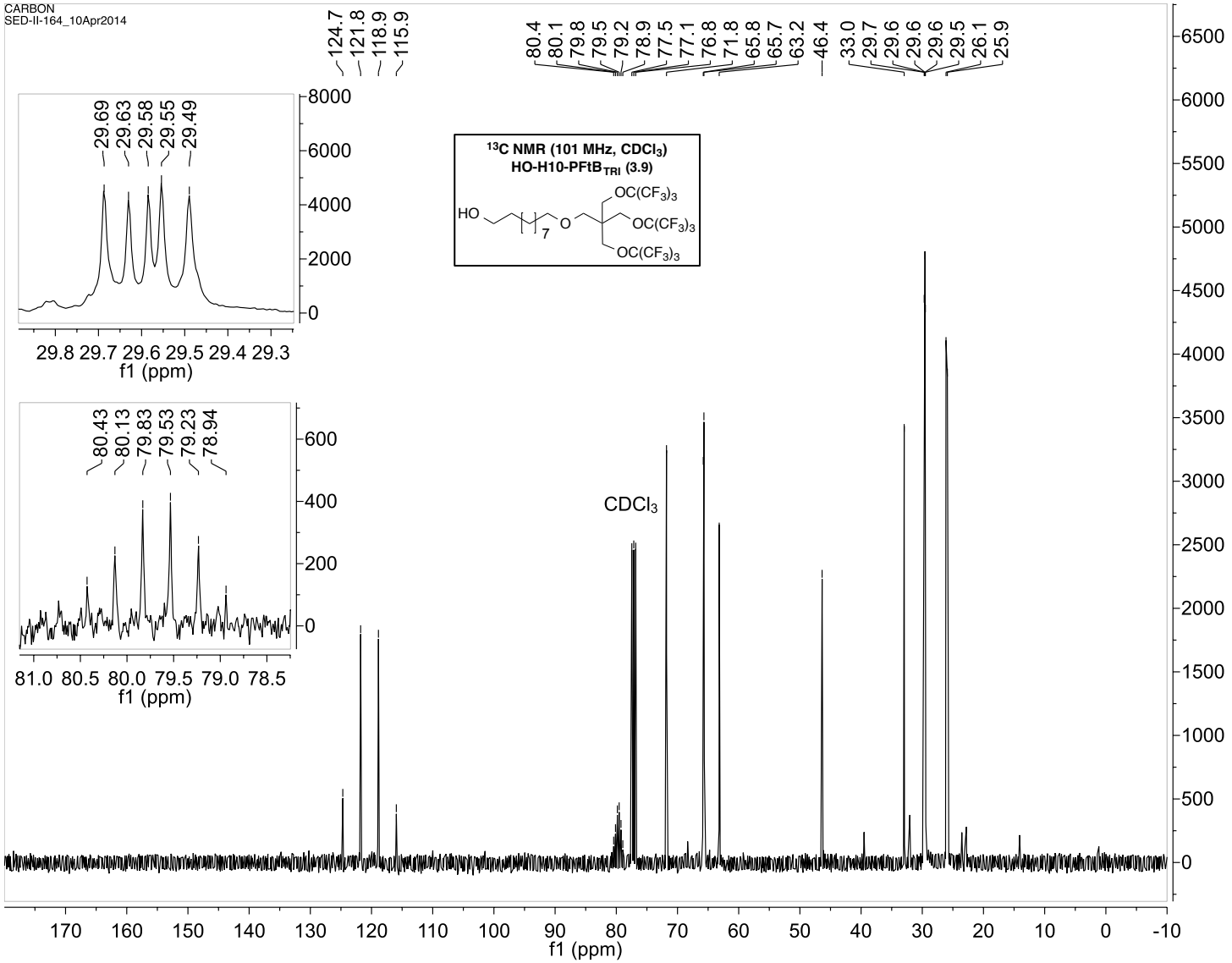
CARBON
SED-II-164_10Apr2014
124.7
121.8
118.9
115.9
80.4
80.1
79.8
79.5
79.2
78.9
77.5
77.1
76.8
71.8
65.8
65.7
63.2
46.4
33.0
29.7
29.6
29.6
29.6
29.5
26.1
25.9
29.69
29.63
29.58
29.55
29.49
29.8 29.7 29.6 29.5 29.4 29.3
f1 (ppm)
80.43
80.13
79.83
79.53
79.23
78.94
81.0 80.5 80.0 79.5 79.0 78.5
f1 (ppm)
13C NMR (101 MHz, CDCl3)
HO-H10-PFtBTRI (3.9)
HO
7
O
OC(CF3)3
OC(CF3)3
OC(CF3)3
CDCl3
f1 (ppm)

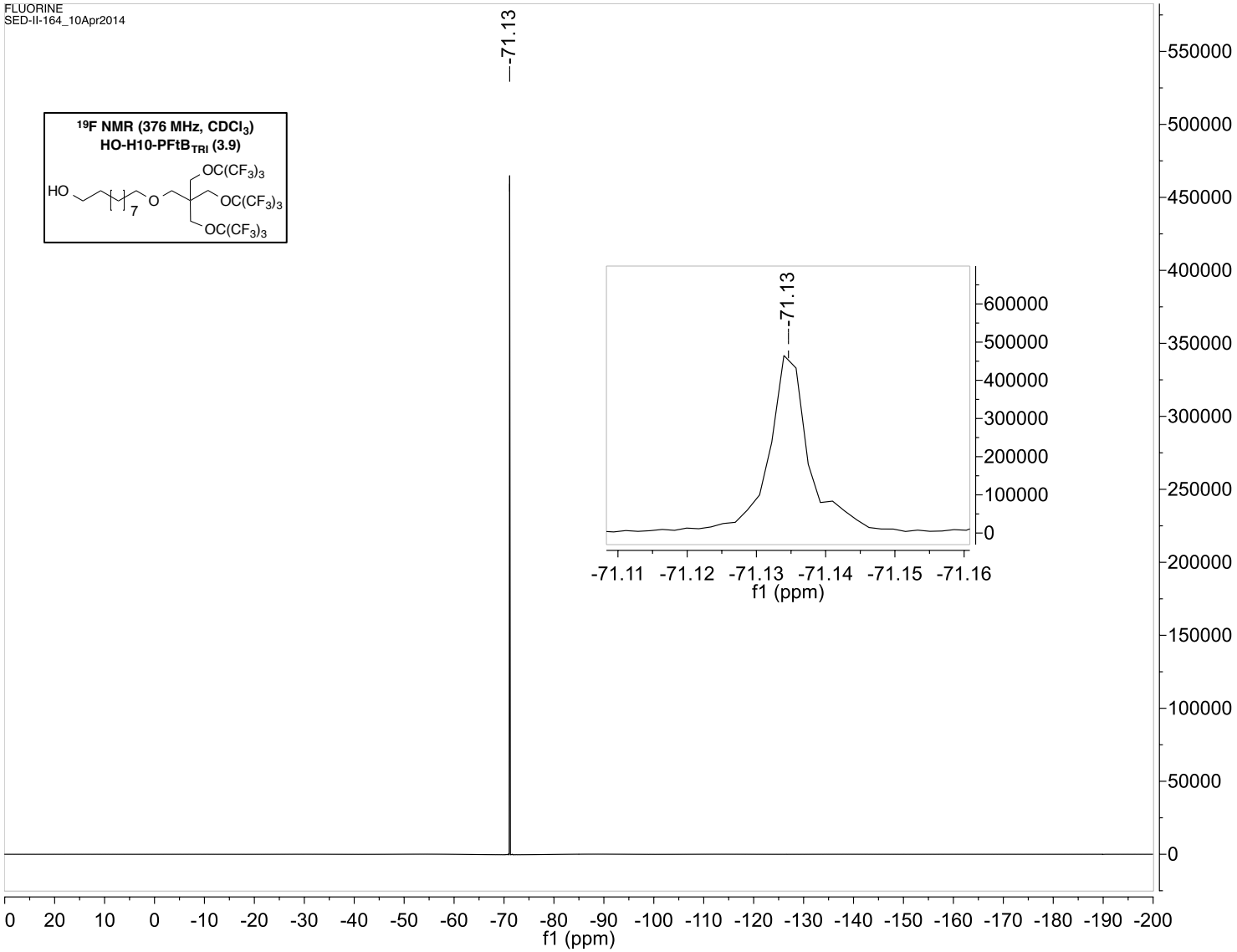
FLUORINE
SED-II-164_10Apr2014
-71.13
19F NMR (376 MHz, CDCl3)
HO-H10-PFtBTRI (3.9)
HO
7
O
OC(CF3)3
OC(CF3)3
OC(CF3)3
-71.13
-71.11 -71.12 -71.13 -71.14 -71.15 -71.16
f1 (ppm)
0 20 10 0 -10 -20 -30 -40 -50 -60 -70 -80 -90 -100 -110 -120 -130 -140 -150 -160 -170 -180 -190 -200
f1 (ppm)

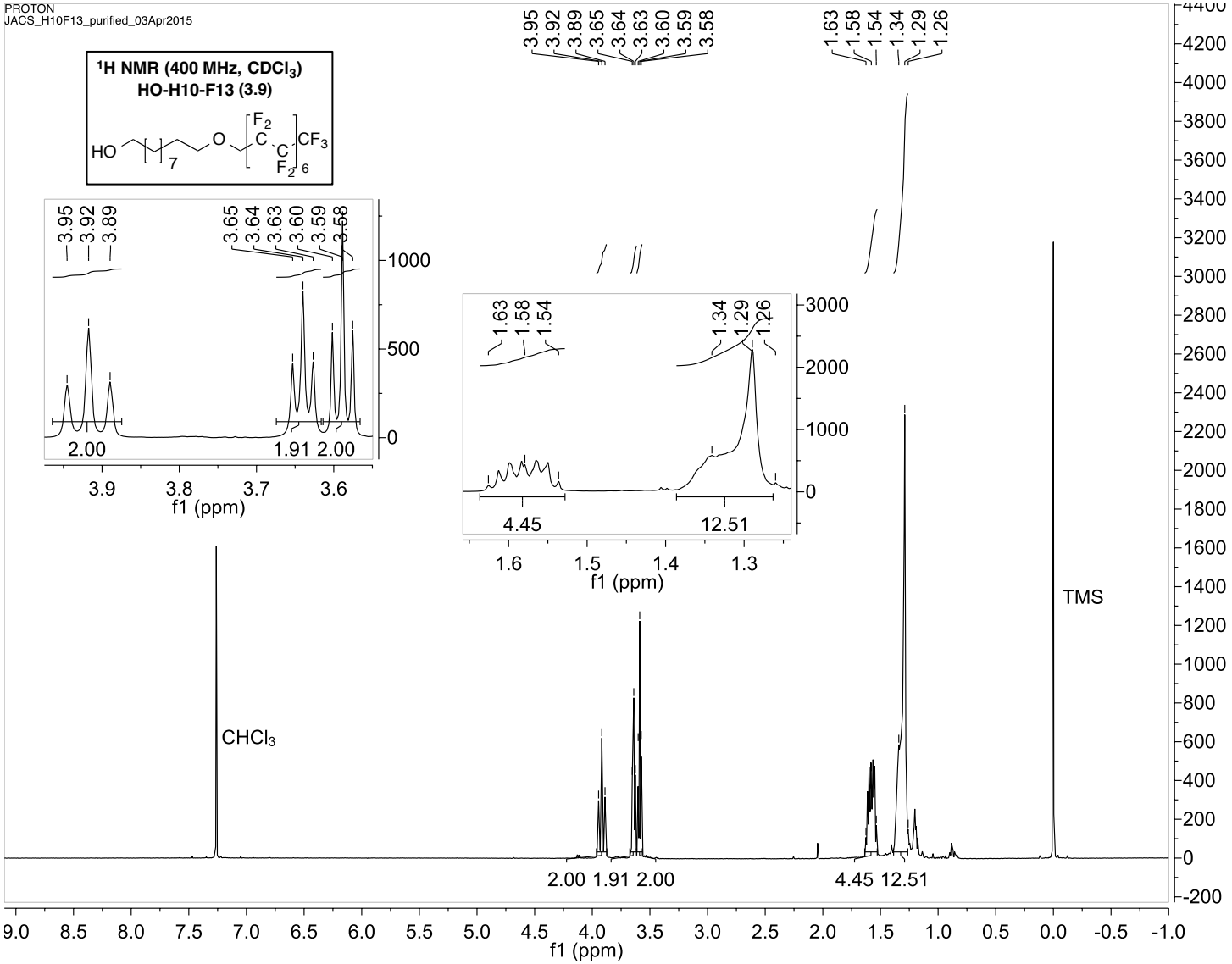
PROTON
JACS_H10F13_purified_03Apr2015
^{1}H NMR (400 MHz, $CDCl_3$)
HO-H10-F13 (3.9)
HO
7
O
F_2
C
C
CF_3
F_2
6
3.95
3.92
3.89
3.65
3.64
3.63
3.60
3.59
3.58
1.63
1.58
1.54
1.34
1.29
1.26
2.00
1.91 2.00
4.45
12.51
f1 (ppm)
$CHCl_3$
TMS

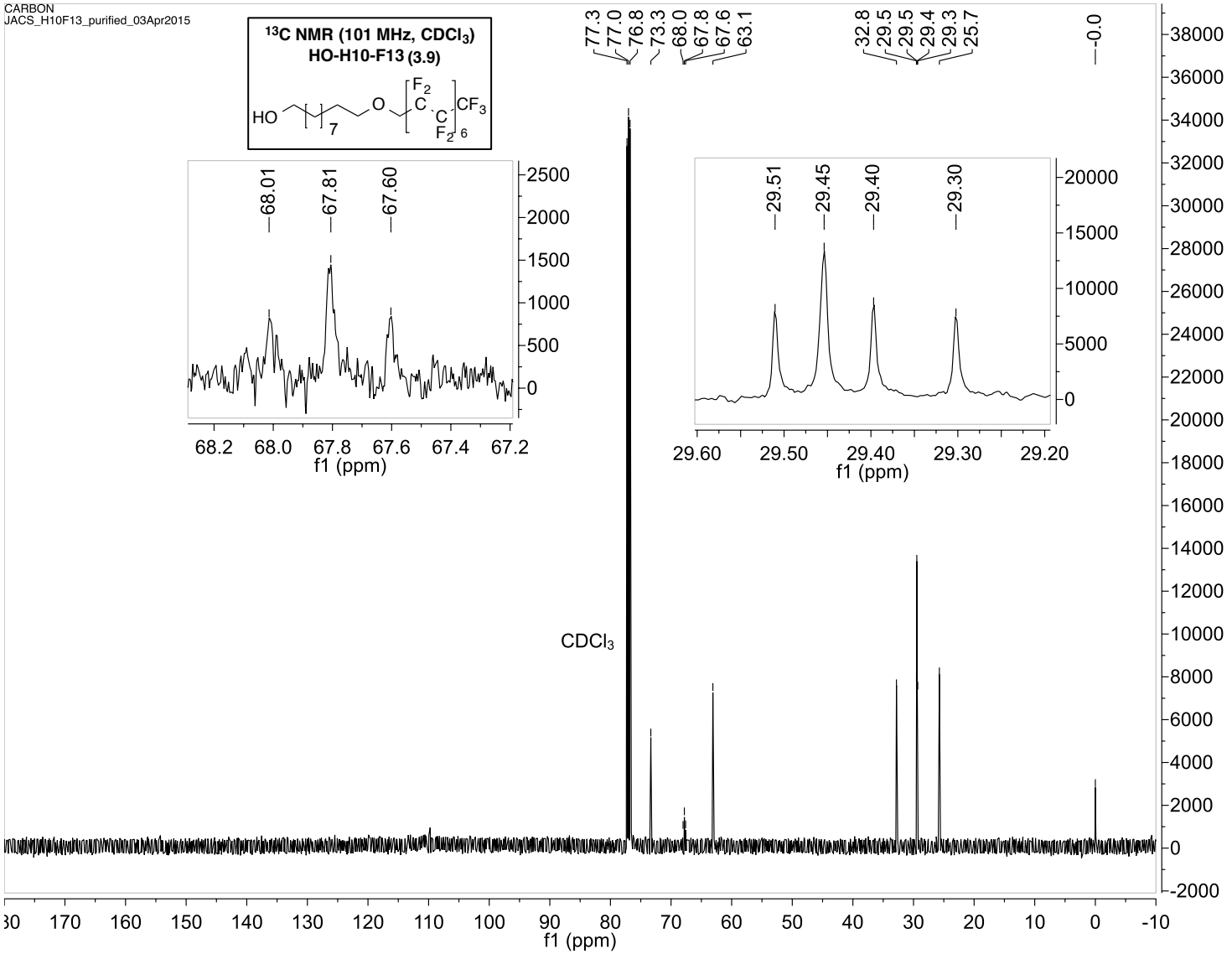
CARBON
JACS_H10F13_purified_03Apr2015
13C NMR (101 MHz, CDCl3)
HO-H10-F13 (3.9)
77.3
77.0
76.8
73.3
68.0
67.8
67.6
63.1
32.8
29.5
29.5
29.4
29.3
25.7
0.0
68.01
67.81
67.60
29.51
29.45
29.40
29.30
CDCl3
f1 (ppm)

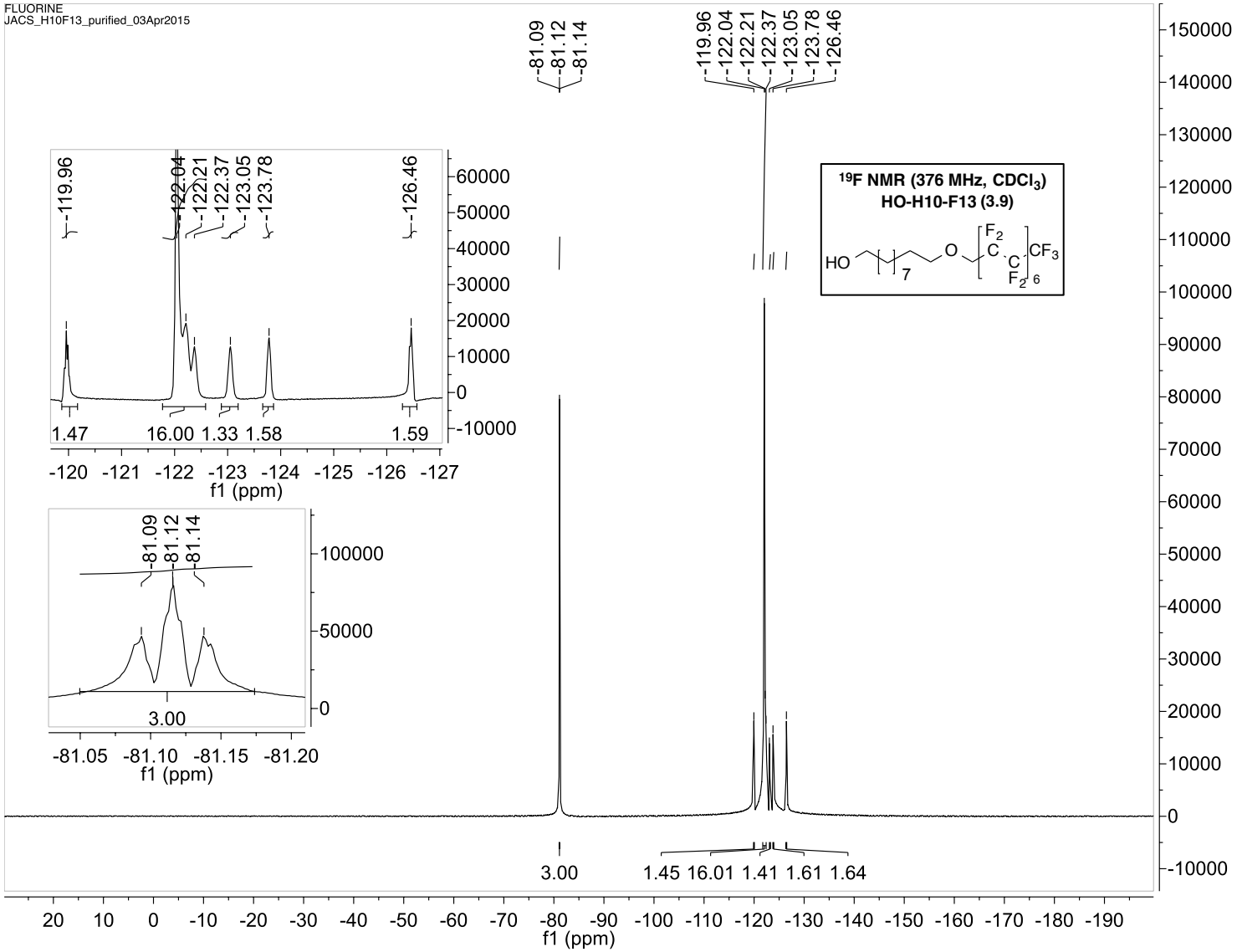
FLUORINE
JACS_H10F13_purified_03Apr2015
-81.09
-81.12
-81.14
-119.96
-122.04
-122.21
-122.37
-123.05
-123.78
-126.46
19F NMR (376 MHz, CDCl3)
HO-H10-F13 (3.9)
HO
7
O
F2
C
C
CF3
F2
6
3.00
1.45 16.01 1.41 1.61 1.64
f1 (ppm)
1.47 16.00 1.33 1.58 1.59
-120 -121 -122 -123 -124 -125 -126 -127
f1 (ppm)
3.00
-81.05 -81.10 -81.15 -81.20
f1 (ppm)

$mPEG_{2k}$-O-H10-R_F (3.11) In a typical reaction at 0 °C was added NaH (10 eq., 6.4 mmol) to a suspension of R_F-H10-OH (1.2 eq., 0.76 mmol) and 4 Å powdered molecular sieves (1 weight eq.) in 10 mL of dry THF under argon. This was allowed to stir for 30 min at 0 °C. After this time, $mPEG_{2k}$-OMs[25] (1 eq., 0.64 mmol) was added at 0 °C. The reaction mixture was allowed to stir as it warmed slowly to room temperature. The mixture was then refluxed and monitored by HPLC. Each day 10 mg of NaH was added to facilitate the reaction. When determined to be complete the reaction mixture was then diluted with 10 mL of DCM, slowly quenched with 1 mL of MeOH, followed by 1 mL of water, washed with sat. NH_4Cl_{aq}, dried over $MgSO_4$, and concentrated to 10 mL *in vacuo* (due to the foaming when R_F = F13 the organic phase was concentrated with a stream of air over several hours). The crude product was then precipitated from the organic phase with cold ether in a dry-ice/acetone bath. The solid was isolated by filtration and then dissolved in 5 mL of dichloromethane and 5 mL of benzene, which was then frozen in dry-ice/acetone bath and freeze-dried overnight *in vacuo*. The crude product was purified by automated flash chromatography using a RediSep C18 reverse phase silica column with a water–MeOH (0.1% FA) to dichloromethane–MeOH gradient. **R_F = $PFtB_{MONO}$**: Yield 79%. ^{1}H NMR (400 MHz, $CDCl_3$): δ 3.99 (t, J = 6.8 Hz, 2H), 3.84–3.81 (m, 1H), 3.75–3.73 (m, 1 H), 3.70–3.54 (m, 152 H), 3.48–3.43 (m, 3 H), 3.38 (s, 3 H), 1.70–1.54 (m, 4 H), 1.39–1.26 (m, 12 H). ^{19}F NMR (376 MHz, $CDCl_3$): δ −70.85 (s, 9 F). MALDI MS: $[M + Na]^+$ calcd. for $C_{93}H_{179}F_9NaO_{41}$ = 2146.2; found: 2146.3. **R_F = $PFtB_{TRI}$**: Yield 63%. ^{1}H NMR (400 MHz, $CDCl_3$): δ 4.04 (s, 6H), 3.83–3.81 (m, 1 H), 3.69–3.54 (m, 171 H), 3.48–3.45 (m, 1H), 3.44 (t, J = 7.2 Hz, 2H), 3.38 (s, 3H), 3.36 (t, J = 6.7 Hz, 2 H), 3.35 (s, 2 H), 1.62-1.50 (m, 4H), 1.38-1.27 (m, 12 H). ^{19}F NMR (376 MHz, $CDCl_3$): δ −70.83 (s). MALDI MS: $[M + K]^+$ calcd. for $C_{110}H_{195}F_{27}KO_{46}$ = 2804.2; found: 2803.2. **R_F = F13**: Yield 38% ^{1}H NMR (400 MHz, $CDCl_3$): δ 3.92 (m, 2H), 3.83–3.81 (m, 1 H), 3.69–3.54 (m, 171 H), 3.48–3.45 (m, 1H), 3.44 (t, J

= 6.8 Hz, 2H), 3.38 (s, 3H), 1.63-1.53 (m, 6 H), 1.38-1.26 (m, 18 H). ^{19}F NMR (376 MHz, $CDCl_3$) δ -81.15 (3 F), -120.01 (2 F), -122.09-122.41 (16 F), -123.10 (2 F), -123.83 (2 F), -126.51 (2 F). MALDI MS: $[M + Na]^+$ calcd. For $C_{103}H_{181}F_{27}NaO_{41}$ = 2610.2; found: 2610.5.

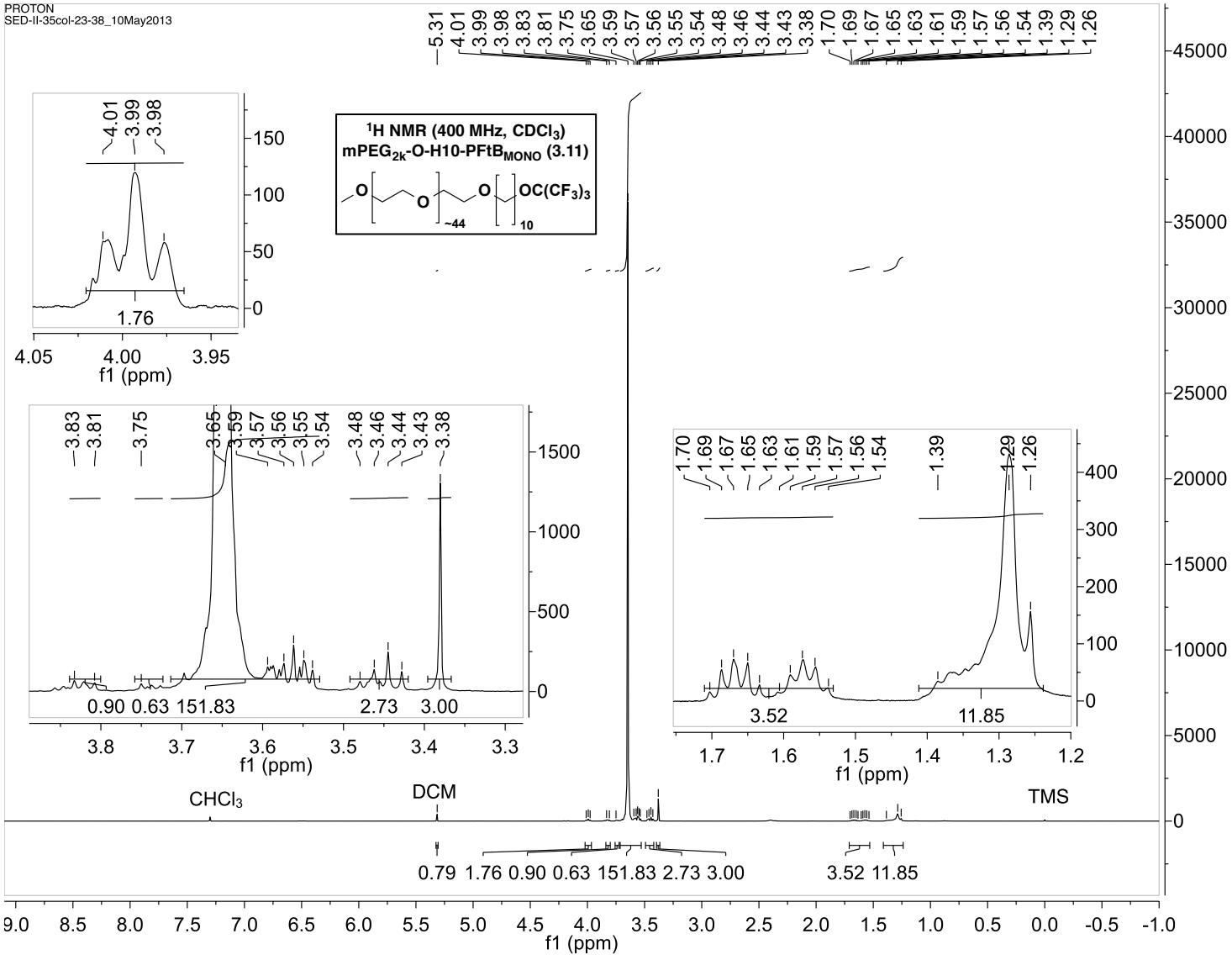
PROTON
SED-II-35col-23-38_10May2013
5.31 4.01 3.99 3.98 3.83 3.81 3.75 3.65 3.59 3.57 3.56 3.55 3.54 3.48 3.46 3.44 3.43 3.38 1.70 1.69 1.67 1.65 1.63 1.61 1.59 1.57 1.56 1.54 1.39 1.29 1.26
^{1}H NMR (400 MHz, $CDCl_3$)
$mPEG_{2k}$-O-H10-$PFtB_{MONO}$ (3.11)
O O O $OC(CF_3)_3$
~44 10
4.01 3.99 3.98
1.76
4.05 4.00 3.95
f1 (ppm)
3.83 3.81 3.75 3.65 3.59 3.57 3.56 3.55 3.54 3.48 3.46 3.44 3.43 3.38
0.90 0.63 151.83 2.73 3.00
3.8 3.7 3.6 3.5 3.4 3.3
f1 (ppm)
1.70 1.69 1.67 1.65 1.63 1.61 1.59 1.57 1.56 1.54 1.39 1.29 1.26
3.52 11.85
1.7 1.6 1.5 1.4 1.3 1.2
f1 (ppm)
$CHCl_3$
DCM
TMS
0.79 1.76 0.90 0.63 151.83 2.73 3.00
3.52 11.85
9.0 8.5 8.0 7.5 7.0 6.5 6.0 5.5 5.0 4.5 4.0 3.5 3.0 2.5 2.0 1.5 1.0 0.5 0.0 -0.5 -1.0
f1 (ppm)

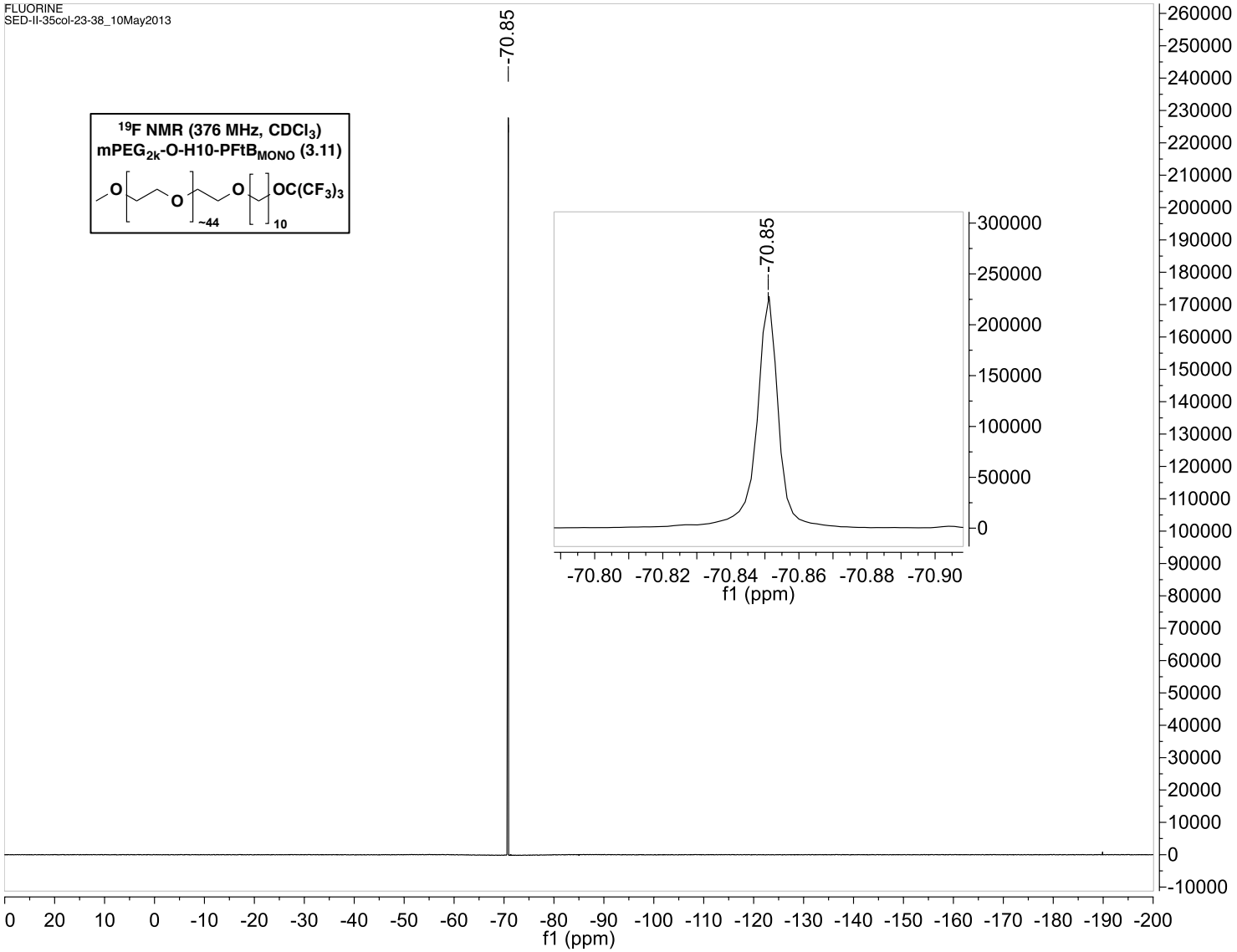
FLUORINE
SED-II-35col-23-38_10May2013
-70.85
19F NMR (376 MHz, CDCl3)
mPEG2k-O-H10-PFtBMONO (3.11)
O
O
O
OC(CF3)3
~44
10
-70.85
-70.80 -70.82 -70.84 -70.86 -70.88 -70.90
f1 (ppm)
0 20 10 0 -10 -20 -30 -40 -50 -60 -70 -80 -90 -100 -110 -120 -130 -140 -150 -160 -170 -180 -190 -200
f1 (ppm)

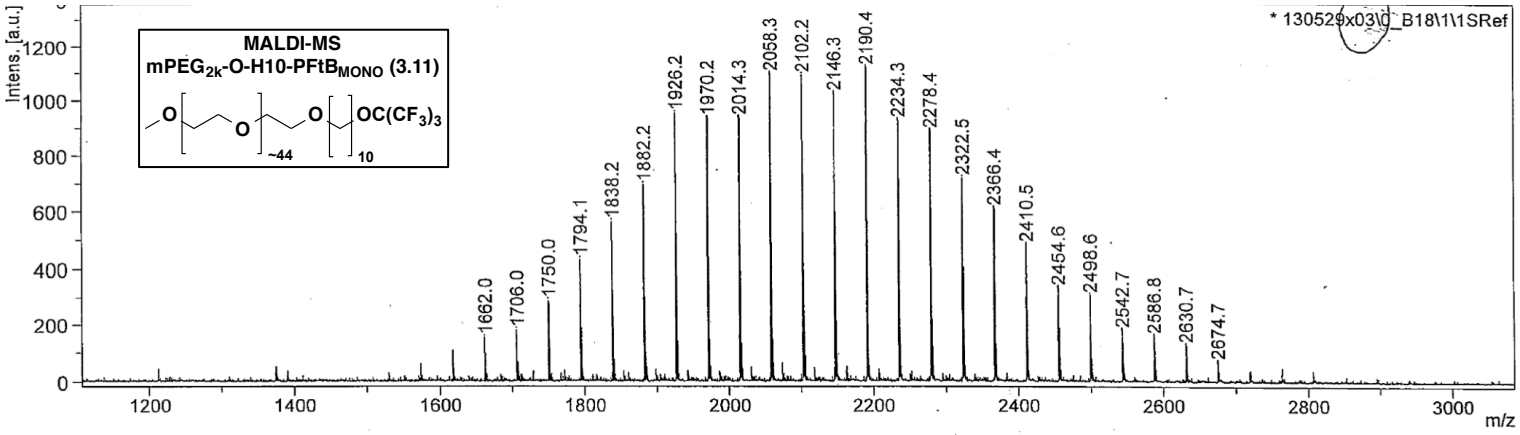
MALDI-MS
mPEG2k-O-H10-PFtBMONO (3.11)
O
O
O
OC(CF3)3
~44
10
* 130529x03\0_B18\1\1SRef
Intens. [a.u.]
1200
1000
800
600
400
200
0
1662.0
1706.0
1750.0
1794.1
1838.2
1882.2
1926.2
1970.2
2014.3
2058.3
2102.2
2146.3
2190.4
2234.3
2278.4
2322.5
2366.4
2410.5
2454.6
2498.6
2542.7
2586.8
2630.7
2674.7
1200
1400
1600
1800
2000
2200
2400
2600
2800
3000
m/z

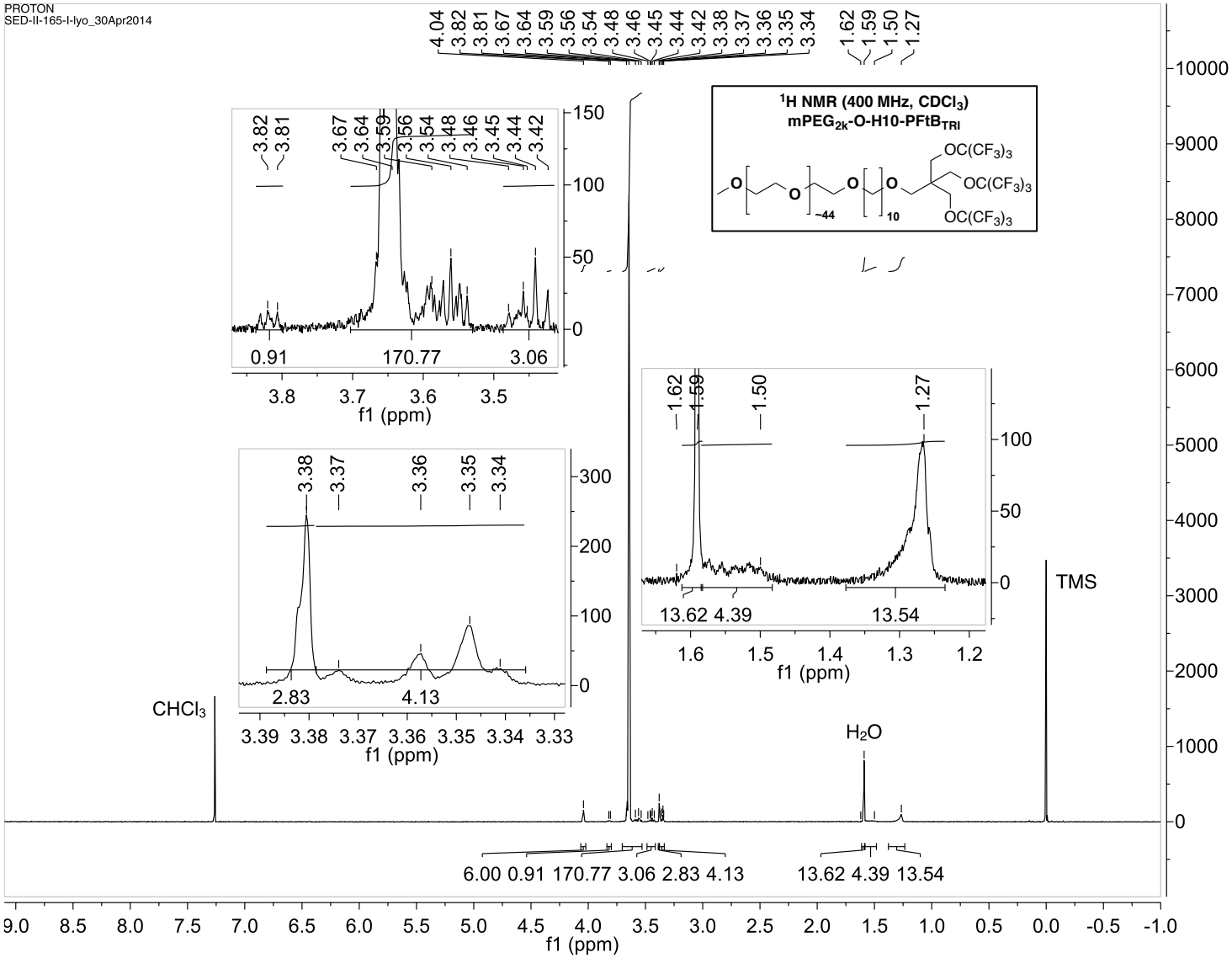
PROTON
SED-II-165-I-lyo_30Apr2014
4.04 3.82 3.81 3.67 3.64 3.59 3.56 3.54 3.48 3.46 3.45 3.44 3.42 3.38 3.37 3.36 3.35 3.34 1.62 1.59 1.50 1.27
^{1}H NMR (400 MHz, CDCl$_3$)
mPEG$_{2k}$-O-H10-PFtB$_{TRI}$
OC(CF$_3$)$_3$
OC(CF$_3$)$_3$
OC(CF$_3$)$_3$
~44
10
3.82 3.81 3.67 3.64 3.59 3.56 3.54 3.48 3.46 3.45 3.44 3.42
0.91 170.77 3.06
f1 (ppm)
3.38 3.37 3.36 3.35 3.34
2.83 4.13
f1 (ppm)
1.62 1.59 1.50 1.27
13.62 4.39 13.54
f1 (ppm)
CHCl$_3$
H$_2$O
TMS
6.00 0.91 170.77 3.06 2.83 4.13
13.62 4.39 13.54
f1 (ppm)

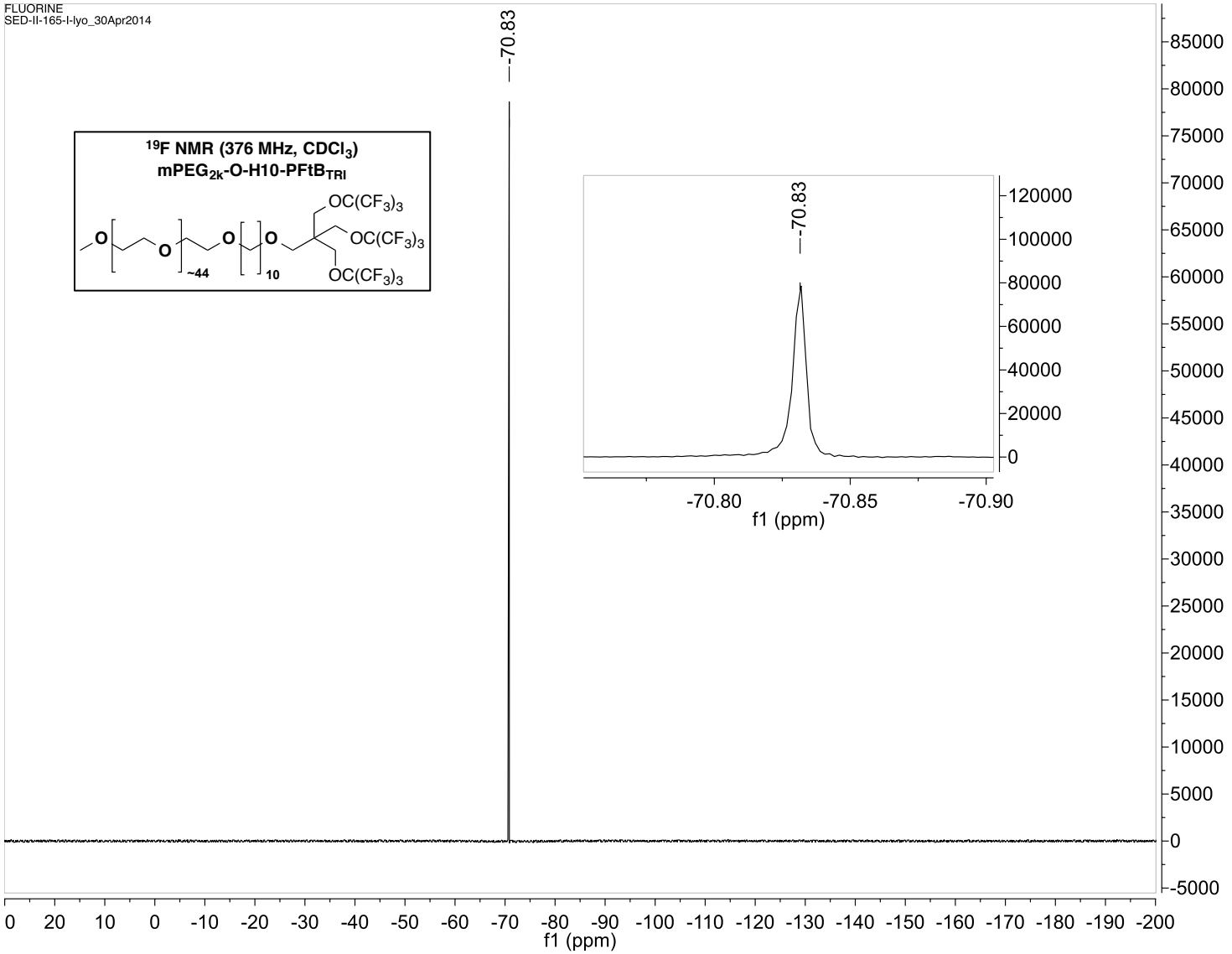
FLUORINE
SED-II-165-I-lyo_30Apr2014
-70.83
^{19}F NMR (376 MHz, $CDCl_3$)
$mPEG_{2k}$-O-H10-$PFtB_{TRI}$
$OC(CF_3)_3$
$OC(CF_3)_3$
$OC(CF_3)_3$
O
O
O
O
~44
10
-70.83
-70.80
-70.85
-70.90
f1 (ppm)
f1 (ppm)

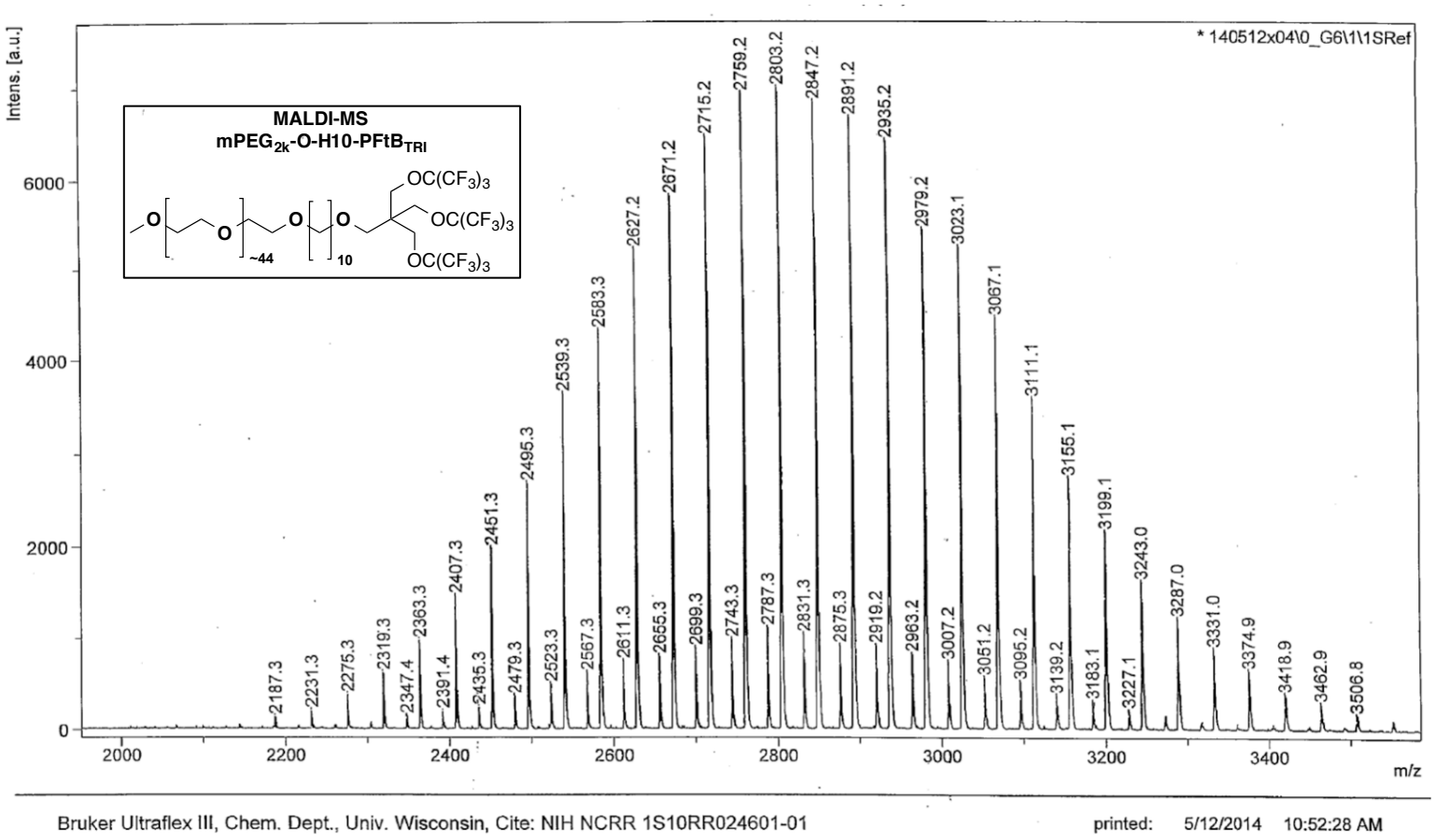
MALDI-MS
mPEG2k-O-H10-PFtBTRI
OC(CF3)3
OC(CF3)3
OC(CF3)3
~44
10
* 140512x04\0_G6\1\1SRef
Intens. [a.u.]
6000
4000
2000
0
2000
2200
2400
2600
2800
3000
3200
3400
m/z
2187.3
2231.3
2275.3
2319.3
2347.4
2363.3
2391.4
2407.3
2435.3
2451.3
2479.3
2495.3
2523.3
2539.3
2567.3
2583.3
2611.3
2627.2
2655.3
2671.2
2699.3
2715.2
2743.3
2759.2
2787.3
2803.2
2831.3
2847.2
2875.3
2891.2
2919.2
2935.2
2963.2
2979.2
3007.2
3023.1
3051.2
3067.1
3095.2
3111.1
3139.2
3155.1
3183.1
3199.1
3227.1
3243.0
3287.0
3331.0
3374.9
3418.9
3462.9
3506.8
Bruker Ultraflex III, Chem. Dept., Univ. Wisconsin, Cite: NIH NCRR 1S10RR024601-01
printed: 5/12/2014 10:52:28 AM

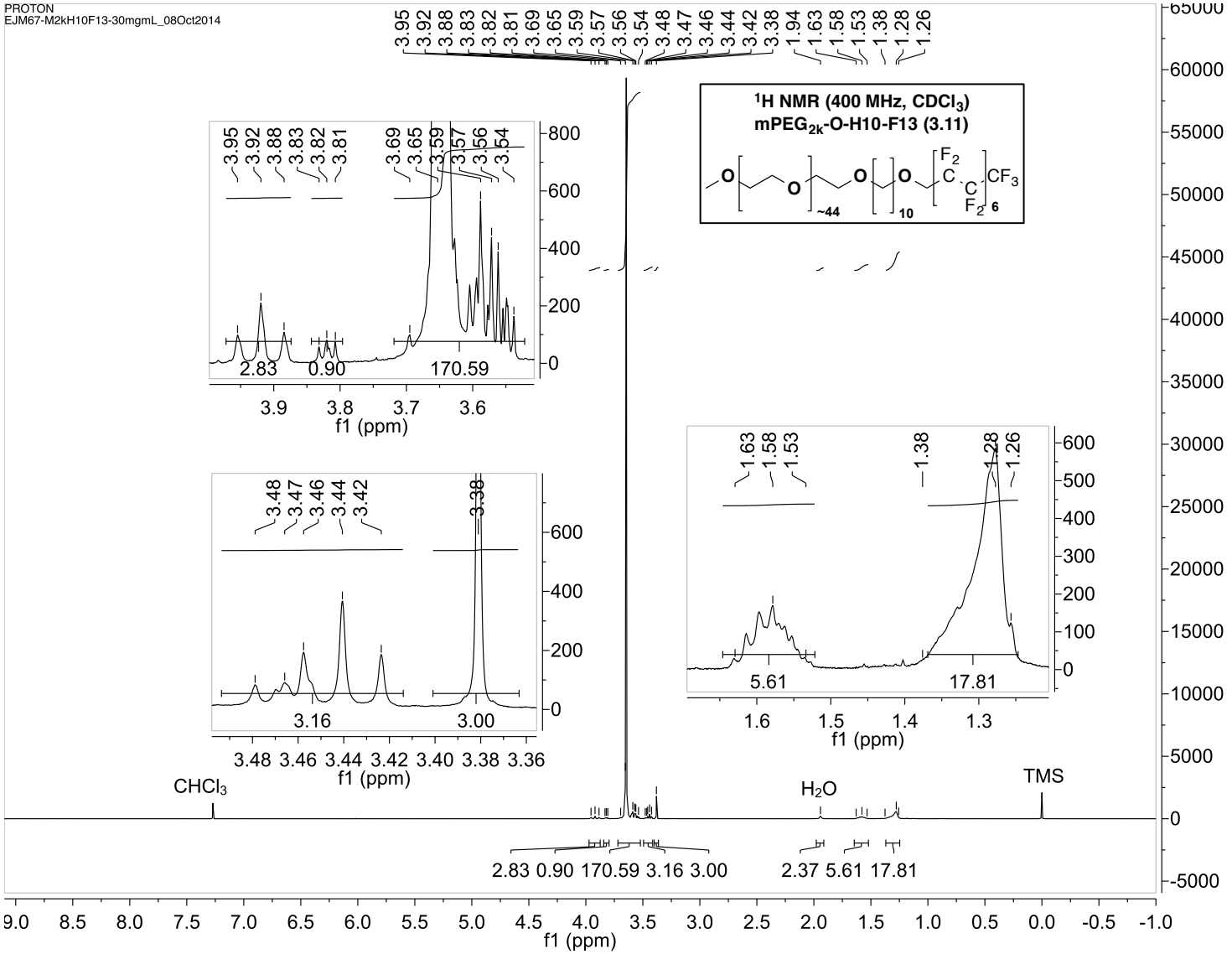
PROTON
EJM67-M2kH10F13-30mgmL_08Oct2014
3.95 3.92 3.88 3.83 3.82 3.81 3.69 3.65 3.59 3.57 3.56 3.54 3.48 3.47 3.46 3.44 3.42 3.38 1.94 1.63 1.58 1.53 1.38 1.28 1.26
1H NMR (400 MHz, CDCl3)
mPEG2k-O-H10-F13 (3.11)
~44
10
6
2.83 0.90 170.59
3.16 3.00
5.61 17.81
CHCl3
H2O
TMS
2.83 0.90 170.59 3.16 3.00 2.37 5.61 17.81
f1 (ppm)

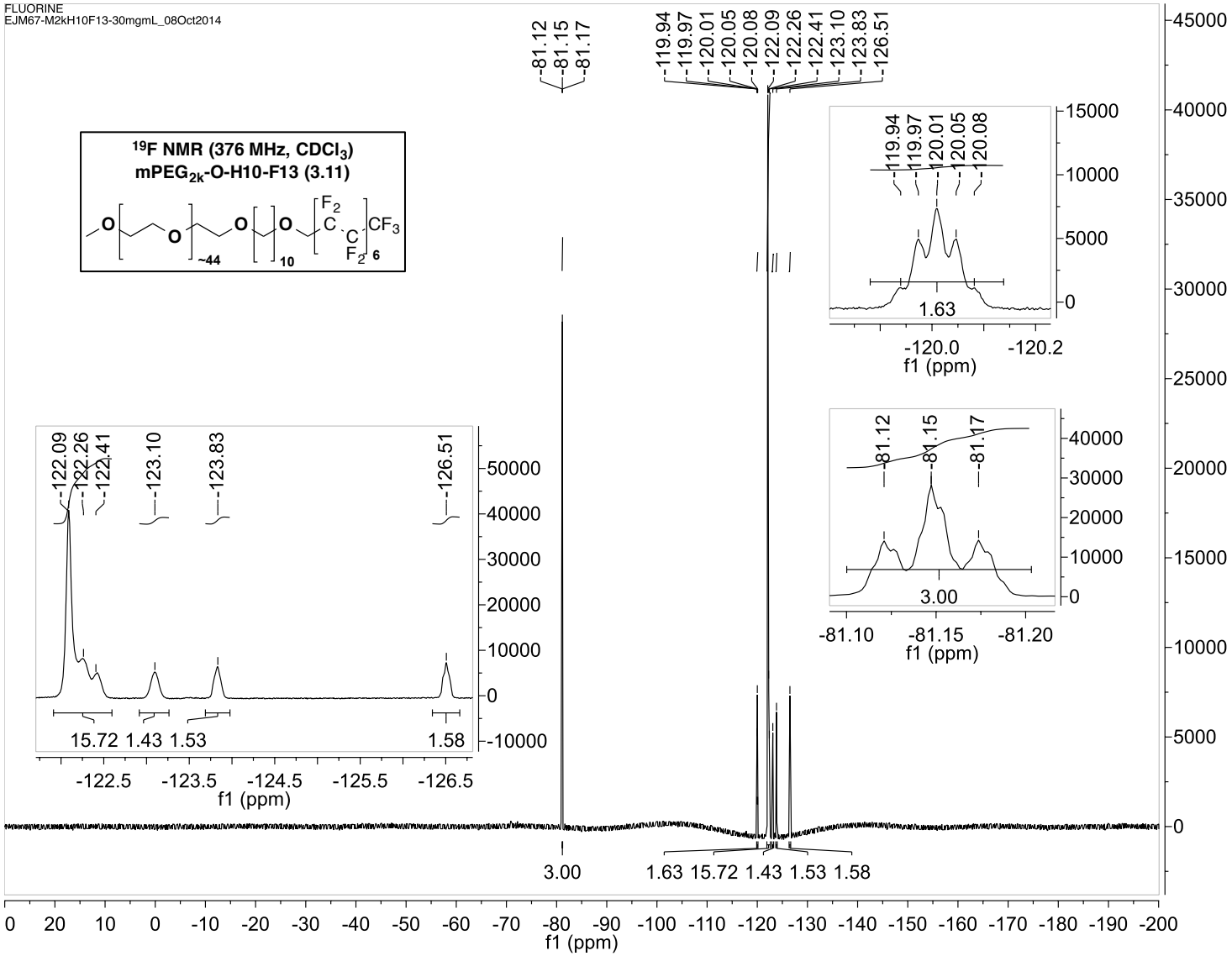
FLUORINE
EJM67-M2kH10F13-30mgmL_08Oct2014
^{19}F NMR (376 MHz, CDCl$_3$)
mPEG$_{2k}$-O-H10-F13 (3.11)
~44
10
6
-81.12
-81.15
-81.17
-119.94
-119.97
-120.01
-120.05
-120.08
-122.09
-122.26
-122.41
-123.10
-123.83
-126.51
3.00
1.63 15.72 1.43 1.53 1.58
f1 (ppm)

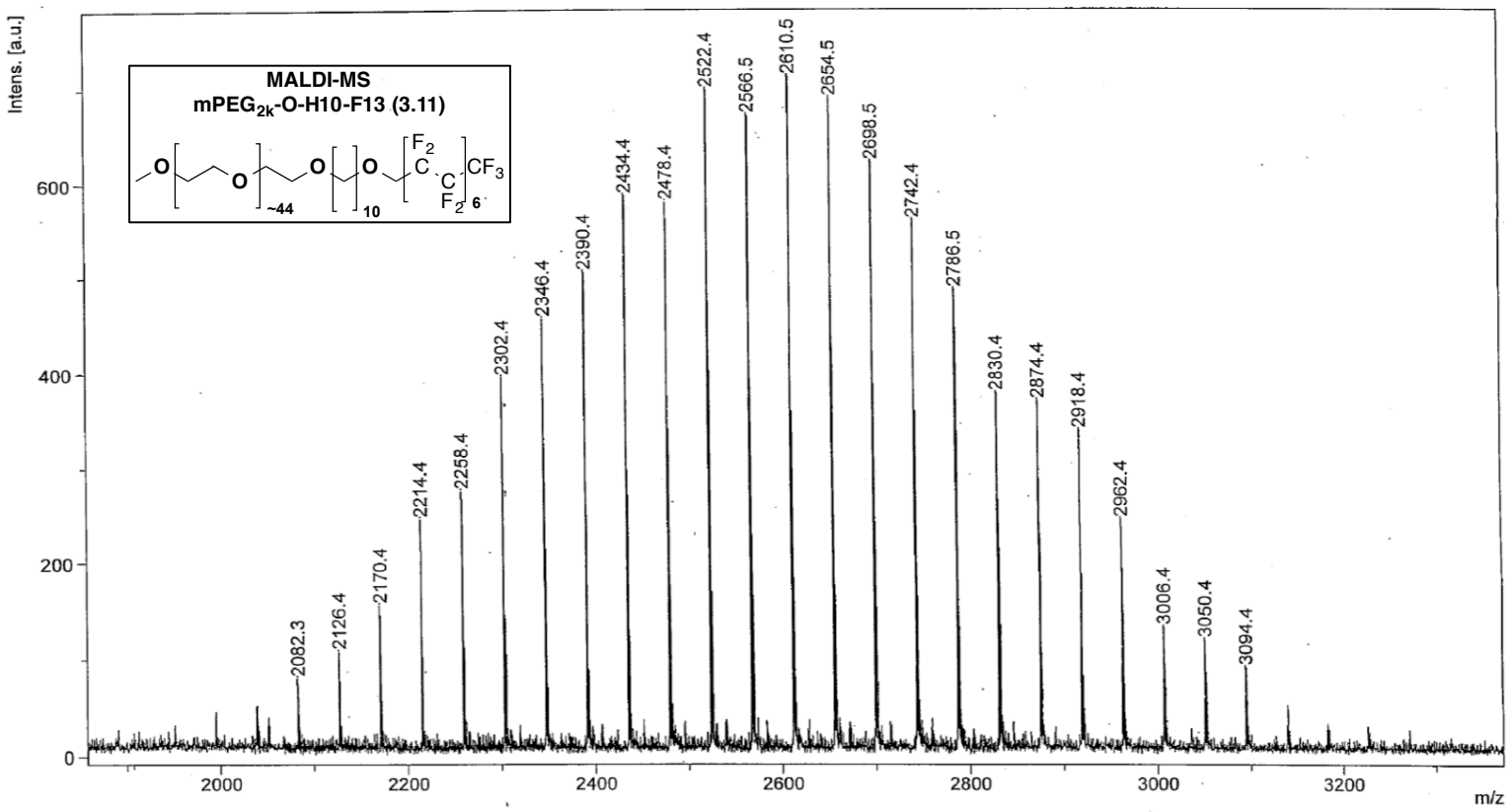
MALDI-MS
mPEG2k-O-H10-F13 (3.11)
~44
10
6
Intens. [a.u.]
m/z
0
200
400
600
2000
2200
2400
2600
2800
3000
3200
2082.3
2126.4
2170.4
2214.4
2258.4
2302.4
2346.4
2390.4
2434.4
2478.4
2522.4
2566.5
2610.5
2654.5
2698.5
2742.4
2786.5
2830.4
2874.4
2918.4
2962.4
3006.4
3050.4
3094.4

3.5.3 Micelle preparation: Solvent evaporation method

Polymer is dissolved in an organic solvent (either MeOH, ACN, or acetone) to a desired concentration. The polymer solution and an optional additive (e.g., PTX) are added to a 25 mL round bottom flask and rotated for 5 minutes at 60 °C on a rotary evaporator (covered in foil if contents are light sensitive). Then the solvent is removed *in vacuo* with rotation for 15 minutes. The remaining film is then dispersed with an aqueous solvent at 60 °C and filtered with a 0.45-μm nylon filter.

3.5.4 Physicochemical characterization: CMC, DLS, and Microviscosity

Critical micelle concentration (CMC): Surface Tensiometry. The appropriate polymer was dissolved in Milli-Q water in a 20 mL disposable scintillation vial to the desired maximum concentration (dependent upon the solubility of the polymer in water and upon the available quantity of polymer). The solution was then shaken, sonicated for 20 minutes, and allowed to equilibrate for 24 hours. (If bubbles were still present after this time, the solution was allowed to continue to equilibrate until all bubbles had dissipated.) Serial dilutions were then prepared from this stock solution to achieve the desired concentrations, again allowing for each dilution to equilibrate before subsequent dilution. After all dilutions were prepared, they were allowed to equilibrate for an additional 24 hours. A custom round platinum rod, with a diameter of 1.034 mm with a wetted length of 3.248 mm from KSV Instruments (Helsinki, Finland), was cleaned with ethanol and dried in a Bunsen burner flame. The surface tension of Millipore water was measured first and the value was confirmed to be within ± 2 mNm^{-1} of the literature value (72.8 mNm^{-1}). The surface tension of each vial was then measured using the Wilhelmy method, beginning with the least concentrated, at room temperature on a KSV sigma 701 tensiometer from KSV Instruments (Helsinki, Finland) equipped with a Schott Titronic Universal dispenser for automatic CMC measurements and a Julabo F12-MC circulator for constant temperature control.

Each sample was measured in quadruplicate and the average recorded. The CMC value was determined from the intersection of the slope at the crossover point and the slope at high concentrations. The error in the CMC measurement was calculated by applying a weighted least squares analysis to the linear sections of interest. The individual uncertainties of the two slopes and intercepts produced by the weighted least squares analysis were then propagated through as described in our previous publication[25]. The weighted least squares analysis was chosen because the uncertainty of each individual data point was known, yielding insight into the precision of the CMC calculation.

$mPEG_{2k}$-O-H10-$PFtB_{MONO}$		
log(M)	**Avg. SurfaceTension (mN/m)**	**Std. Dev. (mN/m)**
-2.56	40.47	0.04
-3.16	42.03	0.11
-3.76	41.94	0.10
-4.36	42.08	0.10
-4.97	46.46	0.15
-5.57	51.94	0.13
-6.17	63.25	0.15
-6.77	71.54	0.05
-7.37	71.66	0.14
-7.98	71.65	0.12
-8.58	71.13	0.10
-9.18	71.40	0.17
-9.78	71.08	0.13
-10.39	71.24	0.05

$mPEG_{2k}$-O-H10-$PFtB_{MONO}$

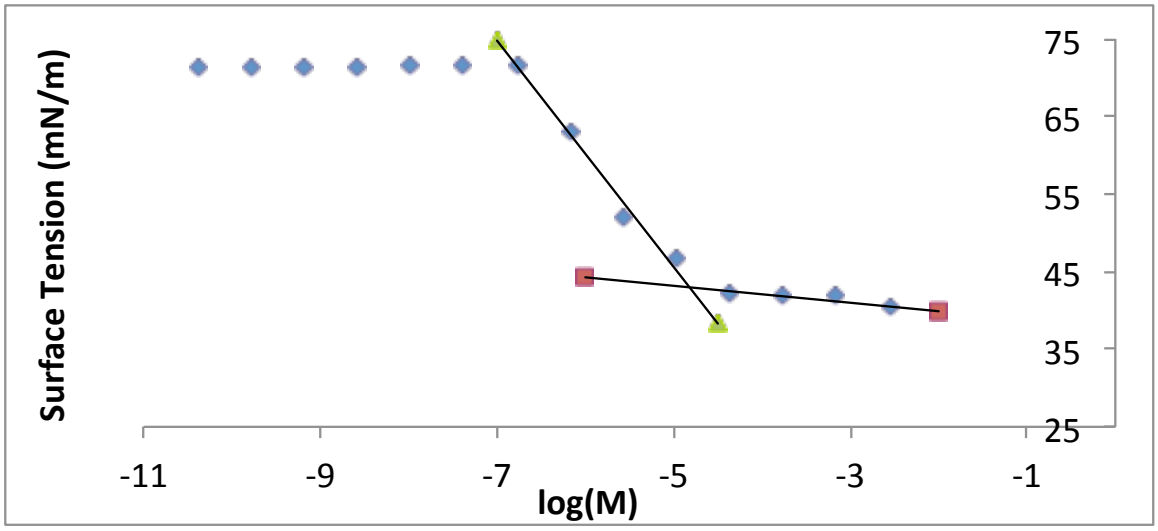

$mPEG_{2k}$-O-H10-$PFtB_{TRI}$		
log(M)	**Avg. SurfaceTension (mN/m)**	**Std. Dev. (mN/m)**
-1.98	32.64	0.51
-2.68	32.46	0.33
-3.38	32.08	0.27
-4.08	34.88	0.13
-4.77	42.23	0.19
-5.47	50.47	0.14
-6.17	61.13	0.10
-6.87	72.78	0.08
-7.57	73.06	0.10
-8.27	72.99	0.07
-8.97	73.02	0.07
-9.67	73.26	0.06
-10.37	73.26	0.10
-11.06	73.15	0.09

$mPEG_{2k}$-O-H10-$PFtB_{TRI}$

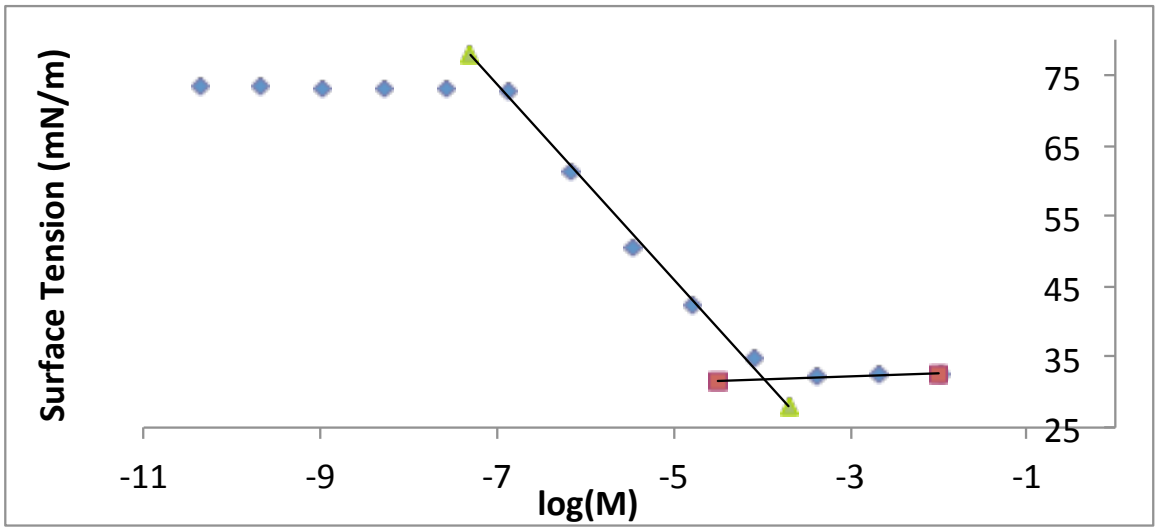

$mPEG_{2k}$-O-H10-F13		
log(M)	Avg. SurfaceTension (mN/m)	Std. Dev. (mN/m)
-2.58	39.67	0.24
-3.28	39.49	0.22
-3.98	42.67	0.35
-4.68	47.68	0.16
-5.37	51.47	0.09
-6.07	58.97	0.07
-6.77	72.60	0.12
-7.47	72.88	0.06
-8.17	72.88	0.16
-8.87	72.71	0.08
-9.57	39.67	0.24

$mPEG_{2k}$-O-H10-F13

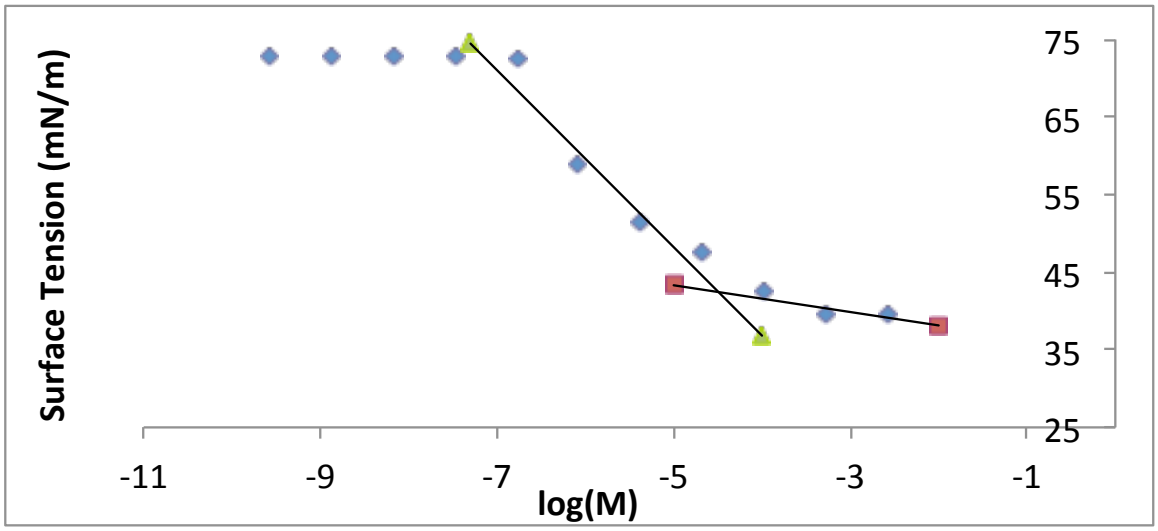

Critical Micelle Concentration (CMC): Pyrene Encapsulation Method: Polymer solutions were prepared as serial dilutions from a 1 mM stock solution in MeOH. Micelles were prepared in triplicate by using the solvent evaporation method described above. To a 25 mL roundbottom flask were added 100 μL pyrene solution and 2 mL of polymer solution to achieve the desired final concentration. The thin films were then re-dispersed with 2 mL of 60 °C PBS and filtered with a 0.45 mm nylon filter. Each solution was allowed to sit for 30 minutes before being analyzed. Fluorescence analysis using an AMINCO-Bowman Series 2 spectrometer with excitation at 339 nm and emission at 390 nm. Sensitivity was set using autorange and the voltage was recorded and kept constant throughout all subsequent measurements. The emission window was set from 370-400 nm. The total area under the curve for each spectrum was then integrated and plotted against the log of the concentration.

$mPEG_{2k}$-O-H10-$PFtB_{MONO}$

log(M)	Total Fluorescence	Total Fluorescence	Total Fluorescence
-8	0.7496	0.7642	0.6082
-6	0.5563	0.5731	0.5432
-5.5	0.5997	0.6378	0.5414
-5	0.629	2.3965	0.7748
-4.5	0.752	1.0938	1.239
-4	14.5541	3.6124	7.4979
-3.5	94.5743	92.0056	36.6833

CMC values	
-4.409	
-4.384	
-4.336	
-4.376	**Ave**
0.037	**Std. Dev.**

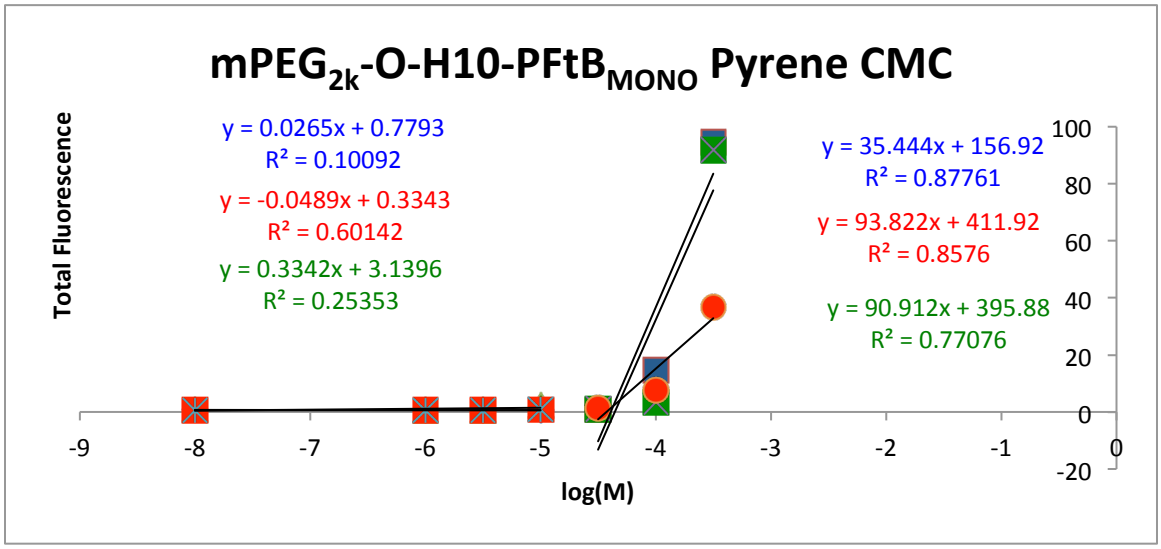

$mPEG_{2k}$-O-H10-$PFtB_{TRI}$

log(M)	Total Fluorescence	Total Fluorescence	Total Fluorescence
-8	0.4147	0.4196	0.4129
-7	0.4169	0.4196	0.4147
-6	0.4205	0.4254	0.4187
-5	0.4465	0.4306	0.4977
-4	3.1561	5.7205	5.4559
-3.5	36.4236	30.5914	20.7449
-3.25	51.8063	57.4265	51.5872

CMC values	
-4.044	
-4.048	
-4.029	
-4.040	**Average**
0.010	**Std. dev.**

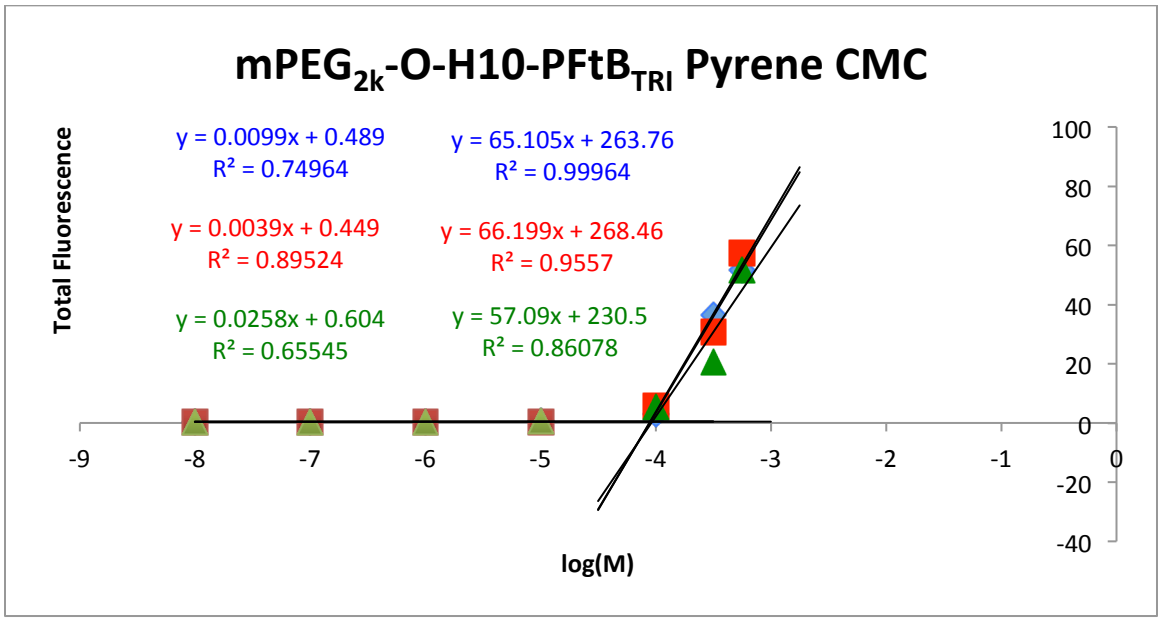

$mPEG_{2k}$-O-H10-F13

log(M)	Total Fluorescence	Total Fluorescence	Total Fluorescence
-8	0.4407	0.7999	0.4617
-7	0.4468	0.4404	0.4407
-6	0.4514	0.4388	0.4379
-5	1.7267	1.5109	0.6421
-4	28.956	30.687	31.5417
-3.5	90.7852	95.2942	82.11701
-3.25	121.1328	131.4056	110.9595

CMC values	
-4.223	
-4.224	
-4.289	
-4.245	**Average**
0.038	**Std. dev.**

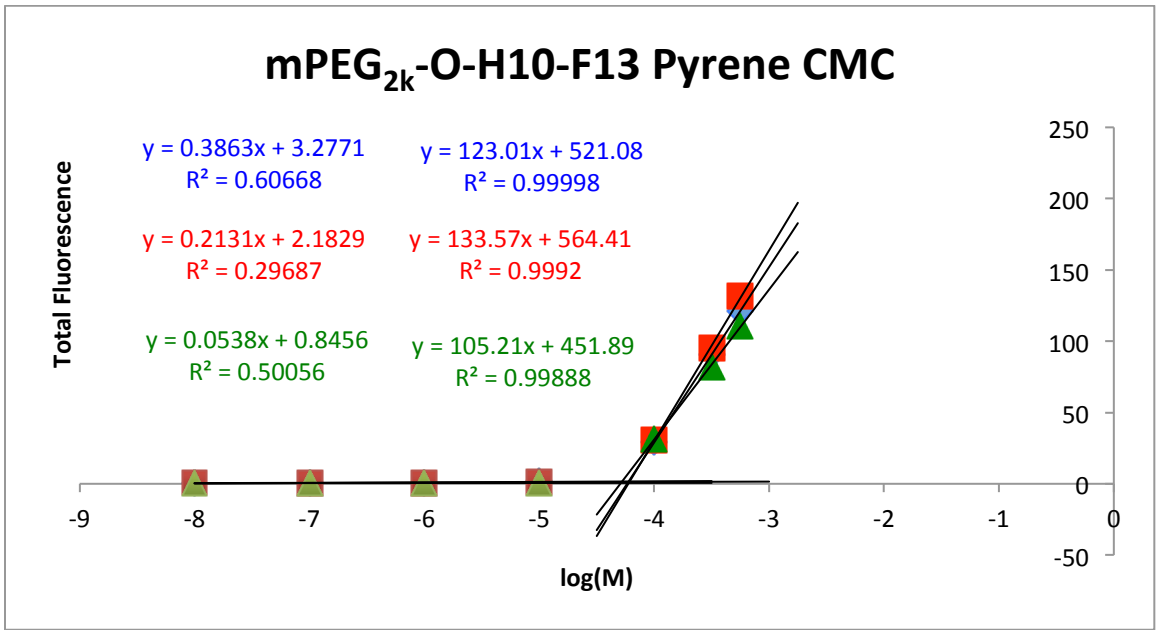

Dynamic light scattering (DLS): Samples were prepared by the solvent evaporation method using acetonitrile as the organic solvent and dispersed with Milli-Q water as the aqueous solvent to afford a the desired concentration above the CMC. Particle sizes of polymer solutions were analyzed by dynamic light scattering using a NICOMP 380ZLS from Particle Sizing Systems (Santa Barbara, CA) without further dilution in Plastibrand 1.5 mL PS semi-micro disposable cuvettes from Sigma Aldrich Co. (Milwaukee, WI). Each sample was measured before and after filtration with a 4 mm dia., 0.45 μm nylon syringe filter from Thermo Fisher Scientific Inc. (Fitchburg, WI). Each particle size analysis was performed at room temperature and repeated in triplicate with the number of scans of each run determined automatically by the instrument according to the concentration of the solution. The data were analyzed using NICOMP analysis spherical fits and reported as volume weighted average diameters. Error was reported as the standard deviation of the particle diameter as reported by the NICOMP software.

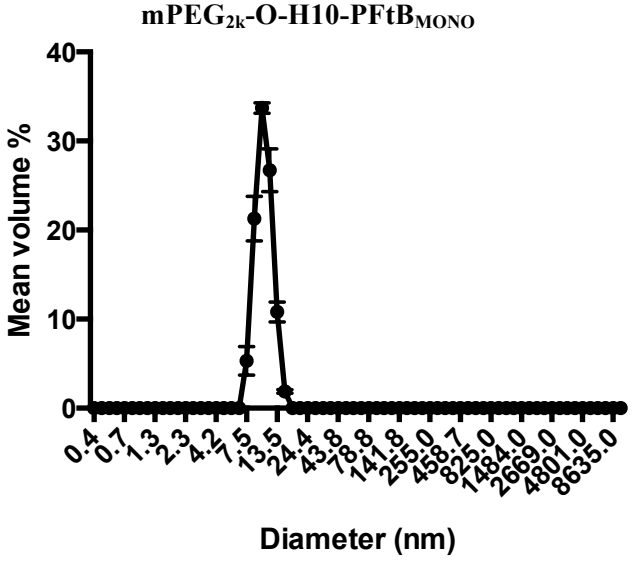

$mPEG_{2k}$-O-H10-$PFtB_{MONO}$ was prepared as a film using the solvent evaporation method to a concentration of 2.4 mM and filtered with a 0.45 μm filter. Results were consistent from sample to sample indicating that these aggregates are stable.

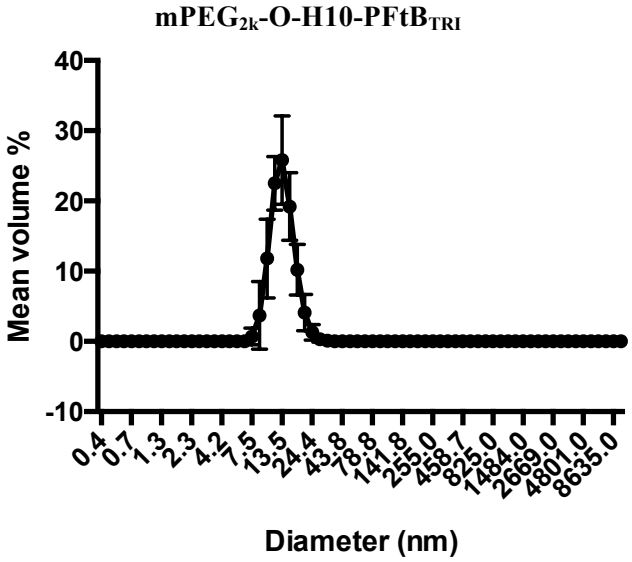

$mPEG_{2k}$-O-H10-$PFtB_{TRI}$ was analyzed at CMC concentration 3 (-3.38 log(M)) and filtered with a 0.45 μm filter. Results were consistent from sample to sample indicating that these aggregates are stable.

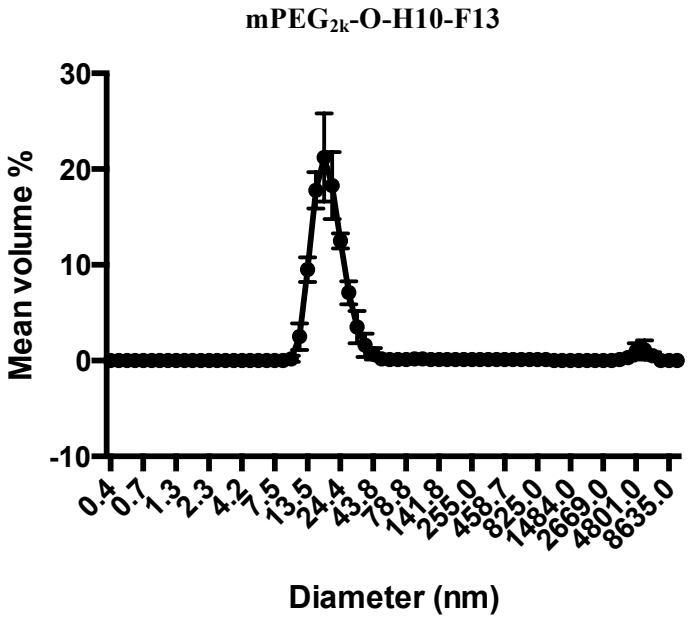

$mPEG_{2k}$-O-H10-F13 was prepared as a film using the solvent evaporation method at a concentration of 1 mM and filtered with 0.45 μm filter. Results were consistent from sample to sample indicating that these aggregates are stable.

Microviscosity: Polymer solutions of 0.2 $mmolL^{-1}$ in acetonitrile and 1,3-bis-(1-pyrenyl)propane (P3P) solution of 2.7 $ngmL^{-1}$ in chloroform were prepared. Micelle solutions were then prepared via the solvent evaporation method using 1 mL of polymer solution, 67 μL of the P3P solution, and 1 mL of phosphate buffered saline (PBS). The samples were shaken vigorously and then filtered with a 4 mm dia., 0.45 μm nylon filter and stored in amber vials. The fluorescence analysis was carried out on an AMINCO-Bowman Series 2 spectrometer from Thermo Fisher Scientific Inc. (Fitchburg, WI) with excitation at 333 nm, emission at 378 nm, and a spectral window of 350–500 nm. Error was reported as the standard deviation from triplicate measurements.

$mPEG_{2k}$-O-H10-$PFtB_{MONO}$

***376* nm**	***480* nm**	***Im/Ie Ratio***	
2.19	0.60	3.62	
1.92	0.49	3.92	
2.36	0.61	3.90	
		3.81	**Ave**
		0.16	**Std. Dev.**

$mPEG_{2k}$-O-H10-$PFtB_{TRI}$

***376* nm**	***480* nm**	***Im/Ie Ratio***	
1.60	0.29	5.53	
1.61	0.31	5.22	
1.55	0.32	4.84	
		5.19	**Ave**
		0.35	**Std. Dev.**

$mPEG_{2k}$-O-H10-F13

***376* nm**	***480* nm**	***Im/Ie Ratio***	
1.88	0.29	6.48	
1.69	0.26	6.50	
1.96	0.31	6.32	
		6.44	**Ave**
		0.10	**Std. Dev.**

3.5.5 Encapsulation of PTX

Paclitaxel (PTX) Encapsulation Measurements: Micelles solutions were prepared in triplicate using the solvent evaporation method. PTX stock solution was generated by dissolving PTX in ACN, aided by sonication, at a concentration of 1 mg/mL. Surfactant was dissolved in ACN to give a final concentration of 2.4×10^{-3} mol/L. 1 mL of surfactant solution was then mixed with 230 µL PTX solution. The sample was then centrifuged at 12,000 rpm for 5 min and filtered through 0.45-µm nylon syringe filter to remove any insoluble precipitate. A 100-µL aliquot of micelle solution was mixed with 900 µL of ACN and the remaining micelle solution was allowed to sit for 24 h. The sample was then re-centrifuged at 12,000 rpm for 5 min and filtered through 0.45 µm nylon syringe filter to remove any insoluble precipitate. A 100-µL

aliquot of micelle solution was mixed with 900 µL of ACN. The paclitaxel loaded in the micelle was quantified by reverse phase using HPLC (Shimadzu prominence HPLC system, Shimadzu, Japan), equipped with a LC-20AT pump, SIL-20 AC HT autosampler, CTO-20 AC column oven and an SPD-M20A diode array detector. 20 µL of the mixture was injected into a C18 column (Agilent XDB-C8, 4.6 Å × 150 mm), eluting with an isocratic mixture of 25% water in acetonitrile. The run time was 7 min, the flow rate was 1.0 mL/min and the detection was set at 227 nm. PTX eluted at 4.15 min.

Amphiphile	**Initial Encapsulation µg/mL (ave ± S.D.) PTX**	**Remaining After 24 h µg/mL (ave ± S.D.) PTX**
$mPEG_{2k}$-DSPE	229.61 ± 5.38	215.83 ± 6.51
$mPEG_{2k}$-O-H10-F13 (**3.3**)	161.28 ± 18.77	68.72 ± 9.69
$mPEG_{2k}$-O-H10-$PFtB_{MONO}$ (**3.1**)	198.17 ± 2.63	35.04 ± 4.99
$mPEG_{2k}$-O-H10-$PFtB_{TRI}$ (**3.2**)	226.68 ± 3.86	220.80 ± 5.63

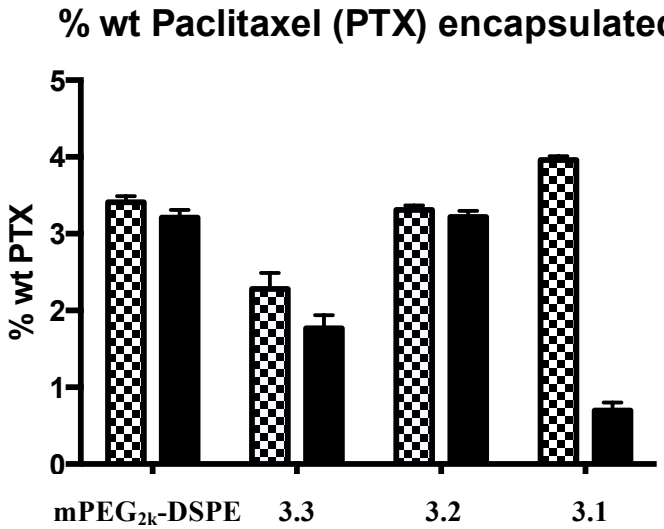

3.5.6 Cell culture: Hemolysis and A59 cell toxicity

Hemolysis assay: Polymer solutions ($mPEG_{1k}$-O-H10-$PFtB_{TRI}$, **3.2**) were made by direct dilution in sterile PBS. Suspended rabbit red blood cells (10%, 15 mL) were centrifuged (2000 rpm, 2 min, 25 °C, 450*g*), the supernatant was removed, and the cells were resuspended in 15 mL

of sterile PBS. To each well of a clear 96-well plate were added varying amounts of rabbit red blood cells and $(100 - x)$ μL of sterile PBS buffer, where x represents the amount of rabbit red blood cells (10, 20, 50, and 100 μL) that was added to the respective well. Finally, 100 μL of the appropriate polymer solution was added to each well to afford final treated polymer concentrations of 20, 2, and 0.2 mM. Each experimental condition was repeated in triplicate. The plates were then incubated statically at 37 °C for 3 h. The plates were then centrifuged to pellet the cells (4 min, 25 °C, 450*g*). A 100 μL portion of supernatant from each well of culture was transferred to a fresh, clear 96-well plate. Absorbance at 420 nm and 540 nm was measured for each well using an EnVision Multilabel Plate Reader from PerkinElmer (Waltham, MA) and percent hemolysis relative to the positive control was determined. Complete hemolysis of the positive control was achieved by treating red blood cells with 100 μL of Milli-Q water in place of polymer solution.

***In vitro* Cell toxicity against A549**: A549 human epithelial lung cancer cell line was obtained from ATCC (CCL-185) and cultured in RPMI 1640 supplemented with 10% FBS and 1% penicillin/streptomycin. A549 cells were seeded at 1,000 cells/well on 96-well plates and incubated for 24 h. Polymer micelle solutions (both with and without PTX) were prepared immediately before plating using the solvent-evaporation method using ACN as the organic solvent and in RPMI 1640 as the aqueous solvent. The free PTX solution was prepared by dissolving in DMSO at 60 °C with sonication and quick dilution to the desired concentrations with supplemented RPMI 1640 to afford a final solution containing 0.1 % DMSO. A 10 μL aliquot of each polymer solution and 90 μL of supplemented RPMI 1640 were added to each well (immediately after preparation to minimize possible drug precipitation). The cells were then incubated with the empty micelles, PTX-loaded micelles, and free PTX for 24 h. The cells were incubated for another 24 h and the assay was carried out according to the manufacturer's protocol

(CellTiter-Blue® Cell Viability Assay). The fluorescence signals were measured 4 h after adding the dye. The results were repeated in triplicate and averaged, represented as percentages of cell viability determined using untreated cells as the control (100 % viability).

3.5.7 In vitro time-release profile

Polymer was dissolved in ACN to a concentration of 2.4 mM. Paclitaxel was dissolved in ACN to a concentration of 1 mg mL^{-1} (1.2 mM). Micelle solutions were then prepared by the solvent evaporation method as described above (addition of 3 mL polymer solution and 690 mL PTX solution), dispersed with 60 °C PBS and filtered with 0.45 mm nylon filter. A t = 0 time point was established by diluting 100 mL of micelle solution in 900 mL ACN. A 3 mL capacity Slide-A-Lyzer Dialysis cassette G2 2,000 MWCO from Thermo Fisher Scientific Inc. (Fitchburg, WI) was hydrated by stirring for 30 min in a 3L PBS bath at 37 °C. After this time, 2.5 mL of PTX-micelle solution was added to the cassette, which was then returned to the PBS bath and allowed to stir for 1 week. Time points were taken at 0.5, 2, 3, 6, 9, 12, 24, 36, 48, 72, 96, 120, 144, 168, 192, 216, 240 h. For each time point a 100 mL aliquot of the micelle solution was removed from the cassette and diluted with 900 mL ACN. The aliquot was then replaced in the cassette with 100 mL of fresh PBS solution. Sink conditions were maintained by replacing the 3L PBS baths at the 3, 6, 9, and 12 h time points and every 12 h thereafter.

The paclitaxel concentration remaining was quantified by reverse phase HPLC. The HPLC system used was a Shimadzu prominence HPLC system (Shimadzu, Japan), equipped with a LC-20AT pump, SIL-20 AC HT autosampler, CTO-20 AC column oven and an SPD-M20A diode array detector. For each time point sample, 20 µL was injected into a C18 column (Agilent XDB-C8, 4.6 Å x 150 mm), and eluted with an isocratic mixture of 25 % water in acetonitrile. The run time was 7 min, the flow rate was 1.0 mL min^{-1} and the detection was set at 227 nm. PTX eluted at 4.15 min. Concentration determined by integrating the area of the peak and extrapolation from

a standard curve. Curve-fitting analysis using one phase exponential association was used to plot the data.

	Encapsulated PTX mg/mL (ave ± S.D.)			
Time (h)	**$mPEG_{2k}$-DSPE**	**$mPEG_{2k}$-O-H10-F13**	**$mPEG_{2k}$-O-H10-$PFtB_{MONO}$**	**$mPEG_{2k}$-O-H10-$PFtB_{TRI}$**
0	205.08 ± 2.77	113.07 ± 1.40	181.65 ± 3.78	226.43 ± 9.19
0.5	197.52 ± 10.59	107.14 ± 4.26	117.84 ± 13.03	209.84 ± 15.18
2	177.91 ± 11.34	80.21 ± 2.35	66.03 ± 8.80	201.48 ± 14.37
3	175.70 ± 11.70	83.79 ± 2.21	42.93 ± 6.61	193.010 ± 0.91
6	156.99 ± 5.40	74.43 ± 8.74	26.98 ± 3.18	176.55 ± 11.55
9	149.51 ± 1.61	80.84 ± 4.84	6.99 ± 6.95	170.14 ± 3.26
12	142.45 ± 8.17	78.87 ± 7.13		160.32 ± 3.91
24	111.84 ± 8.73	54.80 ± 15.28		122.18 ± 24.15
36	99.88 ± 6.22	47.54 ± 11.58		108.77 ± 18.33
48	89.04 ± 8.25	39.86 ± 5.78		88.18 ± 5.07
72	86.87 ± 14.71	31.90 ± 7.55		71.30 ± 20.89
96	82.81 ± 6.33	33.97 ± 6.87		64.63 ± 12.39
120	79.48 ± 2.04	35.48 ± 5.93		62.64 ± 16.13
144	72.80 ± 7.35	29.53 ± 3.51		52.49 ± 15.12
168	70.09 ± 3.07	31.65 ±4.47		47.01 ± 13.59

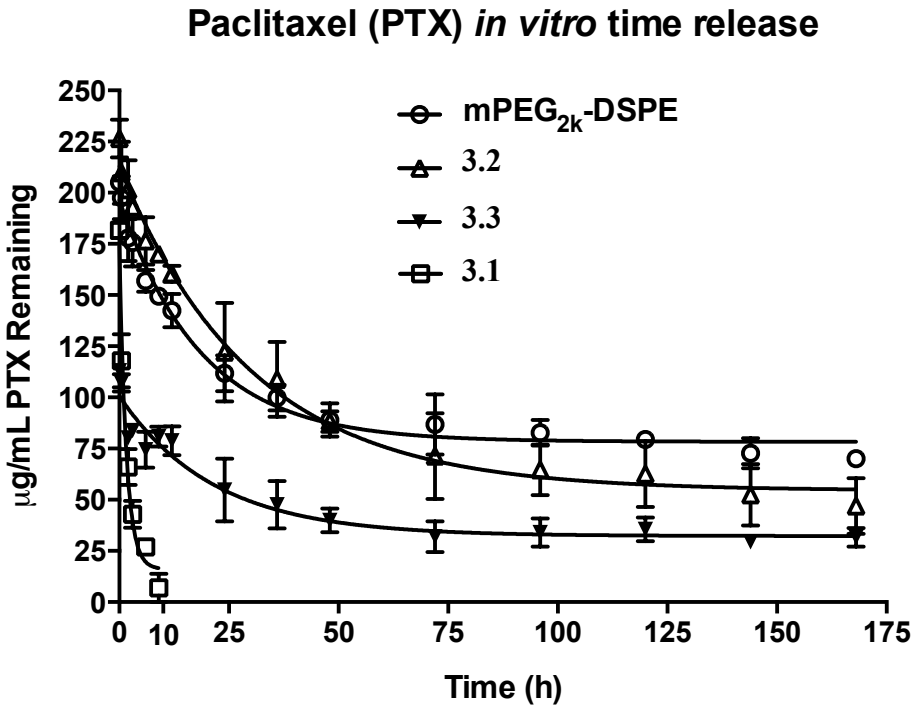

3.5.8 In vitro serum stability: FRET

Föster Resonance Energy Transfer (FRET) Stability: Surfactant solutions of 1 mg/mL in methanol and 0.1 mg/mL of 1,1′-dioctadecyl-3,3,3′,3′-tetramethylindocarbocyanine perchlorate (DiI) and 3,3′-dioctadecyloxacarbocyanine perchlorate (DiO) in methanol were prepared. Micelle solutions were then prepared by the solvent evaporation method. For blank micelles only polymer solution is used; for FRET loaded micelles, 46 μL DiI and 44 μL of DiI are added were added to achieve final concentrations of 5 μmol. Three types of samples were then prepared (the two components were mixed just before analysis): 50 μL of FRET dye loaded micelles and 950 μL PBS (used to set sensitivity), 50 μL empty micelles and 950 μL human serum (used to correct for background), 150 μL FRET dye loaded micelles and 2.85 mL human serum (mixed gently before first measurement and more vigorously before each subsequent measurement; every 15 min,

thereafter. The fluorescence analysis was carried out on an AMINCO-Bowman Series 2 spectrometer with excitation at 484 nm. The FRET ratio calculated was the ratio of $I_{565}/(I_{501} + I_{565})$.

FRET Ratio: $\frac{I_{565}}{(I_{501}+I_{565})}$, where I_{501} = emission of donor dye (DiO) and I_{565} = emission of acceptor dye (DiI)

	$mPEG_{2k}$-O-H10-$PFtB_{TRI}$		$mPEG_{2k}$-O-H10-$PFtB_{MONO}$		$mPEG_{2k}$-O-H10-F13	
Min.	**FRET Ratio**	**Std. Dev.**	**FRET Ratio**	**Std. Dev.**	**FRET Ratio**	**Std. Dev.**
0	0.610	0.005	0.516	0.016	0.652	0.043
15	0.552	0.001	0.497	0.005	0.651	0.023
30	0.556	0.011	0.480	0.001	0.630	0.032
45	0.559	0.017	0.474	0.003	0.620	0.052
60	0.554	0.012	0.460	0.004	0.628	0.043
75	0.556	0.011	0.462	0.006	0.618	0.023
90	0.558	0.010	0.447	0.000	0.607	0.017
105	0.562	0.017	0.453	0.003	0.598	0.012
120	0.555	0.011	0.445	0.017	0.601	0.010
135	0.556	0.006				
150	0.556	0.018				
165	0.551	0.013				
180	0.549	0.014				
1110	0.419	0.009				

	$mPEG_{2k}$-DSPE	
Min.	**FRET Ratio**	**Std. Dev.**
0	0.789	0.013
20	0.723	0.018
40	0.695	0.011
60	0.660	0.014
80	0.634	0.010
100	0.621	0.016
120	0.616	0.013
240	0.626	0.003
360	0.626	0.011

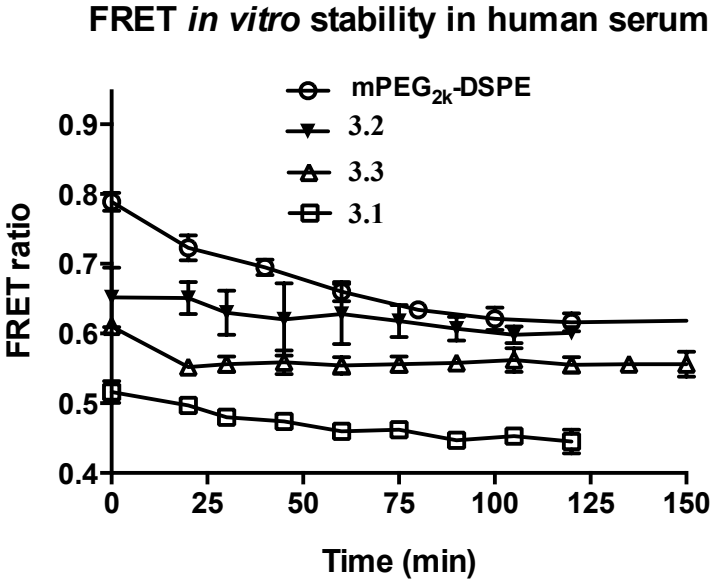

3.6 Acknowledgements

Thank you to Professor Glen S. Kwon, Wisconsin Institutes for Medical Research (WIMR) Imaging Sciences Center, and the Small Molecule Screening Facility (SMSF) for your support and to NSF and JSPS for funding; NSF-EAPSI-1414737 and JSPS-SP14012.

3.7 References

(1) Davis, M. E.; Chen, Z. G.; Shin, D. M. Nanoparticle Therapeutics: An Emerging Treatment Modality for Cancer. *Nat. Rev. Drug Discov.* **2008**, *7* (9), 771–782.

(2) Torchilin, V. P. Multifunctional Nanocarriers. *Adv. Drug Deliv. Rev.* **2006**, *58* (14), 1532–1555.

(3) Shi, J.; Votruba, A. R.; Farokhzad, O. C.; Langer, R. Nanotechnology in Drug Delivery and Tissue Engineering: From Discovery to Applications. *Nano Lett.* **2010**, *10* (9), 3223–3230.

(4) Ding, J.; Chen, L.; Xiao, C.; Chen, L.; Zhuang, X.; Chen, X. Noncovalent Interaction-Assisted Polymeric Micelles for Controlled Drug Delivery. *Chem. Commun.* **2014**, *50*, 11274–11290.

(5) Yameen, B.; Choi, W. Il; Vilos, C.; Swami, A.; Shi, J.; Farokhzad, O. C. Insight into Nanoparticle Cellular Uptake and Intracellular Targeting. *J. Control. Release* **2014**, *190*, 485–499.

(6) Chen, Y. C.; Lo, C. L.; Hsiue, G. H. Multifunctional Nanomicellar Systems for Delivering Anticancer Drugs. *J. Biomed. Mater. Res. - Part A* **2013**, 2024–2038.

(7) Cabral, H.; Kataoka, K. Progress of Drug-Loaded Polymeric Micelles into Clinical Studies. *J. Control. Release* **2014**, *190*, 465–476.

(8) McLaughlin, C. K.; Logie, J.; Shoichet, M. S. Core and Corona Modifications for the Design of Polymeric Micelle Drug-Delivery Systems. *Israel Journal of Chemistry*, 2013, *53*, 670–679.

(9) Tang, L.; Yang, X.; Yin, Q.; Cai, K.; Wang, H.; Chaudhury, I.; Yao, C.; Zhou, Q.; Kwon, M.; Hartman, J. a.; Dobrucki, I. T.; Dobrucki, L. W.; Borst, L. B.; Lezmi, S.; Helferich, W. G.; Ferguson, a. L.; Fan, T. M.; Cheng, J. Investigating the Optimal Size of Anticancer Nanomedicine. *Proc. Natl. Acad. Sci.* **2014**, *111*, 15344–15349.

(10) Tang, L.; Gabrielson, N. P.; Uckun, F. M.; Fan, T. M.; Cheng, J. Size-Dependent Tumor Penetration and in Vivo Efficacy of Monodisperse Drug-Silica Nanoconjugates. *Mol. Pharm.* **2013**, *10* (3), 883–892.

(11) Fang, C.; Shi, B.; Pei, Y.-Y.; Hong, M.-H.; Wu, J.; Chen, H.-Z. In Vivo Tumor Targeting of Tumor Necrosis Factor-Alpha-Loaded Stealth Nanoparticles: Effect of MePEG Molecular Weight and Particle Size. *Eur. J. Pharm. Sci.* **2006**, *27* (1), 27–36.

(12) Greish, K. Enhanced Permeability and Retention of Macromolecular Drugs in Solid Tumors: A Royal Gate for Targeted Anticancer Nanomedicines. *J. Drug Target. 15* (7-8), 457–464.

(13) Fang, J.; Nakamura, H.; Maeda, H. The EPR Effect: Unique Features of Tumor Blood Vessels for Drug Delivery, Factors Involved, and Limitations and Augmentation of the Effect. *Adv. Drug Deliv. Rev.* **2011**, *63* (3), 136–151.

(14) Eetezadi, S.; Ekdawi, S. N.; Allen, C. The Challenges Facing Block Copolymer Micelles for Cancer Therapy: In Vivo Barriers and Clinical Translation. *Adv. Drug Deliv. Rev.* **2014**, No. 2014, 10.1016/j.addr.2014.10.001.

(15) Cabral, H.; Matsumoto, Y.; Mizuno, K.; Chen, Q.; Murakami, M.; Kimura, M.; Terada, Y.; Kano, M. R.; Miyazono, K.; Uesaka, M.; Nishiyama, N.; Kataoka, K. Accumulation of Sub-100 Nm Polymeric Micelles in Poorly Permeable Tumours Depends on Size. *Nat. Nanotechnol.* **2011**, *6* (12), 815–823.

(16) Alexis, F.; Pridgen, E.; Molnar, L. K.; Farokhzad, O. C. Factors Affecting the Clearance and Biodistribution of Polymeric Nanoparticles. *Mol. Pharm.* **2008**, *5* (4), 505–515.

(17) Owens, D. E.; Peppas, N. A. Opsonization, Biodistribution, and Pharmacokinetics of Polymeric Nanoparticles. *Int. J. Pharm.* **2006**, *307* (1), 93–102.

(18) Yang, C.; Ebrahim Attia, A. B.; Tan, J. P. K.; Ke, X.; Gao, S.; Hedrick, J. L.; Yang, Y. Y. The Role of Non-Covalent Interactions in Anticancer Drug Loading and Kinetic Stability of Polymeric Micelles. *Biomaterials* **2012**, *33* (10), 2971–2979.

(19) Owen, S. C.; Chan, D. P. Y.; Shoichet, M. S. Polymeric Micelle Stability. *Nano Today* **2012**, *7* (1), 53–65.

(20) Tucker, W. B.; McCoy, A. M.; Fix, S. M.; Stagg, M. F.; Murphy, M. M.; Mecozzi, S. Synthesis, Physicochemical Characterization, and Self-Assembly of Linear, Dibranched, and Miktoarm Semifluorinated Triphilic Polymers. *J. Polym. Sci. Part A Polym. Chem.* **2014**, *52* (23), 3324–3336.

(21) Jee, J.-P.; McCoy, A.; Mecozzi, S. Encapsulation and Release of Amphotericin B from an ABC Triblock Fluorous Copolymer. *Pharm. Res.* **2012**, *29* (1), 69–82.

(22) Zhou, Z.; Li, Z.; Ren, Y.; Hillmyer, M. a.; Lodge, T. P. Micellar Shape Change and Internal Segregation Induced by Chemical Modification of a Tryptych Block Copolymer Surfactant. *J. Am. Chem. Soc.* **2003**, *125*, 10182–10183.

(23) Wang, R.; Xiao, R.; Zeng, Z.; Xu, L.; Wang, J. Application of Poly(ethylene Glycol)-Distearoylphosphatidylethanolamine (PEG-DSPE) Block Copolymers and Their Derivatives as Nanomaterials in Drug Delivery. *Int. J. Nanomedicine* **2012**, *7*, 4185–4198.

(24) Vuković, L.; Khatib, F. a.; Drake, S. P.; Madriaga, A.; Brandenburg, K. S.; Král, P.; Onyuksel, H. Structure and Dynamics of Highly PEG-Ylated Sterically Stabilized Micelles in Aqueous Media. *J. Am. Chem. Soc.* **2011**, *133*, 13481–13488.

(25) Decato, S.; Bemis, T.; Madsen, E.; Mecozzi, S. Synthesis and Characterization of Perfluoro-Tert-Butyl Semifluorinated Amphiphilic Polymers and Their Potential Application in Hydrophobic Drug Delivery. *Polym. Chem.* **2014**, *5*, 6461–6471.

(26) El-Sayed, M.; Kiani, M. F.; Naimark, M. D.; Hikal, A. H.; Ghandehari, H. Extravasation of Poly(amidoamine) (PAMAM) Dendrimers across Microvascular Network Endothelium. *Pharm. Res.* **2001**, *18* (1), 23–28.

(27) Grant, C. D.; DeRitter, M. R.; Steege, K. E.; Fadeeva, T. A.; Castner, E. W. Fluorescence Probing of Interior, Interfacial, and Exterior Regions in Solution Aggregates of Poly(ethylene Oxide)- Poly(propylene Oxide)-Poly(ethylene Oxide) Triblock Copolymers. *Langmuir* **2005**, *21* (5), 1745–1752.

(28) Dhanikula, A. B.; Panchagnula, R. Preparation and Characterization of Water-Soluble Prodrug, Liposomes and Micelles of Paclitaxel. *Curr. Drug Deliv.* **2005**, *2* (1), 75–91.

(29) Ma, P. Paclitaxel Nano-Delivery Systems: A Comprehensive Review. *J. Nanomed. Nanotechnol.* **2013**, *4* (2), 1000164.

(30) Amado, E.; Blume, A.; Kressler, J. Novel Non-Ionic Block Copolymers Tailored for Interactions with Phospholipids. *React. Funct. Polym.* **2009**, *69* (7), 450–456.

(31) Diezi, T. A.; Bae, Y.; Kwon, G. S. Enhanced Stability of PEG-Block-poly(N-Hexyl Stearate L-Aspartamide) Micelles in the Presence of Serum Proteins. *Mol. Pharm.* **2010**, *7* (4), 1355–1360.

CHAPTER 4:

In vivo evaluation of theranostic PFtB nanoparticles

*This chapter will be published, in part as "Long-circulating drug nanocarriers: branched semi-fluorous cores enhance stability of triphilic polymer self-assemblies" by Sarah E. Decato, William B. Tucker, Eric J. Madsen, Yutaka Miura, Kazunori Kataoka and Sandro Mecozzi.

Abstract.

The *in vivo* behavior of the fluorous formulations was investigated to serve as a preliminary proof of concept for the theranostic (dual therapeutic and imaging) design of the PFtB triphilic micelles. Firstly the enhanced kinetic stability gained by the installation of the fluorous moiety was confirmed by the direct imaging of fluorescent triphilic polymer micelles in circulation. IVRTCLSM studies showed that the $PFtB_{TRI}$ micelles had a prolonged circulation time (8 h) greatly increased over the free fluorescent dye (3 h). IVRTCLSM studies also showed that despite the small size of the micelles, designed for increased extravasation and tumor penetration, the micelles were not rapidly uptaken by the kidney. The increased circulation time and absence of rapid renal clearance of the fluorous polymeric micelle drug-delivery vehicles facilitate the enhanced accumulation and targeting of the tumor tissue. To establish MR imaging capabilities, the triphilic micelles were evaluated *in vitro* and demonstrated similar characteristics as the first-generation PFtB polymer design with minimal perturbation in relaxivity and SNR with the addition of the hydrocarbon segment. Following, a xenografted prostate tumor model mouse was exposed to a PFtB micelle solution to observe biodistribution and selective tumor delivery via the EPR effect. *In-vivo* and *ex-vivo* ^{19}F-MR imaging showed a small accumulation of the polymer within the tumor; however, a significant amount of polymer was visualized within the organs associated with the RES. Although the polymer showed prolonged circulation, the EPR effect alone did not enable the triphilic micelles to achieve adequate accumulated concentrations in the late-stage tumor for high intensity ^{19}F-MRI. Despite the fact the anatomy visualized was not the tumor, the potential of the triphilic polymer micelles as theranostic particles has been demonstrated, and with further modifications to the formulation (for example the appendage of active-targeting ligands) the *in vivo* accumulated concentrations of the nanocarrier could be increased to not only improve ^{19}F-MRI but also tumor targeting. The PFtB design has been shown

to be a stabilizing moiety in nanoscale self-assemblies to decrease the CMC, to deter destabilizing interactions *in vivo* for prolonged circulation times, and lastly to serve as a tracer for ^{19}F-MR imaging.

4.1 Motivation and intent

Theranostics is an emerging subset of multifunctional nanomedicinal compounds that provides both diagnosis and treatment within the same nanoformulation. One popular approach is to develop nanomaterials that combine the capability for therapeutic delivery and medical imaging. The installation of a handle, typically on the surface, for one or multiple imaging modalities, such as positron emission tomography (PET), computed tomography (CT), fluorescence imaging, or magnetic resonance imaging (MRI), allows for direct nanoparticle tracking. Monitoring the nanocarrier *in vitro* and *in vivo* provides a way to visualize the behavior of nanoparticles leading to accumulation or biodistribution and even to quantify or trigger drug release. Additionally theranostic particles are particularly primed to predict individual response to a specific formulation, allowing for the continued sophistication of personalized chemotherapy. Personalized medicine has become increasingly sought after due to the heterogeneity of cancer tissue, especially from patient to patient.

Colloidal formulations, especially polymeric micelle nanoparticles, are versatile platforms for theranostic nanoparticle development, with their easily modifiable surface, size, and shape by simple manipulation of the unimer polymer structure. The facile conjugation of imaging handles to the nanoparticle surface or the encapsulation of fluorescent probes are two versatile and rapid ways by which to add theranostic capabilities to a therapeutic nanoparticle delivery system. For the fluorous polymeric micelles, an alternative efficient and multifunctional approach was envisioned. The fluorous moiety in the amphiphilic polymer, which had been originally installed to provide enhanced stability to the colloidal drug formulations, was reconfigured to allow for simultaneous ^{19}F-MR imaging. The PFtB design was used to maintain symmetry and mobility even within a dynamic self-assembling micelle system, allowing for a single intense ^{19}F-MRI resonance signal (See Chapter 2).

With the identification of an amenable ^{19}F-MR imaging handle for fluorous micelle systems, the polymer structure was then expanded to include an intermediate hydrocarbon segment for hydrophobic drug loading. The triphilic micelles demonstrated enhanced therapeutic characteristics including prolonged circulation time *in vitro* by fluorous repulsion of hydrophobic blood components. The next step was then to establish the diagnostic and imaging capabilities of the theranostic design. The following chapter describes the use of fluorescence and ^{19}F-MR imaging to elucidate the *in vivo* behavior of the triphilic fluorous micelles not only to garner information for improvement for next-generation designs, but also to demonstrate the potential of PFtB micelles to serve as multifunctional theranostic nanoparticles.

4.2 Results and discussion

4.2.1 Prolonged blood circulation of triphilic fluorous micelles in vivo (IVRTCLSM)

As indicated by the FRET serum stability assay from Chapter 3, the fluorous core in a micelle increases the micelle's kinetic or *in vivo* stability by repelling hydrophobic components of the RES. The $PFtB_{TRI}$ triphilic polymer micelles demonstrated enhanced stability in serum over traditional $mPEG_{2k}$-DSPE hydrocarbon-core micelles. However, the properties of a colloidal delivery vehicle *in vivo* cannot be entirely modeled *in vitro* by simple dilution and mixing in serum. *In-vivo* the self-assembly is subject to dilution, to increased pressure within the vasculature, and most importantly to dissociation by numerous blood components. With the PFtB design, small micelles composed of $mPEG_{2k}$-O-H10-$PFtB_{TRI}$ polymers should exhibit enhanced kinetic stability by inhibiting recognition via hydrophobic interactions with hydrophobic blood components. The fluorous core should deter micelle disassembly, which in turn should prolong circulation and reduce premature release of the drug.

To measure the *in vivo* circulation time the theranostic triphilic micelles were formulated via encapsulation of a fluorescent dye into the hydrophobic shell in order to achieve high-resolution

fluorescence imaging for single particle tracking. *In vivo* real-time confocal laser scanning microscopy (IVRTCLSM) was used to non-invasively videograph the micelles in real-time.[1,2] In this study the relatively new IVRTCLSM method was chosen because it is one of the few methods that can directly visualize the particles to provide more data points using fewer animals. Real-time videography also allows one to observe critical behavior, such as burst release, that may occur within the first few seconds after injection. The $mPEG_{2k}$-O-H10-$PFtB_{TRI}$ micelles were loaded with a fluorescent dye 1,1′-dioctadecyl-3,3,3′,3′-tetramethylindocarbocyanine perchlorate (DiI) and injected into the tail-vein of a nude mouse. The fluorescent micelles were then monitored through the ear dermis continuously for the first minute, then as a time-lapse every minute over the next 10 h.

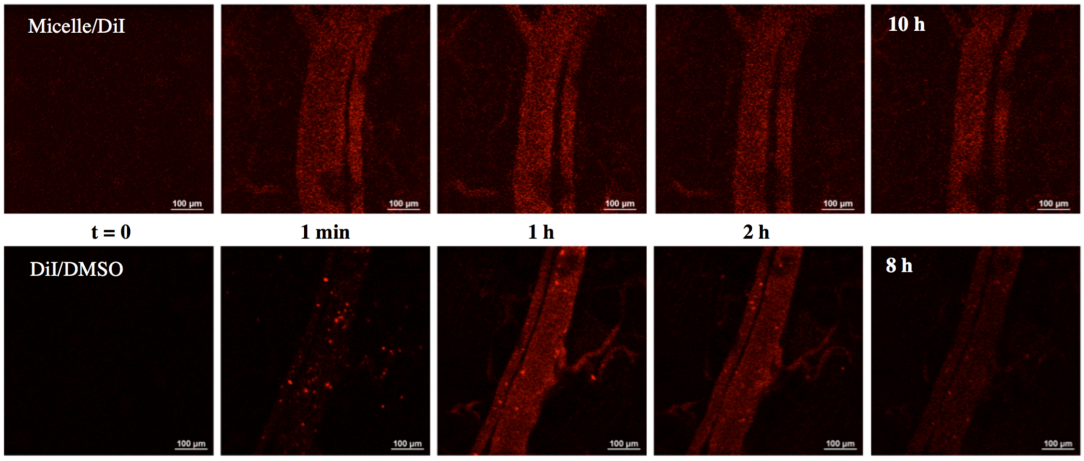

Figure 4.1 IVRTCLSM: prolonged circulation of fluorescent micelles.
In-vivo real time confocal laser microscopy (IVRTCLSM) image frames have been extracted from video of the vasculature of a nude mouse ear at 0 sec, 1 min, 1 h, 2 h, and 8 h (free dye) or 10 h (micelle). This was repeated in triplicate. **Top** – $mPEG_{2k}$-O-H10-$PFtB_{TRI}$ micelles with encapsulated DiI fluorescent dye (Micelle/DiI). **Bottom** – free DiI in a 0.2% DMSO solution (DiI/DMSO).

In comparing the video frames at sequential time points, it is apparent that the micelle formulation remained as small, homogenous particles in circulation, whereas the free, unencapsulated DiI immediately formed large aggregated particles (**Figure 4.1**). These large

particles, either dye-dye or dye-serum protein aggregates, could potentially cause lethal embolism and thus demonstrate the need for proper formulation of hydrophobic drugs. Most notably, the triphilic micelle formulation exhibited significant fluorescence intensity in circulation even after 10 h. Analysis of the fluorescence intensity over time shows a prolonged *in vivo* half-life of 8.5 h (95% confidence interval range: 6.7 – 11.5 h) in comparison to free dye that had a half-life of 3.2 h (95 % confidence interval range: 2.6-3.9 h), (**Figure 4.2**).

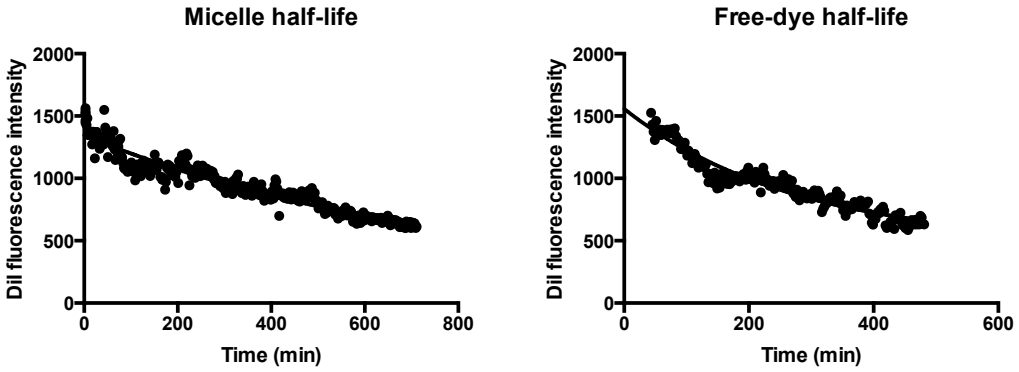

Figure 4.2 Fluorescent mPEG$_{2k}$-O-H10-PFtB$_{TRI}$ micelle and free-dye *in vivo* half-life.
Left: Encapsulated DiI in fluorous polymer micelle and **Right**: Free unencapsulated DiI fluorescent dye in a 0.2% DMSO solution (DiI/DMSO). Fluorescence intensity is plotted over time and fitted with an exponential one-phase decay starting from the maximum fluorescence intensity.

When trying to compare these blood circulation times with the variety of nanocarriers in the literature it is important to note that there is no standard assay to measure blood circulation half-life. The drastic variability between the methods makes it difficult to differentiate between formulations. To provide some context to these results, typical non-covalent micelles exhibit a limited circulation time lasting from several minutes to several hours.[3,4,5,6,7] In a recent paper, ridoforolimus, a chemotherapeutic with similar molecular weight and lipophobicity to paclitaxel, was encapsulated in mPEG$_{2k}$-DSPE micelles. The approximately 30 nm sized micelles showed a blood-circulation half-life of 3.2 h, as determined by LC/MS of rat serum.[8] In comparison to such classical micelle assemblies the triphilic mPEG$_{2k}$-O-H10-PFtB$_{TRI}$ polymer micelles demonstrated

significantly prolonged circulation times via enhanced evasion from the RES for delayed blood clearance.

In addition to evasion of the RES, the fluorescent theranostic micelles were studied *in vivo* to ascertain the extent of renal clearance. The approximately 14 nm sized triphilic micelles are only several nanometers larger than the theoretical renal filtration cut-off.[9] Traditional micelles are typically designed to be larger than the $PFtB_{TRI}$ micelles to ensure minimal clearance;[10] however, at the expense of extravasation and tumor penetration. Although the IVRTCLSM experiment described above confirmed the prolonged blood circulation time of the triphilic micelles, a second fluoresecent-theranostic micelle study was performed to directly image the circulation and clearance (if any) of micelles in the kidney.

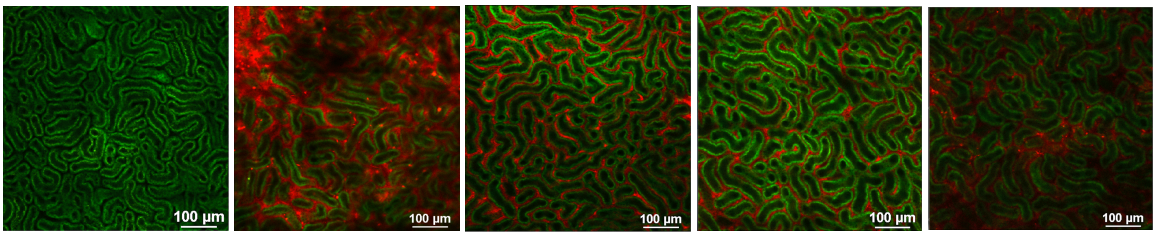

Figure 4.3 *In-vivo* kidney imaging of fluorescent micelle and free-dye.
Image frames have been extracted from video at the identified time points. **t = 0**: Autofluorescence imaging of the mouse hepatic lobule. **Following**: Overlay of DiI emission overlayed on top of autofluorescence of kidney of the free DiI in 0.2% DMSO solution (DiI/DMSO) after 8 h **(Free dye: 8h)**, and of the DiI encapsulated micelles after 2, 15, and 24 h (**Micelle: 2h, Micelle: 15 h**, and **Micelle 24 h**).

Deeper kidney structures, such as glomeruli, could not be imaged directly due to absorption and scattering by the renal tissue. Despite this, shallow features of the renal cortex including the proximal and distal tubules and capillary vessels were imaged to indirectly evaluate glomerular filtration. This tubular network is part of the first stage in the filtration process of the blood and therefore localization of the DiI fluorescence within the tubules would clearly indicate renal filtration.[11] The kidney was surgically exteriorized and the superficial tubular network was

imaged via autofluorescence and overlayed with the DiI fluorescence from either the free or encapsulated DiI dye (**Figure 4.3**). Significant free DiI fluorescence was seen from the IVRTCLSM throughout the free dye image and again it was apparent that the dye solution had formed large aggregates. As for the micelle-encapsulated dye, even after 24 h the DiI was only localized within the interstitial space corresponding with blood flow. Absence of colocalization of the tubules and encapsulated DiI suggested that there was no significant renal filtration. The triphilic micelles exhibit a rare balance between small size and evasion of rapid renal clearance, which suggests their potential application for efficient kidney drug delivery. Also, 24 h post-injection of the micelle solution a few larger aggregates are visible, which may be an indication of the slow, controlled release from fluorous micelles. Aggregates may be due to the fact that after this time the hydrophobic material (in this case the DiI) has begun to diffuse from the micelle and with limited solubility *in vivo* has formed larger aggregates.

These *in vivo* results corroborate the *in vitro* data to further demonstrate that these triphilic polymeric micelles allow for prolonged circulation times due to the enhanced kinetic stability of the self-assemblies. Installation of a branched, fluorous tail at the terminus of a PEGylated amphiphile allows for the formation of small, discrete micelles that can encapsulate hydrophobic compounds with increased bioavailability. Additionally, this prolonged circulation of fluorous micelles enables increased efficiency of active-targeting modifications towards the potential for improved tumor targeting.

4.2.2 In vitro ^{19}F-NMR and ^{19}F-MRI of triphilic PFtB micelles

Although the previous *in vivo* results demonstrate the theranostic capability of the fluorous micelles via fluorescence imaging, the origin of the PFtB design was to enable ^{19}F MR imaging. To assess any alterations in the ^{19}F-MRI capabilities of the triphilic micelles the ^{19}F-NMR relaxivity *in vitro* was compared to the first generation PFtB polymer design (**Table 4.1**). Both

the T_1 and T_2 relaxivity were not significantly affected from the installation of the intermediate hydrocarbon segment; for the $PFtB_{TRI}$ there was essentially no change in T_1 and only a small decrease in T_2 (110 ms to 70 ms), which may be attributed to the slight increase in micelle diameter (approximately 12 nm vs 14 nm).

Table 4.1 ^{19}F-NMR relaxivity measurements of triphilic fluorous micelles.
^{19}F-NMR relaxivity measurements of fluorous micelle above the CMC concentration in D_2O at 9.4 T. The T_1 and T_2 values are not significantly altered from the $mPEG_x$-$PFtB_y$ polymers despite the addition of the intermediate hydrocarbon segment.

Compound	T_1 (sec)	T_2 (sec)
$mPEG_{2k}$-O-H10-$PFtB_{MONO}$	0.77 ± 0.03	0.16 ± 0.01
$mPEG_{2k}$-O-H10-$PFtB_{TRI}$	0.49 ± 0.01	0.07 ± 0.001

The most significant effect from the alteration in the polymer structure was the decrease in the percent fluorine per molecule, which is directly proportional to signal intensity. However, ^{19}F-MR phantoms were imaged and showed similar signal intensity to the first generation polymer phantoms (**Figure 4.4**) providing distinct signal at a polymer concentration of 4 mM (whereas the $mPEG_{1k}$-$PFtB_{TRI}$ showed a limit of detection at approximately 1 mM).

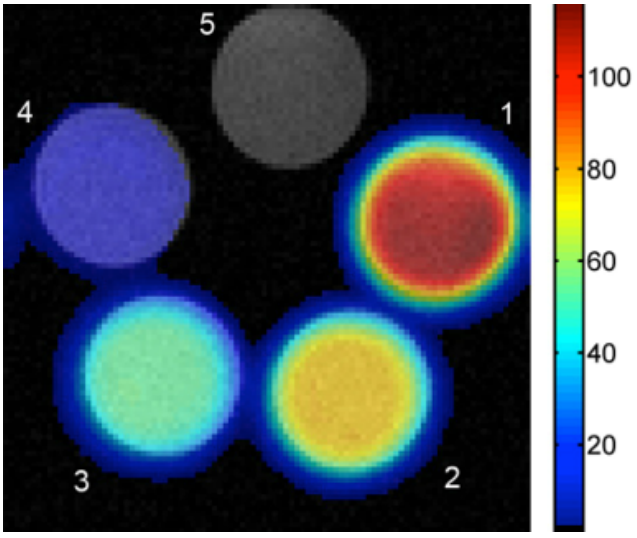

Figure 4.4 Triphilic PFtB polymer ^{19}F-MR imaging phantoms.
^{19}F-MR phantom spin-echo images superimposed upon ^{1}H-MR images of $mPEG_{2k}$-O-H10-$PFtB_{MONO}$ polymer solutions in Milipore water, with 25 min scan time, at 4.7 T. The scale is set to the signal-to-noise ratio (SNR) of the ^{19}F vials. From top center moving clock-wise: **5**) Blank—0 mM, **1**) 62 mM, **2**) 42 mM, **3**) 28 mM, and **4**) 4 mM. Phantoms demonstrate high signal intensity with short imaging time even as self-assembled micelles with a single ^{19}F resonance.

Therefore the additional hydrocarbon segment has not disturbed the mobility of the PFtB moiety inside the core of the fluorous micelles so as to maintain symmetry and thus NMR equivalence for all fluorine atoms. The successful imaging of the triphilic micelle solutions *in vitro* was then extended to the direct ^{19}F-MR imaging of the biodistribution and tumor-targeting efficacy *in vivo*.

4.2.3 In vivo full-body imaging of normal mice

The first objective for *in vivo* imaging was to assess the biodistribution of the polymer solutions upon and after injection. Due to the time length of the experiment, the mouse subject needed to be immobilized and sedated during the entirety of the study to prevent image artifacts from movement. This proved difficult, as the typical veterinary anesthetics used are fluorous and could provide detrimental background noise, preventing conclusive identification of the fluorous micelles. To assess the extent of the fluorous anesthetic interference, full-body imaging was performed on normal Balb/c mice using isoflurane (**Figure 4.5**). The $mPEG_{2k}$-O-H10-$PFtB_{MONO}$ micelle solution (10 mM aqueous solution in a plastic syringe) was placed alongside the mouse to serve as a reference.

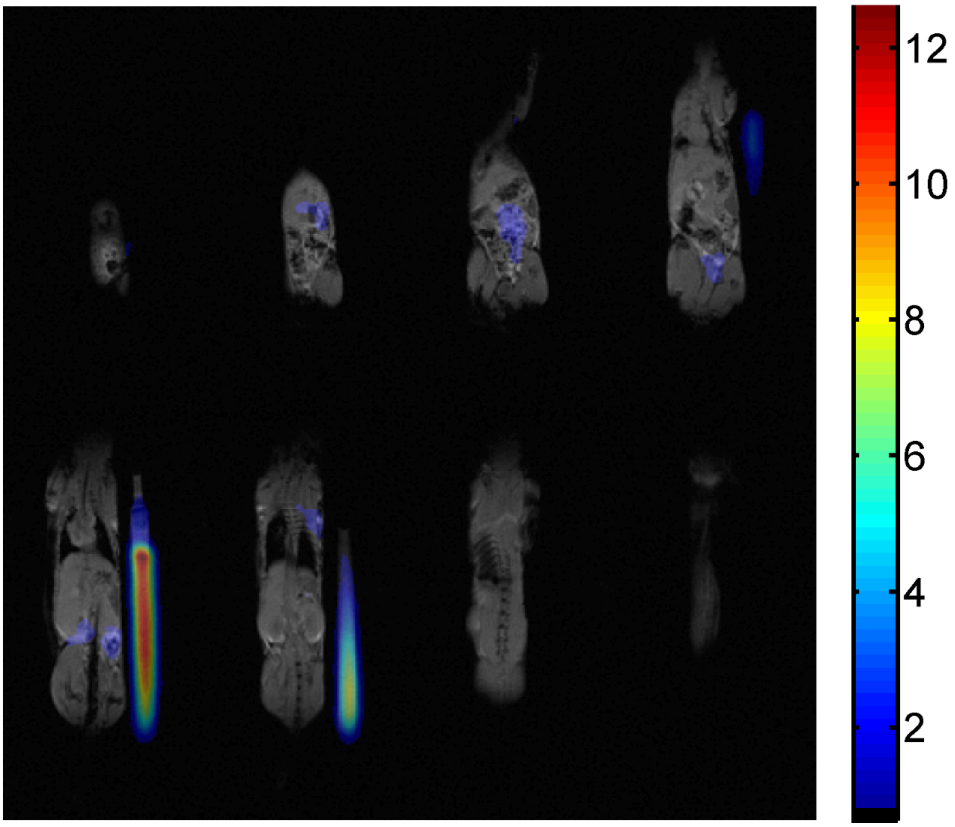

Figure 4.5 ^{19}F-MR imaging of isoflurane background signal in normal mice.
^{19}F-MR images were performed with 1 h scan time on 4.7 T small animal scanner using the volume coil and superimposed upon ^{1}H-MR full body images of Balb/c normal mice. The $mPEG_{2k}$-O-H10-$PFtB_{MONO}$ micelle solution (10 mM in Milipore water) was used as a reference. The individual slices are presented and the isoflurane signal (blue) is distinctly visible in the majority of slices.

In the initial background imaging, ^{19}F signal was apparent in the majority of the full-body slices, exhibiting approximately 30 % of the maximum signal from the fluorous micelle reference, 10 mM. Anticipated maximum accumulated concentrations *in vivo* would not exceed 1 mM, and therefore the significant ^{19}F signal from the isoflurane prompted us to explore the use of alternative non-fluorinated anesthetics. Unfortunately, the injectable anesthetics were problematic due to the small size of the mouse model. Injectable anesthetics (such as ketamine-xylazine) were difficult to dose for the 20-25 g mice and therefore presented adverse side effects. Additionally these anesthetics did not allow for controlled sedation over long scan times (> 30 min) due to

inherent cardiac and respiratory suppression. Consequently, a surface coil, rather than the larger volume coil, was used for localized imaging and to assess tumor uptake via the EPR effect.

4.2.4 In vivo tumor imaging of prostate cancer xenograft

To image accumulation of the fluorous micelle within the tumor, prostate cancer xenograft mice were used, which were donated by a collaborator. The female nude mice were injected with a prostate cancer cell line and the tumors were allowed to develop to approximately 3 mm in size. In order to ensure the maximum signal from the injected micelle solution, the $mPEG_{1k}$-$PFtB_{TRI}$ polymer was used, which has the highest percent fluorine per molecule and therefore highest potential ^{19}F signal intensity. Also the ^{19}F surface coil was used rather than the quadrature volume coil. The surface coil is a loop that can be placed directly on or over the region of interest (in this case the tumor) to increase sensitivity and improve signal to noise since the signal decreases with distance from the coil. In this way the interference from the isoflurane anesthetic is minimized.

An initial scan was performed to assess the amount of background signal from the isoflurane anesthetic (**Figure 4.6**). The images demonstrate that the localized RF transmission from the surface coil minimizes the isoflurane signal. Additionally, since the tumor and adjacent tissues are typically lean, there is relatively less accumulation of isoflurane compared to other tissue.

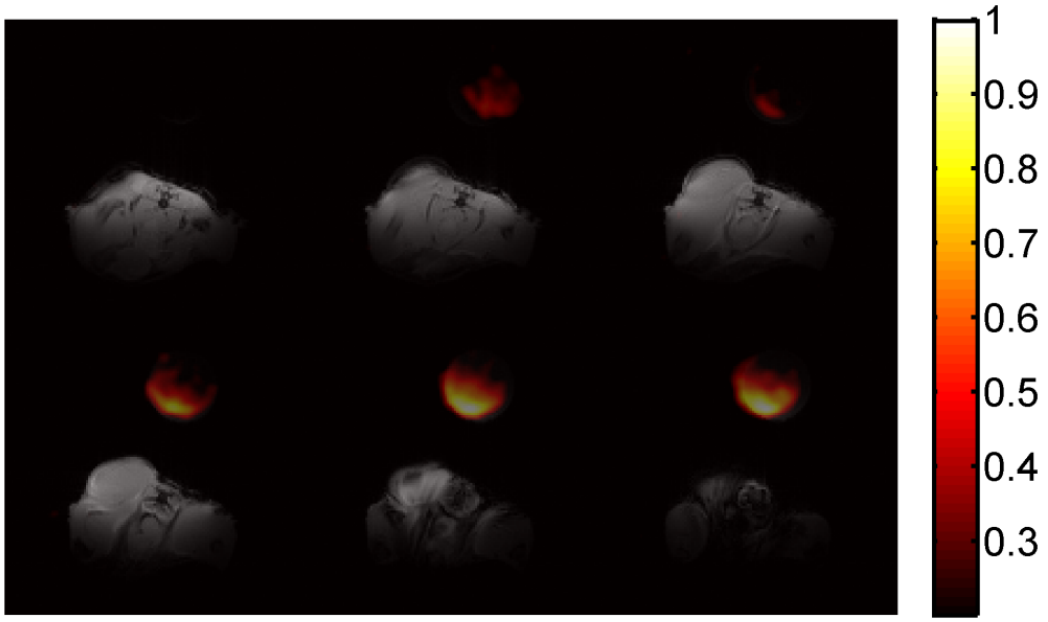

Figure 4.6 *In vivo* ^{19}F-MRI of prostate cancer xenograft tumor: Isoflurane background.
^{19}F-MR images performed with 30 min scan time on the 4.7 T small animal scanner and superimposed upon ^{1}H-MR images of tumor xenograft before administration of fluorous micelles. This demonstrates that the isoflurane required for sedation gave no background signal in the region of the tumor using the surface coil. The ^{19}F-MR signal (hot scale) is from the fluorous micelle reference solution ($mPEG_{1k}$-$PFtB_{TRI}$ 1 mM solution in Milipore water).

With essentially no background signal coming from the anesthetic, the mice were then imaged to assess tumor uptake. After 5 weeks (post-xenograft) the mice were injected with 250 µL of a 10 mM polymer solution in sterilized normal saline. Mice were anesthetized with isoflurane and imaged 1, 2, 6, and 24 h post injection via ^{1}H and ^{19}F MRI. No signal was visible after 1, 2, or 6 h post-injection (**Figure 4.7**). However, after 24 h ^{19}F signal was visible below the tumor. Although it was difficult to confirm the anatomy of the signal (the distance from the surface coil diminished the signal clarity), it appears to be in the location of the kidney (**Figure 4.8**).

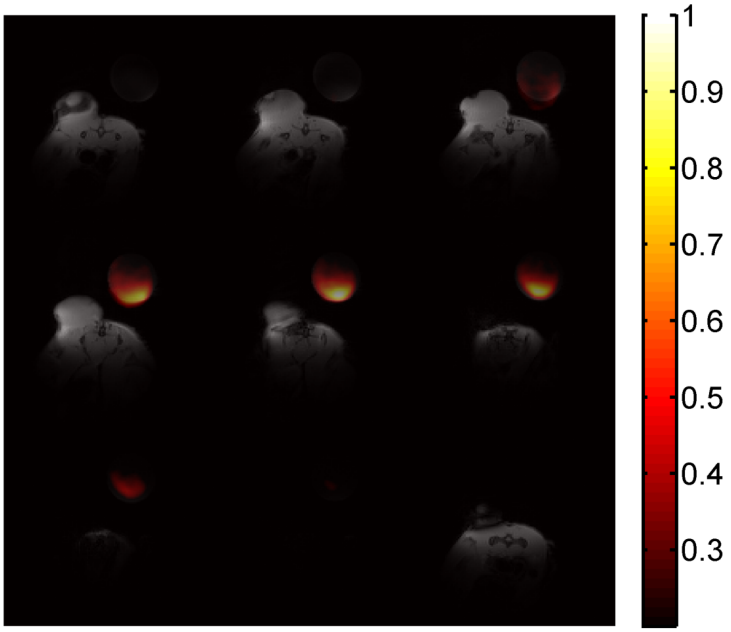

Figure 4.7 *In vivo* ^{19}F-MRI of xenograft tumor: 6 h post injection of micelles.
^{19}F-MR images performed with 30 min scan time on the 4.7 T small animal scanner using a surface coil and superimposed upon ^{1}H-MR images of prostate cancer tumor xenograft after administration of 10 mM solution of $mPEG_{1k}$-$PFtB_{TRI}$ micelles. The only ^{19}F-MR signal (hot scale) is from the micelle reference, 1 mM solution.

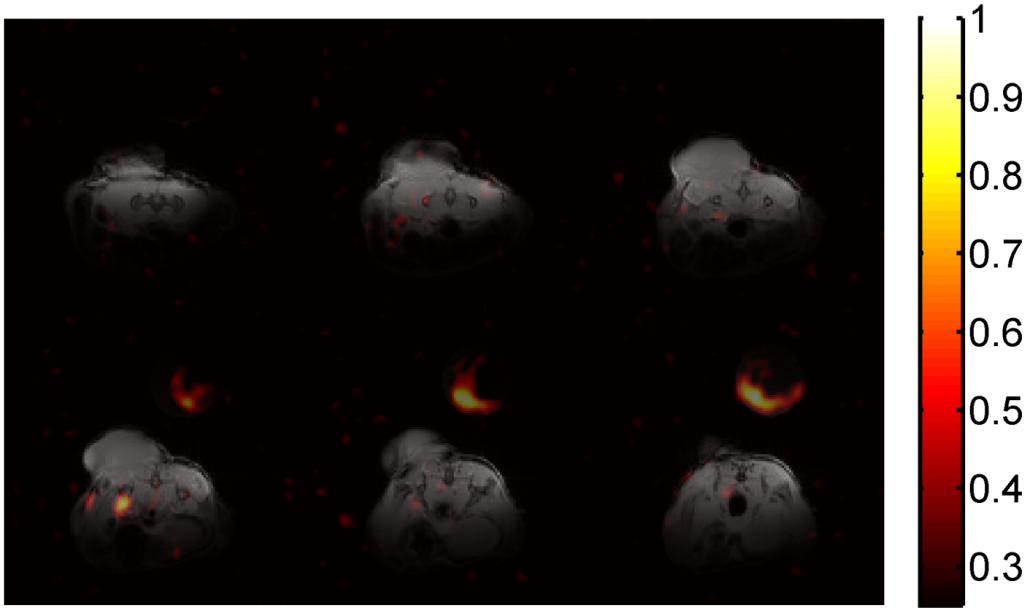

Figure 4.8 *In vivo* ^{19}F-MRI of xenograft tumor: 24 h post injection of micelles.
^{19}F-MR images performed with 30 min scan time on the 4.7 T small animal scanner using a surface coil and superimposed upon ^{1}H-MR images of prostate cancer tumor xenograft after administration of 10 mM solution of $mPEG_{1k}$-$PFtB_{TRI}$ micelles. ^{19}F signal is apparent below the tumor, possibly from accumulation in the kidney.

4.2.5 Ex-vivo imaging of tumor and RES organs

To attempt to identify the origin of the *in vivo* ^{19}F signal and to assess any other accumulation that may have been masked by the intensity of the fluorous micelle reference, two mice were sacrificed. The organs of the RES, specifically the liver and spleen, the kidneys, and the tumor were surgically removed (and any blood was cleansed from the surface) and isolated in a glass vial with Milli-Q water. A single slice comprising the entire vial was imaged for each organ. The spleen showed no signal, whereas the kidney and liver showed significant signal after a 30 minute scan time. The tumor did show ^{19}F signal that was significant from the noise; however, only after 5 h scan time (**Figure 4.9**). The limited accumulation within the tumor is not entirely surprising considering the lack of active-targeting ligands and the late stage of the tumor development. Due to difficulties in simultaneous animal procurement and MRI instrumentation scheduling, the tumor had grown rather large and may have reached a necrotic stage in which extravasation and penetration were decreased.

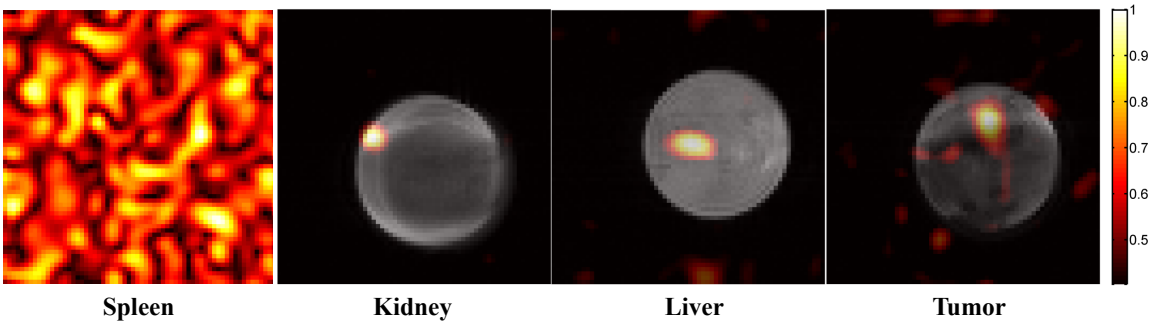

Figure 4.9 *Ex vivo* ^{19}F-MRI: Accumulation in tumor and excretory organs.
^{19}F-MR image performed with surface coil using the 4.7 T small animal scanner and superimposed onto ^{1}H-MR image. **From left to right**: Spleen (only noise) after 30 min, kidney after 30 min, liver (with translational misalignment) after 30 min, and tumor (significant signal and background noise) after 5 h scan time.

Although the *in vivo* and *ex vivo* imaging suggest minimal accumulation within the tumor via the EPR effect, the successful imaging after 24 h post injection (most likely arising from

accumulation within the kidney) supports the fluorous theranostic design. Despite the anatomy of accumulation, the fluorous micelles can concentrate *in vivo* to allow for distinctive ^{19}F-MRI. These promising imaging results for the empty fluorous micelle polymer solutions provide a direct comparison to the potential theranostic capabilities of drug encapsulated PFtB-micelle formulations and a preliminary foundation for emulsion formulation imaging. In terms of theranostic chemotherapy, further modifications to the nanoparticle surface (particularly the addition of active targeting ligands) and the judicious selection of injection time (so as to coincide with optimal tumor penetration) should allow for enhanced tumor accumulation and successful ^{19}F-MR imaging within the tumor.

4.3 Experimental

4.3.1 IVRTCLSM

All animal experimental procedures were executed in accordance with the Guidelines for the Care and Use of Laboratory Animals as stated by the University of Tokyo. Balb/c nude mice (female; Charles River Laboratories, Tokyo, Japan) were anesthetized with 3.0%–4.0% isoflurane (Abbott Japan Co., Ltd., Tokyo, Japan) using a Univenter 400 Anaesthesia Unit (Univentor Ltd., Zejtun, Malta). Mice were then subjected to lateral tail vein catheterization with a 30-gauge needle (Dentronics Co., Ltd., Tokyo, Japan) connected to a nontoxic, medical grade polyethylene tube (Natsume Seisakusho Co., Ltd., Tokyo, Japan). Mice were placed onto a custom-designed temperature-controlled microscope stage. The ear lobe dermis was accessible without surgical procedure and was attached beneath the cover slip with a single drop of immersion oil. The kidney was accessed following exteriorization through a small skin incision. To minimize bleeding during the incision, a Surgitron ® radiofrequency surgical device equipped with a Vari-Tip ™ Wire Electrode (A8D) from Ellman International Inc (Oceanside, NY) was used for micro smooth incision with minimal tissue alteration. All picture/movie acquisitions were performed

using a Nikon A1R confocal laser scanning microscope system attached to an upright ECLIPSE FN1 machine equipped with a CFI Apo 40Å~WI λS objective lens (Nikon, Tokyo, Japan). Acquired data were further processed using Nikon NIS Elements software. The region of interest (ROI) was manually defined. Video acquisition of the dermis tissue and the kidney was performed continuously over 1 min and then as a time-lapse every minute after that for the allotted time. Two-hundred microliters of free DiI (200 µL of 40 µg/mL solution in 2% DMSO in saline) and DiI-loaded micelles (115 µL of a 0.1 mg/mL solution of DiI in MeOH encapsulated in 5 mg/mL of $mPEG_{2k}$-O-H10-$PFtB_{TRI}$ in saline via the solvent evaporation method) were administered via the tail vein catheter 10 s after video acquisition was initiated.[2,1] Fluorescence intensity was plotted using GraphPad PRISM 6 software using an exponential one-phase decay fit from the maximum fluorescence intensity.

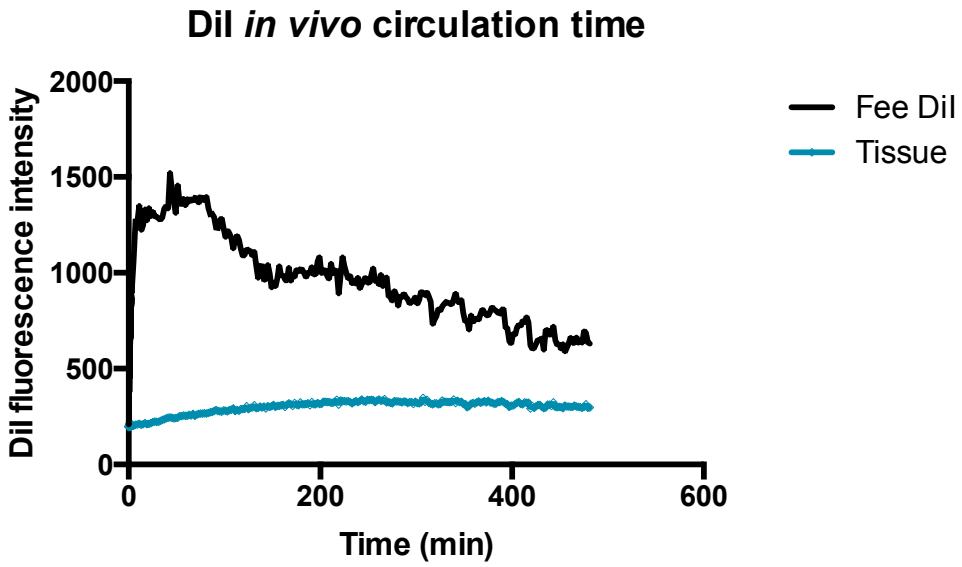

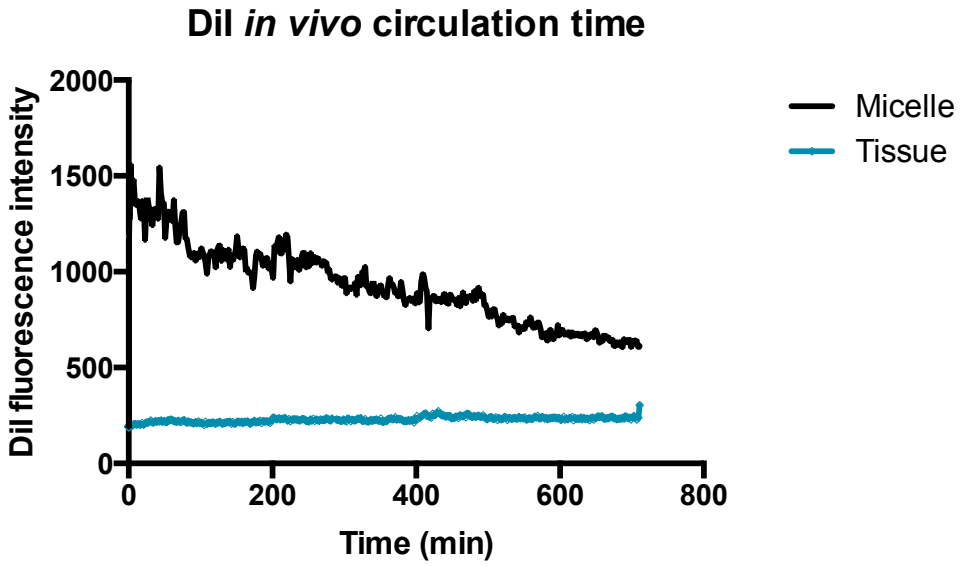

4.3.2 In vitro ^{19}F-NMR and ^{19}F-MRI studies

^{19}F-NMR Relaxivity studies: Samples were prepared by direct dilution to achieve 10 mM concentration in D_2O with tetramethylsilane as an internal standard. Micelle formation was confirmed by DLS. The temperature was maintained at 25 °C. The ^{19}F relaxation parameters, T_1 and T_2 measurements of the micelles were conducted on a Varian Unity-Inova 400 MHz spectrometer. The T_1 was determined using an inversion recovery experiment acquired with 12 independent, quadratically spaced variable (tau) values covering a range up to 5 times the estimated T_1, 0.4 s. The T_2 was determined using a Carr-Purcell–Meiboom–Gill, CPMG, pulse sequence experiment acquired with 12 independent, quadratically spaced variable (tau) values covering a range up to 5 times the estimated T_2, 0.4 s. For T_1 and T_2 measurements: 90° pulse = 13.4 μs, nt = 4, spectral window (T_1) = 21 575.0 Hz and spectral window (T_2) = 15 763.5 Hz.

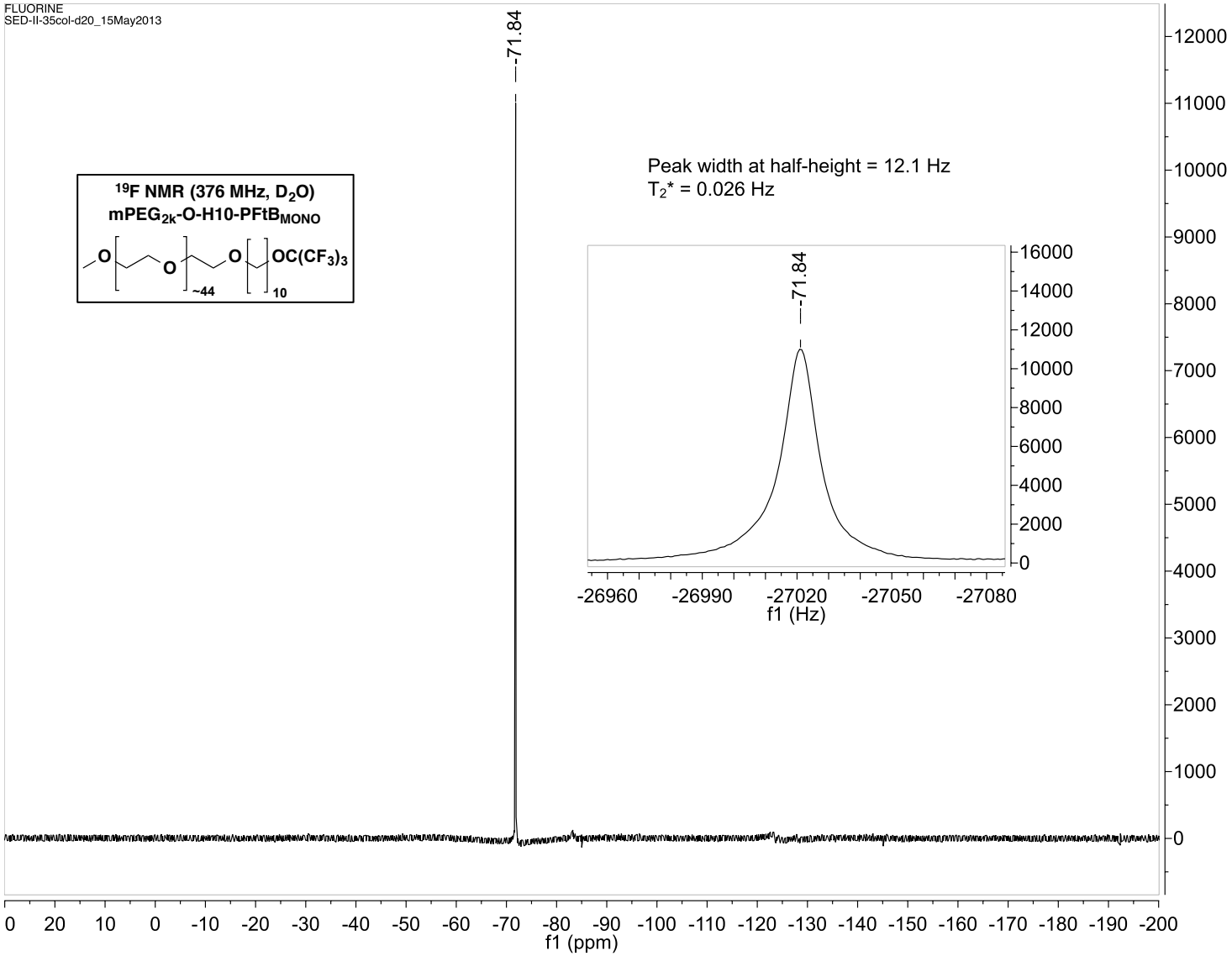
FLUORINE
SED-II-35col-d20_15May2013
-71.84
^{19}F NMR (376 MHz, D_2O)
$mPEG_{2k}$-O-H10-$PFtB_{MONO}$
O
O
O
OC(CF_3)$_3$
~44
10
Peak width at half-height = 12.1 Hz
T_2* = 0.026 Hz
-71.84
-26960
-26990
-27020
-27050
-27080
f1 (Hz)
f1 (ppm)

T_1: $mPEG_{2k}$-O-H10-$PFtB_{MONO}$

Time (s)	Intensity (obs.)	Intensity (calc.)	Difference
0.01389	-57.2	-54.0	-3.16
0.05556	-44.3	-46.4	2.05
0.125	-34.5	-34.5	-0.00752
0.2222	-17.3	-19.6	2.29
0.3472	-2.88	-3.03	0.146
0.5	13.8	13.9	-0.122
0.6806	29.5	30.1	-0.587
0.8889	44.3	44.6	-0.275
1.125	56.2	56.9	-0.664
1.389	65.3	66.8	-1.5
1.681	75.8	74.5	1.23
2	81	80.2	0.8

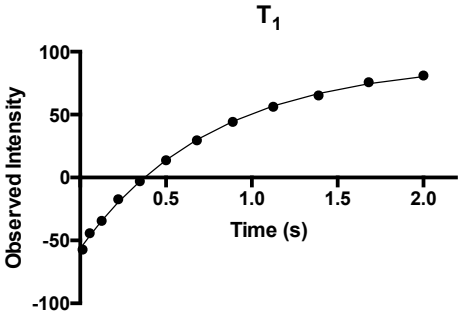

T_2: $mPEG_{2k}$-O-H10-$PFtB_{MONO}$

Time (s)	Intensity (obs.)	Intensity (calc.)	Difference
0.032	162	159	2.6
0.096	103	108	-5.04
0.224	51.9	50	1.87
0.384	21.5	19.3	2.27
0.608	5.76	5.36	0.399
0.88	1.56	1.49	0.0678
1.184	0.83	0.721	0.109
1.552	0.64	0.592	0.0475
1.986	-0.42	0.578	-0.998
2.432	0.4	0.577	-0.177
2.944	0.35	0.577	-0.227
3.504	-0.47	0.577	-1.05

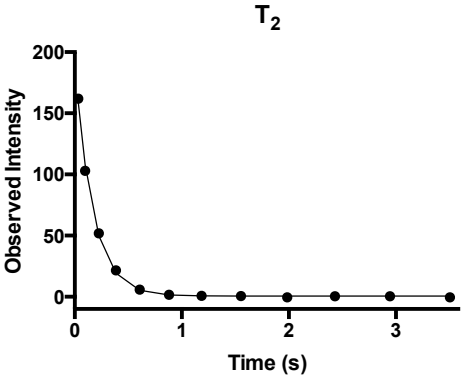

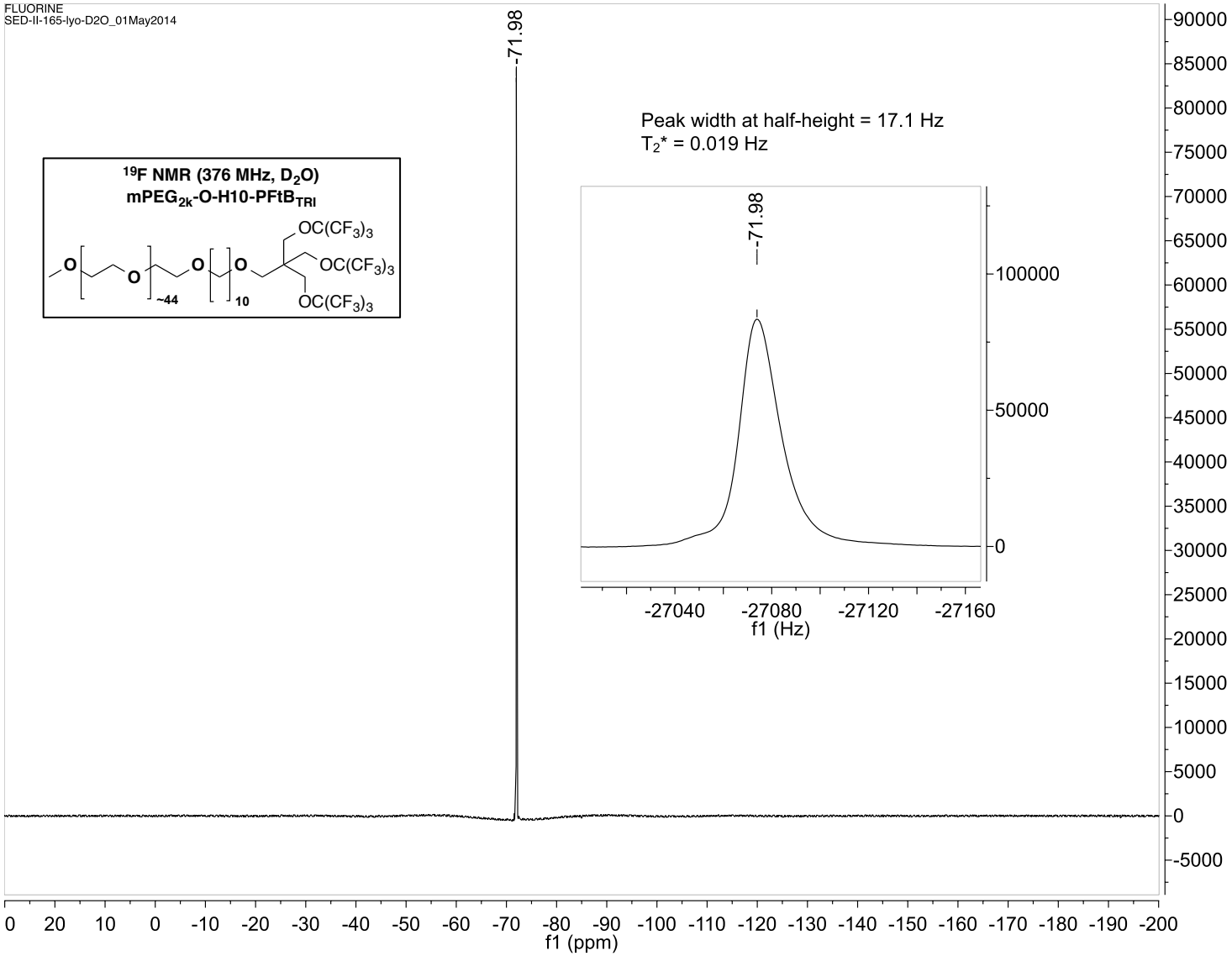
FLUORINE
SED-II-165-lyo-D2O_01May2014
-71.98
^{19}F NMR (376 MHz, D_2O)
$mPEG_{2k}$-O-H10-$PFtB_{TRI}$
OC(CF3)3
OC(CF3)3
OC(CF3)3
~44
10
Peak width at half-height = 17.1 Hz
T_2* = 0.019 Hz
-71.98
-27040
-27080
-27120
-27160
f1 (Hz)
f1 (ppm)

T_1: $mPEG_{2k}$-O-H10-$PFtB_{TRI}$

Time (s)	Intensity (obs.)	Intensity (calc.)	Difference
0.01389	-71.3	-70.6	-0.694
0.05556	-55.9	-56.1	0.153
0.125	-33.9	-34.4	0.495
0.2222	-8.36	-8.69	0.332
0.3472	17.9	17.7	0.191
0.5	42	42.1	-0.0549
0.6806	62.4	62.7	-0.268
0.8889	78.2	78.8	-0.579
1.125	90.4	90.4	-0.0218
1.389	98.1	98.3	-0.157
1.681	104	103	0.604
2	106	106	0.0222

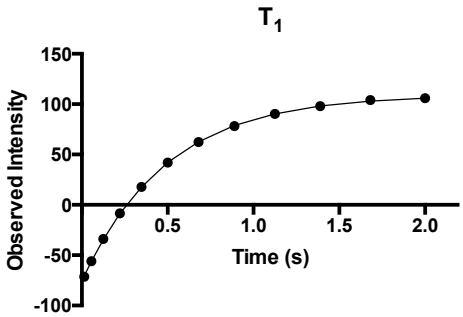

T_2: $mPEG_{2k}$-O-H10-$PFtB_{TRI}$

Time (s)	Intensity (obs.)	Intensity (calc.)	Difference
0.016	162	161	0.796
0.048	97.8	99.3	-1.5
0.128	30.2	29.7	0.447
0.224	9.23	7.19	2.04
0.352	2.09	1.34	0.749
0.496	0.63	0.474	0.156
0.688	0.3	0.37	-0.0698
0.896	0.2	0.364	-0.164
1.12	-0.23	0.364	-0.594
1.392	-0.16	0.364	-0.524
1.68	-0.4	0.364	-0.764
2	-0.26	0.364	-0.624

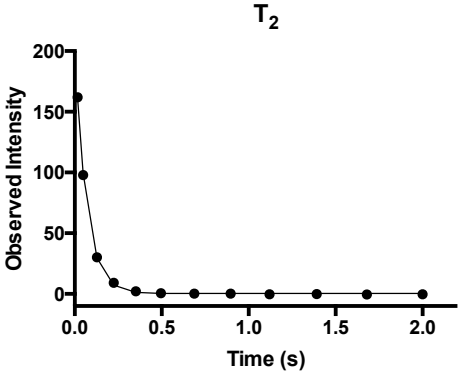

^{19}F-MRI phantoms: images were acquired using a Varian 4.7 T small animal scanner using a home-built ^{19}F quadrature volume coil with a 1.5″ diameter and 3″ in length. A polymer stock solution of $mPEG_{2k}$-H10-$PFtB_{MONO}$ was prepared by direct dilution of the lyophilized solid polymer sample to the highest phantom concentration in Milli-Q water. Lower phantom concentrations were made as serial dilutions from the stock solution in Milli-Q water. Micelle

formation was confirmed by DLS. Phantom polymer solutions starting from the top and going clock-wise, 0 mM, 62.4 mM, 41.6 mM, 27.7 mM, and 4.0 mM, were transferred to Teflon-free glass vials and ^{1}H images of the phantoms were acquired using a gradient echo pulse sequence with 0.3 x 0.3 x 2.0 mm^3 spatial resolution, 32 x 32 mm^2 field-of-view (FOV), 0.1 s TR, 2.12 ms TE, 20° flip angle, 350 Hz per pixel bandwidth, 8 averages and 1 min 17 s imaging time. ^{19}F images of the phantoms were acquired using a spin echo pulse sequence with a 1.0 x 1.0 x 2.0 mm^3 spatial resolution, 32 x 32 mm^2 FOV, 2 s TR, 6 ms TE, 32 echoes, 1050 Hz per pixel bandwidth, 24 averages, and 25 min 36 s imaging time. Images were summed along the echo dimension to increase SNR efficiency by taking advantage of the relatively long T_2.

^{19}F-MRI *in vivo and ex vivo*: All animal studies were done in accordance animal protocols approved by UW-Madison's institutional animal care and use committee, along with Professor Weichert's imaging pilot studies protocol M02169. Images were acquired using a Varian 4.7 T small animal scanner using a home-built ^{19}F quadrature volume coil with a 1.5″ diameter and 3″ in length or a $^{1}H/^{19}F$ surface coil, approximately 25 mm in diameter. The system is equipped with a rodent isoflurane gas anesthesia system, physiologic monitoring system, temperature control, which was maintained at 36 °C. A polymer stock solution of $mPEG_{2k}$-H10-$PFtB_{MONO}$ or $mPEG_{2k}$-$PFtB_{TRI}$ was prepared by direct dilution of the lyophilized solid polymer sample to the desired concentration (10 mM for injection and 1 or 10 mM for reference solution) in Milli-Q water and filtered with a 4 mm dia, 0.22 μm nylon syringe filter. Micelle formation was confirmed by DLS. Balb/c and nude mice from Charles River International Inc. (Hollister, CA) were donated by Professor J. P. Weichert. The female immune-suppressed nude mice (nu/nu), 20-25 g (D.O.B. 7/28/13) were injected with PC-3 (prostate cancer cell line, $1x10^6$ PC-3 cells) on 9/23/13. ^{1}H images of the phantoms were acquired using a gradient echo pulse sequence with 0.3 x 0.3 x 2.0 mm^3 spatial resolution, 32 x 32 mm^2 field-of-view (FOV), 0.1 s TR, 2.12 ms TE, 20° flip angle,

350 Hz per pixel bandwidth, 8 averages and 1 min 17 s imaging time. ***In vivo***: ^{19}F images with the surface coil were acquired using a spin echo pulse sequence with a 1.0 x 1.0 mm^2 resolution, 109.3 ms TR, 2.7 ms TE, 10 kHz bandwidth, 400 averages, slice thickness of 2 mm, and an average 30 min scan time. ***Ex vivo****:* Animals were treated in a sterile environment. Twenty-eight hours after injection of fluorous micelles, mice were sacrificed by CO_2 asphyxia. A midline incision was done with microsurgical instruments under white light illumination, and organs such as liver, spleen, kidneys, and tumor tissue were removed. The skin of the mice was also removed over the tumor when the tumor excision was performed. ^{19}F images with the surface coil were acquired using a spin echo pulse sequence with a 1.0 x 1.0 mm^2 resolution, 14.4 ms TR, 2.0 ms TE, 5 kHz bandwidth, 8000 averages, and an average 30 min scan time over a single slice comprising the entire tube (except for the tumor, which was scanned for 5 h). Images composed and compiled using Matlab software, version R2012a by Dr. Jeremy Gordon.

4.4 Acknowledgements

This research was done in part with collaborators Professor Kataoka and Assistant Professor Miura at the University of Tokyo with funding from JSPS (SP14012) and NSF-EAPSI (1414737). Sincere thanks to Dr. Jeremy Gordon, Beth Rauch, and the UWCCC Small Animal Imaging Facility for all their help with ^{19}F imaging and also thanks to Professor J. Weichert, Professor G. S. Kwon, and Dr. Hyunah Cho for their helpful discussions and donation of animals, supplies, and injection and surgical expertise.

4.5 References

(1) Matsumoto, Y.; Nomoto, T.; Cabral, H.; Matsumoto, Y.; Watanabe, S.; Christie, R. J.; Miyata, K.; Oba, M.; Ogura, T.; Yamasaki, Y.; Nishiyama, N.; Yamasoba, T.; Kataoka, K. Direct and Instantaneous Observation of Intravenously Injected Substances Using Intravital Confocal Micro-Videography. *Biomed. Opt. Express* **2010**, *1* (4), 1209–1216.

(2) Nomoto, T.; Matsumoto, Y.; Miyata, K.; Oba, M.; Fukushima, S.; Nishiyama, N.; Yamasoba, T.; Kataoka, K. In Situ Quantitative Monitoring of Polyplexes and Polyplex Micelles in the Blood Circulation Using Intravital Real-Time Confocal Laser Scanning Microscopy. *J. Control. Release* **2011**, *151* (2), 104–109.

(3) Chandran, T.; Katragadda, U.; Teng, Q.; Tan, C. Design and Evaluation of Micellar Nanocarriers for 17-Allyamino-17-Demethoxygeldanamycin (17-AAG). *Int. J. Pharm.* **2010**, *392* (1-2), 170–177.

(4) Letchford, K.; Burt, H. M. Copolymer Micelles and Nanospheres with Different in Vitro Stability Demonstrate Similar Paclitaxel Pharmacokinetics. *Mol. Pharm.* **2012**, *9* (2), 248–260.

(5) Yang, D.; Yu, L.; Van, S. Clinically Relevant Anticancer Polymer Paclitaxel Therapeutics. *Cancers (Basel).* **2010**, *3* (1), 17–42.

(6) Harada, M.; Ohuchi, M.; Hayashi, T.; Kato, Y. Prolonged Circulation and in Vivo Efficacy of Recombinant Human Granulocyte Colony-Stimulating Factor Encapsulated in Polymeric Micelles. *J. Control. Release* **2011**, *156* (1), 101–108.

(7) Tran, T.-H.; Nguyen, C. T.; Gonzalez-Fajardo, L.; Hargrove, D.; Song, D.; Deshmukh, P.; Mahajan, L.; Ndaya, D.; Lai, L.; Kasi, R. M.; Lu, X. Long Circulating Self-Assembled Nanoparticles from Cholesterol-Containing Brush-like Block Copolymers for Improved Drug Delivery to Tumors. *Biomacromolecules* **2014**, *15* (11), 4363–4375.

(8) Remsberg, C. M.; Zhao, Y.; Takemoto, J. K.; Bertram, R. M.; Davies, N. M.; Forrest, M. L. Pharmacokinetic Evaluation of a DSPE-PEG2000 Micellar Formulation of Ridaforolimus in Rat. *Pharmaceutics* **2012**, *5* (1), 81–93.

(9) Fang, J.; Nakamura, H.; Maeda, H. The EPR Effect: Unique Features of Tumor Blood Vessels for Drug Delivery, Factors Involved, and Limitations and Augmentation of the Effect. *Adv. Drug Deliv. Rev.* **2011**, *63* (3), 136–151.

(10) Kumar, N.; Ravikumar, M. N. V; Domb, a. J. Biodegradable Block Copolymers. *Adv. Drug Deliv. Rev.* **2001**, *53*, 23–44.

(11) Ohno, Y.; Birn, H.; Christensen, E. I. In Vivo Confocal Laser Scanning Microscopy and Micropuncture in Intact Rat. *Nephron - Exp. Nephrol.* **2005**, *99* (1), 17–25.

Appendix 1:

Physicochemical characterization of chain mobility in fluorous micelles via CMC, SAXS, and DSC

S1.1 Motivation and intent

The architecture and crystallization of an amphiphilic polymer, particularly of the hydrophobic tail, strongly influence the physical properties of their respective micelle self-assemblies. The effects arising from core crystallinity have been studied in the literature, and modulation of the core fluidity was investigated as an indicator of micelle stability or as a tool to enhance the loading or release of encapsulated material. The alteration of the stereostructure and crystallintiy of poly(lactic acid) (PLA) was found to directly influence the size, stability, drug loading and release behavior, and cellular uptake of the corresponding PLA copolymer micelles.[1] Ning *et al*. also reported that the (poly(ethylene glycol)-block-poly(L-lactide) (PEG-*b*-PLLA) and poly(ethylene glycol)-block-poly(D-lactide)) (PEG-*b*-PDLA) stereocomplexed micelles showed higher colloid stability than amorphous PLA/PEG copolymer micelles.[2] In terms of the thermodynamic stability, Albertsson *et al.* also showed that micelles with amorphous cores (such as poly-ε-decalactone) have higher critical micelle concentrations (CMCs) than those with semicrystalline cores (such as poly(ε-caprolactone) (PCL) or PLA).[3]

The fluidity of the core changes with temperature and thus the thermal properties can indicate phase transitions between core crystalline and fluid states. PCL (semicrystalline polymer) exhibited a higher melting temperature (T_m) of 55°C, whereas the amorphous PLA gave a glass transition temperature (T_g) of 50°C. In this case the poly(ethylene glycol)-block-poly(ε-caprolactone) PEG-*b*-PCL micelles displayed "glassy" characteristics, which resulted in higher drug loading and slower drug release in comparison to the amorphous PEG-*b*-PLA micelles.[4] Similarly, the well-established hydrophobic drug carrier, $mPEG_{2k}$-DSPE micelle (which was used as a control for many studies throughout this thesis), has a melting transition in the lipid core at 12.8°C (ascribed to core chain melting, meaning that these micelles have a fluid core at room temperature).[5] Lower T_g/T_m values may be due in part to the aggregate geometry, dictated by the large PEG corona that prevents regular crystalline packing of lipid cores. Additionally, fluid

micelles may quickly rearrange, whereas glassy cores may experience slower diffusion coefficients and monomer desorption rates. The altered dynamics of the glassy micelles can be advantageous in drug delivery applications in that glassy micelles should disassemble more slowly upon dilution to experience prolonged circulation times *in vivo*.[5] Although there is no global T_g or T_m range that determines successful application for drug delivery, thermal properties can be used to relate core crystallinity (derived from the polymer structure) to micelle performance and ultimately as a tool to optimize the micelle design for various applications.

These studies demonstrate how tuning micelle core crystallinity can serve to tailor the micelle properties for optimized drug delivery. For our purposes, the investigation between the micelle properties and core crystallinity was expanded to the fluorous micelles, specifically to elucidate the effect of an amphiphilic (hydrophobic and fluorophilic) core. In this study CMC, T_g, and SAXS analyses of bi- and triphilic micelles were used to investigate the micelle core and the possible role of the core crystallinity.

S1.2 CMC values of biphilic vs. triphilic fluorous micelles

S1.2.1 Results and discussion

In drug delivery applications the micelles need to be stable to provide adequate bioavailability of the encapsulated drug. An indication of inherent micelle stability is the CMC. For fluorous micelles, a significant anomaly was observed when comparing the CMC values of biphilic PFtB polymer micelles described in Chapter 2 versus those of triphilic PFtB polymer micelles in Chapter 3. Typically, the increased hydrophobicity of the polymer tail would result in the decrease of the CMC value. However, when the triphilic polymers were measured, the CMC value increased in comparison to the biphilic polymers despite the addition of a H10, hydrocarbon segment. To investigate if this phenomenon was specific to the PFtB polymers, a series of triphilic linear PFC polymers were synthesized. The CMC values of the triphilic series (including the H10 segment) demonstrated a similar phenomenon, with the CMC decreasing

slightly with each increase in the fluorocarbon chain length (see Table below). Additionally this effect seemed to be driven by the two dissimilar segments of the hydrophobic core, as varying the PEG blocks (1k vs. 2k vs. 5k) showed no distinct effect on the CMC value. The anomalous decrease in pCMC is most pronounced for $mPEG_{1k}$-F13 vs. $mPEG_{2k}$-O-H10-F13, 6.08 vs. 4.49 respectively.

CMC values of fluorous polymers.

The critical micelle concentration (CMC) values of $mPEG_x$-O-H10-R_F polymers are contrasted with those of the corresponding $mPEG_x$-R_F polymers. [a]CMC was determined by surface tensiometry. [b]CMC was determined by pyrene encapsulation method. [c]Synthesis and characterization reported in Chapter 3. [d]Synthesis and characterization reported in Chapter 2.

Compound	pCMC (-log(M))
$mPEG_{1k}$-H10-F8[6]	5.85 ± 0.06
$mPEG_{2k}$-H10-F8	5.44 ± 0.08
$mPEG_{5k}$-H10-F8	5.61 ± 0.04
$mPEG_{2k}$-O-H10-F10	4.73 ± 0.04
$mPEG_{2k}$-O-H10-F13[c]	4.49 ± 0.18
$mPEG_{2k}$-O-H10-$PFtB_{TRI}$[c]	3.98 ± 0.14
$mPEG_{1k}$-F13[d]	6.08 ± 0.13
$mPEG_{2k}$-$PFtB_{TRI}$[d]	5.32 ± 0.06

Although the absolute cause for the increase in the CMC can not be identified at this time, it is possible that the amphiphilic core of the triphilic fluorous micelles may engender more amorphous character (as was seen by Albertsson *et al.*).[3] In order to investigate this further, the T_g of a biphilic/triphilic polymer pair was analyzed.

S1.3 Differential scanning calorimetry (DSC)

S1.3.1 Results and discussion

To determine if the installation of the hydrocarbon segment had altered the core crystallinity of the fluorous micelles, DSC measurements were performed on the biphilic/triphilic polymer pair of $mPEG_{2k}$-$PFtB_{TRI}$ and $mPEG_{2k}$-O-H10-$PFtB_{TRI}$ (heat flows as a function of temperature and T_g calculations are provided below). Both polymers were measured by heating to 150°C and cooling to -80°C and a single T_g was found (the $mPEG_{2k}$-O-H10-$PFtB_{TRI}$ was repeated with faster cooling, hence the slight difference in the heat flow graphs).

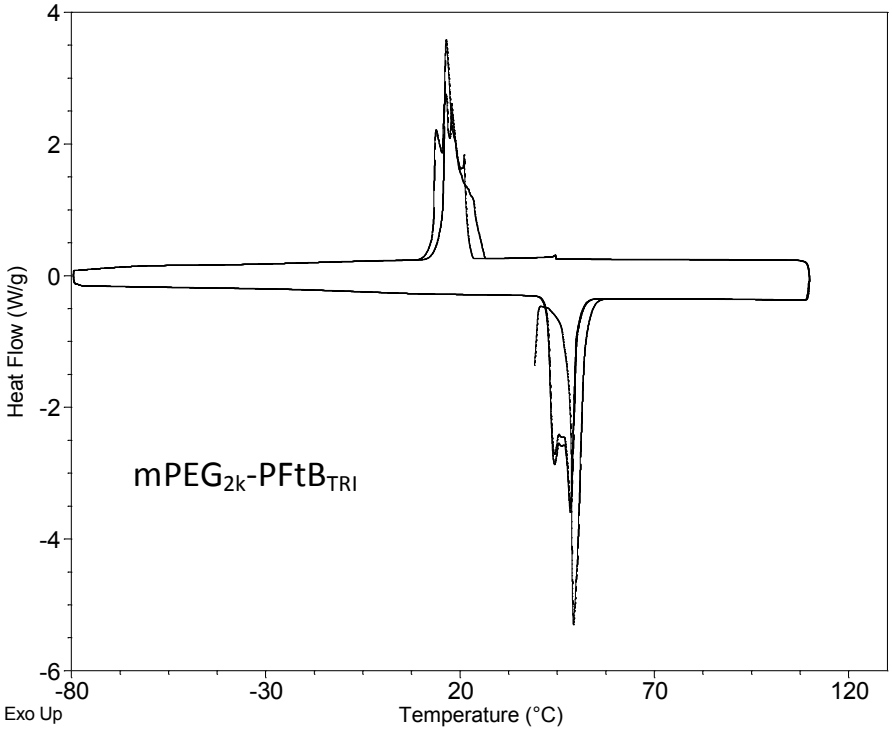
mPEG2k-PFtBTRI
Heat Flow (W/g)
Exo Up
Temperature (°C)
4
2
0
-2
-4
-6
-80
-30
20
70
120

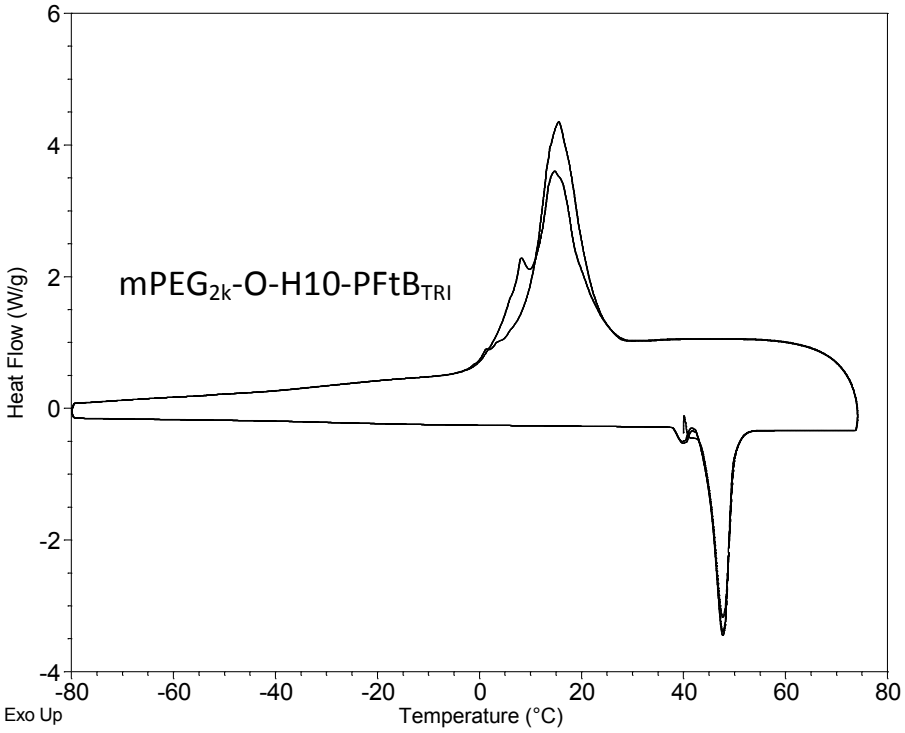
mPEG2k-O-H10-PFtBTRI
Heat Flow (W/g)
Exo Up
Temperature (°C)
6
4
2
0
-2
-4
-80
-60
-40
-20
0
20
40
60
80

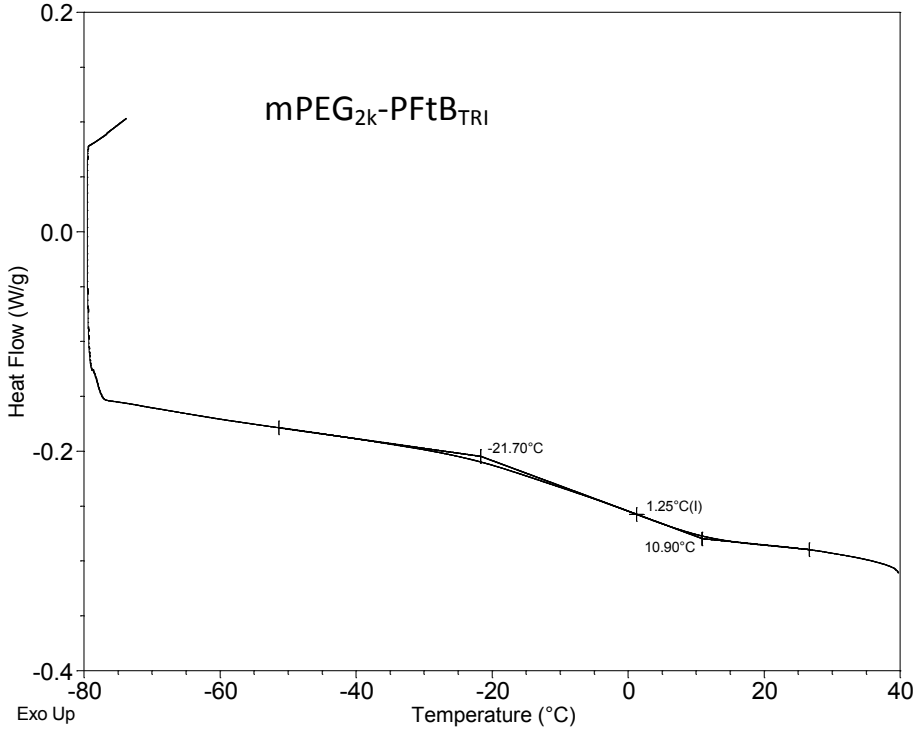
mPEG2k-PFtBTRI
0.2
0.0
-0.2
-0.4
Heat Flow (W/g)
-21.70°C
1.25°C(I)
10.90°C
-80
-60
-40
-20
0
20
40
Exo Up
Temperature (°C)

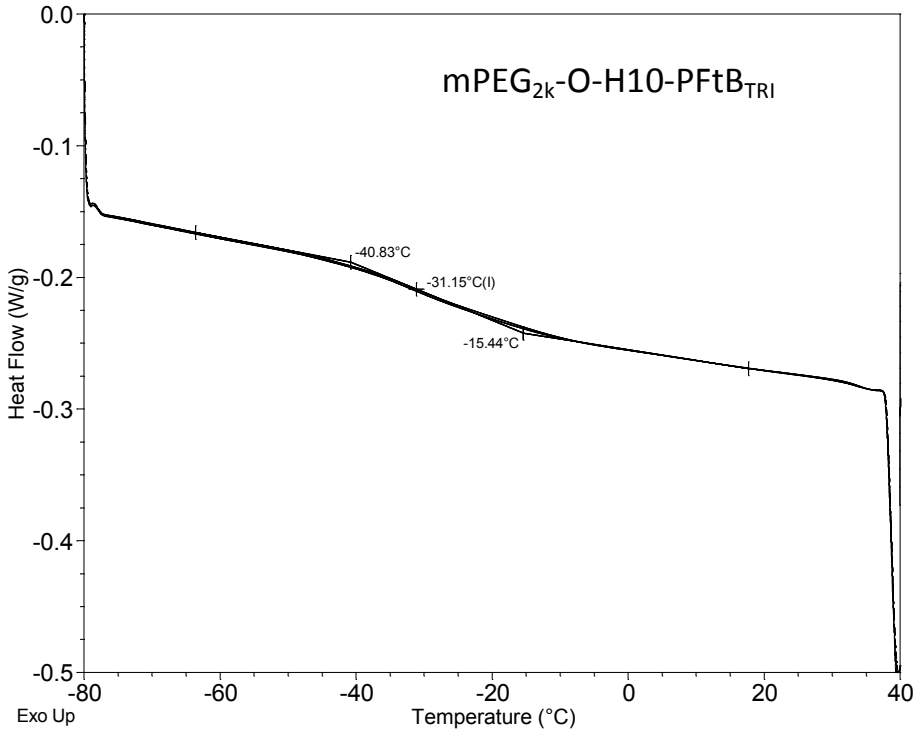
mPEG2k-O-H10-PFtBTRI
0.0
-0.1
-0.2
-0.3
-0.4
-0.5
Heat Flow (W/g)
-40.83°C
-31.15°C(I)
-15.44°C
-80
-60
-40
-20
0
20
40
Exo Up
Temperature (°C)

From these preliminary measurements it appears that the installation of the hydrocarbon segments has shifted the T_g ($mPEG_{2k}$-$PFtB_{TRI}$ T_g = -21.7°C vs. $mPEG_{2k}$-O-H10-$PFtB_{TRI}$ T_g = -40.8°C). The lower T_g of the triphilic micelle could support a more amorphous core leading to increased CMC values. To see if we could corroborate this data we wanted to try a separate technique to determine differences in core crystallinity.

S1.4 Small angle X-ray scattering (SAXS)

S1.4.1 Results and discussion

Core crystallinity can also be inferred from X-ray scattering experiments. Additionally, this technique can be used to determine several other important micelle characteristics, such as particle size and shape. Since there had been several difficulties in direct imaging of the micelles via TEM, SAXS was performed initially on $mPEG_{2k}$-O-H10-$PFtB_{TRI}$ and $mPEG_{2k}$-O-H10-F13 to ascertain whether this technique would even be feasible for these small fluorous micelles.

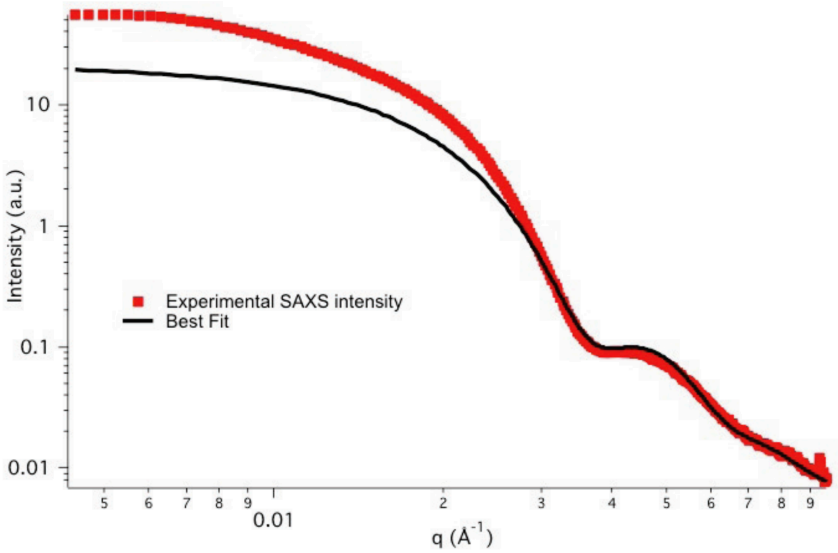

Reference SAXS data for $PVAc_{132}$-*b*-PVA_{95} spherical micelles.
Synchrotron SAXS data for a spherical micelle dispersion of $PVAc_{132}$-*b*-PVA_{95}. Fitting with a spheroid model (aspect ratio 1) with a radius r = 13.4 nm (std. dev. = 0.26) provides a modest fit, with higher observed scattering intensity at low q (due to the presence of micelles aggregated by hydrogen bonding as determined by DLS; vide infra). Adapted from Reference 7.

The SAXS data for $PVAc_{132}$-*b*-PVA_{95} spherical micelles are shown above to serve as a reference. Below the results for the fluorous micelles are provided as 2-D plots of intensity vs. q($Å^{-1}$) without background correction. No modeling has been applied due to limited software availability. However, comparison between the reference spherical micelles and the fluorous micelles demonstrate clear similarities, providing some support for the formation of small, spherical micelles (which corroborates the DLS data described in Chapter 3 for both the $PFtB_{TRI}$ and F13).

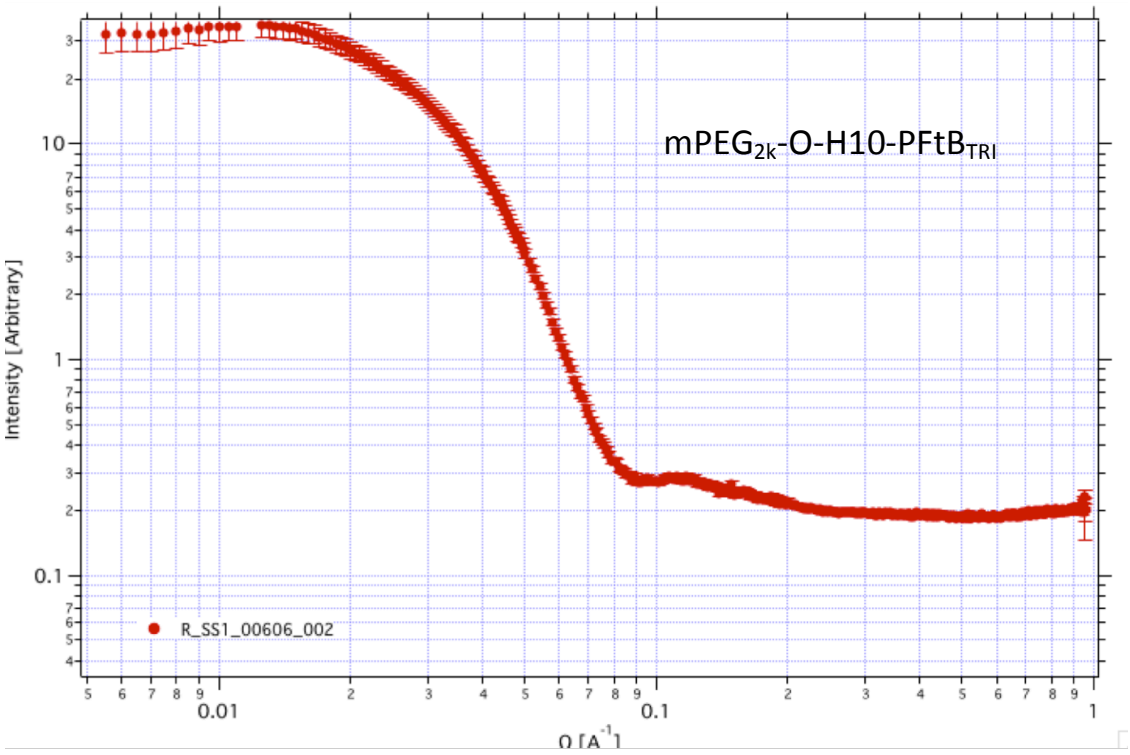

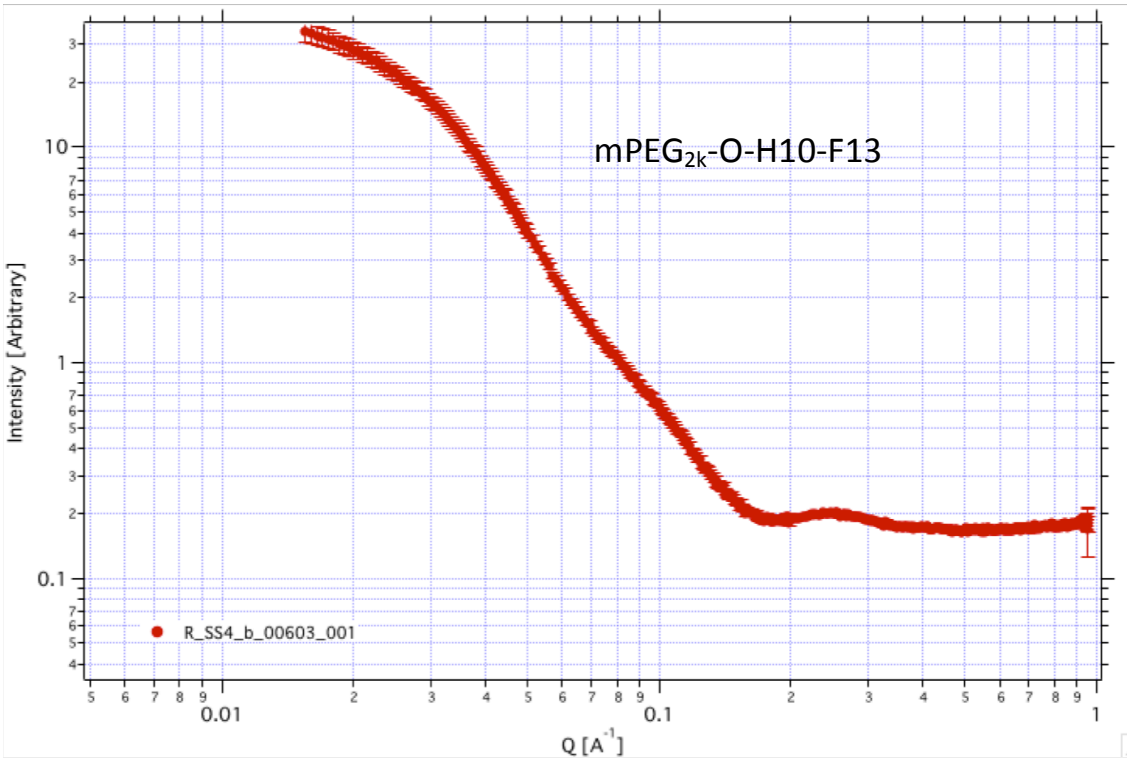

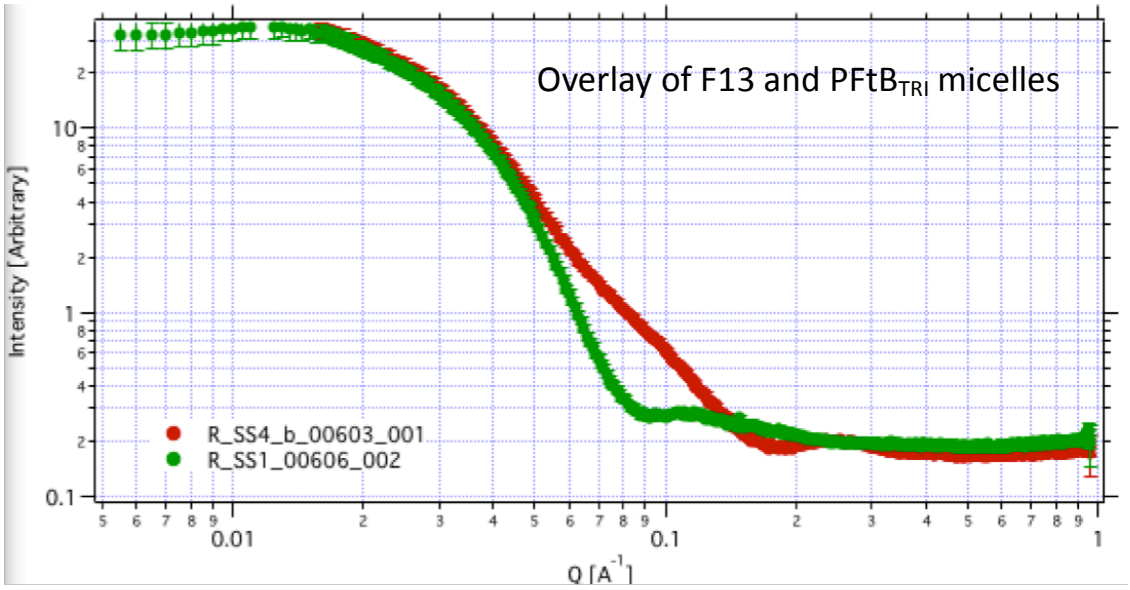

From this study it appears the SAXS (and most likely wide angle x-ray scattering (WAXS), which could be more applicable for our purposes) are promising techniques to investigate the fluorous micelle properties. Further studies, possibly over various temperatures and

concentrations (to observe the effects above and below the T_g) and modeling will be an ongoing effort in the group.

S1.5 Conclusion

The investigations into the physicochemical properties of the fluorous micelle cores have revealed interesting behavior, including slightly increased CMC values and shifted T_g values in the triphilic system. In Chapter 3 it was shown that the triphilic PFtB polymers exhibited increased stability *in vivo*. However, the CMC and T_g phenomenon both support the development of a more amorphous core with the installation of a hydrocarbon segment. Further analysis is therefore needed to truly understand the nature of the fluorous core. To establish whether X-ray scattering measurement would be beneficial in this effort, the fluorous micelles were analyzed via SAXS. The results supported the formation of small, spherical micelles and therefore SAXS seems to be a promising analytical technique for these systems.

S1.6 Experimental

S1.6.1 Synthesis

mPEG$_x$-O-H10-R$_F$: In a typical reaction at 0 °C was added NaH (10 eq., 6.4 mmol) to a suspension of R_F-H10-OH (1.2 eq., 0.76 mmol) and 4 Å powdered molecular sieves (1 weight eq.) in 10 mL of dry THF under argon. This was allowed to stir for 30 min at 0 °C. After this time, mPEG$_x$-OMs[8] (1 eq., 0.64 mmol) was added at 0 °C. The reaction mixture was allowed to stir as it warmed slowly to room temperature. The mixture was then refluxed and monitored by HPLC. Each day 10 mg of NaH was added to facilitate the reaction. When determined to be complete the reaction mixture was then diluted with 10 mL of DCM, slowly quenched with 1 mL of MeOH, followed by 1 mL of water, washed with sat. NH_4Cl_{aq}, dried over $MgSO_4$, and concentrated to 10 mL *in vacuo.* The crude product was then precipitated from the organic phase with cold ether in a dry-ice/acetone bath. The solid was isolated by filtration and then dissolved in

5 mL of dichloromethane and 5 mL of benzene, which was then frozen in dry-ice/acetone bath and freeze-dried overnight *in vacuo*. The crude product was purified by automated flash chromatography using a RediSep C18 reverse phase silica column with a water–MeOH (0.1% FA) to dichloromethane–MeOH gradient. **mPEG$_{2k}$-O-H10-F8**: Yield 34%. ^{1}H NMR (400 MHz, $CDCl_3$): δ 3.92 (t, J = 6.8 Hz, 2H), 3.79–3.77 (m, 2 H), 3.67–3.49 (m, 184 H), 3.45–3.43 (m, 2 H), 3.38 (s, 3 H), 1.68–1.54 (m, 4 H (overlapped with water peak), 1.39–1.26 (m, 18 H). ^{19}F NMR (376 MHz, $CDCl_3$): δ -81.07, -119.93, -122.04, -122.04, -122.22, -123.76, -123.76, -126.43. MALDI MS: $[M + Na]^+$ calcd. for $C_{99}H_{183}F_{17}NaO_{41}$ = 2374.19; found: 2373.9. **mPEG$_{5k}$-O-H10-F8**: Yield 87%. ^{1}H NMR (400 MHz, $CDCl_3$): δ 3.82 (t, J = 6.8 Hz, 2H), 3.71–3.50 (m, 184 H), 3.47–3.43 (m, 3 H), 3.38 (s, 3 H), 1.66–1.52 (m, 3 H), 1.41–1.26 (m, 17 H). ^{19}F NMR (376 MHz, $CDCl_3$): δ -81.17, -122.11, -122.33, -123.15, -123.93, -126.51. MALDI MS: $[M + Na]^+$ calcd. for $C_{237}H_{459}F_{17}NaO_{110}$ = 5411.9; found: 5417.2. **mPEG$_{2k}$-O-H10-F10**: Yield 11% ^{1}H NMR (500 MHz, $CDCl_3$): δ 3.92 (m, 2H), 3.83–3.81 (m, 1 H), 3.69–3.54 (m, 171 H), 3.48–3.45 (m, 1H), 3.44 (t, J = 6.8 Hz, 2H), 3.38 (s, 3H), 1.63-1.53 (m, 6 H), 1.38-1.26 (m, 18 H). ^{19}F NMR (470 MHz, $CDCl_3$) δ -81.15 (3 F), -120.01 (2 F), -122.09-122.41 (16 F), -123.10 (2 F), -123.83 (2 F), -126.51 (2 F). MALDI MS: $[M + Na]^+$ calcd. for $C_{100}H_{181}F_{21}NaO_{41}$ = 2460.16; found: 2803.2

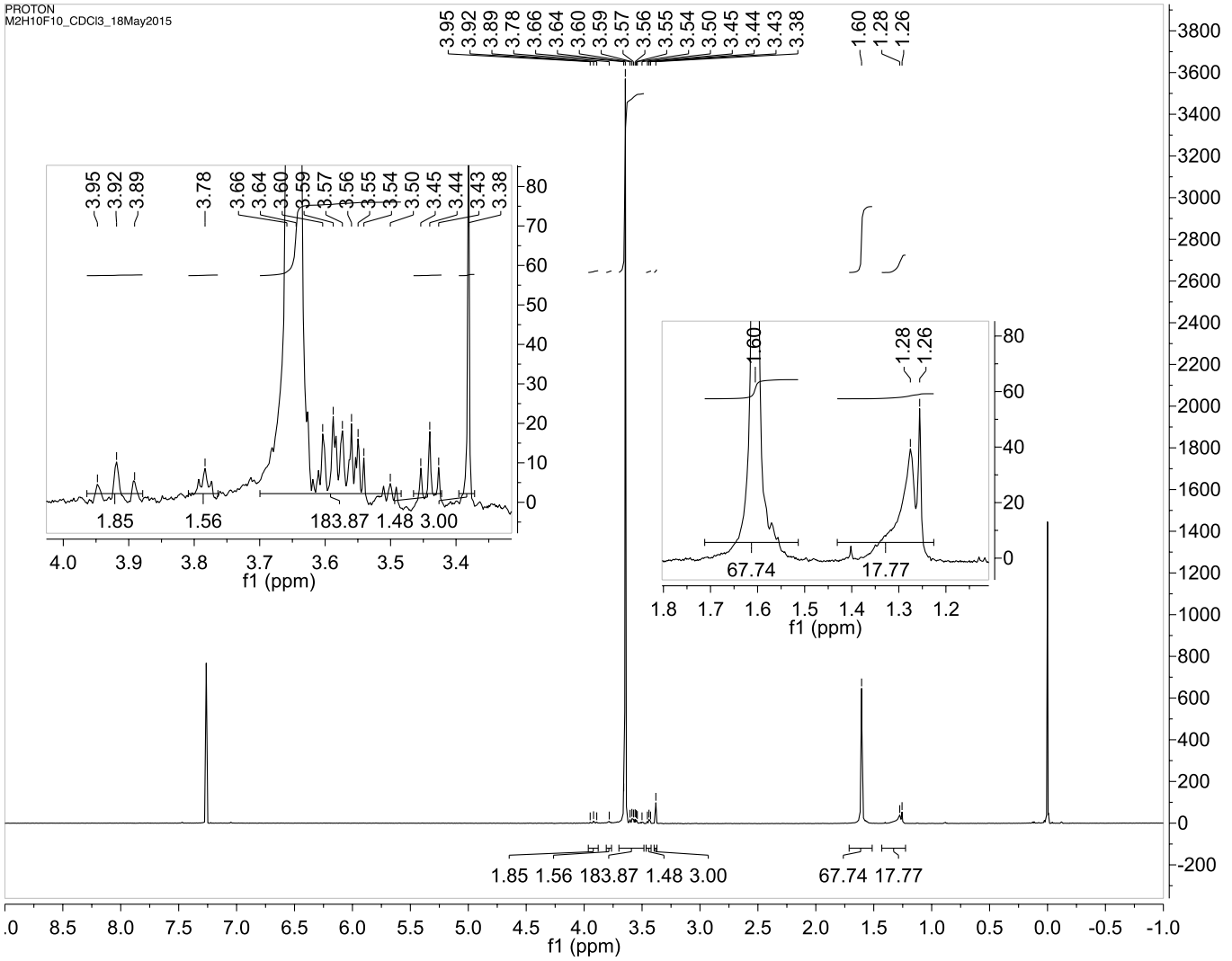
PROTON
M2H10F10_CDCl3_18May2015
3.95 3.92 3.89 3.78 3.66 3.64 3.60 3.59 3.57 3.56 3.55 3.54 3.50 3.45 3.44 3.43 3.38
1.60 1.28 1.26
1.85 1.56 183.87 1.48 3.00
67.74 17.77
f1 (ppm)

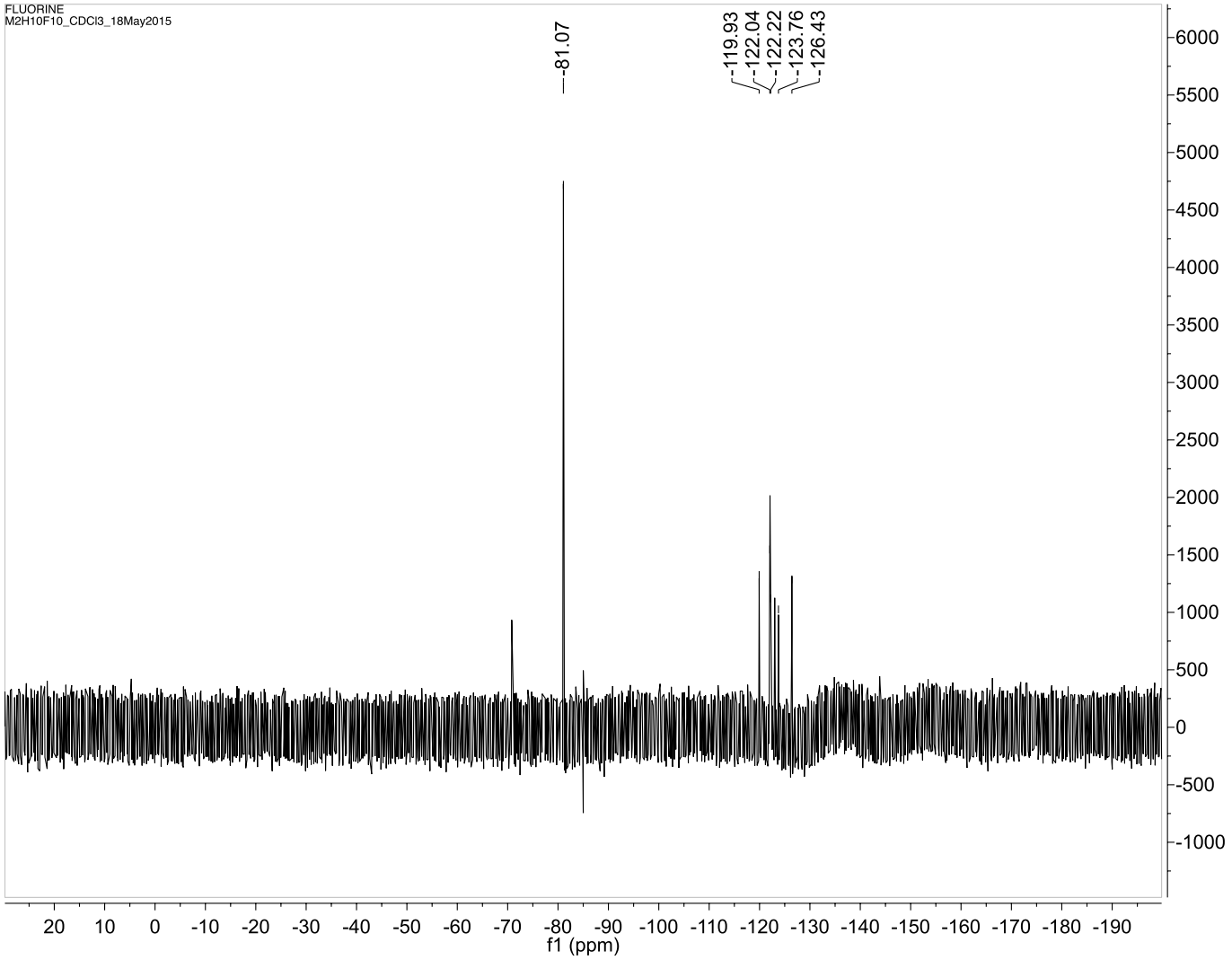
FLUORINE
M2H10F10_CDCl3_18May2015
-81.07
-119.93
-122.04
-122.22
-123.76
-126.43
6000
5500
5000
4500
4000
3500
3000
2500
2000
1500
1000
500
0
-500
-1000
20 10 0 -10 -20 -30 -40 -50 -60 -70 -80 -90 -100 -110 -120 -130 -140 -150 -160 -170 -180 -190
f1 (ppm)

D:\Data\Mecozzi\141229x01\0_E5\1

Comment 1 Tucker 4117 // DHB + NaTFA // RP_PepMix.par

Comment 2 300 shots, 90% lp (74)

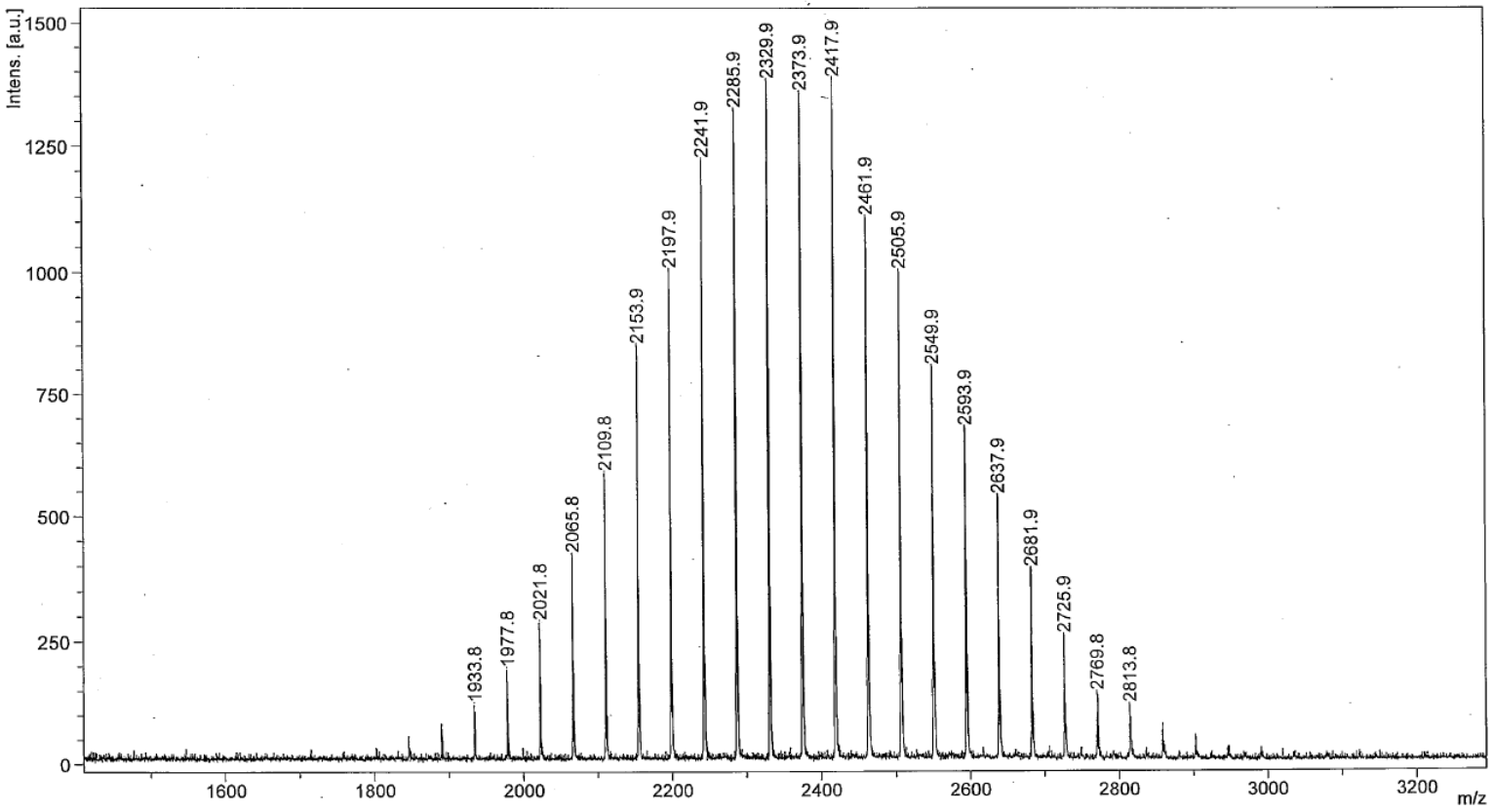

Bruker Ultraflex III, Chem. Dept., Univ. Wisconsin, Cite: NIH NCRR 1S10RR024601-01

printed: 12/29/2014 12:44:51 PM

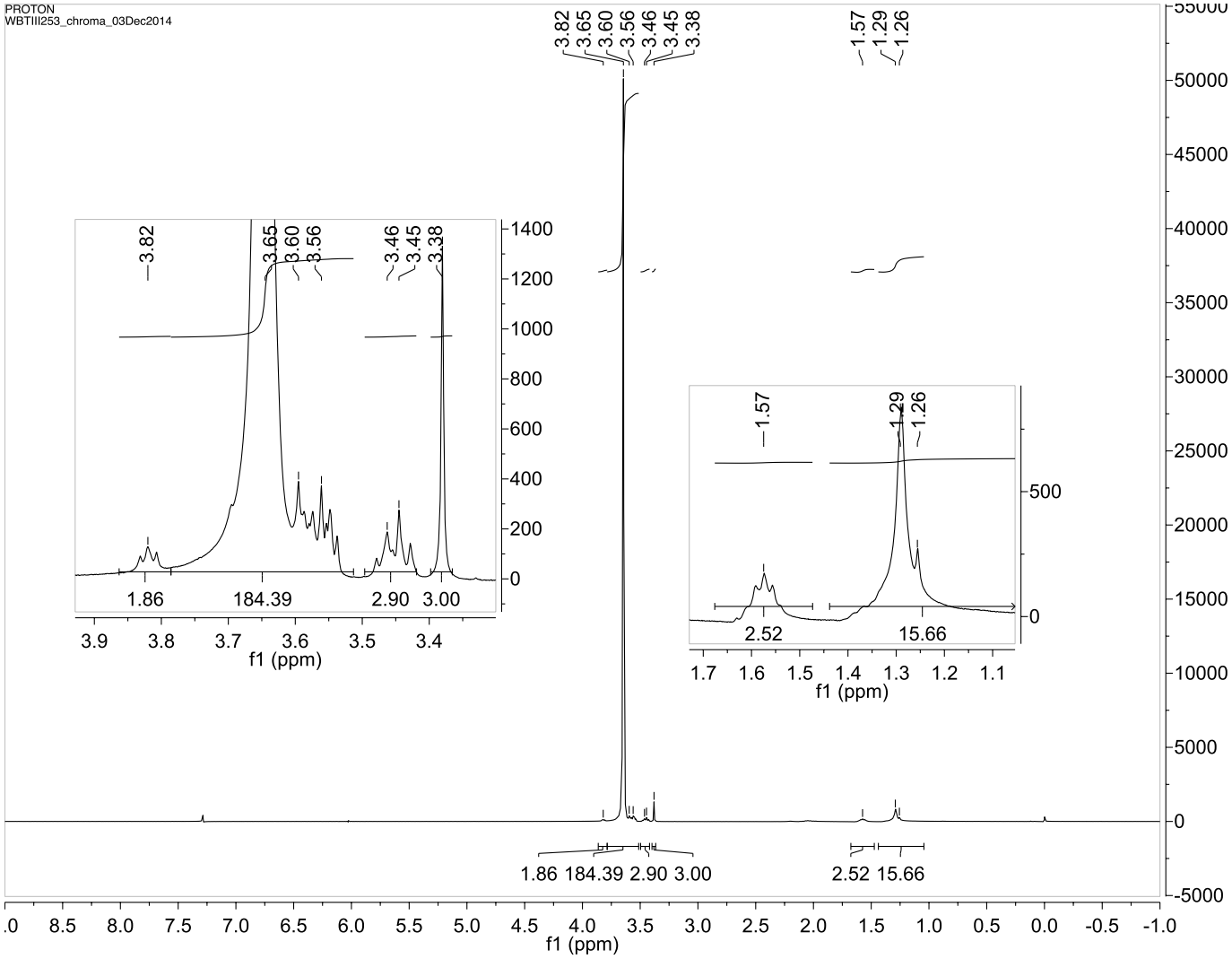
PROTON
WBTIII253_chroma_03Dec2014
3.82
3.65
3.60
3.56
3.46
3.45
3.38
1.57
1.29
1.26
1.86 184.39 2.90 3.00
2.52 15.66
f1 (ppm)

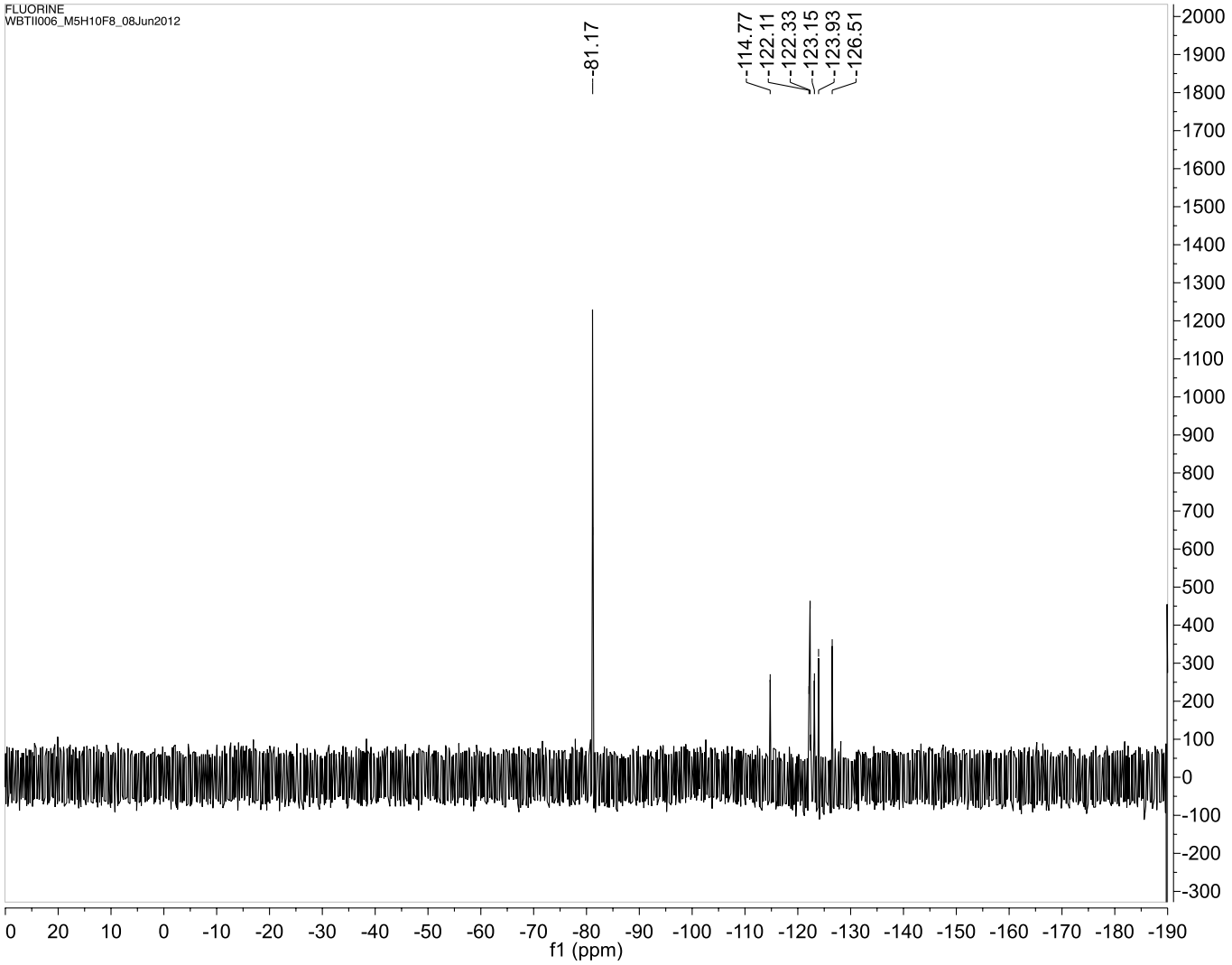
FLUORINE
WBTII006_M5H10F8_08Jun2012
-81.17
-114.77
-122.11
-122.33
-123.15
-123.93
-126.51
f1 (ppm)

D:\Data\mmv\120323x05\0_E6\1

Comment 1 Tucker 1196 // CHCA // RP_PepMix.par

Comment 2 300 shots, 10% Ip (72). 2020-720 defl

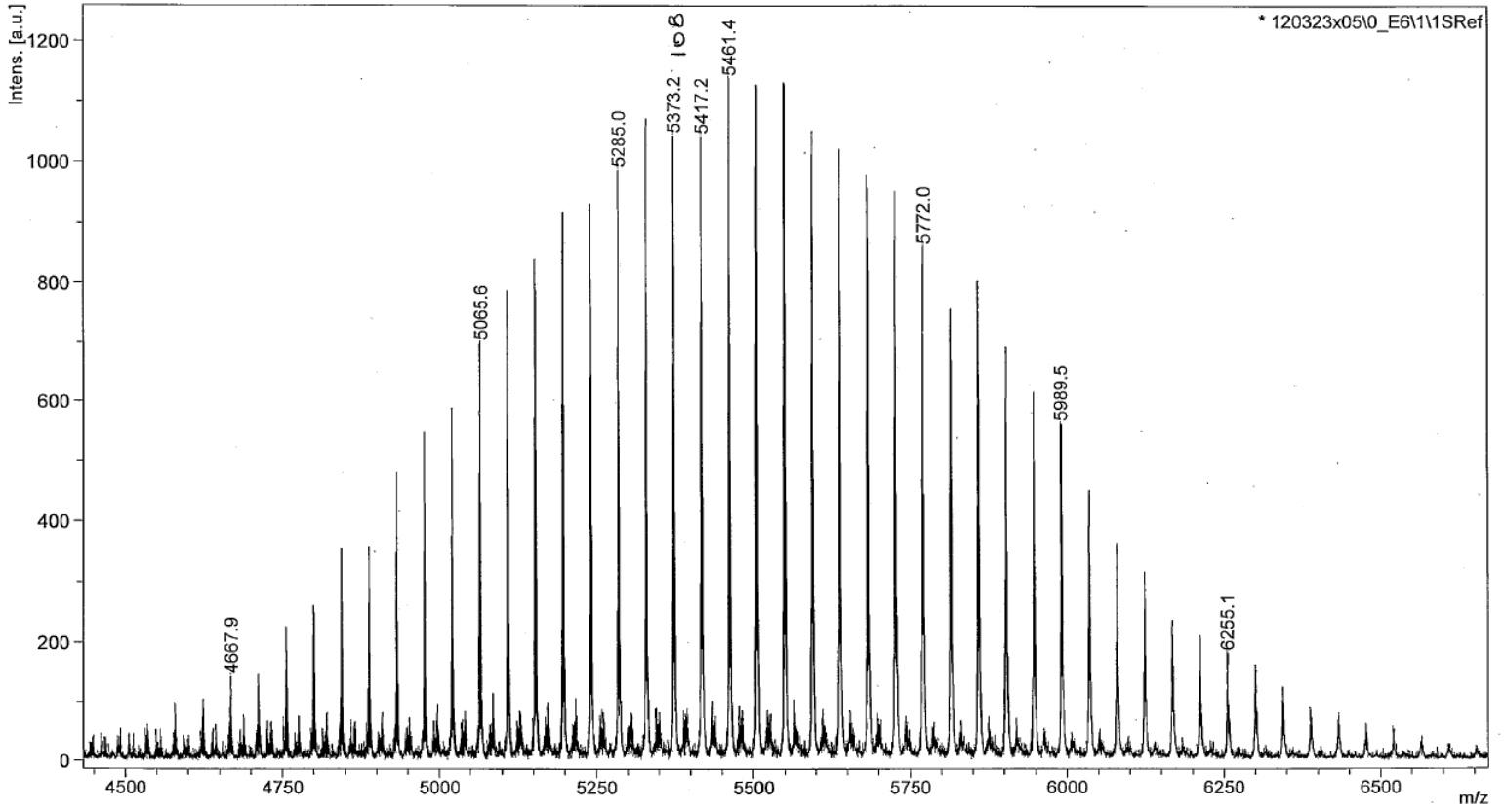

Bruker Ultraflex III, Chem. Dept., Univ. Wisconsin, Cite: NIH NCRR 1S10RR024601-01

printed: 3/23/2012 3:16:46 PM

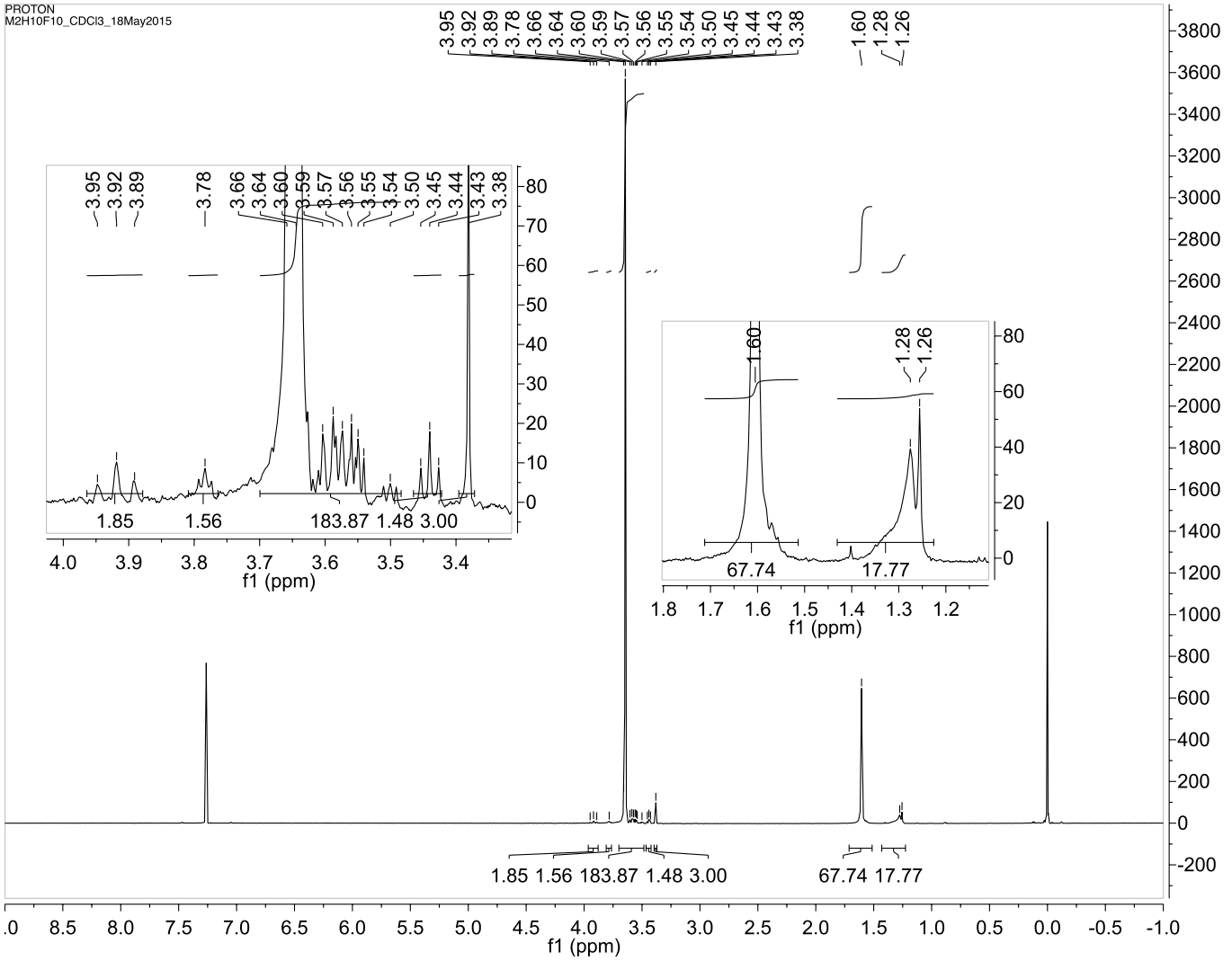
PROTON
M2H10F10_CDCl3_18May2015
3.95
3.92
3.89
3.78
3.66
3.64
3.60
3.59
3.57
3.56
3.55
3.54
3.50
3.45
3.44
3.43
3.38
1.60
1.28
1.26
1.85 1.56 183.87 1.48 3.00
67.74 17.77
f1 (ppm)

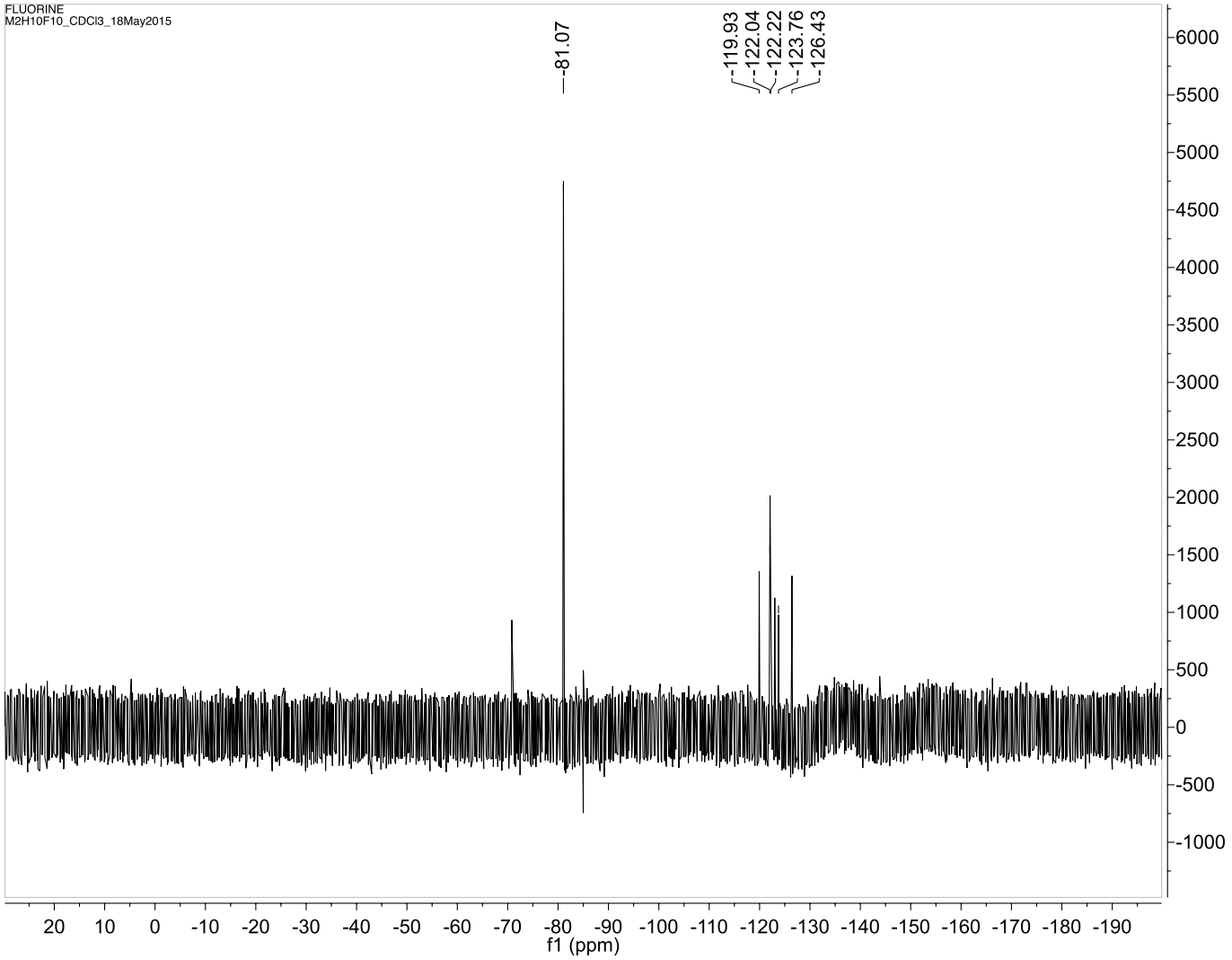
FLUORINE
M2H10F10_CDCl3_18May2015
-81.07
-119.93
-122.04
-122.22
-123.76
-126.43
6000
5500
5000
4500
4000
3500
3000
2500
2000
1500
1000
500
0
-500
-1000
20 10 0 -10 -20 -30 -40 -50 -60 -70 -80 -90 -100 -110 -120 -130 -140 -150 -160 -170 -180 -190
f1 (ppm)

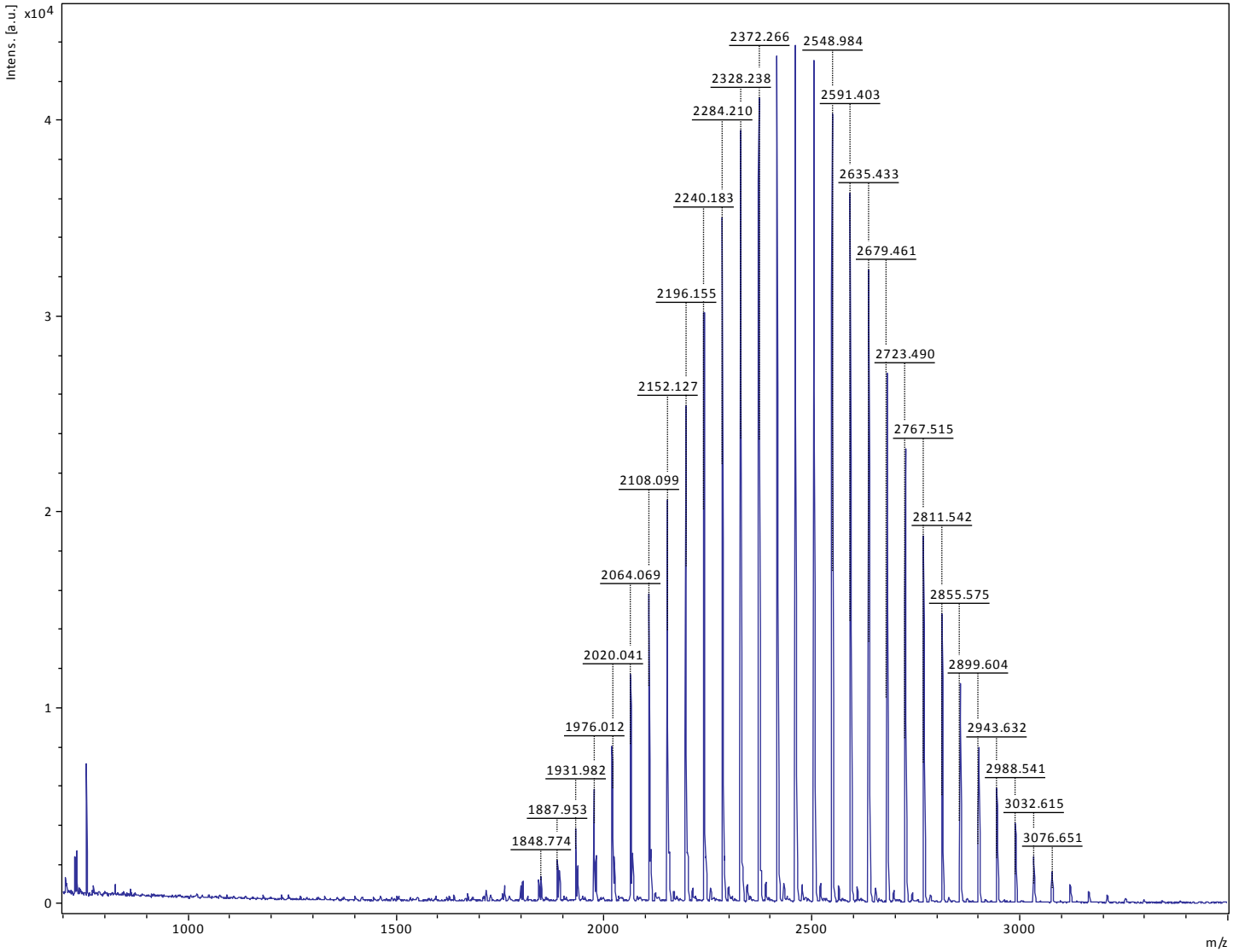
Intens. [a.u.]
x10^4
4
3
2
1
0
1000
1500
2000
2500
3000
m/z
1848.774
1887.953
1931.982
1976.012
2020.041
2064.069
2108.099
2152.127
2196.155
2240.183
2284.210
2328.238
2372.266
2548.984
2591.403
2635.433
2679.461
2723.490
2767.515
2811.542
2855.575
2899.604
2943.632
2988.541
3032.615
3076.651

S1.6.2 CMC measurement

(For procedure of both tensiometry and pyrene methods see Chapter 3 experimental)

mPEG$_{2k}$-H10-F8 (Surface tensiometry method)

mPEG$_{2k}$-H10-F8		
log(M)	**Avg. SurfaceTension (mN/m)**	**Std. Dev. (mN/m)**
-2.99	38.14	0.05
-3.49	38.11	0.06
-3.99	39.79	0.08
-4.49	41.52	0.08
-4.99	43.43	0.13
-5.49	44.48	0.08
-5.99	56.04	0.09
-6.49	69.18	0.15
-6.74	72.26	0.12
-6.99	72.82	0.17
-7.49	73.33	0.12

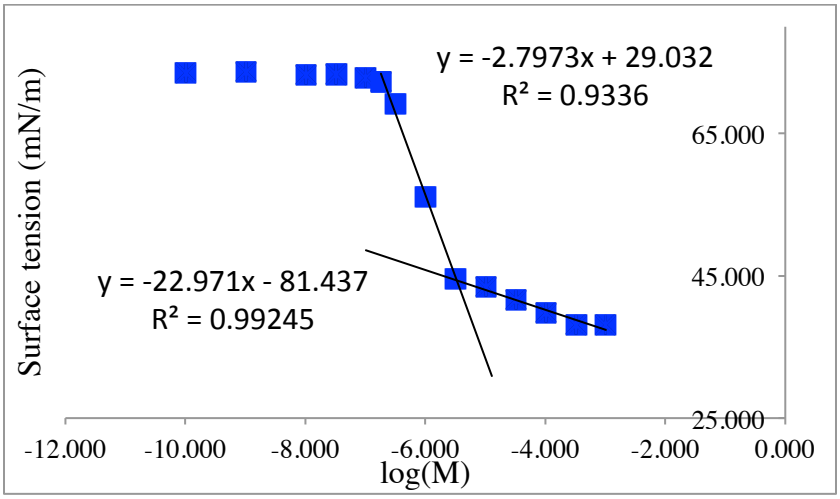

mPEG$_{5k}$-H10-F8 (Pyrene encapsulation method)

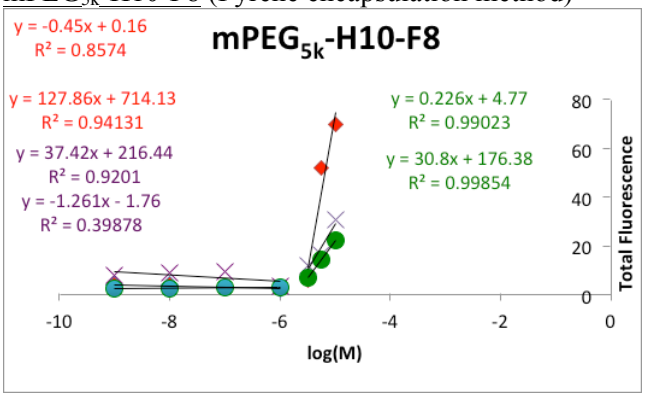

CMC values	
-5.564	
-5.641	
-5.613	
-5.606	**Ave**
0.039	**Std. Dev.**

mPEG$_{2k}$-H10-F10 (Surface tensiometry method)

mPEG$_{2k}$-O-H10-F10		
log(M)	**Avg. SurfaceTension (mN/m)**	**Std. Dev. (mN/m)**
-2.501807439	36.78775	0.050089087
-3.103867431	37.79775	0.112241926
-3.705927422	39.3115	0.427289519
-4.307987413	39.36775	0.149669358
-4.910047405	40.564	0.122558829
-5.512107396	43.85175	0.137179627
-5.688198655	59.50225	0.062168454
-6.114167387	64.74125	0.035528158
-6.716227379	72.92625	0.066810054
-2.501807439	36.78775	0.050089087
-3.103867431	37.79775	0.112241926

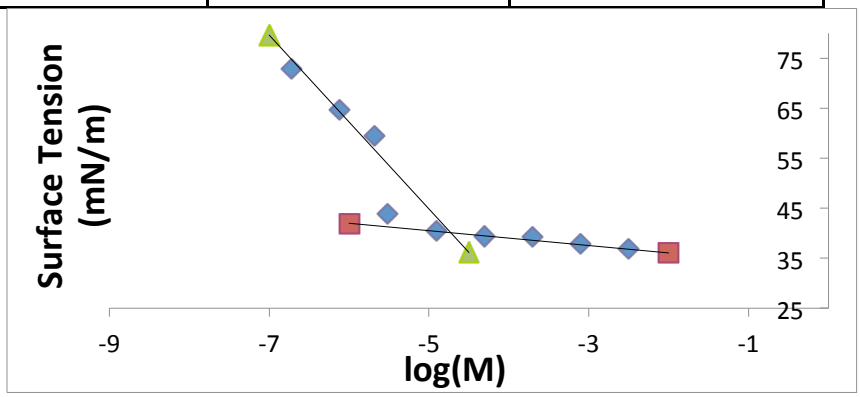

S1.6.3 DSC

Differential scanning calorimetry (DSC) was performed with a TA Instruments DSC Q2000. A total of 4−6 mg of material was loaded in a crimped aluminum pan and scanned at a rate of 10 °C/ min. Several heat/cool cycles were performed to ensure that the data represented equilibrium measurements. Transition temperatures specified correspond to the average of the peak temperatures.

S1.6.4 SAXS

Polymer micelle solutions of mPEG$_{2k}$-O-H10-F13 and mPEG$_{2k}$-O-H10-PFtB$_{TRI}$ were made by the solvent evaporation method (see chapter 3 for details). The thin film was made with ACN as the organic solvent and was redispersed with Mili-Q water to afford a 10 mM concentration.

The solutions were filtered with 0.45 m filter and micelle formation was confirmed by DLS. An aliquot of each solution was loaded into a 2 mm quartz capillary and sealed with epoxy.

Synchrotron SAXS analyses were conducted at the DuPont-Northwestern-Dow Collaborative Access Team (DND-CAT) 5-ID- D beamline of the Advanced Photon Source at Argonne National Laboratory (Argonne, IL). Capillary samples were exposed for 1 s to X-rays with anincident beam energy of 16 keV (λ = 0.7293 Å) and a 3.068 m sample-to-detector distance (calibrated using silver behenate). Two-dimensional SAXS patterns were recorded on a MAR-CCD detector (133 mm diameter active circular area). 2D SAXS patterns were plotted as one-dimensional intensity I(q) versus scattering wave vector (q) plots using Jan Ilavsky's IRENA software.[9]

S1.7 Acknowledgements

Thank you to Travis Powell for his help with DSC measurements, to Dr. Dominic Perroni and Dr. Frank Speetjens for their help with SAXS measurements and analysis, and to William Tucker for his equal contribution to the synthesis and CMC measurement of the fluorous compounds.

S1.8 References

(1) Pan, P.; Shan, G.; Bao, Y.; Fujita, M.; Maeda, M. Core − Shell Structure, Biodegradation, and Drug Release Behavior of Poly(lactic acid)/Poly(ethylene Glycol) Block Copolymer Micelles Tuned by Macromolecular Stereostructure. *Langmuir* **2015**, *31*, 1527–1536.

(2) Kang, N. Stereocomplex Block Copolymer Micelles : Core − Shell Nanostructures with Enhanced Stability. *Nano Lett.* **2005**, *5* (2), 315–319.

(3) Glavas, L.; Olsén, P.; Odelius, K.; Albertsson, A. C. Achieving Micelle Control through Core Crystallinity. *Biomacromolecules* **2013**, *14* (11), 4150–4156.

(4) Cho, H.; Lai, T. C.; Tomoda, K.; Kwon, G. S. Polymeric Micelles for Multi-Drug Delivery in Cancer. *AAPS PharmSciTech* **2014**, *16* (1), 10–20.

(5) Kastantin, M.; Ananthanarayanan, B.; Karmali, P.; Ruoslahti, E.; Tirrell, M. Effect of the Lipid Chain Melting Transition on the Stability of DSPE-PEG (2000) Micelles. *Langmuir* **2009**, *25* (13), 7279–7286.

(6) Tucker, W. B.; McCoy, A. M.; Fix, S. M.; Stagg, M. F.; Murphy, M. M.; Mecozzi, S. Synthesis, Physicochemical Characterization, and Self-Assembly of Linear, Dibranched, and Miktoarm Semifluorinated Triphilic Polymers. *J. Polym. Sci. Part A Polym. Chem.* **2014**, *52* (23), 3324–3336.

(7) Repollet-Pedrosa, M. H.; Mahanthappa, M. K. Fusion of Poly(vinyl Acetate-B-Vinyl Alcohol) Spherical Micelles in Water Induced by Poly(ethylene Oxide). *Soft Matter* **2013**, *9* (32), 7684.

(8) Decato, S.; Bemis, T.; Madsen, E.; Mecozzi, S. Synthesis and Characterization of Perfluoro-Tert-Butyl Semifluorinated Amphiphilic Polymers and Their Potential Application in Hydrophobic Drug Delivery. *Polym. Chem.* **2014**, *5*, 6461–6471.

(9) Ilavsky, J.; Jemian, P. R. Irena : Tool Suite for Modeling and Analysis of Small-Angle Scattering. *J. Appl. Crystallogr.* **2009**, *42* (2), 347–353.

Appendix 2:

MALDI-MS/MSI analysis of toxicity in a zebrafish model after exposure to semifluorinated polymer micelles

S2.1 Motivation and intent

The Mecozzi lab has begun toxicity and bioaccumulation studies for the novel semifluorinated amphiphiles described previously using a zebrafish model. The zebrafish model (ZF; *Danio rerio*) was chosen as it is an established model species used in routine chemical toxicity analysis and has a fully sequenced and well-annotated genome.[1] Preliminary results demonstrated no evidence of acute toxicity from exposure to high concentration of semifluorinated polymer solutions (0.01 mM to 1 mM) (Publication currently in preparation: "Toxicity of perfluoroalkyl derivatives assessed using a Zebrafish early life stage test" by Samantha M. Fix, Joseph Gawdzik, Warren Heideman, and Sandro Mecozzi). However, it was desirable to have direct evidence that the lack of toxic symptoms was indeed due to the non-toxic nature of the compounds rather than their inability to be readily internalized via the zebrafish embryo and/or zebrafish larvae. Ineffective internalization of semifluorinated micelles could be in part possible due to the relatively small size of the chorion pores channels[2] (with an outer diameter of 0.5 ± 0.7 μm vs. micelle diameter of approximately 12 nm). Therefore MALDI-mass spectrometry imaging (MSI) was attempted to confirm internalization of the semifluroniated polymers. The advantage of MSI is that it provides the opportunity to examine the spatial context of both small molecules and larger macromolecules in the whole organism without modification of the polymer structure (e.g. fluorescent labeling), which could affect polymer toxicity or accumulation.

MSI sample preparation and handling has been identified as the first most important and challenging aspect of the whole organism analysis.[3] The numerous steps and method options are critical to the experiment success. For example the embedding medium, matrix selection and application all greatly affect the quality of the data and ability to detect the compounds of interest. Unfortunately, the MSI literature contains little information for processing small fish or fish larvae despite their increasing utility over more expensive, higher vertebrate models. Procedures

for cryo-sectioning are extremely important for zebrafish not only for their small size, but also as they may have an air-filled swim bladder that once frozen can be crushed and dislocate neighboring organ structures.[4,5] It was for these reasons that the following preliminary study was performed to assess whether MSI would be an appropriate technique to confirm the internalization of semifluroinated compounds.

S2.2 Results and discussion

In order to first confirm that the semifluorinated polymer could be visualized on the MALDI-MSI instrument (and if so, to identify the limit of detection), the micelle solutions of $mPEG_{1k}$-F13 polymer were analyzed at varying concentrations on the MALDI-Orbitrap (see following spectra). Both 2,5-Dihydroxybenzoic acid **(**DHB) and α-cyano-4-hydroxycinnamic acid (CHCA) matrix were used and CHCA was found to be far superior for this application. The detection limit was set to *m/z* 1550 in order to eliminate the CHCA peak at *m/z* = 1517. The semifluroinated polymers were readily visualized over the entire concentration range, from 0.1 mg/mL (0.05 mM) to 0.5 ag/mL. Although this does not indicate the detection limit for the zebrafish analysis (as there will be multiple endogenous salts, polymers, etc. to suppress the semifluorinated polymer signal), the initial solution spot MS parameters allowed us to proceed to the zebrafish analysis.

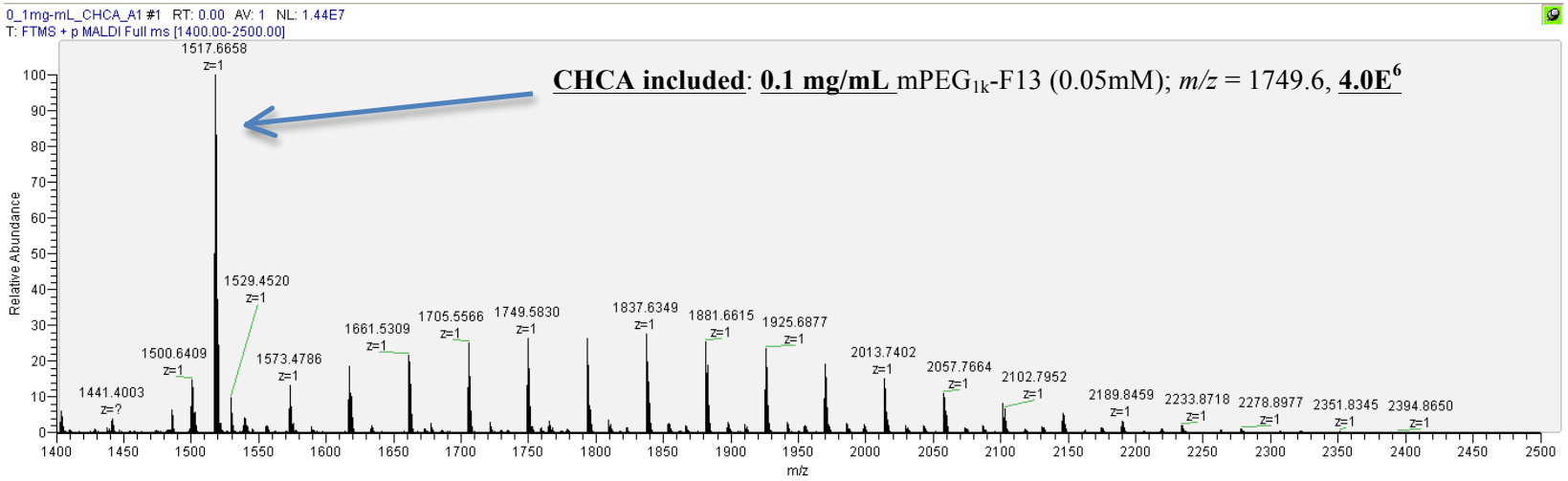
0_1mg-mL_CHCA_A1 #1 RT: 0.00 AV: 1 NL: 1.44E7
T: FTMS + p MALDI Full ms [1400.00-2500.00]
CHCA included: 0.1 mg/mL mPEG1k-F13 (0.05mM); m/z = 1749.6, 4.0E6
Relative Abundance
m/z
1517.6658 z=1
1529.4520 z=1
1500.6409 z=1
1573.4786 z=1
1441.4003 z=?
1661.5309 z=1
1705.5566 z=1
1749.5830 z=1
1837.6349 z=1
1881.6615 z=1
1925.6877 z=1
2013.7402 z=1
2057.7664 z=1
2102.7952 z=1
2189.8459 z=1
2233.8718 z=1
2278.8977 z=1
2351.8345 z=1
2394.8650 z=1

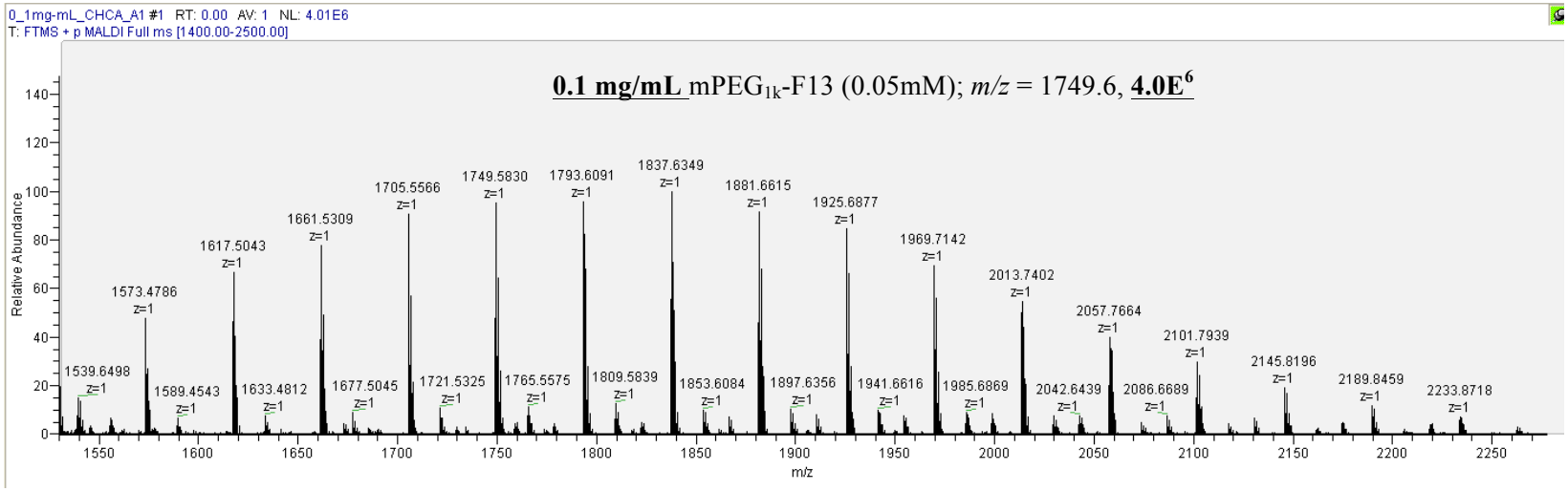
0_1mg-mL_CHCA_A1 #1 RT: 0.00 AV: 1 NL: 4.01E6
T: FTMS + p MALDI Full ms [1400.00-2500.00]
0.1 mg/mL mPEG1k-F13 (0.05mM); m/z = 1749.6, 4.0E6
Relative Abundance
m/z
1539.6498 z=1
1573.4786 z=1
1589.4543 z=1
1617.5043 z=1
1633.4812 z=1
1661.5309 z=1
1677.5045 z=1
1705.5566 z=1
1721.5325 z=1
1749.5830 z=1
1765.5575 z=1
1793.6091 z=1
1809.5839 z=1
1837.6349 z=1
1853.6084 z=1
1881.6615 z=1
1897.6356 z=1
1925.6877 z=1
1941.6616 z=1
1969.7142 z=1
1985.6869 z=1
2013.7402 z=1
2042.6439 z=1
2057.7664 z=1
2086.6689 z=1
2101.7939 z=1
2145.8196 z=1
2189.8459 z=1
2233.8718 z=1

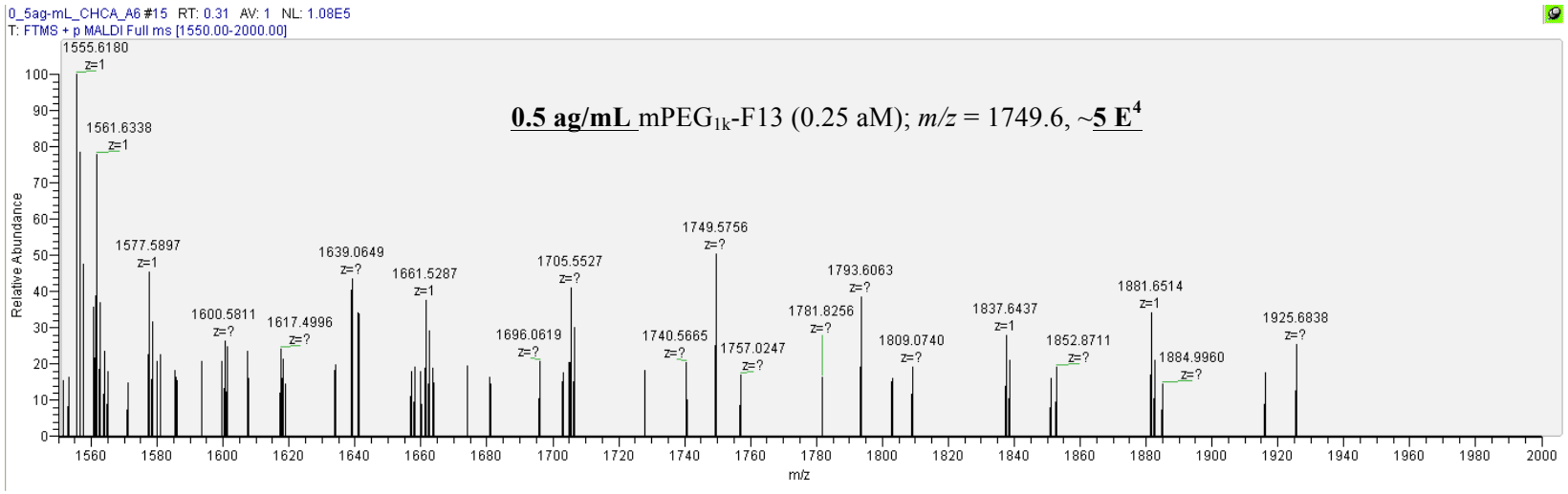
0_5ag-mL_CHCA_A6 #15 RT: 0.31 AV: 1 NL: 1.08E5
T: FTMS + p MALDI Full ms [1550.00-2000.00]
0.5 ag/mL mPEG1k-F13 (0.25 aM); m/z = 1749.6, ~5 E4
Relative Abundance
m/z
1555.6180 z=1
1561.6338 z=1
1577.5897 z=1
1600.5811 z=?
1617.4996 z=?
1639.0649 z=?
1661.5287 z=1
1696.0619 z=?
1705.5527 z=?
1740.5665 z=?
1749.5756 z=?
1757.0247 z=?
1781.8256 z=?
1793.6063 z=?
1809.0740 z=?
1837.6437 z=1
1852.8711 z=?
1881.6514 z=1
1884.9960 z=?
1925.6838 z=?

To confirm internalization of the polymer inside the zebrafish cryo-section, we had to ensure that residual polymer on the surface of the fish was not translocated into the slice during sectioning. Therefore a washing procedure was developed and evaluated by MSI by comparing the pre- ("dirty") and post-washing ("clean") whole fish. Three areas of the fish were analyzed including the tail, middle body, and head (see following spectra). The washing procedure was successful in removing the polymer from all three areas of the fish surface as evident by dramatic loss of polymer signal from the dirty to the clean fish. The washing procedure was performed quickly without long exposure to fresh water in order to minimize excretion of the semifluorinated polymer from inside the fish. One thing to note is that since the fish were mounted without sectioning, areas with significant variation in height (e.g. the fish head) experienced slight mass shift of the polymer.

"**Clean**" $mPEG_{1k}$-F13 fish water (10 mM); *m/z* = 1749.6, **4.0E^4**

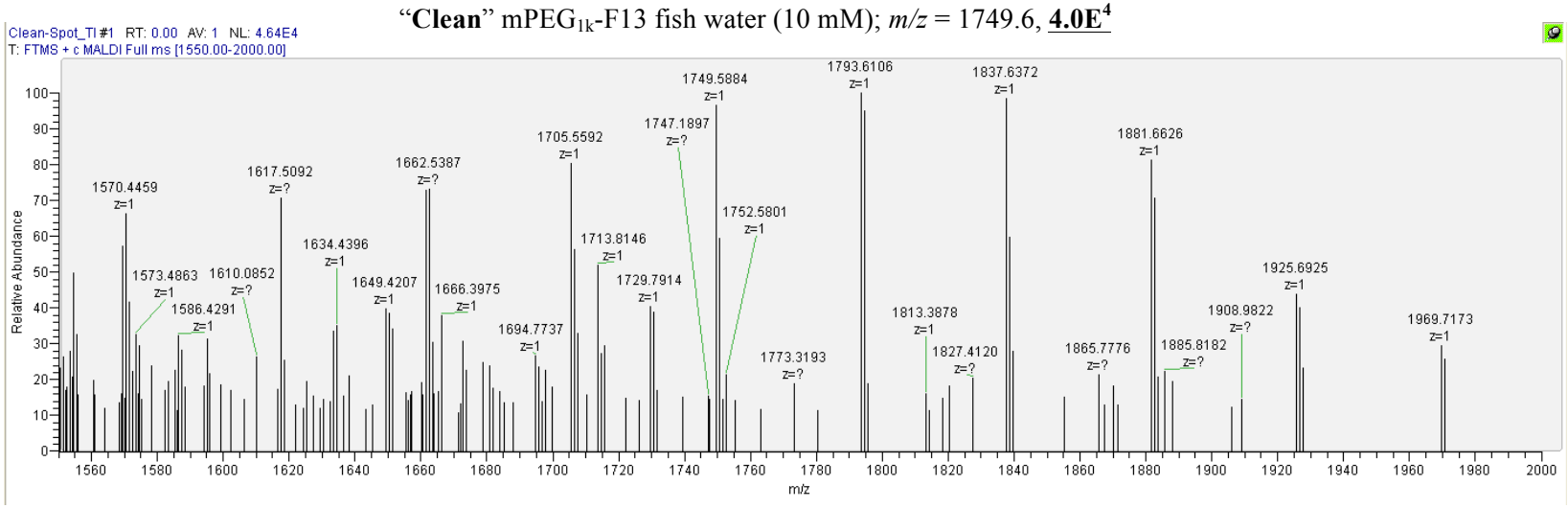

"**Dirty**" $mPEG_{1k}$-F13 fish water (10 mM); *m/z* = 1749.6, **1.0E^7**

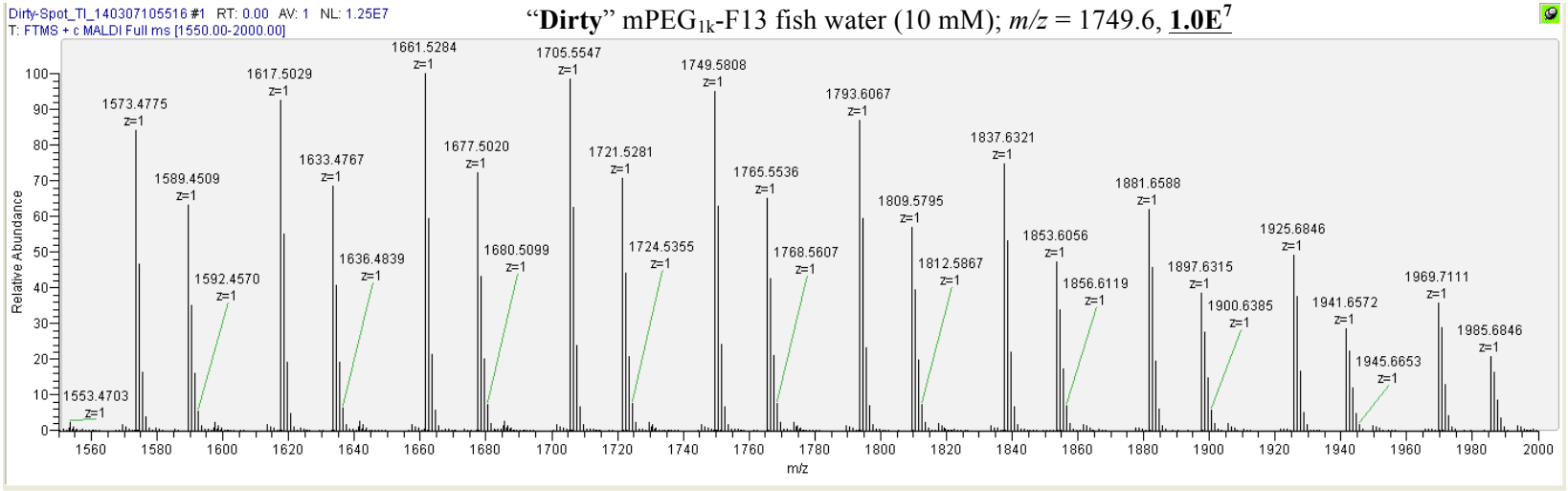

"**Clean**" $mPEG_{1k}$-F13 fish tail (10 mM)

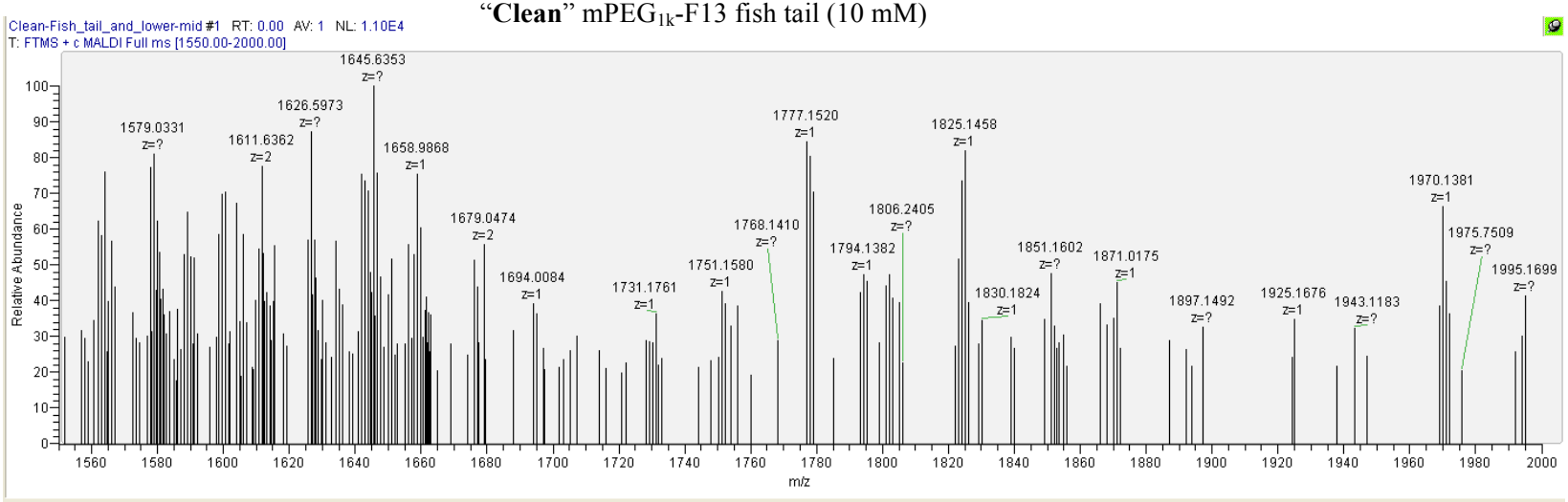

"**Dirty**" $mPEG_{1k}$-F13 fish tail (10 mM); *m/z* = 1749.6, **$\underline{4.0E^4}$**

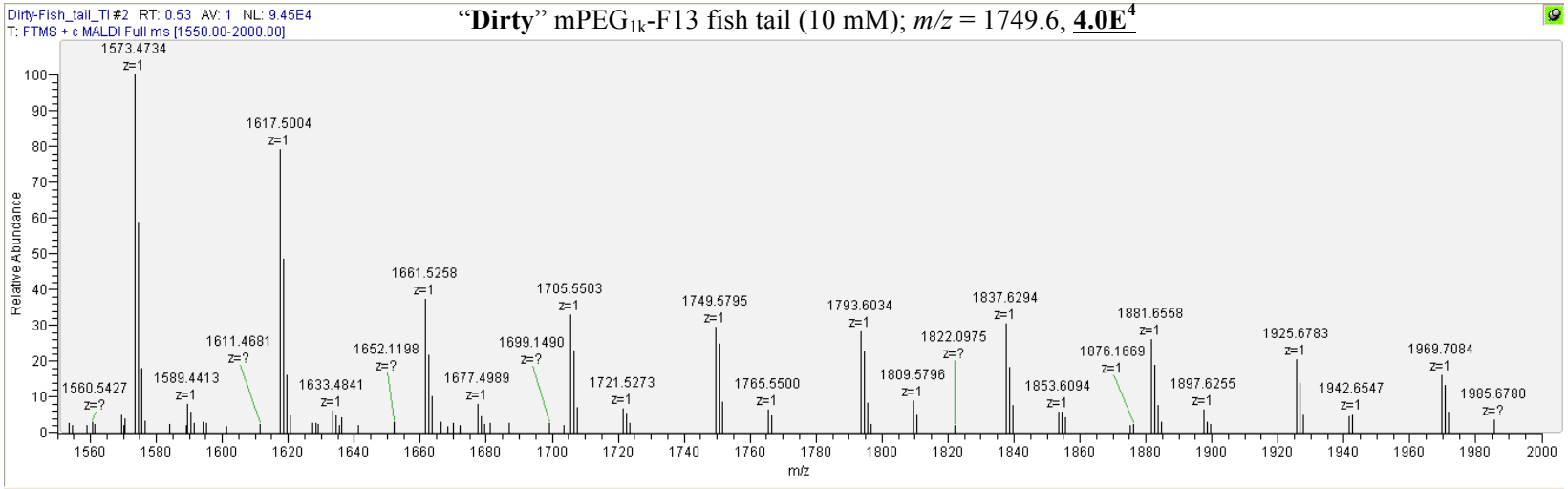

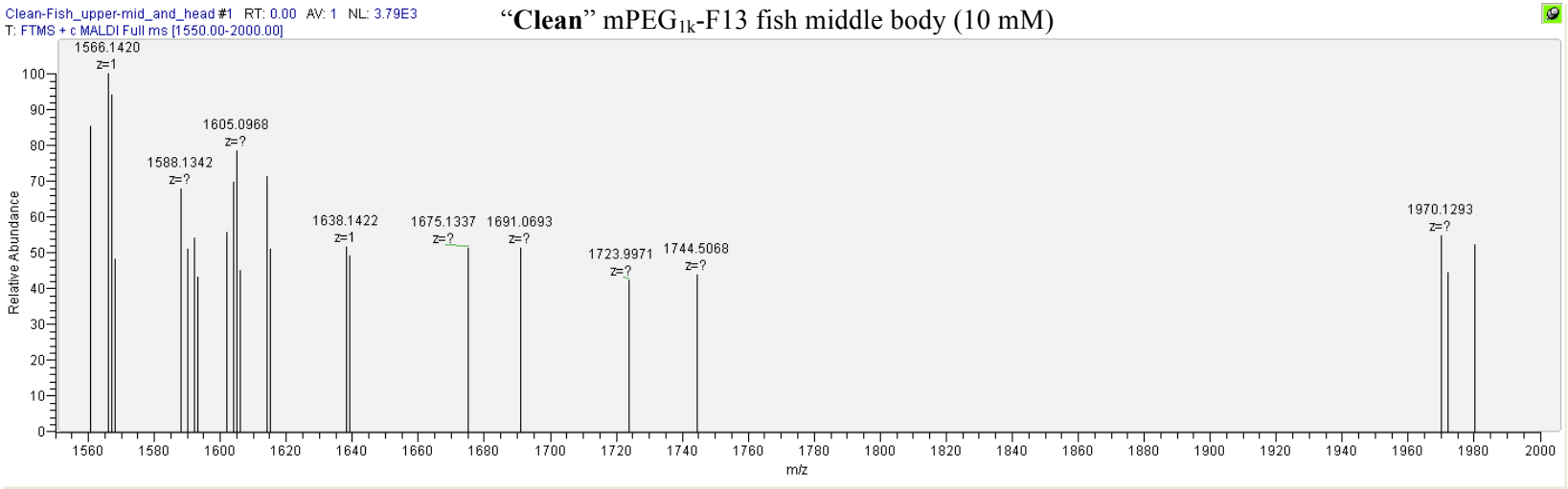
Clean-Fish_upper-mid_and_head #1 RT: 0.00 AV: 1 NL: 3.79E3
T: FTMS + c MALDI Full ms [1550.00-2000.00]
"Clean" mPEG1k-F13 fish middle body (10 mM)
1566.1420 z=1
1605.0968 z=?
1588.1342 z=?
1638.1422 z=1
1675.1337 z=?
1691.0693 z=?
1723.9971 z=?
1744.5068 z=?
1970.1293 z=?
Relative Abundance
m/z

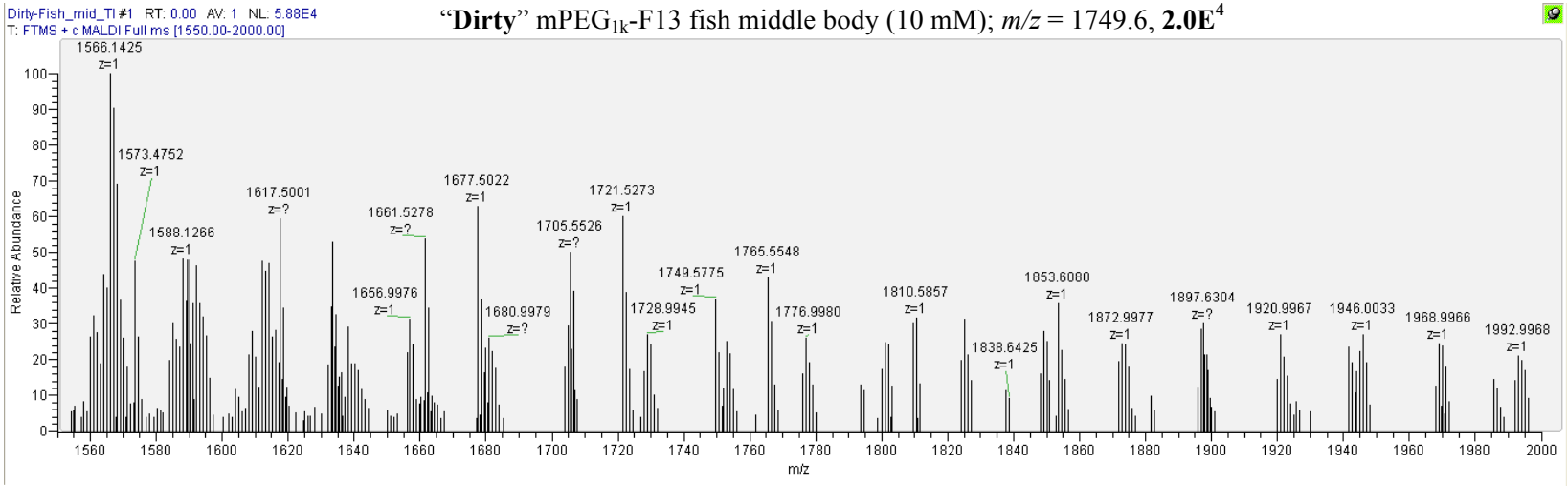
Dirty-Fish_mid_TI #1 RT: 0.00 AV: 1 NL: 5.88E4
T: FTMS + c MALDI Full ms [1550.00-2000.00]
"Dirty" mPEG1k-F13 fish middle body (10 mM); m/z = 1749.6, 2.0E4
1566.1425 z=1
1573.4752 z=1
1617.5001 z=?
1588.1266 z=1
1661.5278 z=?
1677.5022 z=1
1721.5273 z=1
1705.5526 z=?
1765.5548 z=1
1749.5775 z=1
1656.9976 z=1
1728.9945 z=1
1680.9979 z=?
1776.9980 z=1
1810.5857 z=1
1853.6080 z=1
1838.6425 z=1
1872.9977 z=1
1897.6304 z=?
1920.9967 z=1
1946.0033 z=1
1968.9966 z=1
1992.9968 z=1
Relative Abundance
m/z

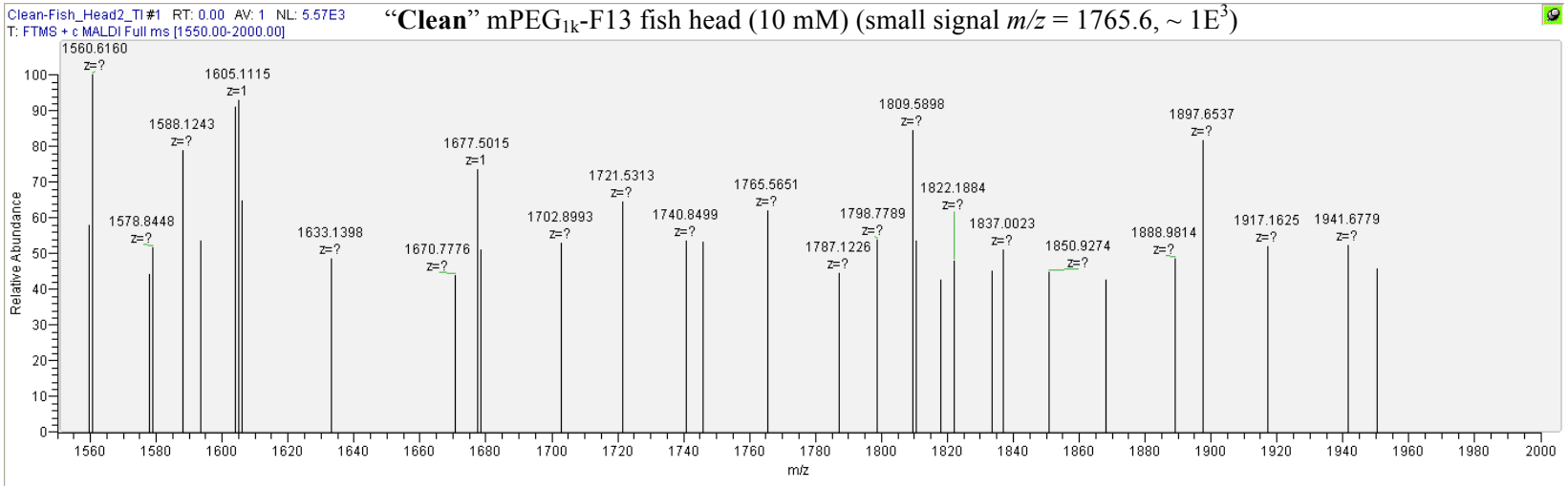
Clean-Fish_Head2_TI #1 RT: 0.00 AV: 1 NL: 5.57E3
T: FTMS + c MALDI Full ms [1550.00-2000.00]
"Clean" mPEG1k-F13 fish head (10 mM) (small signal m/z = 1765.6, ~ 1E3)
Relative Abundance
m/z
1560.6160 z=?
1605.1115 z=1
1588.1243 z=?
1677.5015 z=1
1809.5898 z=?
1897.6537 z=?
1721.5313 z=?
1765.5651 z=?
1822.1884 z=?
1578.8448 z=?
1633.1398 z=?
1670.7776 z=?
1702.8993 z=?
1740.8499 z=?
1798.7789 z=?
1837.0023 z=?
1917.1625 z=?
1941.6779 z=?
1787.1226 z=?
1850.9274 z=?
1888.9814 z=?

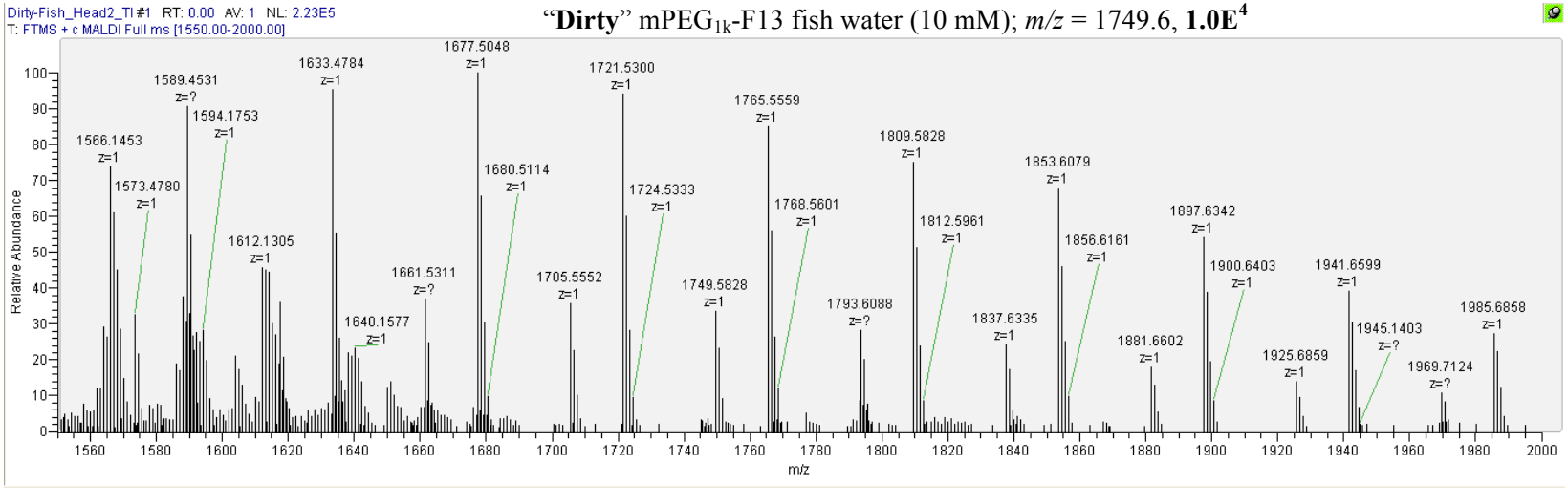
Dirty-Fish_Head2_TI #1 RT: 0.00 AV: 1 NL: 2.23E5
T: FTMS + c MALDI Full ms [1550.00-2000.00]
"Dirty" mPEG1k-F13 fish water (10 mM); m/z = 1749.6, 1.0E4
Relative Abundance
m/z
1677.5048 z=1
1633.4784 z=1
1589.4531 z=?
1721.5300 z=1
1765.5559 z=1
1809.5828 z=1
1853.6079 z=1
1594.1753 z=1
1566.1453 z=1
1680.5114 z=1
1724.5333 z=1
1768.5601 z=1
1812.5961 z=1
1897.6342 z=1
1573.4780 z=1
1612.1305 z=1
1856.6161 z=1
1900.6403 z=1
1941.6599 z=1
1661.5311 z=?
1705.5552 z=1
1749.5828 z=1
1793.6088 z=?
1837.6335 z=1
1985.6858 z=1
1640.1577 z=1
1881.6602 z=1
1945.1403 z=?
1925.6859 z=1
1969.7124 z=?

After a successful washing procedure was established the fish were then cryo-sectioned and analyzed via MSI. This preliminary imaging was done to attempt imaging with simple, routine cryo-sectioning parameters. Of the parameters attempted, the cryo-sectioned slices were the most intact when stabilized with gelatin, sectioned with a 20 μm slice thickness and cold-mounted onto the glass slide. The slices containing the whole body were mounted onto standard glass slides and images were averaged over areas of interest (head, eye, yolk sack, tail) and over the whole body. Only the yolk sack averaged image clearly identified the semifluorinated polymer at a very low intensity. All images showed a significant amount of polymer and large macromolecules that could not be readily identified (the origin of which could be from a multitude of sources, e.g. plastic in the petri-dish, mounting gel, endogenous amphiphilic phospholipids, etc.).

Image of $mPEG_{1k}$-F13 fish cryo-sections mounted onto glass slides

Image of zebrafish larvae (Adapted from reference)[7]

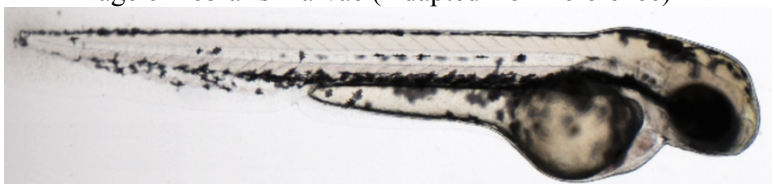

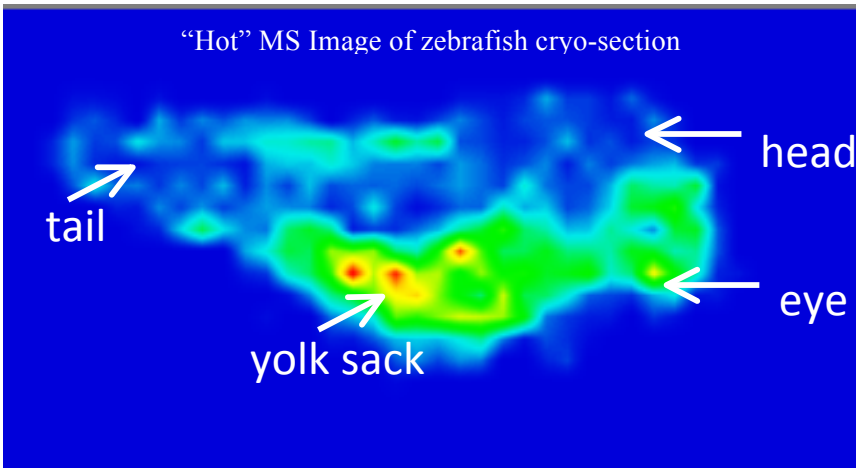

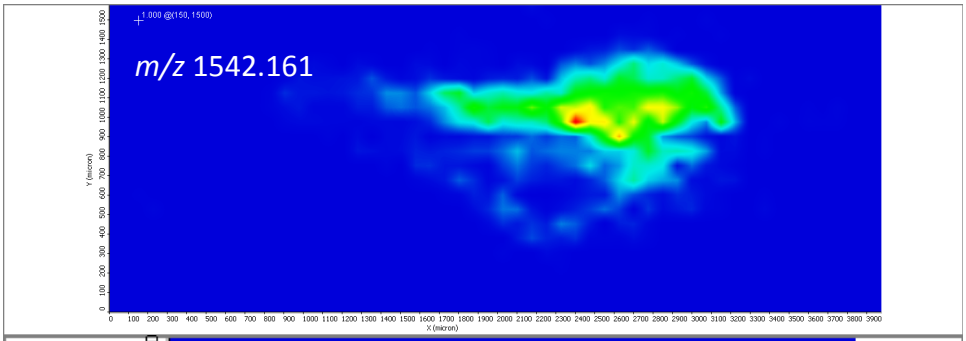

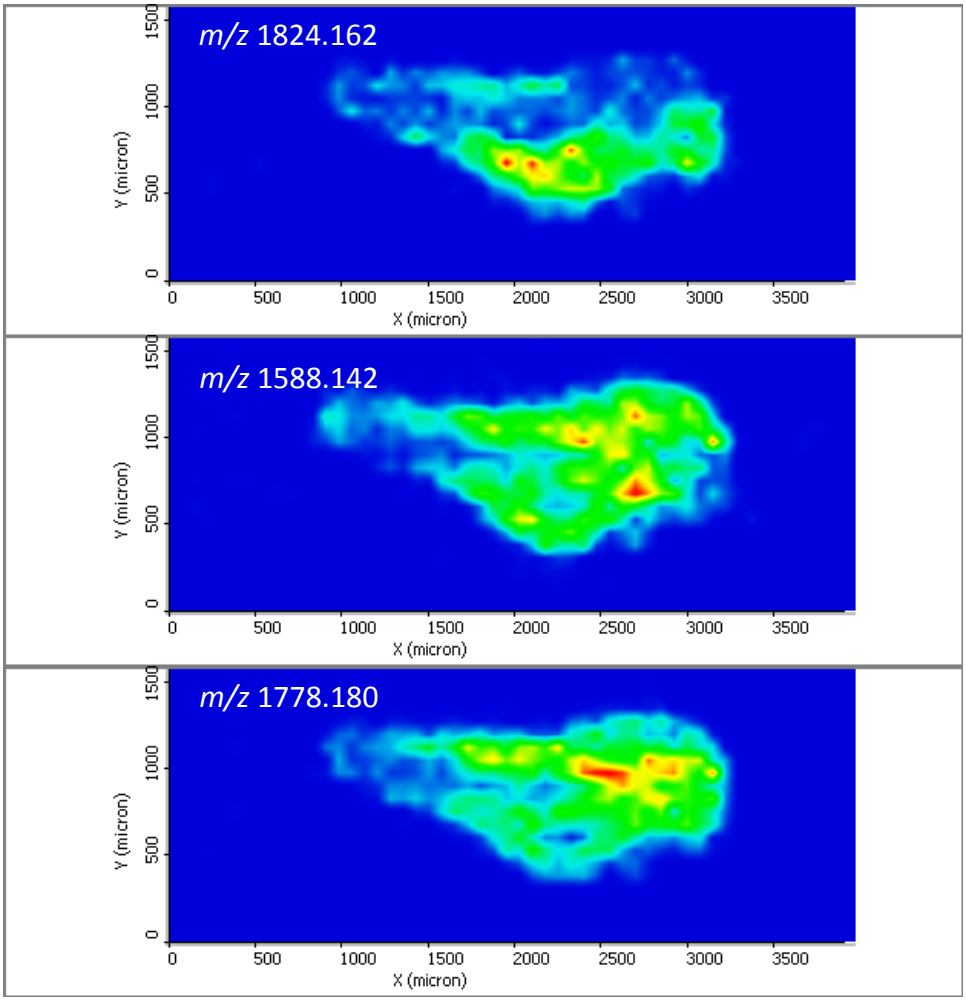
m/z 1824.162
m/z 1588.142
m/z 1778.180
Y (micron)
X (micron)
0
500
1000
1500
2000
2500
3000
3500

Average spectra of fish head (boxed region in image)

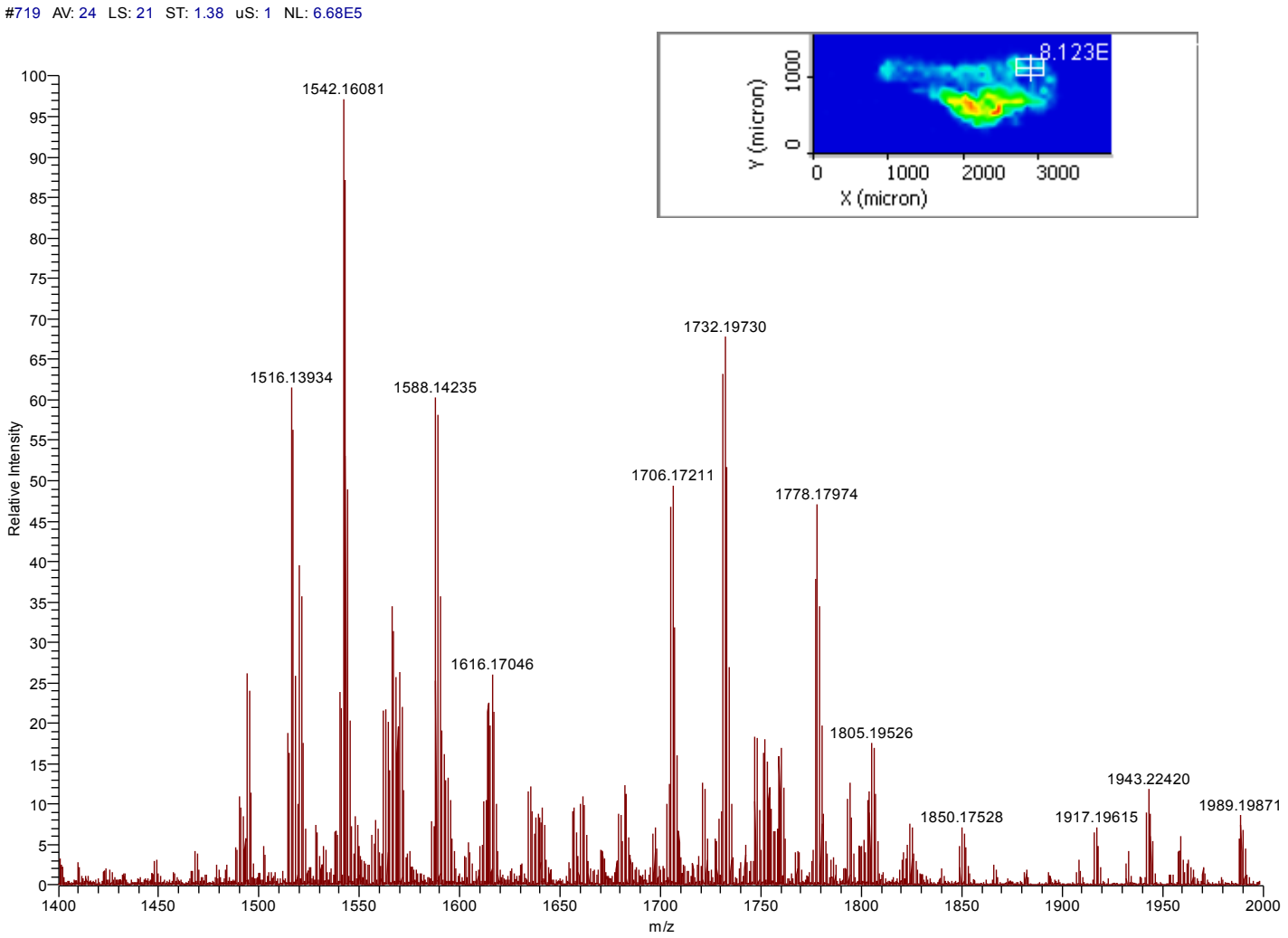

Average spectra of fish eye boxed region in image)

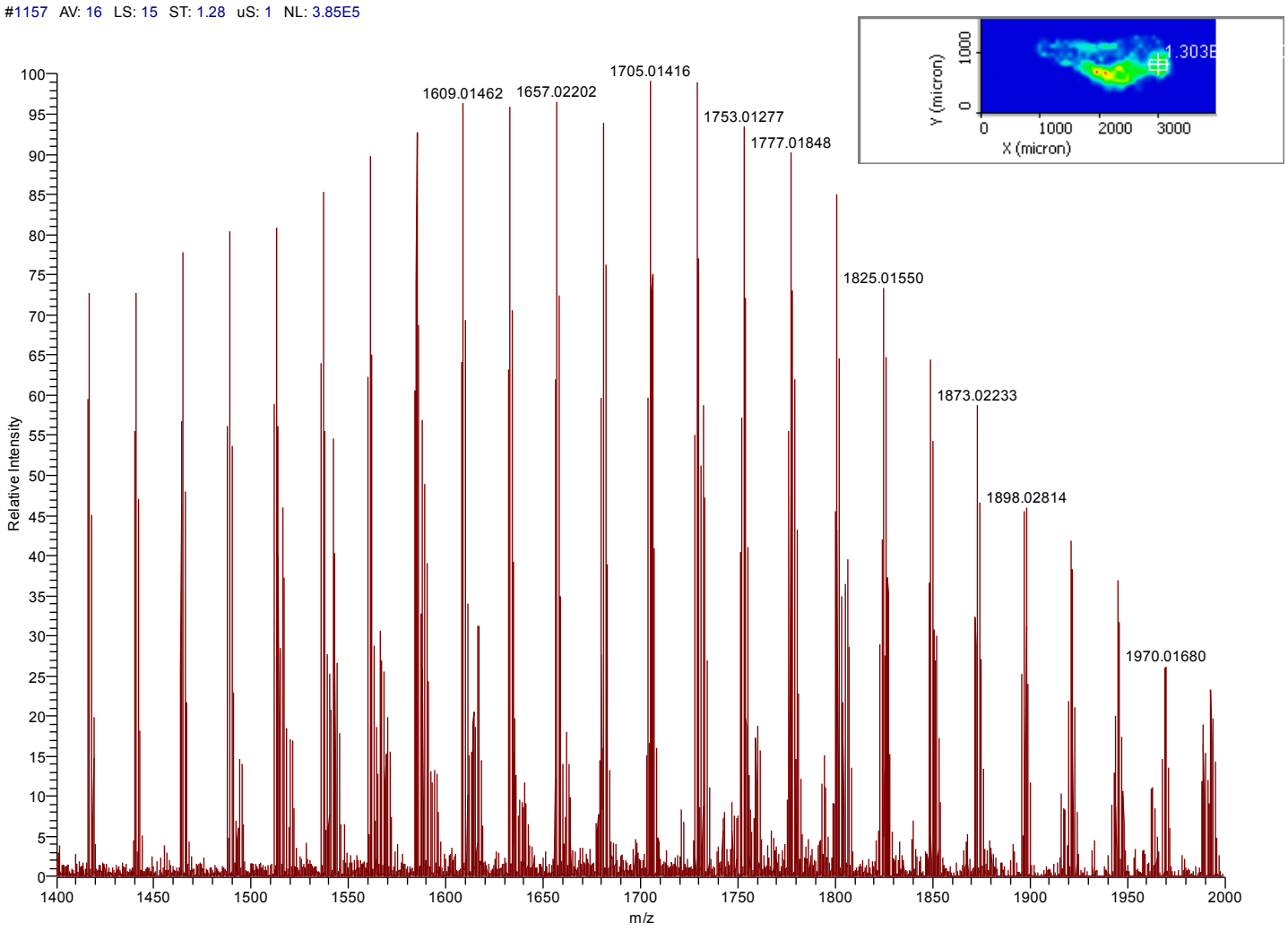

Average spectra of fish yolk sack (boxed region in image): polymer visible at arrow

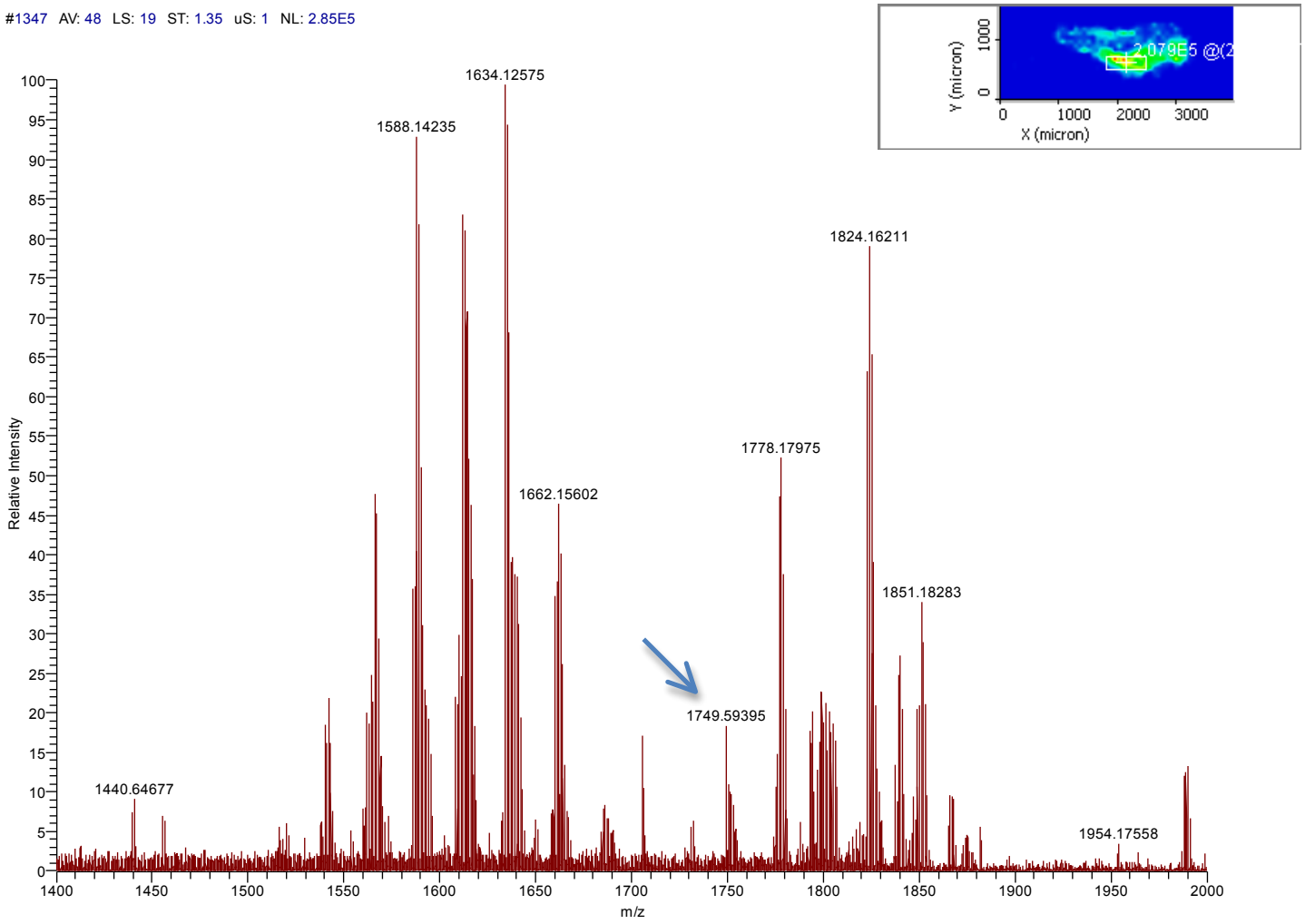

Average spectra of fish tail (boxed region in image)

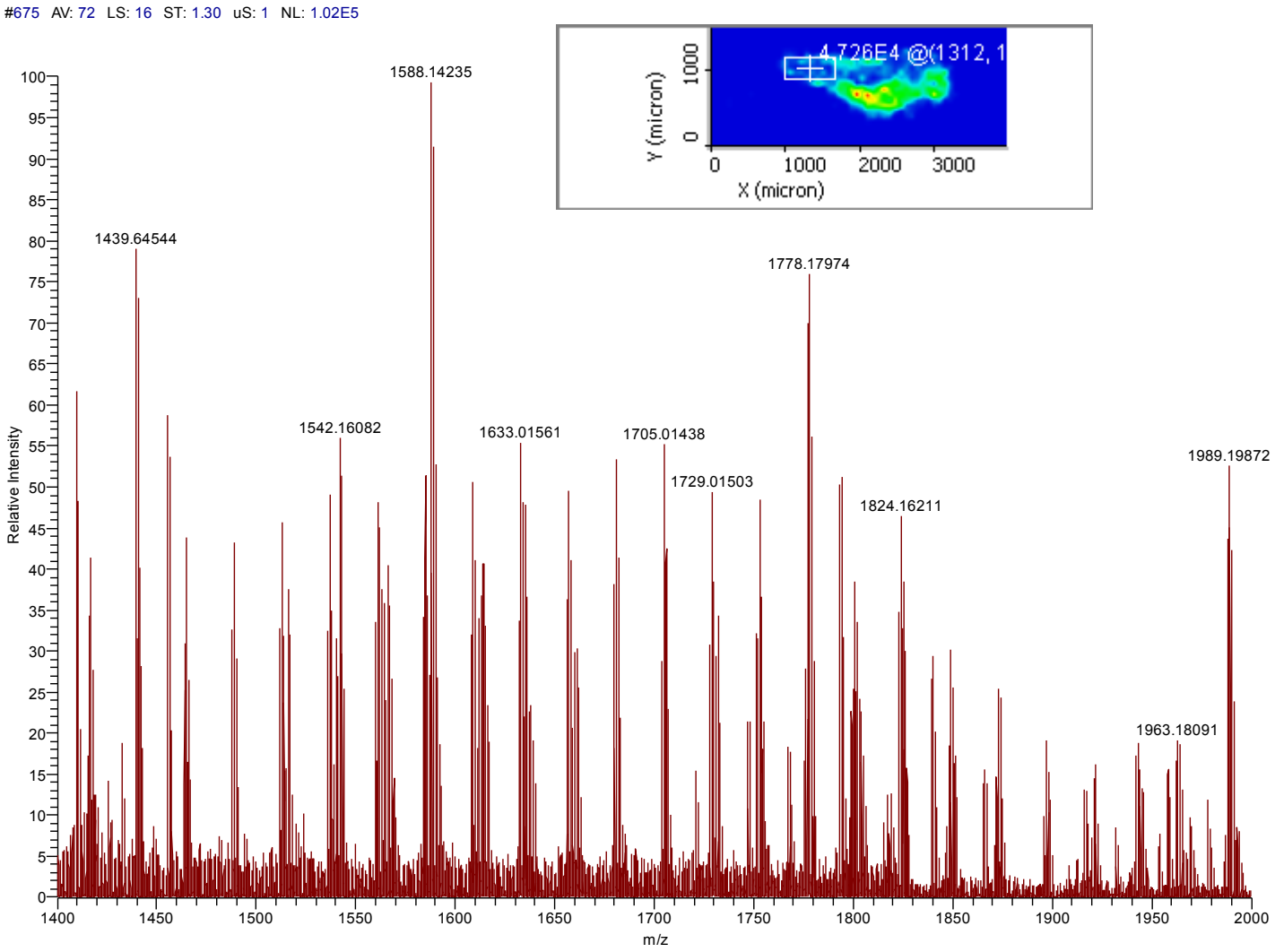

Average spectra of fish whole body (boxed region in image)

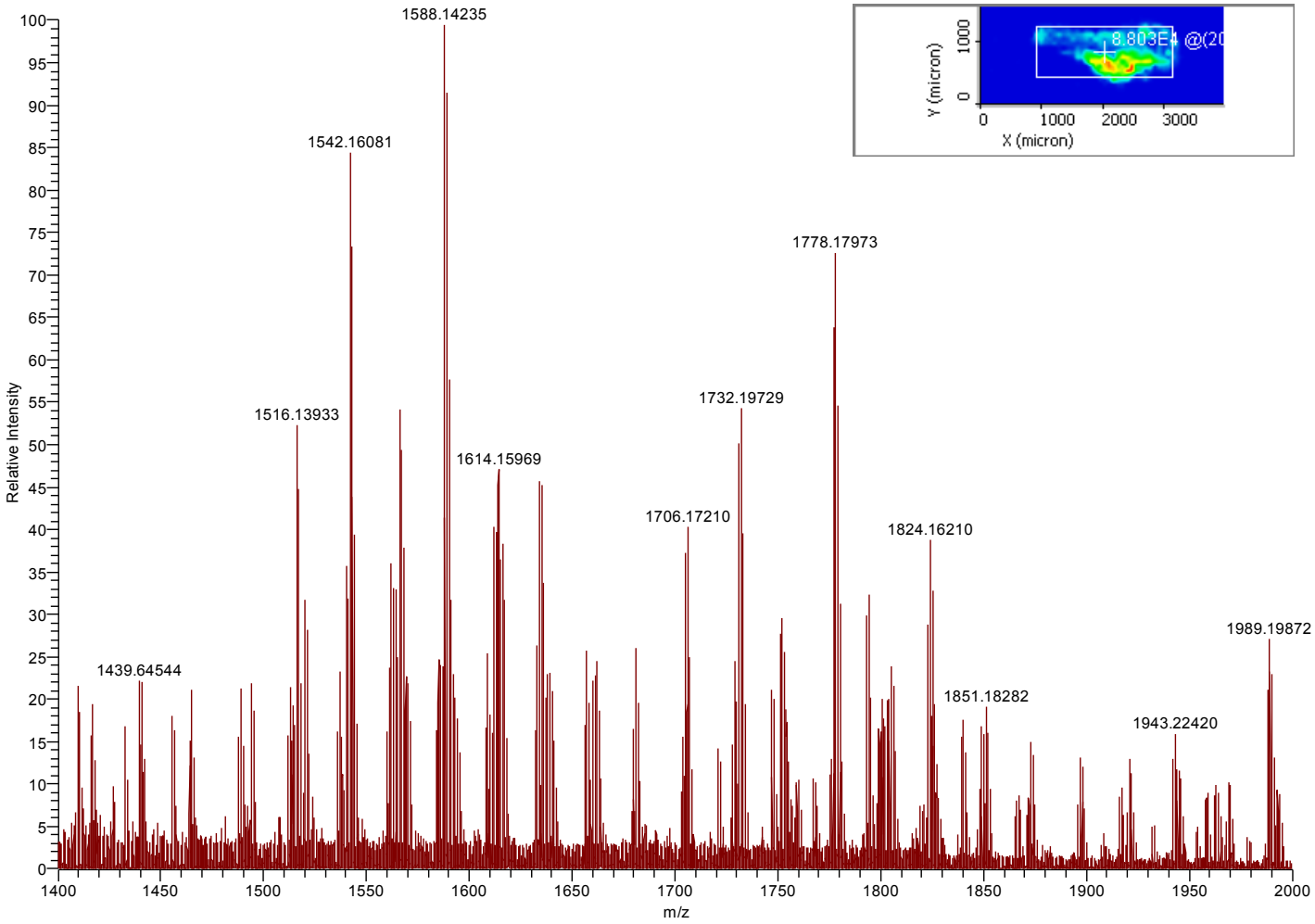

To identify the background spectra without exposure to semifluroinated compounds, an unexposed fish ("control") was also analyzed alongside an exposed fish (see following spectra). The very apparent similarity between the "exposed" and the "control" fish clearly show that this analysis was not successful in visualizing the polymer in the cryo-section slices.

S2.3 Conclusion

The reasons for the absence of the semifluroninated polymer are numerous. Firstly the parameters may not be optimized and the polymer signals may be masked or suppressed. Alterations to the embedding media and matrix may be needed as described by the recent paper by Hemmer *et al*. (5% carboxymethyl cellulose and 10% gelatin for the embedding medium and the addition of ammonium phosphate monobasic (AmP) to the CHCA matrix spray may enhance whole body zebrafish MALDI-MSI (although this was not optimized for larvae-stage fish))[4]. The lack of polymer signal may also be due to the washing procedure, which could potentially encourage excretion of the polymer. Alternatively, the exchange into and out of the fish may be rapid, or the polymer may be rapidly excreted during euthanasia. In order to circumnavigate these issues an alternative approach may be warranted. Due to the transparency of the zebrafish larvae it is feasible to covalently conjugate a fluorescent label to the polymer structure and visualize the internalization of the polymer via fluorescence imaging in real-time. For these reasons the MALDI-MSI experiments have been disbanded for the time being.

"**Exposed fish**" Average spectra of fish whole body

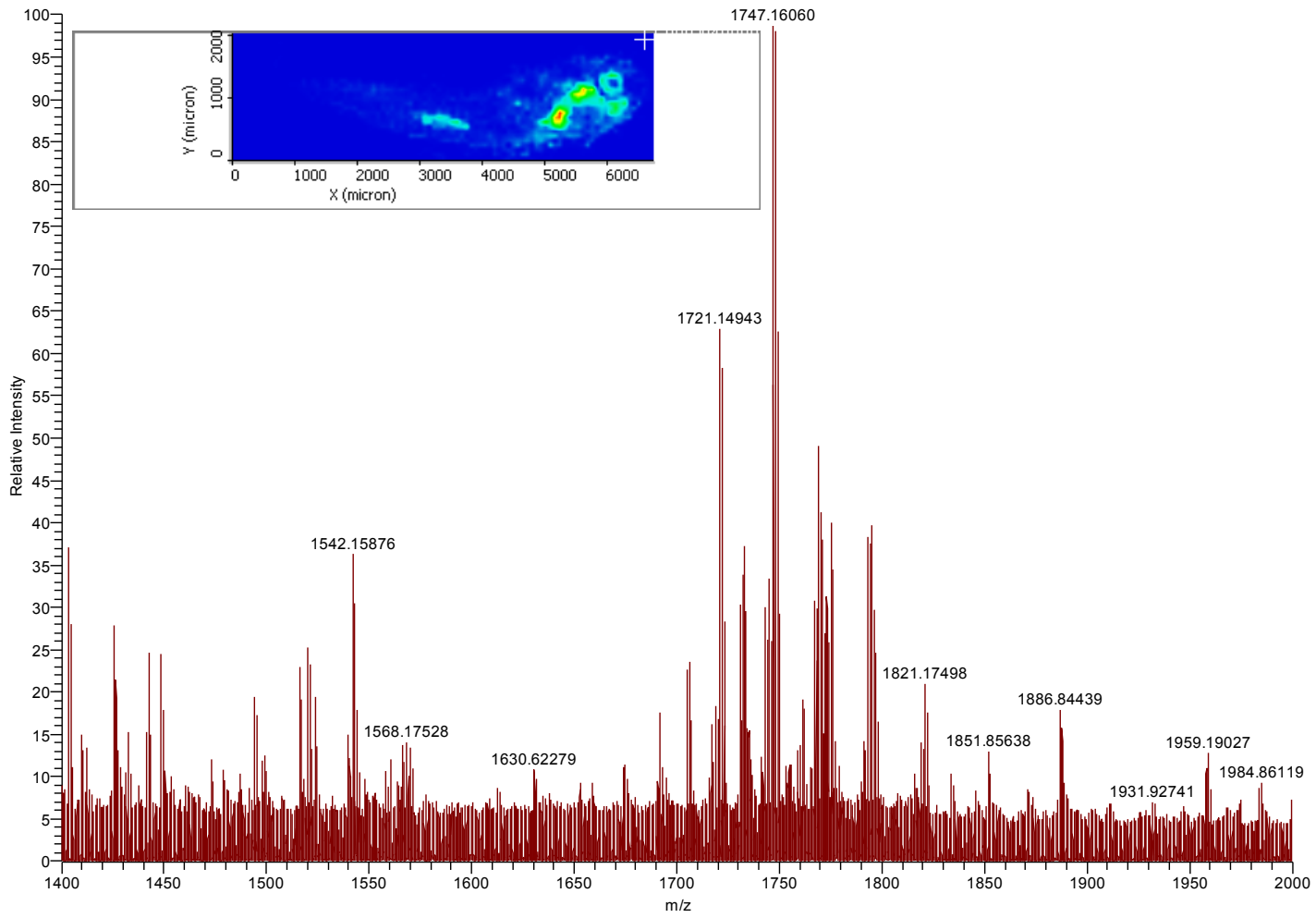

"**Unexposed (control) fish**" Average spectra of fish whole body

#357 AV: 4466 LS: 9 ST: 1.17 uS: 1 NL: 1.28E5

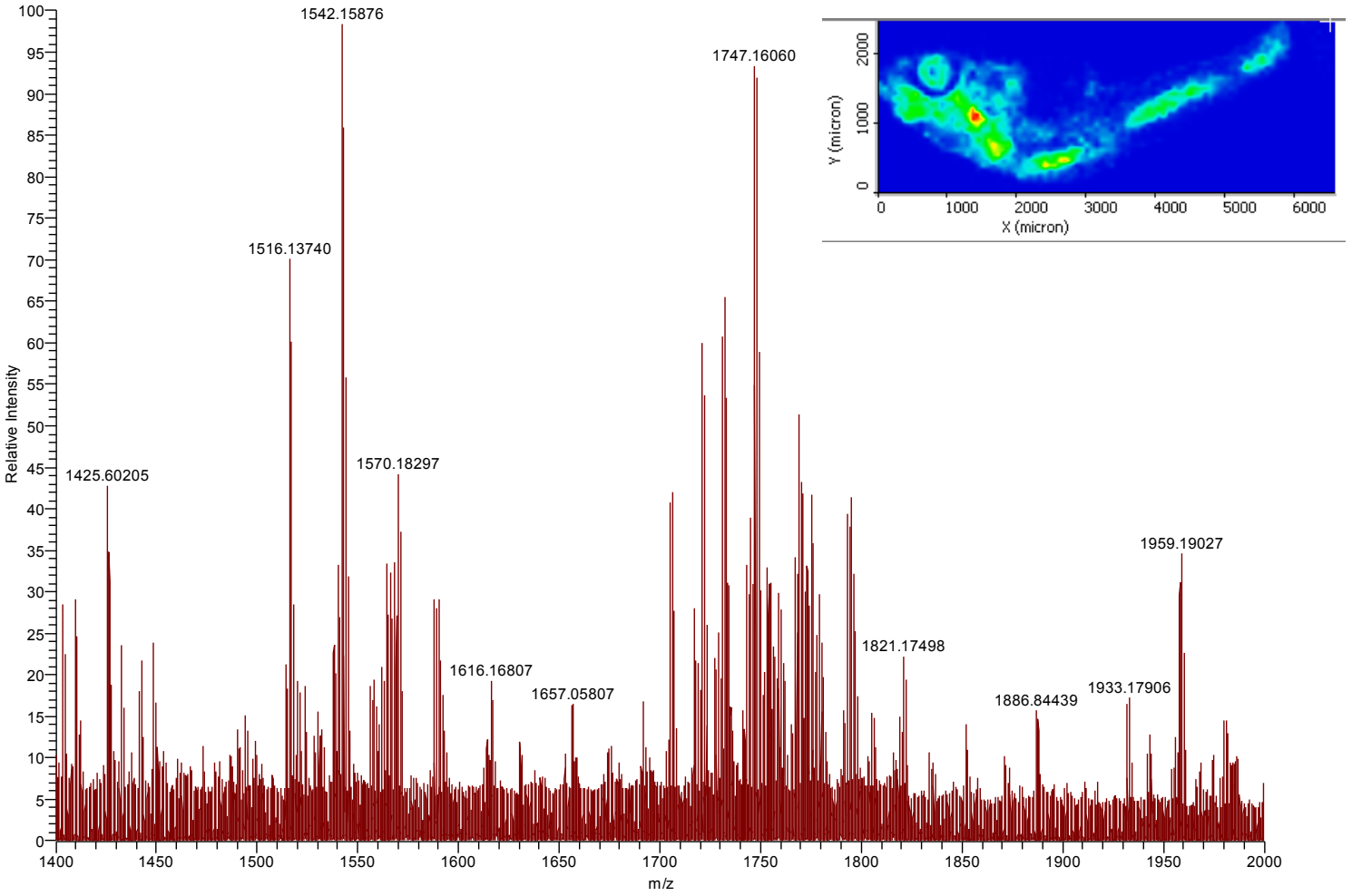

MALDI MS of the mounting glue

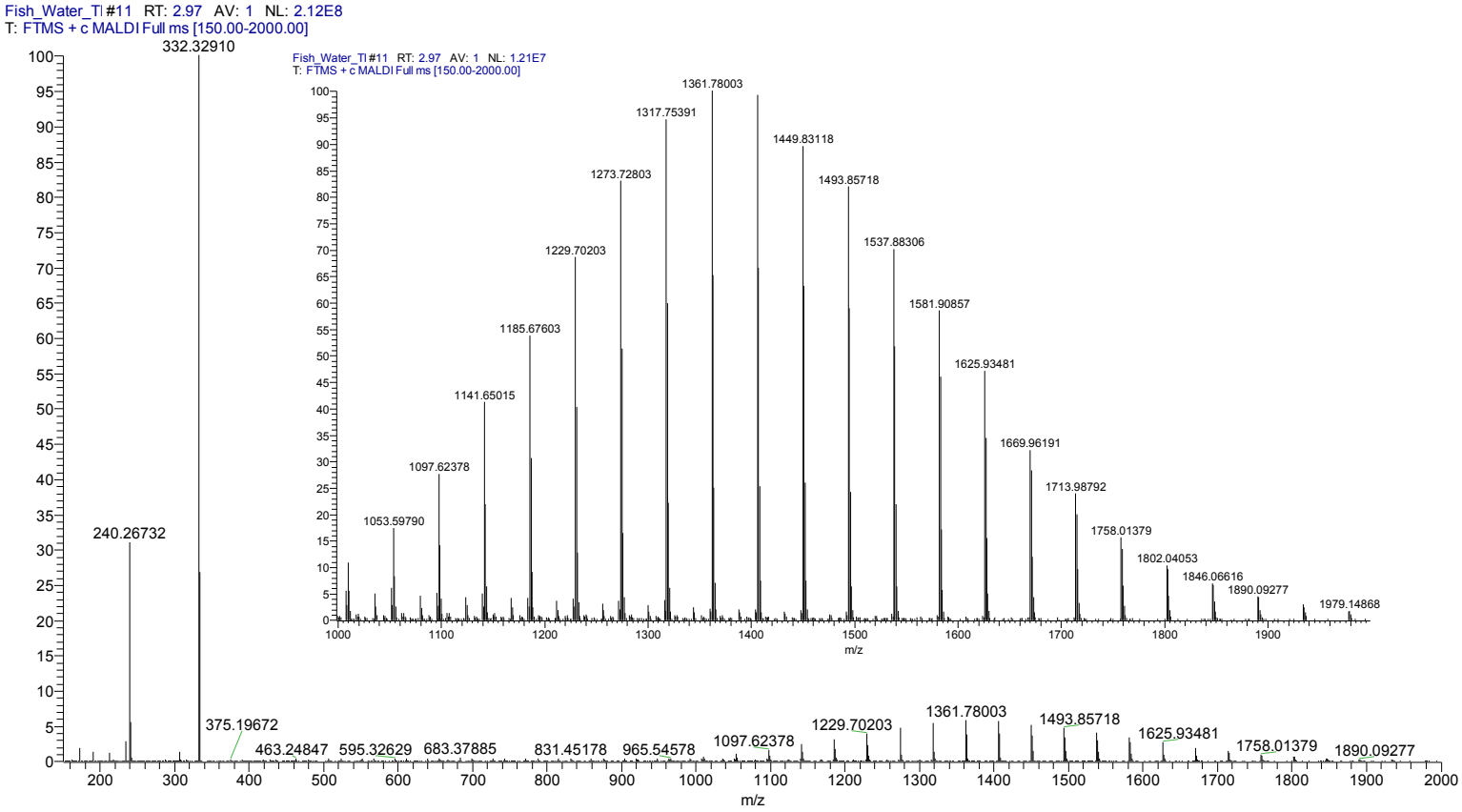

MALDI MS of the CHCA matrix

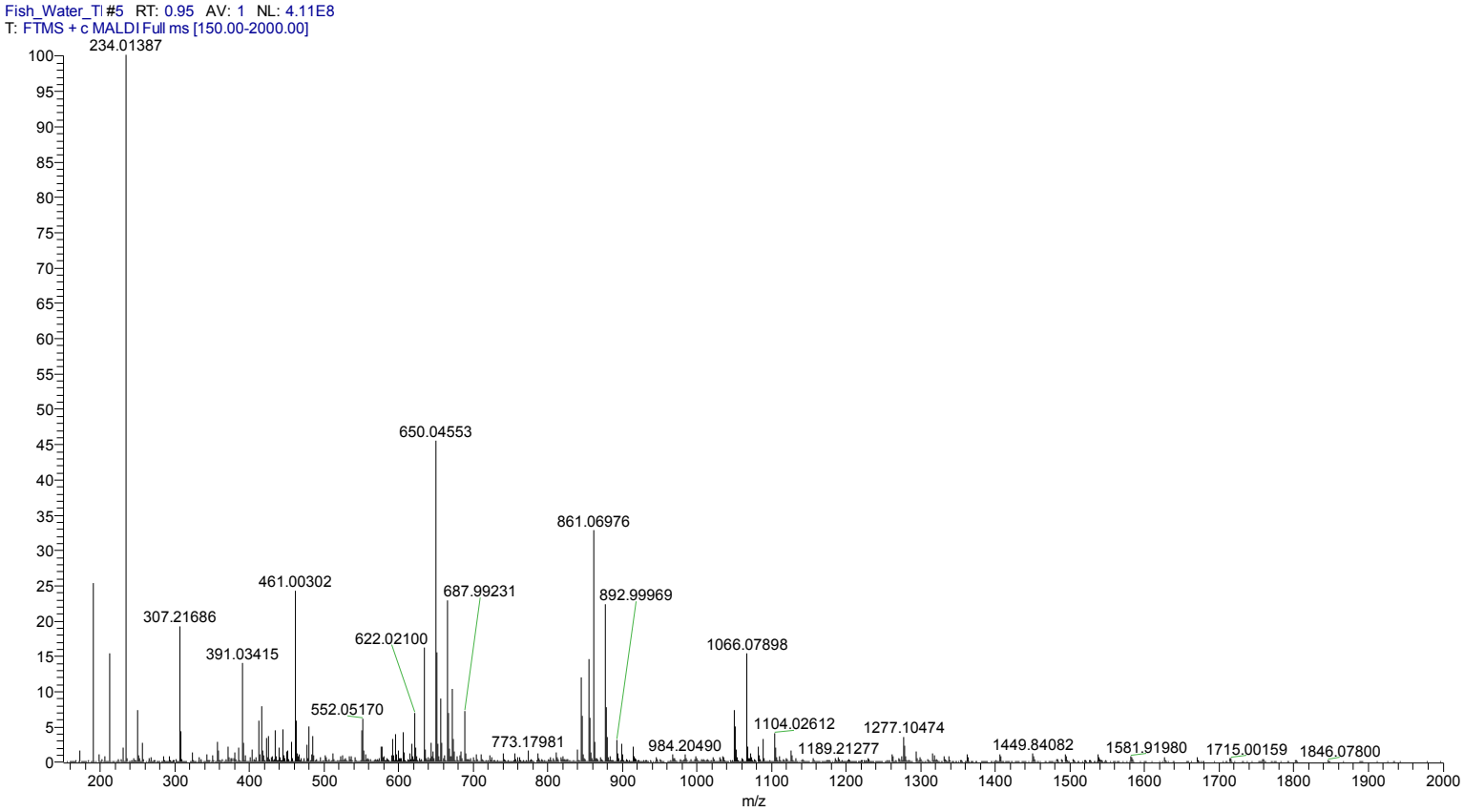

S2.4 Experimental

S2.4.1 Micelle solution preparation

$mPEG_{1k}$-F13 polymer micelle solutions were prepared at a concentration of 0.1 mg/mL by direct dilution in 30/70 water/ACN. Subsequent concentrations were prepared as serial dilutions from this stock concentration. Aliquots (0.5 μL) of each polymer solution were then individually spotted onto the MALDI plate mixed along with (0.5 μL) matrix, CHCA (10 mg/mL in 30/70 water/ACN 0.1% FA). 2,5-Dihydroxybenzoic acid (150 mg/mL in 50/50 water/ACN 0.1 % FA) was also used but found to be less effective).

S2.4.2 Zebrafish exposure and washing

Fertilized eggs were obtained from adult AB strain zebrafish (*Danio rerio*) and bred as described by Westerfield *et al.*[6] Embryos from adult AB strain zebrafish were collected shortly after spawning and placed in embryonic water. Approximately 30 embryos were assigned to each exposure concentration and placed in small petri dishes. Excess embryonic water was removed. The embryos were washed twice with a small aliquot of exposure solution before being fully submerged in fresh exposure solution (to prevent dilution of the exposure solution with embryonic water).

Zebrafish embryos were exposed to 1 mM micelle solutions of $mPEG_{1k}$-F13 prepared in embryonic water (0.6 g/L Instant Ocean aquarium salt and 0.01 mg/L methylene blue in distilled water) and buffered with 10 mM 3-(*N*-morpholino)propanesulfonic acid (MOPS). (The solutions were filtered with a 0.45 μm filter and a control solution was prepared using embryonic water and 10 mM MOPS buffer). The pH of all solutions was adjusted to be within ± 0.1 of embryonic water (7.12) using 1.0 M NaOH. Embryo exposure was completed within 2.5 h post fertilization (hpf) and embryos were inspected using a stereomicroscope. Fertilized and undamaged embryos were transferred to 24-well plates containing 2 mL of exposure solution per well (one embryo per

well, one plate per test solution, two plates of controls, and each performed in triplicate). The 24-well plates were kept in an incubation chamber at 28.5 °C and subjected to a 14/10 hour light/dark cycles. A trial was considered valid if ≥ 85% controls survived and did not show developmental abnormalities.

For MALDI-MSI purposes the embryos were monitored 46 hpf and then sacrificed with Tricane mesylate (Sigma Aldrich). The "dirty fish" were extracted directly from the well with a pipet and placed into an eppendorf tube. The "clean fish" were extracted out of the well with a pipet and put into a petri-dish with fresh egg water for 5 seconds and quickly removed and this was repeated two more times with fresh petri-dishes with fresh egg water. The fish was then put onto a Kim wipe to absorb the surface water and then put into an eppendorf tube. The excess liquid was removed from the tube.

To mount the whole fish onto the glass microscope slide, an ImmEdge hydrophobic barrier pen (Vector Labs) was used to outline and separate the fish. An aliquot (1 µL) of the water in the fish eppendorf tubes was also spotted onto the slide. The CHCA matrix was then applied to the glass slide with a TM Sprayer (HTX Technologies, LLC, Carrboro, NC, USA).

S2.4.3 Zebrafish cryo-sectioning

Fish were sacrificed and washed according to the previously described methods. The individual fish were embedded in gelatin (100 mg/mL in double-distilled water) and gently frozen on dry ice (cryo-sectioning was also attempted in ice; however, gelatin provided much better sections). After equilibrating in the chamber for several minutes, each frozen fish was placed on its side and was then sliced into approximately 16 coronal cross-sections of 12-µm or 20-µm thickness using a cryostat at –20°C. (Under the microscope the thicker sections appear much more intact). The sections were then mounted onto a standard glass microscope slide using either thaw or cold mounting methods (cold mounting appeared to give the best results). Matrix (10

mg/mL CHCA in 30/70 water/ACN) was applied using a TM Sprayer (HTX Technologies, LLC, Carrboro, NC, USA). CHCA was purchased from Sigma Aldrich (St. Louis, MO, USA).

S2.4.4 MALDI-Orbitrap MS and MSI

A MALDI-Orbitrap LTQ mass spectrometer (Thermo Scientific, Waltham, MA, USA) that was equipped with an N2 laser (spot diameter of 75 μm) was used in positive ion mode for spot analysis and imaging. For micelles solutions, a mass range of *m/z* 1550-2000, 30,000 resolution, and laser energy of 8.4 μJ was used. For the washed, whole fish, a mass range of *m/z* 1550-2000, 30,000 resolution, and laser energy of 8.8 μJ was used. For cryo-slices, multiple layers of the fish were imaged using a mass range of *m/z* 1550–2000, a mass resolution of 30,000, laser energy of 8.8 μJ, and a mass error of ≤ 5 ppm. The tissue region to be imaged and the raster step size were controlled using the LTQ Tune software (Thermo Scientific, Waltham, MA, USA). The instrument methods were created using Xcalibur (Thermo Scientific, Waltham, MA, USA). To generate images, the spectra were collected at 75 μm intervals in both the x and y dimensions across the surface of the sample. The manual interpretation of the averaged mass spectrum was performed using ImageQuest (Thermo Scientific, Waltham, MA, USA).

S2.5 Acknowledgements

Thank you to Erin Gemperline for all her expertise in sample preparation and imaging and her helpful discussions. Also thank you to Dr. Warren Heideman for the use of his facilities and materials and to Joseph Gawdzik and Samantha Fix, for their work with zebrafish handling and polymer exposure experiments.

S2.6 References

(1) Yang, L. L.; Wang, G. Q.; Yang, L. M.; Huang, Z. B.; Zhang, W. Q.; Yu, L. Z. Endotoxin Molecule Lipopolysaccharide-Induced Zebrafish Inflammation Model: A Novel Screening Method for Anti-Inflammatory Drugs. *Molecules* **2014**, *19* (2), 2390–2409.

(2) Rawson, D. M.; Zhang, T.; Kalicharan, D.; Jongebloed, W. L. Field Emission Scanning Electron Microscopy and Transmission Electron Microscopy Studies of the Chorion , Plasma Membrane and Syncytial Layers of the Gastrula-Stage Embryo of the Zebra ® Sh Brachydanio Rerio : A Consideration of the Structural and Functio. *Aquac. Res.* **2000**, 325–336.

(3) Goodwin, R. J. a. Sample Preparation for Mass Spectrometry Imaging: Small Mistakes Can Lead to Big Consequences. *J. Proteomics* **2012**, *75* (16), 4893–4911.

(4) Nelson, K. a.; Daniels, G. J.; Fournie, J. W.; Hemmer, M. J. Optimization of Whole-Body Zebrafish Sectioning Methods for Mass Spectrometry Imaging. *J. Biomol. Tech.* **2013**, *24*, 119–127.

(5) Khatib-shahidi, S.; Andersson, M.; Herman, J. L.; Gillespie, T. a; Caprioli, R. M. Direct Molecular Analysis of Whole-Body Animal Tissue Sections by Imaging MALDI Mass Spectrometry Direct Molecular Analysis of Whole-Body Animal Tissue Sections by Imaging MALDI Mass Spectrometry. *Anal. Chem.* **2006**, *78* (18), 6448–6456.

(6) Westerfield, M. The Zebrafish Book a Guide for the Laboratory Use of Zebrafish (Danio Rerio)., 2000.

(7) Brooks, S. S.; Wall, a. L.; Golzio, C.; Reid, D. W.; Kondyles, a.; Willer, J. R.; Botti, C.; Nicchitta, C. V.; Katsanis, N.; Davis, E. E. A Novel Ribosomopathy Caused by Dysfunction of RPL10 Disrupts Neurodevelopment and Causes X-Linked Microcephaly in Humans. *Genetics* **2014**, *198* (2), 723–733.

Appendix 3:

Mixed Micelles formed by a

binary fluorinated surfactant system

S3.1 Motivation and intent

Advantageous properties, such as enhanced stability, can be achieved by the installation of a fluorous domain in polymeric self-assemblies. In Chapter 3 of this thesis the benefits of a triphilic polymer design have been thoroughly described, including high drug loading and retention and kinetic stability *in vivo* via inhibition of serum protein binding. These desirable properties were derived from the novel configuration and orientation of the fluorous moiety, which was covalently conjugated to afford the triphilic polymeric structure via strategic synthetic manipulation. Rather than synthesize a new triphilic polymer to meet the needs and specifications of each diverse application, an alternative approach was explored, which would use a two-component surfactant system. The binary system would utilize a consistent hydrocarbon–fluorocarbon to maintain the advantageous properties developed for the triphilic systems, while the hydrophilic-hydrocarbon or hydrophilic-fluorocarbon component could be altered to attain complementary and diverse beneficial properties (and which also could allow for the use of at least one cheap and commercially available surfactant).

Mixed surfactant systems have been studied in the literature over the past several decades mainly for the development of emulsion and vesicle formulations. Several studies by Riess *et al.*[1] and Krafft *et al.*[2] have demonstrated that 1:1 mixtures of a traditional phospholipid and a hydrocarbon–fluorocarbon were able to form small, stable vesicles (22 nm in diameter) with a mixed bilayer membrane. These mixed vesicles were favored over non-mixed aggregates as evidenced by the absence of phospholipid-coated hydrocarbon–fluorocarbon emulsion droplets. In the mixed vesicles, the fluorinated segments assembled in a continuous layer in the center of the vesicle bilayer (see figure below) and the vesicles showed enhanced stability in comparison to the non-fluorinated analogs.

Representation of the fluorous bilayer formed by mixed vesicles

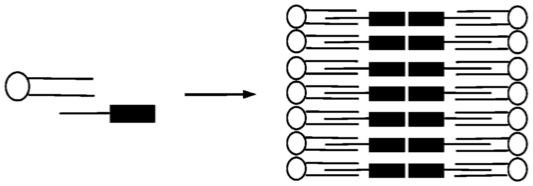

Mixed vesicles are formed by mixing a hydrogenated phospholipid (PL) and a semifluorinated alkane (FnHm). Adapted from Reference 2.

In this study, instead of a fluorous bilayer, a fluorous intermediate shell was envisioned, which would not only stabilize the mixed micelle system, but would also deter and thereby control the release of encapsulated hydrophobic material from the mixed micelle.[3] In this system a PEG-fluorocarbon ($mPEG_{1k}$-F13, due to its extensive characterization in our lab) and a hydrocarbon–fluorocarbon were used. For simplicity, preliminary studies were performed with 1-(perfluorodecyl)octane, F10H8, due to its commercial availability and relatively low cost. The F10H8 surfactant also has a significant fluorous segment and hydrophobic segment, so it has potential to form mixed micelles with $mPEG_{1k}$-F13 in an aqueous environment. The following outlines the results from this preliminary study using the dual fluorinated surfactant system. Various preparation techniques were attempted and analyzed by either DLS or NMR to confirm the formation of mixed micelles.

S3.2 Results and Discussion

S3.2.1 Mixed micelle characterization: DLS method

Single-component micelles were prepared for comparison and exhibited the anticipated behavior with $mPEG_{1k}$-F13 forming discrete micelles approximately 12 nm in size and F10H8 showing random aggregates arising from its significant immiscibility in water (see the following DLS measurements using spherical fits.

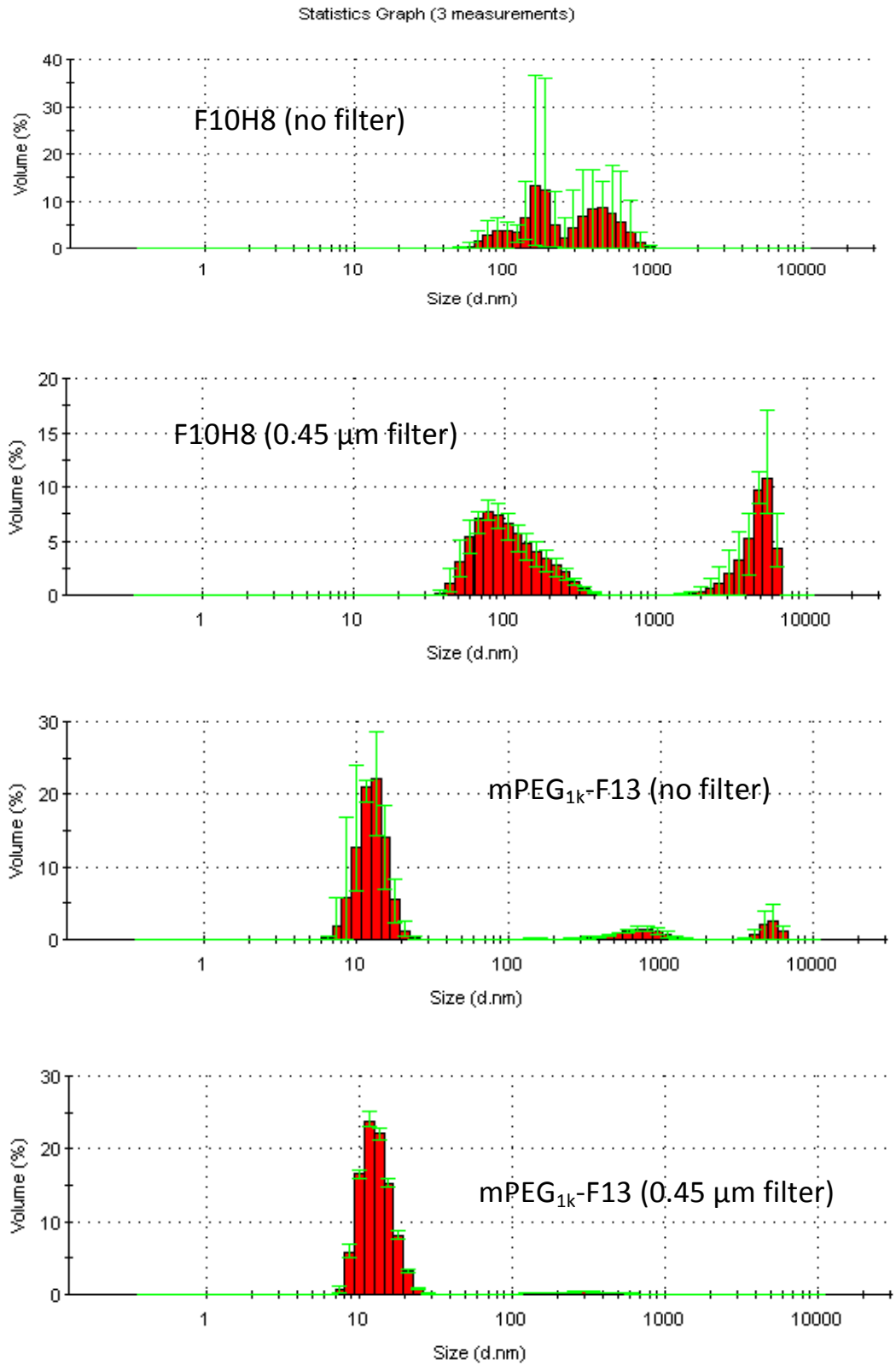
Statistics Graph (3 measurements)
F10H8 (no filter)
Volume (%)
Size (d.nm)
F10H8 (0.45 µm filter)
Volume (%)
Size (d.nm)
mPEG1k-F13 (no filter)
Volume (%)
Size (d.nm)
mPEG1k-F13 (0.45 µm filter)
Volume (%)
Size (d.nm)

The mixed samples unfortunately did not show any clear indication of the formation of mixed micelles (DLS depicted below). Both "solution" and "solid" methods (described in the experimental section) gave similar results. The particle size distribution of these samples mainly reflected the same characteristics (narrow size distribution with an average diameter of 12 nm) as the $mPEG_{1k}$-F13 single-component micelles. With the addition of F10H8 in the "excess" sample a trailing of particles that were significantly larger size were present, which resemble mainly the immiscible, dispersed droplets present in the F8H10 single-component system.

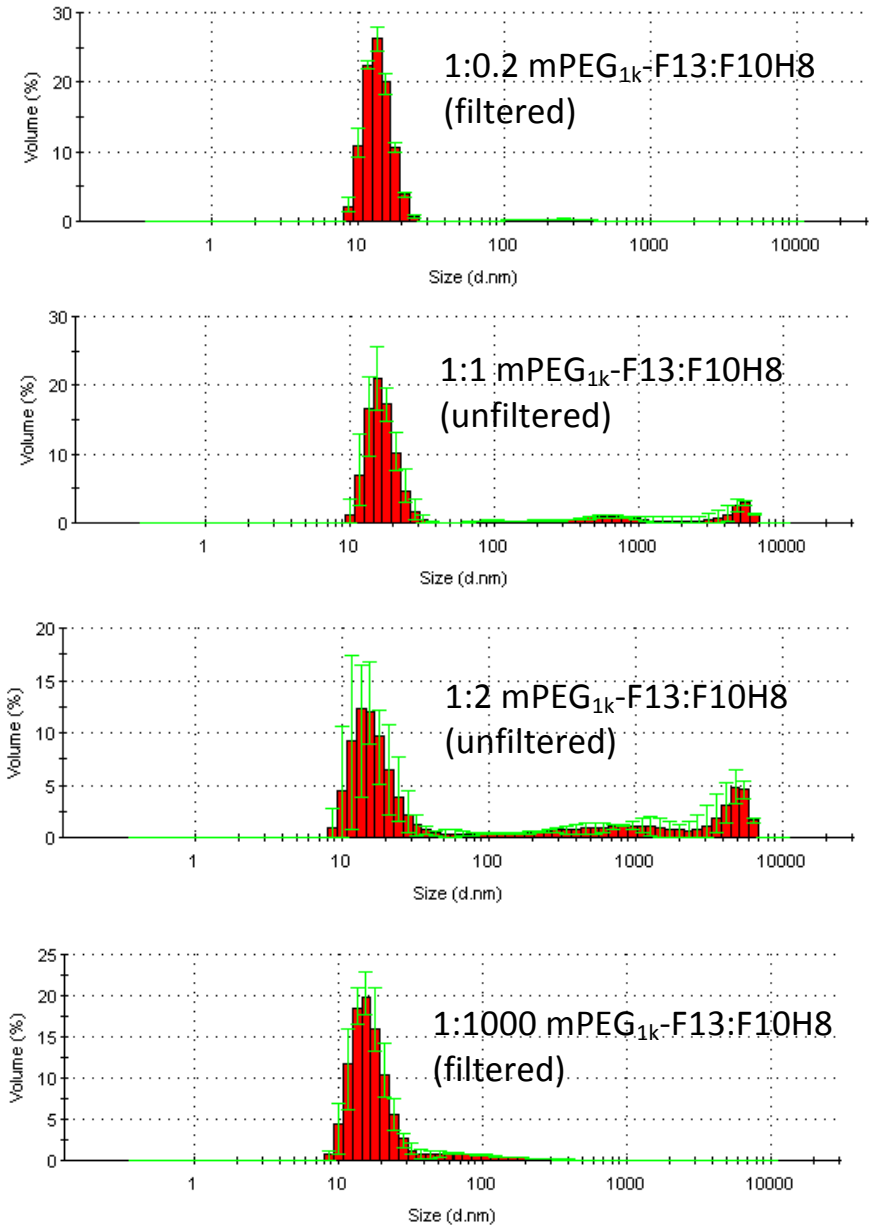

S3.2.2 Mixed micelle characterization: NMR method

The indirect analysis of the mixed micelles via DLS was not very informative; however, the results do not confirm the lack of formation of mixed micelles. It is possible that the mixed micelles form but do not significantly modify the size of the particles. Therefore, an alternative analysis using ^{19}F and ^{1}H NMR was used. A consistent 1:1 molar ratio of the two surfactants was used, and the method of preparation was altered slightly over 8 trials. The mixed aggregates were formed in D_2O to allow for direct NMR measurements of the prepared samples. The formation of mixed aggregates would be inferred by the broadening or chemical shift of various peaks specific to each of the surfactants.

Unfortunately, no indicative broadening or chemical shift of the protons of interest was observed in any of the trials. Additionally, due to the intensity and broadening of the protons of the PEG block, the signal-to-noise was greatly reduced for the protons of interest, making comparisons between the single-component and mixed aggregate NMR spectra difficult (one example spectra for Trial 8, which showed the largest change between single-component and mixed aggregate samples, is provided). There were small, broad peaks that appeared in the region of the hydrocarbon segment; however, no definitive mixing could be deduced (their appearance may simply be due to immiscible F10H8 droplets (dissolved in residual solvent, e.g. BTF) that were pushed through the filter). The aggregation also significantly reduced the signal to noise of the ^{19}F NMR, which did not give adequate resolution from baseline even with long scan times.

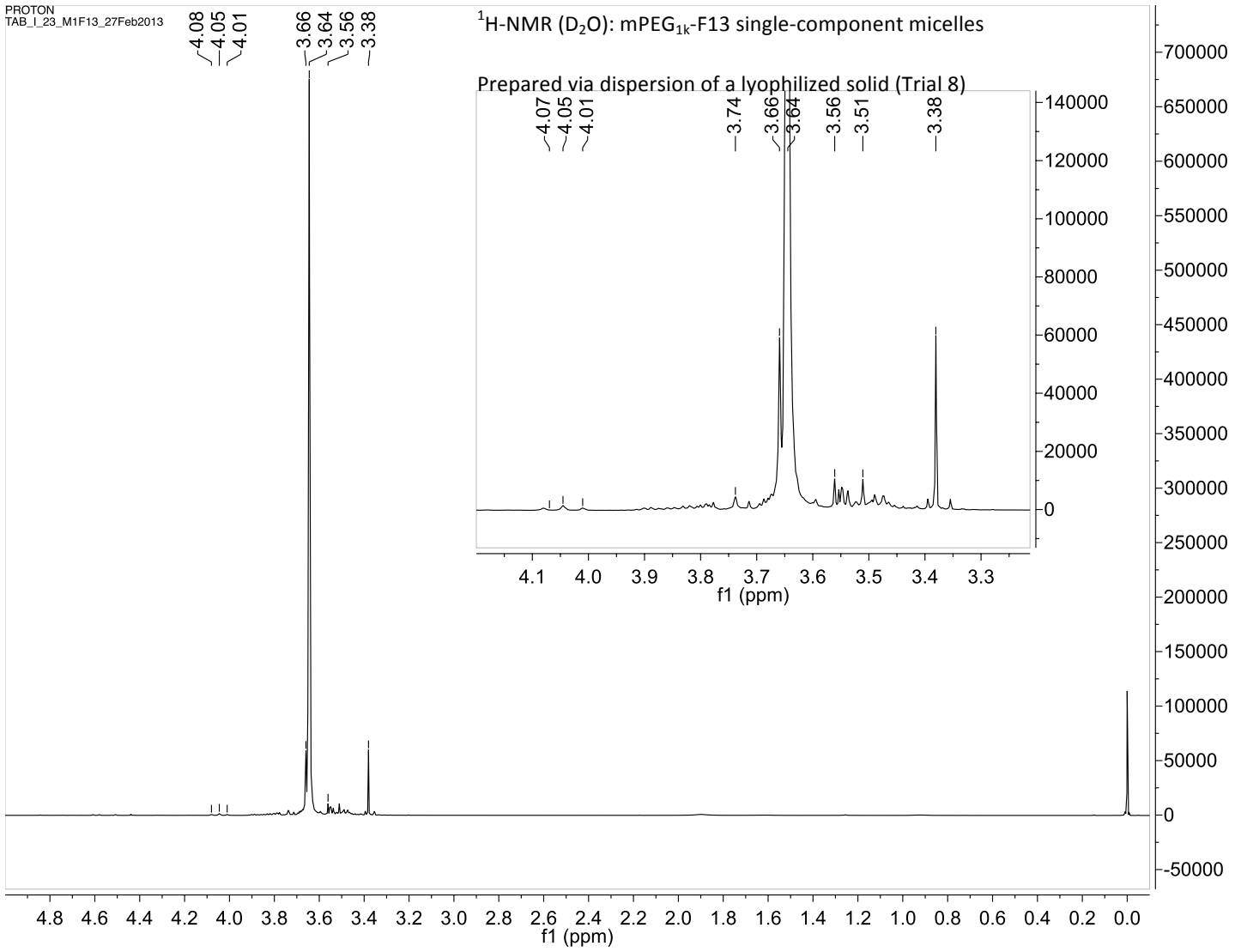
PROTON
TAB_I_23_M1F13_27Feb2013
4.08
4.05
4.01
3.66
3.64
3.56
3.38
^{1}H-NMR (D_2O): mPEG$_{1k}$-F13 single-component micelles
Prepared via dispersion of a lyophilized solid (Trial 8)
4.07
4.05
4.01
3.74
3.66
3.64
3.56
3.51
3.38
f1 (ppm)
f1 (ppm)

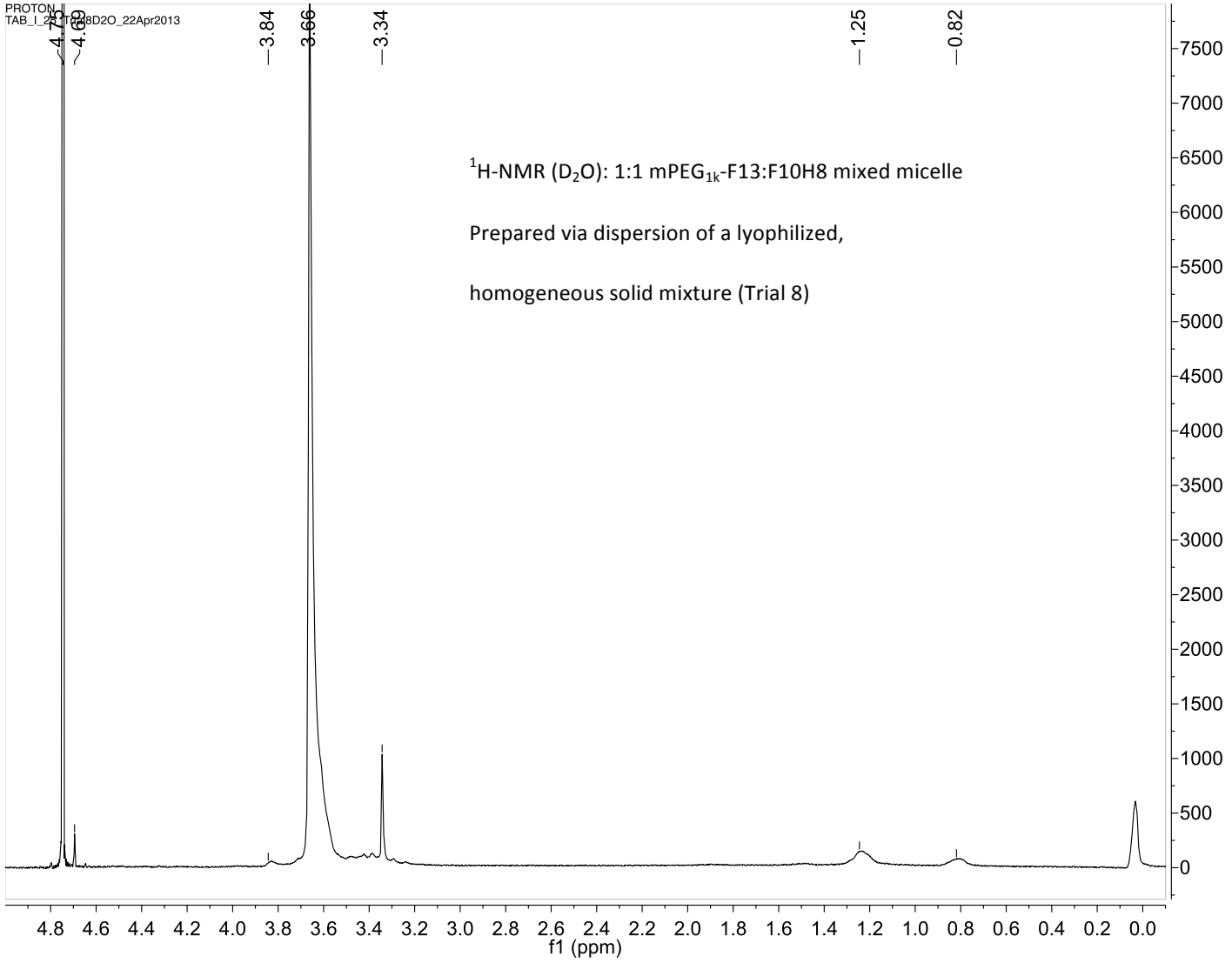
PROTON
TAB_I_25_TAB8D2O_22Apr2013
4.79
4.69
3.84
3.66
3.34
1.25
0.82
^{1}H-NMR (D_2O): 1:1 mPEG$_{1k}$-F13:F10H8 mixed micelle
Prepared via dispersion of a lyophilized,
homogeneous solid mixture (Trial 8)
f1 (ppm)

S3.3 Conclusion

The methods used appear to be inadequate to formulate the two-component fluorous mixed micelles. It may be possible to form stable mixed aggregates by a slow formulation process such as dialysis (possibly trapping a kinetically stable micelle self-assembly). Alternatively, the weak intermolecular interactions between fluorocarbons in comparison to hydrocarbons may prevent the formation of stable mixed micelles in a dual fluorinated surfactant system. In the previous system described by Riess *et al.* and Krafft *et al.* the mixed vesicle bilayer was formed by the interdigitation of the hydrocarbon segments from both surfactants.[2] In our case it could be more productive to form mixed micelles with a fluorous core and an intermediate hydrocarbon shell. A traditional amphiphile (consisting of a hydrophilic and hydrocarbon segment) and a hydrocarbon–fluorocarbon would comprise the binary surfactant system. The novel aspect in this system would be the formulation of micelles (rather than vesicles) and the possible application as theranostic particles if the PFtB moiety were installed.

S3.4 Experimental

S3.4.1 DLS Method: Sample preparation of Benzotrifluoride (BTF) mixed micelles via the solvent evaporation method

All samples were prepared by the solvent evaporation method. The solid surfactants were dissolved in BTF, the solvent was heated with spinning for 15 minutes, and then the solvent was removed under vacuum. After this time the film was cooled for 5 minutes and redispersed with 60˚C D_2O and allowed to equilibrate for 15 minutes. The aggregate system was then analyzed by DLS. Following, the solution was filtered with 0.45 μm nylon small volume syringe filter and measured again by DLS.

F10H8 single-component micelle: 1 mL of a 0.323 mg/mL BTF solution of F10H8 was diluted in 1 mL of BTF to afford a 0.25 mM solution. The film was redispersed with 1 mL of D_2O to afford a final solution of 0.51 mM.

$mPEG_{1k}$-F13 single-component micelle: 4 mg of $mPEG_{1k}$-F13 was diluted in 2 mL of BTF, and the film was dispersed with 1 mL of D_2O to afford a final 2.25 mM solution.

Mixed micelle systems: Ratio = $mPEG_{1k}$-F13: F10H8: The "Solution" mixed micelle was prepared by first making each component a solution in BTF and then mixing the two dissolved components together. Then the film was prepared as usual and dispersed with 1 mL of D_2O to afford the same concentration as the single-component samples for each component. The "Solid" mixed micelle was prepared by mixing to the two solids together and then dispersing the solid mixture with BTF. Then the film was prepared as usual. The "excess" mixed micelle was prepared using the "solid" preparation but F10H8 was used in a 1:1000 excess of $mPEG_{1k}$-F13. The 1:1 mixed micelle was prepared using the "solid" method but was not filtered. The 1:2 mixed micelle was prepared using "solid" method and was also not filtered.

S3.4.2 NMR Method:Mixed micelle preparation in D_2O

General procedure: $mPEG_{1k}$-F13 was weighed into a flask, and a solution of F10H8 in BTF was added to afford a 1:1 mole ratio mixture of $mPEG_{1k}$-F13:F10H8. This solution was then prepared using the solvent evaporation method. The film was then dispersed with 1 mL of 60°C D_2O and filtered with 0.45 μm nylon filter. The ^{19}F and ^{1}H NMR data was then collected in D_2O. After the initial NMR measurements, the filtered solution was also lyophilized over 2 days and then dissolved in 1 mL of $CDCl_3$. The ^{19}F and ^{1}H NMR data was then collected again.

Several trials were performed with varying modifications to the procedure as follows (scale is in mg of $mPEG_{1k}$-F13):

Trial 1:

- 4.0 mg scale (did not allow for quick NMR scans or proper integration)
- Between step 1 and 2 the BTF solution was sonicated for 10 min.

Trial 2:

- 4.1 mg scale (same problems as Trial 1)
- In step 4 the solution was filtered with a 0.20 μm nylon filter instead (This showed no significant difference in the NMR data).

Trial 3:

- 50.2 mg scale (allowed for quick NMR scans and better integration)
- In step 2, the bath was heated to 70°C.
- In step 3, 10 mL of D_2O was used.
- Between step 3 and 4, the sample was sonicated for 1 h. During this time the temperature was monitored: 20 min - 39°C, 40 min – 50 °C, 60 min - 56°C.
- In step 4, the solution was cloudy and white but became clear upon filtration.

Trial 4:

- 51.3 mg scale
- In step 2, the bath was heated to 70°C.
- In step 3, 10 mL of D_2O was used.
- Between step 3 and 4, the sample was sonicated and heated for 1 h. During this time the temperature was monitored: 20 min - 53°C, 40 min – 63 °C, 60 min - 65°C.
- In step 4, the solution was cloudy and white but became clear upon filtration, which was very difficult and required multiple filters.

Trial 5 (same as Trial 4 except with ACN instead of BTF)

- 53.8 mg scale

Trial 6 (same as Trial 4 except with chloroform instead of BTF)

- 52.5 mg scale

Trial 7 (instead of creating a thin-film using the solvent evaporation method, the mixed solutions were lyophilized to create a homogenous solid mixture of the two surfactants, which were then redispersed to form aqueous aggregates)

- 50.8 mg scale

Mixed solutions in chloroform were sonicated for 1 h with heat and then cooled to room temperature. The solution was frozen in a dry-ice acetone bath and lyophilized. The mixed solid was redispersed with 10 mL of 55°C D_2O. The solution was clear at first but began to precipitate over the next several minutes. The solution was sonicated for 1 h with heat, allowed to cool for 5 minutes and then filtered with a 0.45 μm syringe filter. NMR and DLS were used for analysis.

Trial 8 (same as Trial 7 except with BTF instead of chloroform)

- 57.9 mg scale
- only sonicated once

S3.5 Acknowledgements

Sincere thanks to my former undergraduate student, Troy Bemis, for his assistance with the described experiments.

S3.6 References

(1) Riess, J. G. Fluorinated Vesicles. *J. Drug Target.* **1994**, *2* (5), 455–468.

(2) Schmutz, M.; Michels, B.; Marie, P.; Krafft, M. P. Fluorinated Vesicles Made from Combinations of Phospholipids and Semifluorinated Alkanes. Direct Experimental

Evidence of the Location of the Semifluorinated Alkane within the Bilayer. *Langmuir* **2003**, *19* (12), 4889–4894.

(3) Jee, J.-P.; McCoy, A.; Mecozzi, S. Encapsulation and Release of Amphotericin B from an ABC Triblock Fluorous Copolymer. *Pharm. Res.* **2012**, *29* (1), 69–82.